

PLANT-MIMETIC GENERATION OF NEGATIVE PRESSURE IN WATER:
FROM FUNDAMENTAL THERMODYNAMICS TO APPLICATIONS IN
TRANSPORT AND HEAT TRANSFER

A Dissertation

Presented to the Faculty of the Graduate School

of Cornell University

In Partial Fulfillment of the Requirements for the Degree of

Doctor of Philosophy

by

I-Tzu Chen

May 2016

© 2016 I-Tzu Chen

**PLANT-MIMETIC GENERATION OF NEGATIVE PRESSURE IN WATER:
FROM FUNDAMENTAL THERMODYNAMICS TO APPLICATIONS IN
TRANSPORT AND HEAT TRANSFER**

I-Tzu Chen, Ph. D.

Cornell University 2016

When the pressure of a liquid is reduced below its saturation pressure, instead of forming vapor, the liquid can exist in a metastable state; at pressures below zero, the liquid becomes stretched and is under tension. This metastable liquid will eventually cavitate and return to stable equilibrium with vapor as the pressure falls to the stability limit. The behavior of water under tension and its cavitation limit are relevant to various topics in real life, e.g. the ascent of sap flow in trees. Also, scientists have pursued the use of liquid at negative pressure in technologies, e.g. synthetic ‘trees’ that allowed for water transportation with large negative pressure gradient (≥ 21 MPa).

Fundamentally, a picture of the structure of water’s phase diagram remains incomplete. To help elucidate the debate, researchers have used various techniques to place liquid water under tension to measure its properties; however experimental measurements for water stability limits obtained with different techniques show a large scatter. This dissertation reports the design and operation of a plant-mimetic experimental system which enables tests of water stability limits by the metastable vapor-liquid equilibrium method with nanoporous silicon membranes. This system provides a practical platform to place static, bulk volumes of liquid into metastable region that can be studied, manipulated and coupled to existing technologies.

Also presented is the design and analysis of superheated loop heat pipes (SHLHPs); the SHLHP captures the main attributes of transpiration in trees. A steady-state model

was developed for both conventional LHPs and SHLHPs; our analytical model shows that SHLHPs could exploit negative pressure working fluid to achieve efficient heat transfer over long distance and against large acceleration, and extend the limitations of conventional LHPs imposed by thermodynamic properties of the working fluid.

Finally, this dissertation presents the development of SHLHP prototypes. A central challenge in the experimental realization of SHLHPs is the membrane that allows reliable use of liquid in metastable regions. Two-layer silicon membranes were fabricated to form MEMS-based SHLHPs. Also introduced is an experimental system designed to study SHLHP performances, enabling us to demonstrate the use of liquid at negative pressure in heat transfer technologies.

BIOGRAPHICAL SKETCH

I-Tzu was born September 16th, 1987 in Taipei, Taiwan. She received her B.S. degree from National Taiwan University (NTU) in Chemical Engineering. She started the Ph. D. program in Chemical Engineering at Cornell in fall, 2010. She was intrigued by this question, “If plants can do it, why don’t we?” asked Prof. Abe Stroock. She decided to join Stroock group and began work on projects she takes great pride in – the study on the fundamental thermodynamics of stability limits of water, and the modeling and development of heat transfer systems which mimic trees.

To my parents, 陳金順 & 吳秀華

ACKNOWLEDGMENTS

Abe, thank you for just about everything. During those times I'd really like to give up finishing my PhD, you always found me, encouraged me in your own way, and motivated me to do more than my best. Prof. William Olbricht and Prof. Brian Kirby, thank you for forming my committee and for your helpful discussion as well as interesting (and inspiring) stories shared with me during my A and B exams.

My lab mates, past and present: Dave, the most valuable things I've learned during my PhD were learned from you, so my special thanks go to you. Vikram, Pavithra, Vinay, Eugene, Michael, Erik, Olivier, Winston, Hanwen and Siyu, thank you for forming the best group ever; being the most anti-social Asian girl you've ever met, I'm so thankful that my lab mates were you – always helpful, supportive and open. The vascular subgroup, thank you for all the mind-opening talks (back when we still had group meetings) and your support during my exams. Zack Sonner, Zach Shermann and Jiamin, thank you for being the brightest undergrads I've ever seen.

I'd like to thank Glenn for his custom-machined pieces and well-crafted jigs, and for fixing my bike in a blink. I also thank the staff members of Cornell Nanoscale Science and Technology Facility (CNF) and Nanobiotechnology Center (NBTC) for the suggestions on device fabrications and on doing experiments in general. I'd like to extend my gratitude to Shelby, Carol, Sally, Sue and Johanna for being patient with me and handling all my department paper works.

Finally, I thank all my friends in Ithaca for making my experience at Cornell a memorable one. Special thanks go to Po, Rachel, Jiun-Ruey, Kay, Lindy, Patricia, Julia, Sarah, Joyce, Li-An, Jerry, Kan-Heng, Alice, Henry, Ko-Hsin, and my cat Duke. Please help me remember all the important details of the unimportant things we've been through together.

TABLE OF CONTENTS

1 Introduction: Negative Pressure – A Metastable Liquid State	1
1.1 Stability Limit of Water at Negative Pressure.....	5
1.1.1 Water’s phase diagram – a major scientific challenge	5
1.1.2 Experimental methods to generate tension and discrepancies between results.....	7
1.2 Technological Applications of Water at Negative Pressure.....	11
1.3 Heat Pipes – Challenges and Opportunities	19
1.3.1 Operation and limitations of conventional heat pipes	19
1.3.2 A-tree-in-a-pipe – opportunities with negative pressure working fluid	25
1.4 Dissertation Outline.....	25
2 Design and Modeling of Superheated Loop Heat Pipes	27
2.1 Introduction	27
2.2 Design and Operating Principles	30
2.3 Specifics of Sub-Saturated SHLHP Design	37
2.3.1 Nanoporous membrane.....	37
2.3.2 Regulator	40
2.4 Model and Analysis for Steady-State Operation.....	41
2.4.1 Mass, heat and momentum balances	42
2.4.2 Local thermodynamic equilibria.....	46
2.4.3 Linear analysis and expression of LHP effective thermal resistance ..	48
2.4.4 Comparison between the R_{eff} of conventional LHPs and SHLHPs	55
2.5 Results and Discussion.....	56

2.5.1 Comparison of the response of conventional LHPs and SHLHPs	58
2.5.2 Validity of SHLHP linear response	61
2.5.3 Contributions of loop elements to R_{eff} for SHLHPs	63
2.5.4 Impact of activity pinned by the regulator and negative pressures in the liquid.....	65
2.5.5 Limits of operation of SHLHP	69
2.6 Conclusions	70
Notation	72
3 Stability Limit of Water by Metastable Vapor-Liquid Equilibrium with Nanoporous Silicon Membranes	76
3.1 Introduction	76
3.2 Theory	80
3.2.1 Metastable vapor-liquid equilibrium (MVLE)	80
3.2.2 Kinetic theory of the homogeneous nucleation	84
3.2.3 Other mechanisms of cavitation	85
3.3 Experimental Methods	87
3.3.1 Sample fabrication.....	87
3.3.2 Vapor control system.....	90
3.3.3 Determination of probability of cavitation	95
3.4 Results and Discussion.....	95
3.4.1 Characterization of free-standing porous silicon membrane.....	95
3.4.2 Cavitation event history and survival probability curve.....	97
3.4.3 Spatial heterogeneity	105
3.4.4 Comparison of temperature-dependence of cavitation threshold across different methods.....	109

3.4.5 Other mechanisms of cavitation	112
3.5 Conclusions	114
4 Superheated Loop Heat Pipe Prototype – Design of Porous Silicon Wick Structure and Experimental System.....	116
4.1 Introduction	116
4.2 A Review – Formation and Structural Properties of Porous Silicon.....	118
4.3 Porous Silicon Wick Design and Fabrication.....	124
4.3.1 Materials and methods.....	124
4.3.2 KOH-etched cavities coupled with porous silicon membrane	126
4.3.3 Multilayer porous silicon membrane.....	129
4.3.4 Two-layer porous silicon membrane.....	132
4.4 Results and Discussion.....	134
4.4.1 Challenges with the KOH-cavity and the multilayer designs	134
4.4.2 Effect of etching parameters on the structure of porous silicon.....	139
4.4.3 Two-layer porous silicon membrane characterizations.....	142
4.5 Experimental System Studying SHLHP Performance	152
4.6 Integration of Nanoporous Materials onto Porous Silicon Membrane and SHLHP Prototype.....	162
4.6.1 Porous anodic aluminum oxide	167
4.6.2 Graphene oxide membrane.....	174
4.6.3 Other potential candidates	177
4.7 Conclusions	181
5 Summary and Conclusions.....	183
5.1 Summary of Study Regarding Stability Limits of Water under Tension ...	183

5.2 Summary of Modeling and Experimental Work for Superheated Loop Heat Pipe	185
5.3 Speculation on the Future of Technologies Exploiting Liquid at Negative Pressure	188
APPENDIX	191
A.1 Lumped Parameter Analysis for SHLHP Startup Response	191
A.1.1 Mathematical model	191
A.1.2 Results and discussion	192
A.1.3 Conclusions	196
A.2 Maple and Mathematica Scripts Used for SHLHP Modeling	197
A.2.1 Steady state calculations for conventional LHPs and SHLHPs (Maple)	197
A.2.2 Linear analysis and expression of SHLHP effective thermal resistance (Maple)	207
A.2.3 Lumped parameter analysis (Maple)	213
A.2.4 Steady state calculations for conventional LHP, saturated and unsaturated MEMS-based SHLHPs (Mathematica).....	217
A.3 MATLAB Scripts	226
A.3.1 Image processing and cavitation history analysis	226
A.3.2 Survival probability curves fitting (CNT, modified CNT with surface tension distribution, and five-point logistic regression).....	231
A.3.3 Randomness index analysis	235
A.4 Modified Liquid Path Pattern for a SHLHP Prototype	237
REFERENCES	238

LIST OF FIGURES

Figure 1.1: Phase diagram of water and vapor-liquid equilibria.	4
Figure 1.2: Competing scenarios proposed to explain water anomalies.	6
Figure 1.3: Experimental methods studying liquid under tension.	10
Figure 1.4: Comparison of the cavitation pressure of water as a function of temperature obtained with different techniques.	13
Figure 1.5: Negative pressure values measured in plants and on octopus sucker.	16
Figure 1.6: Transpiration through a synthetic tree. ¹³	18
Figure 1.7: Schematics of a heat pipe (A) and a loop heat pipe (B).	20
Figure 1.8: (A) Effect of elevation on the trend of steady-state operating temperature. (B) Temperature oscillation at the evaporator and compensation chamber.	24
Figure 2.1: Schematic cross-sectional views of (a) a conventional LHP, (b) a saturated SHLHP and (c) a sub-saturated SHLHP.	28
Figure 2.2: Schematic representations of working cycles on P - T diagram for (a) conventional LHPs, (b) saturated SHLHPs, and (c) sub-saturated SHLHP.	32
Figure 2.3: P - T diagrams for conventional LHP and SHLHP steady state operation. (a) Evolution of the working cycle with increasing adverse acceleration, g_{total} . (b) Evolution of the working cycle with decreasing sink temperature, T_{sink}	35
Figure 2.4: Schematic diagrams of the nanoporous membranes required in the evaporator of the saturated SHLHP and in both the evaporator and condenser of the sub-saturated SHLHP.	39
Figure 2.5: Effect of the adverse acceleration (ranging for 0 to 1 time gravity) on conventional LHP, saturated SHLHP and sub-saturated SHLHP with (a) ammonia and (b) water as working fluid.	57
Figure 2.6: Comparison of the total effective thermal resistance for conventional LHP and saturated SHLHP varying acceleration (a-b) and sink temperature (c-d), with ammonia and water as the working fluid.	60
Figure 2.7: Predicted effective thermal resistances of (a) saturated SHLHP and (b) sub-saturated SHLHP as a function of the sink temperature, T_{sink}	62

Figure 2.8: Total effective thermal resistances of sub-saturated SHLHP (Eq. (2.32)) with water (red curve) and ammonia (blue curve) as working fluid.	66
Figure 2.9: Liquid pressure profile in sub-saturated SHLHP as a function of (a) sink temperature, T_{sink} , and (b) heat load.....	68
Figure 3.1: Metastable vapor-liquid equilibrium (MVLE).....	78
Figure 3.2: Mechanisms of cavitation.	83
Figure 3.3: Fabrication of free-standing porous silicon membrane and membrane-coupled voids.....	89
Figure 3.4: Vapor control system.	92
Figure 3.5: Top (A) and cross-sectional (B) views of the free-standing porous silicon membrane taken by scanning electron microscopy (SEM).....	96
Figure 3.6: Temporal evolution of cavitation events.....	99
Figure 3.7: Survival probability (Σ) for water in porous silicon/glass sample as a function of the liquid pressure (P_{liq}).....	102
Figure 3.8: Variations in cavitation threshold.	108
Figure 3.9: Comparison of the largest tension (the most negative pressure) of liquid water as a function of temperature obtained with different techniques.....	110
Figure 4.1: (A) Typical I - V curve for p-type silicon. (B) Silicon dissolution scheme propose by Lehmann and Gösele ¹⁰⁷	121
Figure 4.2: (A) Schematic diagram showing the cross-sectional view of the electrochemical etch cell. (B) Picture of the actual setup.	125
Figure 4.3: (A) Relation of KOH-etched cavity opening width with mask opening width. (B) Process flow for the KOH-etched cavities coupled with porous Si membrane. ..	128
Figure 4.4: (A) Process flow for the multilayer porous silicon membrane. (B) Macropores filled with nanoporous structure (left) or hollow (right).	130
Figure 4.5: Process flow for SHLHP prototype with two-layer porous silicon membranes.....	133
Figure 4.6: (A) Cross-sectional view of the KOH-etched cavities and porous silicon membrane taken by scanning electron microscopy (SEM). (B) Bottom view of nanoporous membrane from the KOH-etched side taken by optical microscope.	135

Figure 4.7: Cross-sectional views of the multilayer porous silicon membrane taken by scanning electron microscopy (SEM).	138
Figure 4.8: Scanning electron micrographs of the interface between bulk and porous silicon for p-type silicon substrates of different doping levels with different anodization conditions.	143
Figure 4.9: Variation of the etch rate of macroporous silicon layers with (A) current density and (B) silicon substrate resistivity.	144
Figure 4.10: Scanning electron microscopy (SEM) images of the two-layer silicon membrane. (A-B) Cross-sectional views of the two-layer structure; (C) cross-sectional (left) and top (right) views of the nanoporous silicon layer.	146
Figure 4.11: Operating curves and liquid pressures at the membrane surface (insert) for conventional and saturated SHLHP designs with MEMS-based form factor.	148
Figure 4.12: Two-layer silicon membrane stability test.	151
Figure 4.13: Design schematics for a prototype MEMS-based SHLHP with two-layer silicon membranes.	154
Figure 4.14: Custom-made SHLHP assembly to study SHLHP prototype performance.	157
Figure 4.15: Schematic diagrams for the experimental setups: (A) open-loop design; (B) closed-loop design.	161
Figure 4.16: Survival probability for water in SHLHP prototypes as a function of the liquid pressure at room temperature.	164
Figure 4.17: Device images (top view) during stability tests of the two-layer membranes bonded to glass substrates etch with SHLHP liquid paths (A) and individual voids (B).	165
Figure 4.18: Schematic diagrams showing idealized structure of (a) porous anodic aluminum oxide (AAO) on Al foil and (b) cross-sectional view.	168
Figure 4.19: Process flow for AAO-integrated SHLHP prototype with multi-layer porous silicon membranes.	170
Figure 4.20: Top (A) and cross-sectional views (B-D) of the porous AAO-integrated multilayer silicon membranes taken by scanning electron microscopy (SEM). (E) Top view of a sputtered aluminum film with large grain size and the porous AAO membrane formed with it (F).	172

Figure 4.21: (A) Permeability of GO membrane with respect to water and various small molecules. (B) Schematic view for possible permeation of water molecules through the laminates. (C-D) Top and cross-sectional views of the GO membrane taken by scanning electron microscopy (SEM).....	175
Figure 4.22: Static layer by layer assembly method to form polyelectrolyte multilayer membranes.....	179
Figure 4.23: Device images (top view) during stability tests of the two-layer membrane bonded to glass substrate etched with individual voids before (A) and after (B) PEM coating.	180
Figure A.1: (a) Analogous circuit of a SHPHP. (b-c) Transient temperature profiles for SHPHP as a function of time.....	195
Figure A.2: Modified mask design to branch the liquid path network in a SHLHP. .	237

LIST OF TABLES

Table 3.1: Fitting parameters for survival probability curves at different temperatures	104
Table 4.1: Variations of the pore diameter and the etch rate of nanoporous silicon with silicon substrate resistivity	140
Table 4.2: Variations of the pore diameter of nanoporous silicon with electrolyte composition and current density.....	141
Table 4.3: Comparing the contact thermal resistance between the copper finger tips and the silicon membrane.....	159

CHAPTER 1

INTRODUCTION: NEGATIVE PRESSURE – A METASTABLE LIQUID STATE

The tallest tree in the world is a coast redwood (*Sequoia sempervirens*) in Northern California that was measured at over 115 meters (in 2006). When we consider the liquid pressure in the leaf at the very top of this giant tree, one can do a simple estimation based on high school physics – in a continuum column of liquid, the hydrostatic pressure difference between the top and bottom of the column is related to the column height: $P_{bottom} - P_{top} = \rho g H$, where P is hydrostatic pressure, ρ is density of the liquid, g is gravitational acceleration and H is column height. When the tree is transpiring, it pumps water continuously from the root to the top; as the pressure at the root is around 1 atm (atmospheric pressure), we can find that the pressure at the leaf is estimated to be at ~ -11 atm: plants exploit liquid water at negative pressure to remain hydrated in their daily lives.

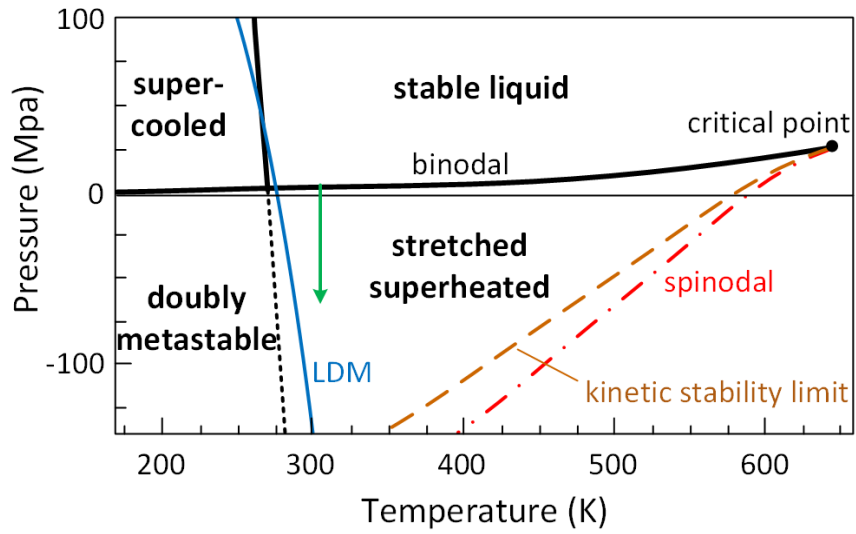
Liquid at negative pressure is in a thermodynamically metastable state. Liquid water in its metastable state is something we are familiar with: when you place a bottle of water in the fridge for a few days, it may remain a liquid until you shake or pour it; in this situation the water is cooled below its melting point and remains a metastable, supercooled liquid. On the other hand, if you heat up a cup of water in the microwave, it remains liquid but may generate a dangerous splash as it is disturbed; the water is heated above its boiling point and becomes a metastable, superheated liquid. A less familiar way to superheat liquid, is to reduce the pressure of a liquid below its saturation pressure; instead of forming vapor immediately, the liquid can exist in its metastable state.¹ In this situation, the liquid is superheated and, at pressures below zero, the liquid

becomes stretched and is under mechanical tension. This thermodynamic path is how plants generate negative pressure in their leaves.

Figure 1.1 shows the schematic phase diagrams of water and illustrates the generation of negative pressures in liquid water following isotherms (green lines with arrows). Figure 1.1(A) is the schematic pressure-temperature cut showing the binodal (thick black solid curve) separating the stable liquid and the metastable liquid regions. The red dashed-dot curve is the spinodal, the thermodynamic stability limit of a metastable liquid; beyond the spinodal the liquid is no longer mechanically stable ($(\partial P_{liq} / \partial \tilde{V}_{liq})_T = 0$, where P_{liq} is the pressure of the liquid, \tilde{V}_{liq} is the molar volume of the liquid, and T is the temperature). The blue solid curve is the line of liquid density maxima (LDM). The kinetic stability limit predicted by homogeneous nucleation theory is represented as the brown dashed curve positioned between the binodal and spinodal. Figure 1.1(B) is schematic pressure-volume cut showing the vapor-liquid coexistence dome (thick black solid curve) and isotherms (thin black solid curves). Saturated liquid is in equilibrium with saturated water vapor in air (the blue points a and a' at the two ends of a tie line); for a liquid at negative pressure, it reaches metastable equilibrium with sub-saturated vapor, as illustrated with blue points b and b'. The metastable liquid will eventually “break” and return to stable equilibrium with vapor by cavitation, the nucleation of vapor bubbles, as the pressure falls to the cavitation limit (i.e. stability limit) – the pressure at which cavitation inevitably occurs.

The properties of water in its negative pressure region of the phase diagram are largely unknown, and the use of water at significant negative pressure is not found in current human technologies. Among many open questions regarding water at negative pressure, recent experiments have questioned the exact value of the stability limit of water. In the Section 1.1, I discuss some techniques used to explore this exotic state and studies of the stability limit of water at negative pressure based on these techniques.

(A)



(B)

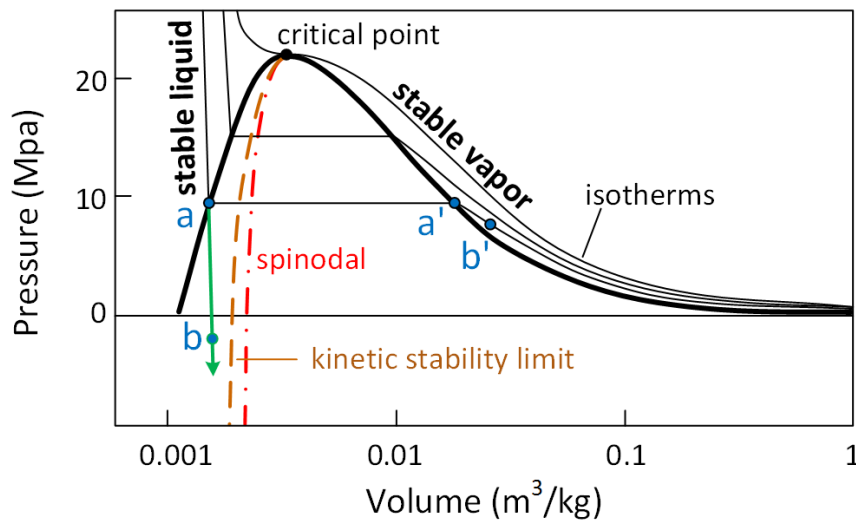


Figure 1.1: Phase diagram of water and vapor-liquid equilibria.

(A) Schematic pressure-temperature cut showing the binodal (thick black solid curve), the spinodal (red dashed-dot curve), and an isotherm (green line with arrow) illustrating the generation of the metastable state of superheated liquid water under tension. The spinodal is the thermodynamic stability limit of a metastable liquid. Beyond the spinodal the liquid is no longer mechanically stable. The blue solid curve is the line of liquid density maxima (LDM). The kinetic stability limit predicted by homogeneous nucleation theory is represented as the dashed curve positioned between the binodal and spinodal. (B) Schematic pressure-volume cut showing the vapor-liquid coexistence dome (thick black solid curve) and isotherms (thin black solid curves). The green curve with an arrow illustrates the generation of metastable liquid water; the pairs of blue points (a-a' or b-b') indicate liquid states (a or b) in thermodynamic equilibrium with vapor states (a' or b').

In Section 1.2, I cover the use of liquid at negative pressure both in nature and in technological context, which motivates the proposal of an application of metastable liquid in heat transfer technology. In Section 1.3, I give a brief review on the operation and limitations of conventional two-phase heat transfer system, and introduce the concept of exploiting metastable liquid. Finally, I conclude this introductory chapter with a summary of the following chapters in Section 1.4.

1.1 Stability Limit of Water at Negative Pressure

1.1.1 Water's phase diagram – a major scientific challenge

We are all familiar with water. Water affects virtually every aspects of our lives, and at the same time water presents numerous anomalous properties. In the metastable state of supercooling, many thermodynamic and dynamic properties of liquid water differ in their dependence with temperature from that expected of simple liquids. At a common temperature of 228K and at ambient pressure, extrapolations of measurements of these properties even appear to diverge beyond the limit of “no-man’s land” (where ordinary measurements are no longer possible because of homogeneous nucleation of the stable crystalline phase).²

Understanding the phase diagram could help us explain the origin of these anomalies. Figure 1.2 shows a few different possible phase diagrams of water that have been proposed to explain water anomalies (for a detailed review one can refer to the work by Debenedetti, 2003²). The stability-limit conjecture (Figure 1.2(A)) states that if the LDM reaches the liquid-vapor (LV) spinodal at negative pressure, the spinodal reaches a minimum and bends to lower tension at lower temperature; the re-entrant of the spinodal at positive pressure provides a line of instability on which several thermodynamic functions would diverge. Figure 1.2(B) shows the second critical-point scenario, which proposes that the LDM bends to lower temperatures at larger tension

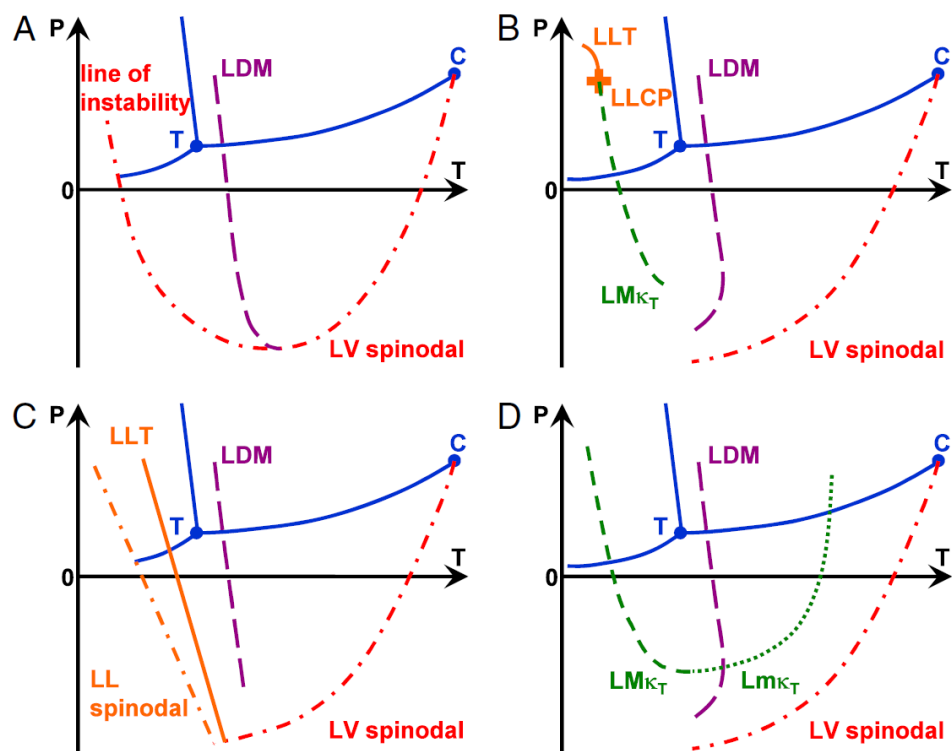


Figure 1.2: Competing scenarios proposed to explain water anomalies.

(A-D) Schematic pressure-temperature cut of phase diagram of water showing the binodal (solid blue curves), the triple point, T, and the liquid-vapor critical point, C. (A) Stability-limit conjecture. (B) Second critical-point scenario. (C) Critical-point free scenario. (D) Singularity-free interpretation.

Abbreviations: LDM – the line of liquid density maxima; LV spinodal – liquid-vapor spinodal; LLT – liquid-liquid transition; LLCPP – liquid-liquid critical point; LM_{κ_T} – the line of isothermal compressibility maxima; LL spinodal – liquid-liquid spinodal; Lm_{κ_T} – the line of isothermal compressibility minima.

This figure adapted from: Pallares, G.; El Mekki Azouzi, M.; Gonzalez, M. A.; Aragonés, J. L.; Abascal, J. L. F.; Valeriani, C.; Caupin, F. Anomalies in Bulk Supercooled Water at Negative Pressure. *Proc. Natl. Acad. Sci.* **2014**, *111* (22), 7936–7941.

and the LV spinodal remains monotonic; the anomalies of supercooled water are due to the vicinity of an liquid-liquid critical point (LLCP) terminating a first order transition line (liquid-liquid transition, LLT). From this LLCP emanates the locus of maxima of the correlation length called the Widom line, on which thermodynamic functions exhibit peaks, such as the line of isothermal compressibility maxima along isobars (LM_{κ_T}). Figure 1.2(C) shows the critical-point free scenario. This is the case where the LLCP falls beyond the LV spinodal. The liquid-liquid (LL) spinodal associated with the LLT causes the divergence of several thermodynamic functions. Figure 1.2(D) shows the singularity-free scenario, which proposes that there is no LLT or LLCP; thermodynamic functions do not diverge, but several exhibit extrema as an inevitable consequences of the existence of density anomalies (LDM) – the LDM reaches its highest temperature when it crosses one of the lines of isothermal compressibility extrema along isobars (i.e., the case with the line of isothermal compressibility minima (Lm_{κ_T}) is demonstrated in Figure 1.2(D)).

To discriminate between these scenarios, many experiments with water or water proxies were conducted. Among these experiments, the recent work by Pallares *et al.*³ with water-filled inclusions in quartz provided evidence for the hypothesis of a second critical point lying at deep supercooling and positive pressures, and suggested that the negative pressure region is a promising experimental territory to put further constraints on or rule out remaining scenarios.

1.1.2 Experimental methods to generate tension and discrepancies between results

Researchers have used a variety of techniques to place liquid water under tension to measure the properties of liquid water at negative pressure and its cavitation limit (i.e., the stability limit).⁴ An extensive review on experimental methods studying water under tension can be found in recent reviews^{4,5}. Here, I refer to a few widely-used methods,

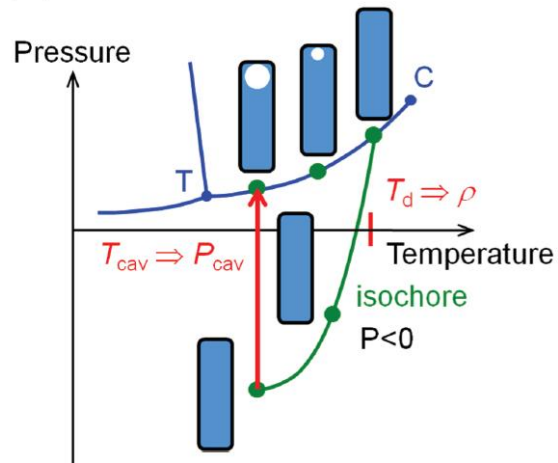
as illustrated in Figure 1.3: 1. Berthelot tube method⁶⁻⁹, in which a rigid container (e.g. sealed glass capillaries and water inclusions in mineral crystal) filled with coexisting liquid and vapor in equilibrium is heated until the vapor bubble disappears, and then cooled following an isochoric path to decrease the liquid pressure until cavitation is observed. 2. Centrifugal method^{10,11}, based on the isothermal extension of water in z-shape tube rotating at high speed. Maximum tension is exerted at the axis of rotation due to the centrifugal force. 3. Acoustic method^{5,12,13}, a dynamic method to quench liquid water to negative pressure with standing or traveling acoustic waves. 4. Metastable vapor-liquid equilibrium (MVLE)¹⁴⁻¹⁶, a method developed to mimic the transpiration mechanism by which the leaves generate the negative pressure that pulls sap up a tree. As the internal bulk liquid water is placed in equilibrium with external sub-saturated vapor (vapor activity, $a_{vap} = \text{relative humidity}/100 = p_{vap}/p_{sat} < 1$, where p_{vap} [Pa] is the actual vapor pressure and p_{sat} [Pa] is the saturation vapor pressure on the binodal) through a porous membrane, its pressure, P_{liq} [Pa], will be below the binodal. The relationship between p_{vap} and P_{liq} can be estimated using Kelvin equation:

$$P_{liq} = p_{vap} + \frac{RT}{v_{liq}} \ln(a_{vap}) \quad (1.1)$$

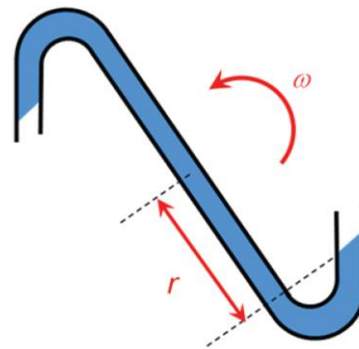
where R [J mol⁻¹] is the ideal gas constant, T [K] is the temperature, and v_{liq} [m³ mol⁻¹] is the molar volume of liquid water; see Chapter 3.2 for more details.

The experimental measurements for water stability limits obtained with these different methods show large scatter. Among all experiments, only the experiments in quartz inclusions^{8,17} frequently measure stabilities as low as -140 MPa, consistent with that predicted by theory (e.g. the classical nucleation theory¹ predicts -168 MPa at room temperature for liquid volume of $\sim 10 \mu\text{m}^3$ and liquid lifetime of ~ 1 s) or simulations¹⁶⁻

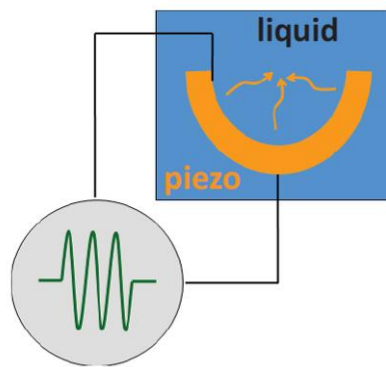
(A)



(B)



(C)



(D)

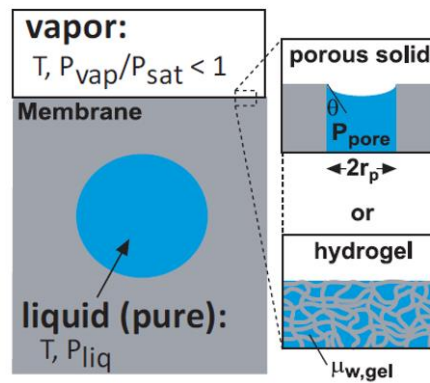


Figure 1.3: Experimental methods studying liquid under tension.

(A) Berthelot tube. A rigid container partially filled with a liquid in equilibrium with its vapor is heated until the liquid expands to fill the entire volume. Upon cooling, the liquid follows an isochore and its pressure decreases. T : the triple point; C : the liquid-vapor critical point; T_d : the dissolution temperature; T_{cav} : the temperature at which cavitation occurs. (B) Centrifugal method. A tube formed with two symmetrical bends at each end (a z-tube) is spun around its mid-point such that the pressure in the liquid drops due to the centripetal acceleration acting on the column of liquid. r : the distance between the center and the liquid-gas interface. (C) Acoustic method. A hemispherical piezoelectric transducer emits focused ultrasound bursts (yellow arrows) into a bulk liquid. (D) Metastable vapor-liquid equilibrium. A nanoporous membrane or gel mediates the equilibrium of a bulk volume of liquid and its sub-saturated vapor. $\mu_{w,gel}$: chemical potential of water contained in hydrogel.

This figure adapted from: Caupin, F.; Stroock, A. The Stability Limit and Other Open Questions on Water at Negative Pressure. *Liq. Polymorph. Adv. Chem. Phys.* **2013**, *152*, 51–80.

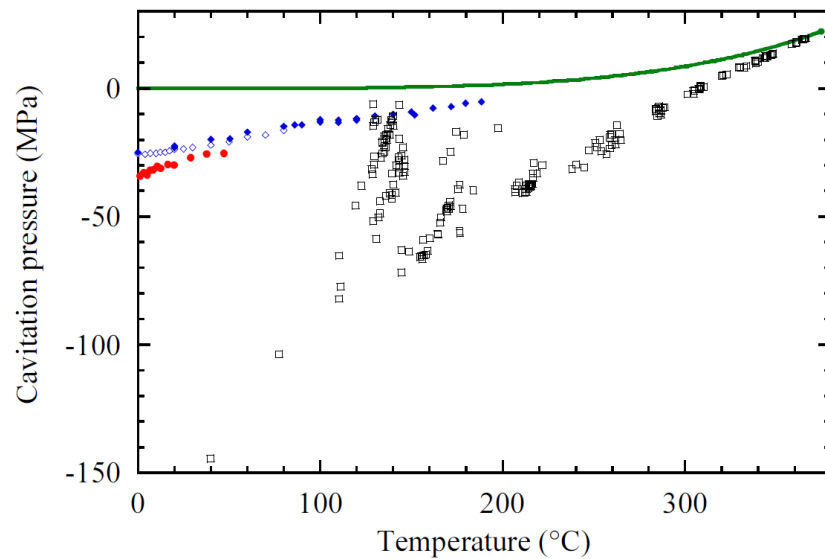
¹⁸. Figure 1.4(A) compares the measurements of the stability limit by Berthelot method in quartz inclusions and the acoustic method; the quartz inclusions appear to give a much more negative stability limit. The majority of the experiments, despite the variety of experimental approaches, have observed stability limits around -20 to -30 MPa^{10,12,13,16,21–25}, a far less negative value compared to theoretical predictions. Thus, in all the systems except for quartz inclusions, there is some other mechanism that limits stability and sets a “practical” stability limit. The mechanism for this limit has not been identified and represents an important outstanding question – fundamental and practical – about metastable liquid water.

Figure 1.4(B) compares the results obtained for the cavitation pressure with different methods,²⁶ excluding those performed in quartz inclusions. Among these experiments that show low stability, there are two sets of data showing contradictory temperature-dependence of the stability limit: Briggs¹⁰ reported a remarkable 10-fold decrease in the maximum tension observed between 6°C and 0°C; in contrast to this abrupt change in the stability limit, Davitt *et al.*²⁴ found a monotonic increase (more negative) trend in the stability limit as temperature approached 0°C. To compare with these two contradictory results and to provide new insights into the debate of the stability limit of water, I present a study of the stability limit of liquid water with the MVLE method in Chapter 3.

1.2 Technological Applications of Water at Negative Pressure

The behavior of liquid under tension and its cavitation limit are relevant to various contexts in nature and in human lives. The first example, as introduced at the beginning of the introduction, is the transpiration and ascent of sap flow in trees.²⁷ Plants utilize the negative pressures in water to transport water from roots to leaves, against gravity. With no turbine to pump water around, it is the loss of water that generates the negative

(A)



(B)

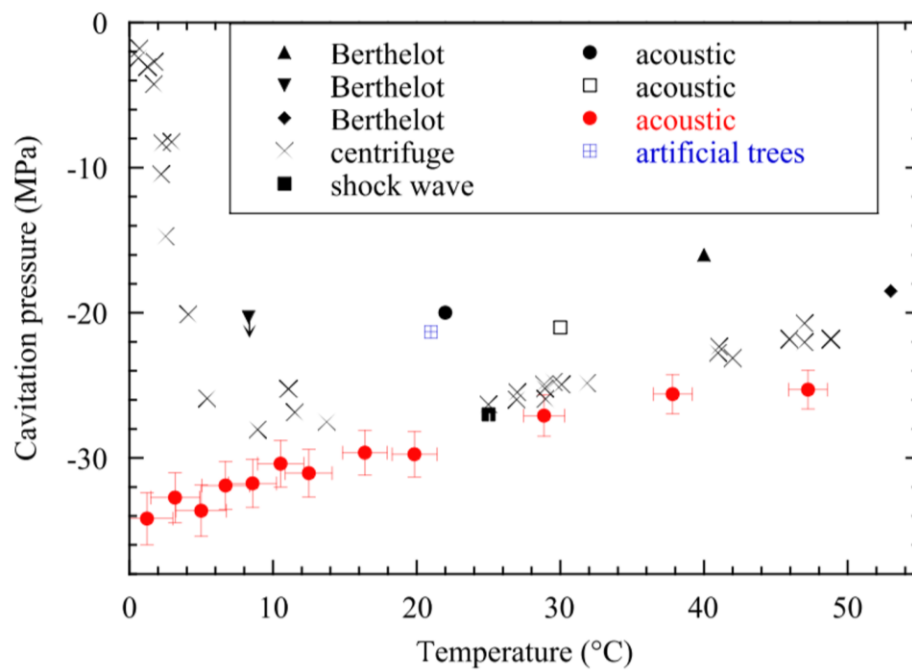


Figure 1.4: Comparison of the cavitation pressure of water as a function of temperature obtained with different techniques.

(A) Comparison of the cavitation pressure of water obtained with acoustic method and quartz inclusions used as Berthelot tubes. The symbols represent: acoustic method with calibration by static pressure method (open diamonds⁵ and solid blue diamonds²⁴), acoustic method with fiber optic probe hydrophone (red bullets²⁸), quartz inclusions (open squares⁸). Green line is the binodal. (B) Cavitation pressure of water for different experiments. The symbols represent: Berthelot tubes (triangles²¹, inverted triangles²², diamonds²³), centrifuge (crosses¹⁰), shock wave (solid squares²⁹), acoustic method (solid black circles¹², open squares¹³, solid red circles²⁴), and artificial trees with MVLE method (blue crossed squares¹⁵). An arrow means that cavitation was not observed. The solid circles represent the pressure converted with IAPWS EoS from the density measurements using the fiber optic probe hydrophone.²⁸

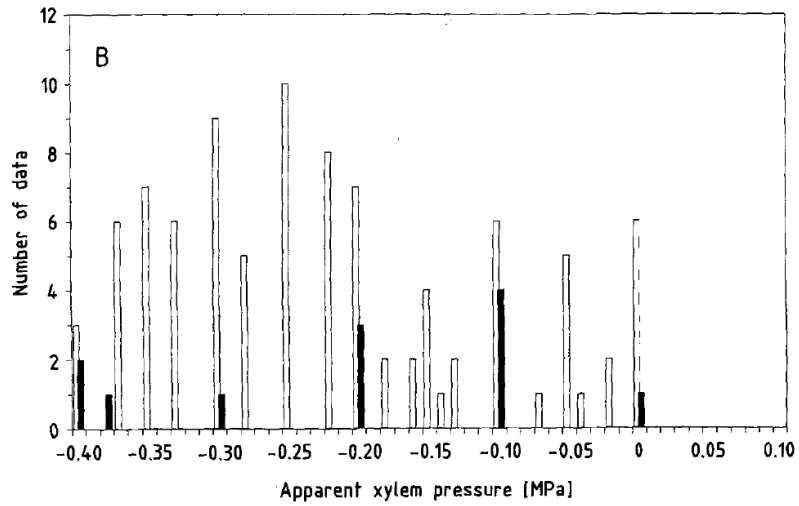
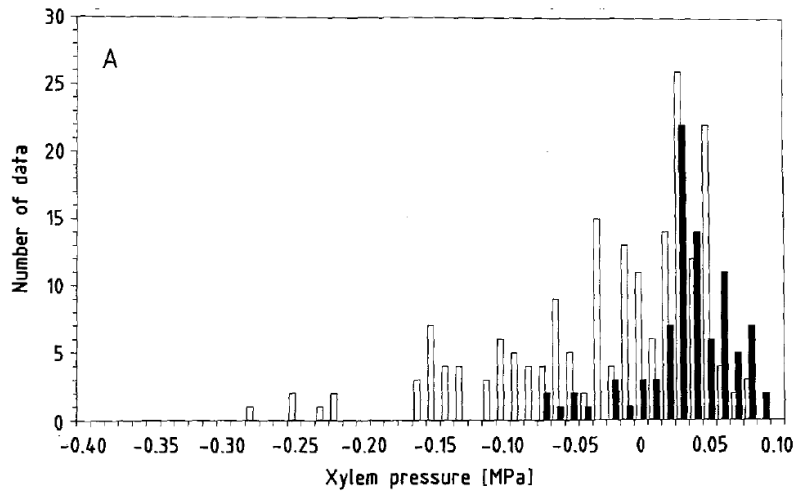
(A) adapted from: Caupin, F.; Stroock, A. The Stability Limit and Other Open Questions on Water at Negative Pressure. *Liq. Polymorph. Adv. Chem. Phys.* **2013**, *152*, 51–80.

(B) adapted from: Caupin, F.; Arvengas, A.; Davitt, K.; Azouzi, M. E. M.; Shmulovich, K. I.; Ramboz, C.; Sessoms, D. A.; Stroock, A. D. Exploring Water and Other Liquids at Negative Pressure. *J. Phys. Condens. Matter* **2012**, *24* (28), 284110.

pressure of the liquid within the leaf; this reduced pressure pulls liquid water out of the soil and up the xylem to maintain hydration. Figure 1.5(i) shows the distribution of the pressure values measured either with the pressure probe (A) or the pressure bomb (B) in the xylem of the petiole (open columns) and of the stem (filled columns) of well-watered *Nicotiana* plants; a few bars of negative pressure is observed repeatedly, and for the same plants which had not been watered for a while the pressure can be even lower.³⁰ Another example is the suckers on Cephalopod limbs;³¹ octopuses are able to generate tension in the sea water between the suckers and surfaces through the mechanical expansion of the suckers. This suction helps them catching prey, hold onto the ground and to move around. As shown in Figure 1.5(ii), pressure as low as -2.6 bar was measured under a real octopus sucker. Other examples relevant to negative pressure liquid and its cavitation include the drying stresses in unsaturated porous materials like soil and concrete³²⁻³⁵, and hydrodynamic cavitation in hydraulic valves and around propeller blades^{36,37}.

Also, scientists have pursued the use of liquid at negative pressure in technologies. The mechanical suction pump invented in 1970 by Hayward was able to generate -0.07 MPa of pressure;³⁸ this invention was the first human made system able to transport flow of water with negative pressure gradient. A few decades later, the synthetic ‘tree’ was created by Wheeler and Stroock (Figure 1.6(A)); this system allowed for continuous extraction of liquid water from sub-saturated vapor, transducing it into negative pressures liquid, and transporting it with large negative pressure gradient (21 MPa or higher); mass flow and evaporative heat flux as a function of the temperature at the leaf of a synthetic tree are presented in Figure 1.6(B).¹⁵ This system demonstrated proof-of-principle for technologies that could exploit transpiration at large negative liquid pressure, such as high performance liquid chromatography, microfluidic pumping, and water extraction and purification. There is also possibility to exploit negative pressure

(i)



(ii)

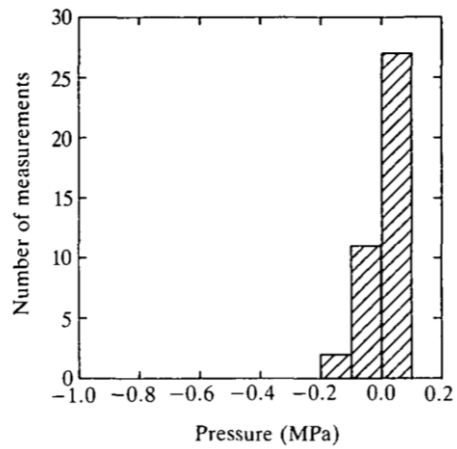


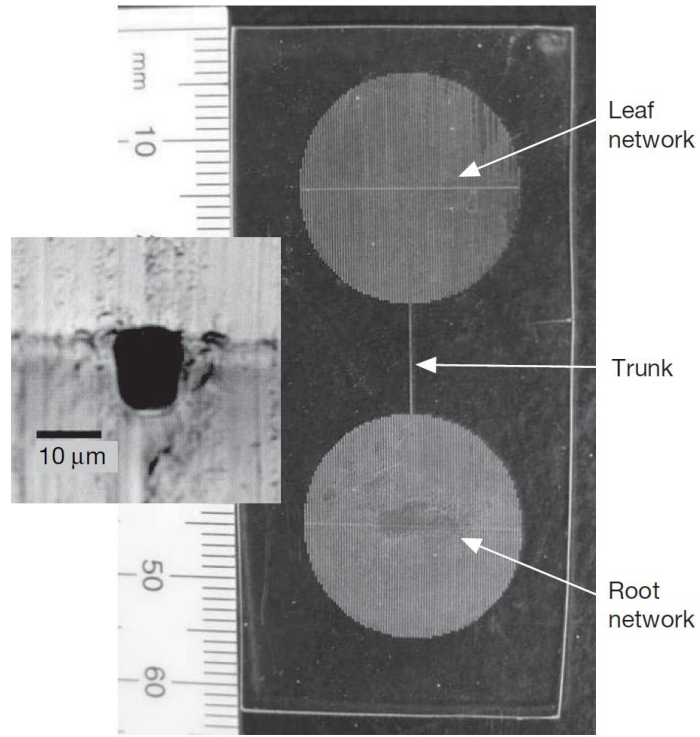
Figure 1.5: Negative pressure values measured in plants and on octopus sucker.

(i) Distribution of the pressure values measured either with the pressure probe (A) or the pressure bomb (B) in the xylem of the petiole (open columns) and of the stem (filled columns) of well-watered *Nicotiana* plants. (ii) The distribution of pressures measured under octopus suckers attached to epoxy.

(i) adapted from: Balling, A.; Zimmermann, U. Comparative Measurements of the Xylem Pressure of *Nicotiana* Plants by Means of the Pressure Bomb and Pressure Probe. *Planta* **1990**, *182* (3), 325–338.

(ii) adapted from: Smith, A. M. Negative Pressure Generated By Octopus Suckers: A Study of the Tensile Strength of Water in Nature. *J. Exp. Biol.* **1991**, *157* (1), 257–271.

(A)



(B)

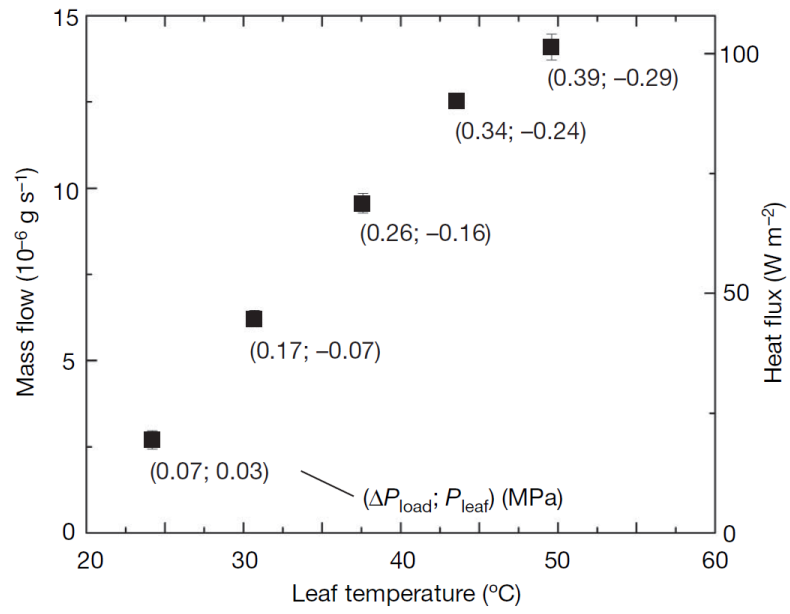


Figure 1.6: Transpiration through a synthetic tree.¹⁵

(A) Optical photograph of a synthetic tree: a transparent sheet of hydrogel (poly(hydroxyethyl methacrylate), 1mm thick) containing a void in the form of a microchannel network at its mid-plane. The structures of the networks in the root and leaf are identical: 80 parallel channels of varying length arranged to form a circle and connected by a single orthogonal channel. The inset shows an optical micrograph of the cross-section of one microchannel (dark area). (B) Mass flow rate of water and heat flux driven by transpiration from a reservoir of pure liquid water above the root to a stream of air with $a_{vap} = 0.95$ above the leaf, plotted against the temperature maintained beneath the leaf section. The root membrane was punctured at the center of the root network. The pressure drop across the trunk, ΔP_{load} , and the pressure at the entrance of the leaf network, $P_{leaf} = P_{atm} - \Delta P_{load}$, are reported next to each data point. The dimensions of the trunk channel in this experiment were: the effective hydraulic diameter = 14.5 μm and length = 3 cm.

This figure adapted from: Wheeler, T. D.; Stroock, A. D. The Transpiration of Water at Negative Pressures in a Synthetic Tree. *Nature* **2008**, *455* (7210), 208–212.

liquid in wick-based heat pipe technology to achieve efficient heat transfer over long distance and against large acceleration.³⁹ The motivation behind this application is discussed in the next section (Section 1.3).

1.3 Heat Pipes – Challenges and Opportunities

Advances in technologies for transferring heat play a central role in the progress of many fields. For example, the rate of heat transfer can limit the practical speed of integrated circuits, systems for the storage of portable energy, the operational conditions of vehicles, environmental controls in buildings, and efficiency of industrial processes.^{40–48} Furthermore, the volume, mass, and complexity of conventional heat exchangers based on sensible heat transfer can place undesirable constraints on these applications.

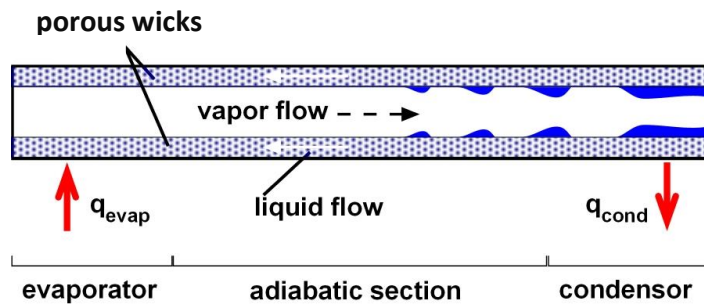
1.3.1 Operation and limitations of conventional heat pipes

Among many different technologies transferring heat, heat pipes (HPs) – closed-circuit systems in which a working fluid transfers its latent heat as it cycles between an evaporator and a condenser – have offered an attractive alternative in an array of applications.⁴⁹ As shown in the schematic of heat pipes (Figure 1.7(A)), the central components required for HPs are wick structures that allow for the existence of a pressure difference, ΔP_c [Pa] between the liquid and vapor phases of the working fluid based on capillarity, as described approximately by the Young-Laplace law:

$$\Delta P_c = 2\gamma \cos \theta_c / r_p \quad (1.2)$$

where γ [Pa m] is the surface tension of the liquid, θ_c is the contact angle and r_p [m] is the radius of the pore. This capillary pressure can drive the working fluid around its

(A)



(B)

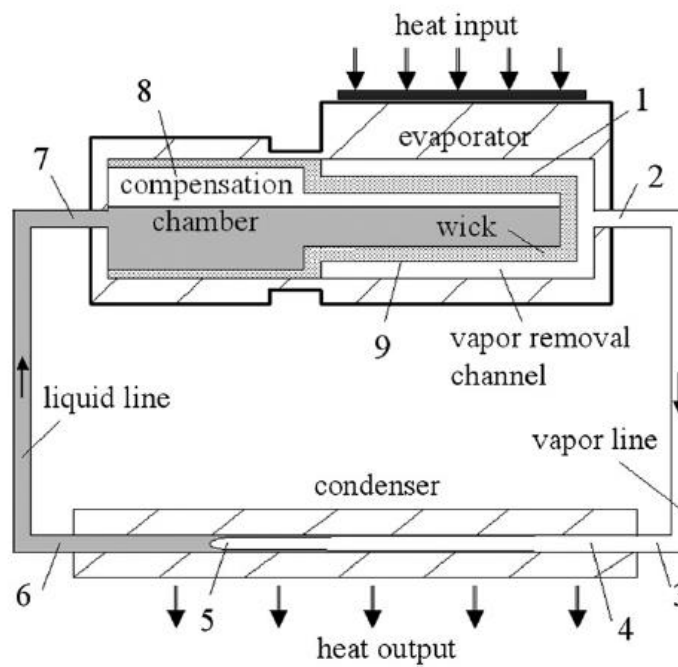


Figure 1.7: Schematics of a heat pipe (A) and a loop heat pipe (B).

(B) The numbers in the diagram correspond to the different location in the loop – 1: start of vapor channel in evaporator; 2: start of vapor line; 3: start of condenser; 4: start of condensation; 5: end of condensation; 6: end of condenser; 7: end of liquid line; 8: compensation chamber; 9: liquid at outer surface of the wick

(B) adapted from: Launay, S.; Sartre, V.; Bonjour, J. Parametric Analysis of Loop Heat Pipe Operation: A Literature Review. *Int. J. Therm. Sci.* **2007**, *46* (7), 621–636.

cycle if a difference of temperature exists between the evaporator and the condenser. The applications of conventional HPs have been constrained regarding the length (typically, < 1 m) and their orientation with respect to gravity or acceleration. The main origins of these limitations are: 1) the use of wicks with large pores ($r_p > 1 \mu\text{m}$) limits magnitude of ΔP_c (e.g., $\Delta P_c < 1$ bar from Eq. (1.2) with $\gamma = 0.072$ [Pa m] at 25°C and $\theta_c = 0^\circ$ for water on a perfectly wetting surface) such that dry out of the wick in the evaporator occurs as the viscous pressure drop grows with length of the pipe and the heat load and as the gravitational pressure drop grows with the length of the pipe and adverse acceleration along its axis. 2) The presence of liquid in the vapor path can obstruct the flow of vapor and increase the conductive thermal resistance at the condenser wall.

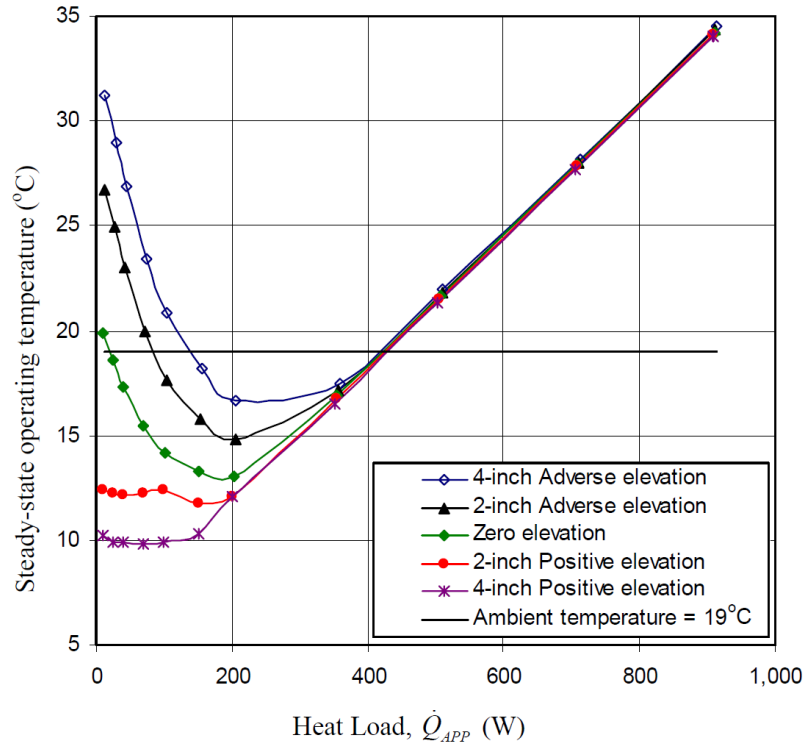
Loop heat pipes (LHPs) have been developed to extend the limits of conventional HPs.^{50,51} To meet the goal of operating effectively over large distance and under any orientation or against acceleration, the main design rules of LHPs⁵¹ (Figure 1.7(B)) are: 1) minimization of the distance that the liquid must move within the wick by placing a thin membrane in the evaporator separating macroscopic conduits for the liquid and vapor; such designs allow for the use of smaller pore diameters in the wick without introducing excessive hydraulic resistance. 2) The introduction of a compensation chamber in the cycle; this chamber accommodates excess working fluid and allows the system to adapt to changing heat loads and temperatures.

LHPs have been shown to provide robust operation and improved performance relative to conventional heat pipes, including higher heat load capacities and compatibility with a wider variety of architectures for adaptation to specific applications.⁵¹ However, in conventional LHPs, vapor-liquid coexistence in the compensation chamber forces the thermal cycle to remain close to the saturation and leads to two important constraints on operation:^{50,52} 1) the motive temperature head

condition, that the pressure difference across the wick membrane is the driving force required to push the fluid motion through vapor and liquid paths. Given that at each sides of the membrane the pressures are near saturated, their temperature difference is determined by the shape of the saturation curve. 2) The sub-cooling condition requires that the heat leaked through the wick membrane into the compensation chamber to be balanced by the sensible heat of returning cold working fluid; this balance implies that the sub-cooling of the liquid grows with the temperature difference across the wick. Combined with the motive temperature head condition, the required sub-cooling is coupled to the pressure driving force as well (see Chapter 2.2 for more detailed explanations for these two conditions).

These two conditions can lead to strong dependence of the global thermal resistance of LHPs on the pressure drop along the liquid flow due to viscous drag and adverse acceleration, and result in the characteristic U-shaped operating curves. Figure 1.8(A) shows the effect of elevation of the evaporator relative to the condenser on the operating temperature of a conventional LHP.⁵³ As the pressure difference across the wick membrane increases due to adverse elevation, the difference in saturation temperatures also increases, which induces an increased heat leak. Since the liquid enthalpy entering to the compensation chamber does not change, the compensation chamber temperature increases in order to provide enough subcooling to compensate for the increased heat leak; at high heat loads, as the gravitational head becomes negligible compared to the frictional pressure drop, the difference in saturation temperatures across the wick becomes independent of the adverse gravitational acceleration. Additionally, in the condenser of a conventional LHP, the film of condensate can add a significant thermal resistance to the heat transfer, and the unbounded vapor-liquid interfaces can cause undesired oscillations during the startup or in response to heat load steps,⁵⁴⁻⁵⁶ as shown in Figure 1.8(B).

(A)



(B)

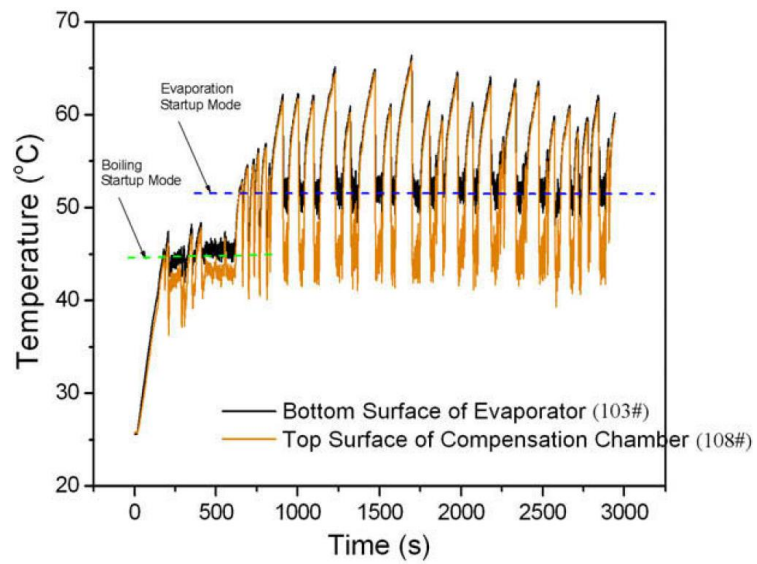


Figure 1.8: (A) Effect of elevation on the trend of steady-state operating temperature. (B) Temperature oscillation at the evaporator and compensation chamber.

(A) adapted from: Chuang, P.-Y. A. An Improved Steady-State Model of Loop Heat Pipe Based on Experimental and Theoretical Analyses, 2003.

(B) adapted from: Li, J.; Wang, D.; Peterson, G. P. Experimental Studies on a High Performance Compact Loop Heat Pipe with a Square Flat Evaporator. *Appl. Therm. Eng.* **2010**, *30* (6-7), 741–752.

1.3.2 A-tree-in-a-pipe – opportunities with negative pressure working fluid

Plants provide inspiration to solve the problems of conventional HPs and LHPs – the operating concepts of a loop heat pipe partially resemble the transpiration process in vascular plants: in the evaporator, or in the leaf, water absorbs heat and evaporates; in the condenser, or at the root, water condensed from the vapor phase is being transferred back to the evaporator or up to the leaf. Unlike in a conventional LHP where a difference in saturation temperature must be established to push the fluid around, in trees, it is the reduction of pressure in the leaves that pulls sap flow up from the roots and overcomes gravity, viscous drag, and even the reduced chemical potential of water in sub-saturated soils. In brief, what is being proposed here is essentially “a tree in a pipe”, which can act like trees and utilize liquid’s ability to sustain negative pressure. The modifications of conventional LHPs to achieve such a plant-inspired loop LHP and a model for steady state operation are described in Chapter 3.

1.4 *Dissertation Outline*

The starting point of my research was the proposal of the plant-mimetic heat pipe system, which is dealt with first in this dissertation. In Chapter 2, I present the design and the model analysis of the superheated loop heat pipe, a heat transfer technology exploiting working fluid at negative pressure to extend the limitations confronting conventional loop heat pipe operation. In Chapter 3, I turn to discuss the open questions regarding fundamental thermodynamics of water at negative pressure, and present a study on the kinetic stability of water, including the design of a new experimental system and the results of temperature-dependence of the stability limit with the metastable vapor-liquid equilibrium (MVLE) method. On top of the theoretical basis provided in Chapter 2 and 3, in Chapter 4, I summarize the experimental development on the materials, device fabrications and experimental platforms of silicon-based

superheated loop heat pipe prototypes. Finally in Chapter 5, I conclude the dissertation by summarizing the main results and providing ideas and directions for future work in this field.

CHAPTER 2

DESIGN AND MODELING OF SUPERHEATED LOOP HEAT PIPES

Adapted from *AIChE J.* **2014**, *60* (2), 762–777

2.1 Introduction

In Chapter 1.3, I introduced the motivation of loop heat pipes (LHPs) exploiting negative pressure liquid. In this chapter, I present the design and analysis of such plant-inspired LHPs that would exploit nanoporous membranes to allow for operation with large capillary pressures and superheated liquid. I also explore, with a mathematical model, the impact of three modifications of conventional LHPs to achieve superheated LHPs: 1) reduction of the diameter of pores in the wick membranes such that larger capillary pressures (Eq. (1.2)) can be maintained between the liquid and the vapor. By using nanoporous materials, the maximum capillary pressures could extend to several hundred bars (e.g. $r_p < 10$ nm for water as working fluid). The increased pressure difference developed by fine pores could extend the operational range of LHPs with respect to heat load, length, and adverse acceleration by resisting dry-out from the surfaces of the wicks. 2) Removal of the compensation chamber such that the entire liquid path can become superheated and hence decoupled from the saturation curve. I will illustrate how this Superheated Loop Heat Pipe (SHLHP – Figure 2.1b) would eliminate the temperature head condition and the sub-cooling condition of conventional designs of LHPs and could substantially decrease the effective thermal conductance at low heat flow and large adverse acceleration. 3) Addition of a nanoporous membrane at the condenser and a regulator of the charge of the pipe such that the entire vapor path and the condenser would remain sub-saturated (Figure 2.1c). The absence of liquid in

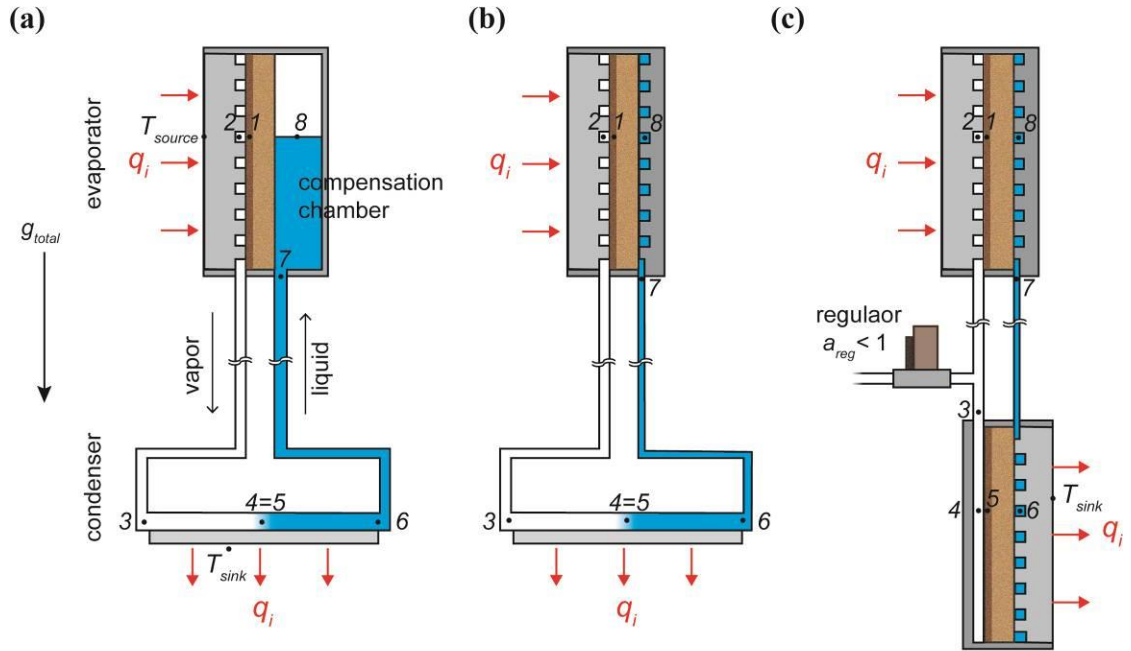


Figure 2.1: Schematic cross-sectional views of (a) a conventional LHP, (b) a saturated SHLHP and (c) a sub-saturated SHLHP.

An acceleration, g_{total} [m s^{-2}] acts along the pipe axis. Heat enters at the evaporator with a rate q_i [W]. The LHP (a) and saturated SHLHP (b) have identical condenser designs. The saturated SHLHP (b) and sub-saturated SHLHP (c) have identical evaporator designs with nanoporous coating to allow for sub-saturated liquid. In the sub-saturated SHLHP (c), a regulator connected to the vapor path pins the vapor pressure at an activity of a_{reg} . All the external surfaces except the heat input and output surfaces are assumed to be ideally insulated. The numbers used in this figure corresponds to those used in Figure 2.2.

the vapor path in this sub-saturated version of the SHLHP could eliminate the added conductive resistances due to condensate film in the condenser (we characterize this effect) and the instabilities that are observed during changes in heat load (this transient phenomenon lies outside the scope of our steady state analysis).

There exist a number of foreseeable challenges for the successful realization of both the SHLHP (Figure 2.1b) and sub-saturated SHLHP (Figure 2.1c). Of particular note are: the potential for increased hydraulic resistance relative to conventional wicks and the increased proneness to dry-out due to boiling along the superheated liquid path. In Section 2.2 and Section 2.3, I discuss specific designs aimed at overcoming these challenges. To motivate the possibility that LHPs could operate reliably with nanoporous wicks and superheat, I note that vascular plants operate with liquid at negative pressures (a superheated state) in their xylem vessels with membranes in their leaves and roots that separate the metastable liquid inside the plant from sub-saturated external phases.^{27,57} In the process of transpiration (motion of water from the soil to the atmosphere through a plant), a plant serves as a wick: at the leaf (evaporator), reduced pressure in the internal liquid drives flow up from the roots against gravity and the viscous drag in the xylem conduits; in the roots (condenser), reduced pressure transmitted from the leaf allows for the extraction of nearly pure liquid from the sub-saturated soils or sea water (e.g., in the case of mangroves). Many species operate regularly with pressures down to -50 bars in the liquid water within their xylem.⁵⁸ Were a plant enclosed within a fixed volume of vapor, it could act as the liquid path of a sub-saturated SHLHP as in Figure 2.1c. We have demonstrated wicking at large negative pressures in a synthetic system inspired by the operation of plants:¹⁵ using an organic gel as a nanoporous membrane, we showed that water could be transported at steady state from a sub-saturated condenser chamber to a further sub-saturated evaporator chamber with pressures in the liquid reaching ~ -70 bars. The success of vascular plants

in managing superheated liquid and our proof-of-principle demonstration motivate our investigation here of the potential benefits that could be derived from operating LHPs with substantial superheat if boiling and dry-out could be avoided. In the *Results and Discussion* (Section 2.5) and the *Conclusions* (Section 2.6), I discuss the challenges of manipulating superheated liquid.

2.2 Design and Operating Principles

Figure 2.1 shows schematic representations of a conventional LHP (Figure 2.1a) and two designs of SHLHPs, one with no membrane in the condenser (saturated SHLHP, Figure 2.1b) and one with an additional membrane in the condenser and a regulator (sub-saturated SHLHP, Figure 2.1c). All three designs separate the liquid and vapor paths such that one can use solid-walled conduits for the vapor and liquid paths instead of having a porous structure throughout. We consider the possibility of nanoporous wick membranes in all three cases. The design of the saturated SHLHP in Figure 2.1b differs from the conventional design (Figure 2.1a) only in the elimination of the compensation chamber from the liquid side of the evaporator. This design allows the liquid to become superheated throughout the liquid path, unpinning the liquid in the evaporator (Point 8) from the coexistence curve of the working fluid. This design closely resembles that of conventional HPs (non-loop designs), except for the separation of the liquid and vapor paths by a non-porous wall outside of the evaporator region. Excess liquid volume would collect in the condenser, as in conventional HPs. The sub-saturated SHLHP in Figure 2.1c includes two additional elements: a regulator to maintain a fixed degree of sub-saturation in the system and a nanoporous membrane in the condenser. These modifications allow the system to be sub-saturated throughout and free from film condensation. Details of these two modifications are described in Section 2.3.

Figure 2.2 illustrates an idealized form of the working cycles of conventional LHPs (Figure 2.2a), the saturated SHLHP (Figure 2.2b) and the sub-saturated SHLHP (Figure 2.2c), with same pressure differences across the vapor path (ΔP_{2-3}) and the liquid path (ΔP_{6-7}) and the same condenser temperature. These cycles will allow us to gain a qualitative understanding of the differences between these designs. The numbered points in the cycles correspond to state of the working fluid at the labeled points in Figure 2.1. We begin by following the cycle for the conventional case and then point out the important differences in the cycles of the proposed SHLHP designs: In the evaporator, the capillary action holds the meniscus of the liquid in the pores at the wick surface from which evaporation occurs; this liquid is represented as Point 1 and is near thermodynamic equilibrium with Point 2, the vapor in the evaporator. The vapor at Point 2 is slightly sub-saturated due to curved menisci (this departure from the saturation curve is often neglected in the literature and Point 2 is placed on the saturation curve). Path 2-3 represents the adiabatic motion of the vapor in the vapor path. As the vapor enters the condenser, the temperature drops until condensation occurs at a macroscopic, vapor-liquid interface on the co-existence line (Point 4 is the vapor; Point 5 is the liquid). Path 5-6 represent sub-cooling of the liquid before it leaves the condenser. The latent heat released upon condensation is evacuated to a sink. Path 6-7 represents the adiabatic motion of the liquid in the liquid path. As the liquid enters the evaporator at Path 7-8, it is heated by the heat conducted through the wick membrane. Due to the presence of vapor in the compensation chamber, Point 8 is brought to saturation. Path 8-1 corresponds to the liquid motion through the wick membrane to the evaporating meniscus; the liquid confined within the wick membrane becomes superheated.

The working cycle for the conventional design (Figure 2.2a) illustrates three important conditions for the operation of a conventional LHP:¹¹

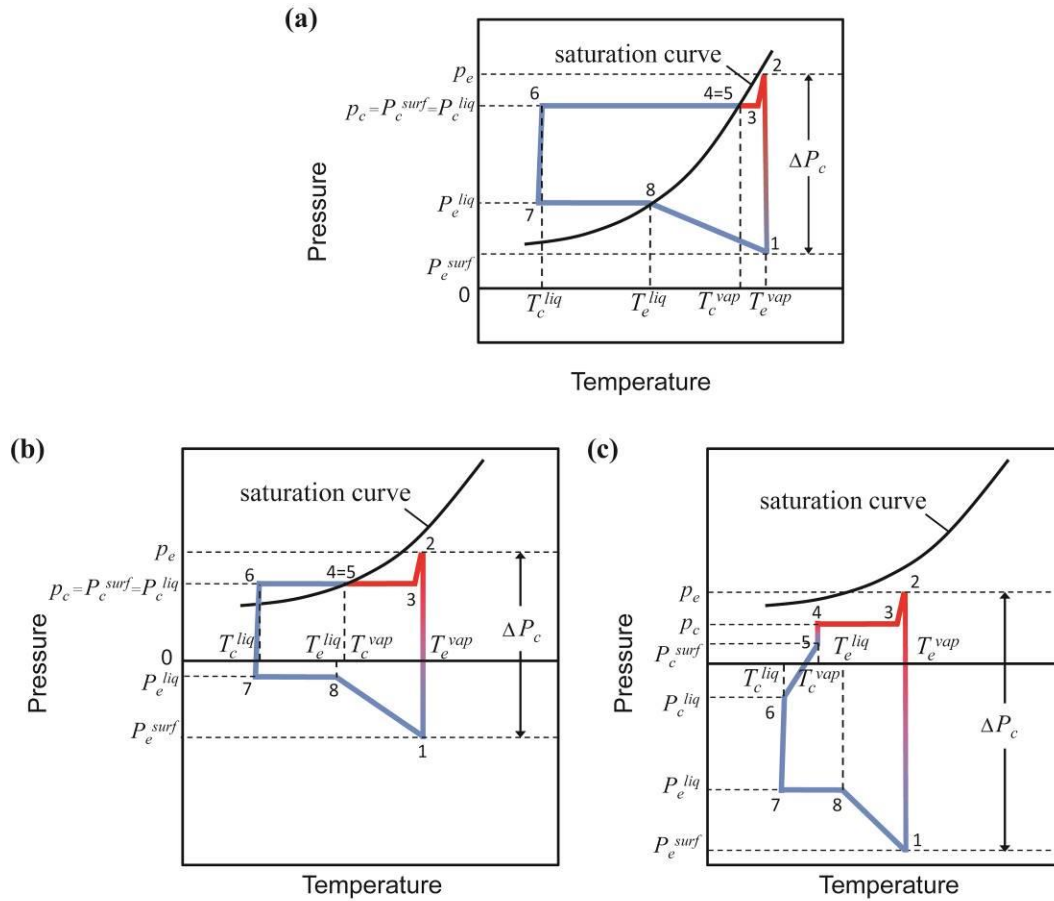


Figure 2.2: Schematic representations of working cycles on P - T diagram for (a) conventional LHPs, (b) saturated SHLHPs, and (c) sub-saturated SHLHP.

Points 1-8 correspond to the numbers in Figure 2.1. The red lines indicate the working fluid is in vapor phase (Path 2-4); the blue lines (Path 5-1) indicate liquid phase. Point 1 represents liquid under the meniscus at the evaporator wick, which is in thermodynamic equilibrium with Point 2, the vapor in the evaporator. Path 2-3 represents the adiabatic motion of the vapor along the vapor path. Point 4 represents vapor in the condenser vapor cavity, in thermodynamic equilibrium with Point 5, the liquid surface in the condenser. Point 6 is liquid before exiting the condenser; Path 6-7 represents motion of the liquid in the liquid path. Point 8 is liquid in the evaporator (in (a), this point is in the compensation chamber).

1) The capillary pressure (ΔP_c) developed by the porous wick must be able to overcome the total pressure drop in the entire loop, including pressure losses in the working fluid along the liquid and vapor paths and through the wick membranes (the pressure losses in the liquid and vapor paths include gravity and accelerations, as in Eq. (2.11) and (2.13)):

$$\Delta P_{c,\max} \geq \Delta P^{vap} + \Delta P^{liq} + \Delta P^{wick} \quad (2.1)$$

2) The pressure difference between Points 2 and 8, ΔP_{2-8} is responsible for driving the fluid motion through all components except the wick membrane. Given that these two points are saturated (or nearly so for Point 2), their temperature difference is determined by the shape of the coexistence line of the working fluid. This temperature difference must be established across the wick to create the corresponding pressure difference that drives fluid around. This condition has been called the motive temperature head condition:¹²

$$\Delta P_{2-8} \cong \left. \frac{dp_s}{dT} \right|_{\bar{T}_e} \Delta T_{2-8} \quad (2.2)$$

where dp_s/dT is the slope of the coexistence line at the evaporator temperature.

3) The heat leaked through the evaporator wick membrane into the compensation chamber, q_{leak} [W], must be balanced by the sensible heat of returning cold working fluid:

$$q_{leak} = \frac{\Delta T_{2-8}}{R_{wick,e}} = Q C_p^{liq} (\Delta T_{8-7}) \quad (2.3)$$

This balance implies that the temperature difference, ΔT_{8-7} (the sub-cooling of the liquid before it enters evaporator) grows with increasing ΔT_{2-8} and decreasing the thermal resistance of the evaporator wick, $R_{\text{wick},e}$. This effect is more pronounced at small heat fluxes for which the mass flow rate Q is small such that a large degree of sub-cooling is required. To minimize the required sub-cooling, $R_{\text{wick},e}$ should be made as large as possible in conventional designs. Combined with Eq. (2.2), the required sub-cooling is coupled to the pressure drop across the wick via ΔT_{2-8} ; we can call this coupling the sub-cooling condition.

Figure 2.2b illustrates the effect of eliminating the compensation chamber from the conventional design in a saturated SHLHP (Figure 2.1b). Without vapor on the liquid side of the evaporator, Point 8 is no longer constrained to be on the coexistence line. As the demand for pressure drop grows with additional heat load, acceleration or viscous drag, the pressures in the liquid at Points 7, 8, and 1 drop deeper into the superheated region. This use of reduced pressure or even tension (i.e. negative pressure, as presented in Figure 2.2b) lessens the demand for elevated pressure in the vapor at Point 2, and the temperature head condition (Eq. (2.2)) of the conventional design does not apply. Hence, if evaporator membrane remains wetted and the column of liquid does not cavitate (boil), a small temperature drop throughout the entire device can be achieved and the evaporator temperature of SHLHPs is essentially independent of the hydrostatic pressure load (see Section 2.5.1 for justification). A second consequence of allowing Point 8 to drop below the coexistence line is the temperature difference, ΔT_{8-7} remains independent of the load (via Eq. (2.3) and as the lack of dependence of ΔT_{2-8} on load). This decoupling further allows us to use membrane materials with larger range of thermal conductivities without constraint of the temperature head condition and the sub-cooling condition. These trends are schematically described in Figure 2.3, in which the working cycle diagrams are used to illustrate the different response of conventional

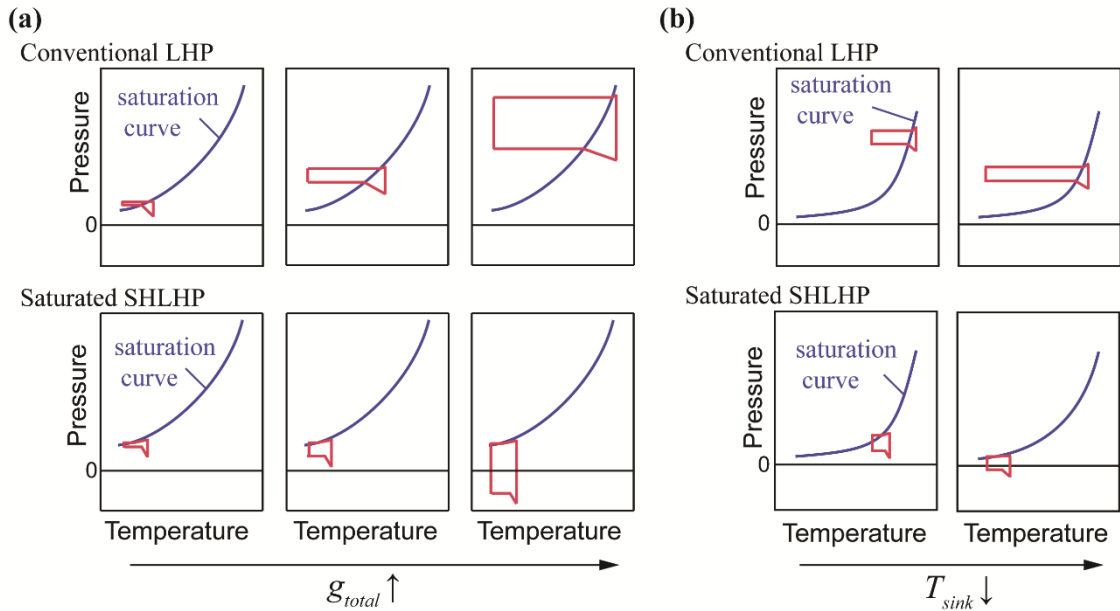


Figure 2.3: P - T diagrams for conventional LHP and SHLHP steady state operation.

(a) Evolution of the working cycle with increasing adverse acceleration, g_{total} . (b)

Evolution of the working cycle with decreasing sink temperature, T_{sink} .

For conventional design, corresponding to Eq. (2.2), as the pressure load goes up, the temperature difference across the evaporator wick goes up (a); as the sink temperature goes down, the slope of coexistence line decreases such that a larger temperature difference is required (b). These demands in the temperature difference across the evaporator wick further affect the sub-cooling temperature difference, according to Eq. (2.3).

LHPs and SHLHPs with increasing acceleration load (Figure 2.3a) and decreasing sink temperature (Figure 2.3b). Of course, the trade-off for this improved performance of SHLHPs is the extension of the superheated state to the entire liquid path, rather than just the membrane as in the conventional design. In consequence, the total volume of the liquid path should be made as small as possible in a SHLHP to minimize the tendency of the liquid to boiling.

Figure 2.3c illustrates the effects of adding a condenser membrane and a regulator that pins the fluid activity < 1 to form a sub-saturated SHLHP (Figure 2.1c, the vapor pressure at Point 4 is controlled by the regulator). In this case, the entire working cycle moves below the saturation line. As our model will illustrate (see Section 2.5.3), replacing the saturated condensation process (as in Figure 2.1a and Figure 2.1b) with condensation of sub-saturated vapor directly on the nanoporous membrane (Figure 2.1c) could substantially reduce the temperature drop in the condenser (smaller ΔT_{5-6} in Figure 2.2c compared to Figure 2.2b). Under sub-saturated conditions, the thermal resistance associated with the condenser is just that of conduction through the wetted membrane. A condenser membrane with low thermal resistivity is therefore desirable in a sub-saturated design. Eliminating liquid from the vapor path could also mitigate entrainment limitations and complex transients in the two phase regions (our model does not attempt to capture either of these effects)^{10, 14}. Nevertheless, the total pressure drop (ΔP_c) in a sub-saturated SHLHP would be larger than those in the conventional or saturated designs, due to the additional membrane in the condenser.

In summary, the important characteristics of the proposed SHLHPs are the large pressure differences between the liquid and vapor phases, the allowance of superheated liquid in the liquid path, and the possibility to work completely below the saturation curve. As I will demonstrate below, these characteristics could improve the

performance of LHPs by unpinning the liquid from saturation curve and allowing the system to be sub-saturated throughout.

2.3 Specifics of Sub-Saturated SHLHP Design

The global design of a sub-saturated SHLHP is similar to that of reversible loop heat pipes (RLHPs)⁵⁹ in which the vapor and liquid paths are separate and there are wick membranes in both the evaporator and condenser. The structure of the condenser and the evaporator can be designed to be identical to one another such that a sub-saturated SHLHP could operate upon reversal of a heat flow, for example, due to changes in environmental conditions. The condenser membrane serves to allow for reduced pressure (below the coexistence pressure) in the liquid in the condenser. This reduced pressure will ensure that the vapor in the condenser remains sub-saturated and free of liquid. The regulator replaces the compensation chamber in this design. Whereas the compensation chamber pins the working fluid to the co-existence line in the evaporator, the proposed regulator would pin the chemical potential of the vapor at a sub-saturated value at a position along the vapor path.

2.3.1 Nanoporous membrane

Basic requirements of membrane materials for SHLHPs (evaporator membrane in saturated design and both evaporator and condenser membranes in sub-saturated design) are similar to those of conventional HPs, including large permeability, high elastic modulus (to sustain pressure differences between the liquid and vapor compartments), and compatibility with the desired range of working temperatures. Moreover, to generate the large ΔP_c (Eq. (1.2)) required for SHLHPs, the pore size should be of sub-micrometer scale (e.g., for 20 bars of pressure difference with water as room temperature, a pore diameter less than ~100 nm is required at the liquid-vapor interface

based on Eq. (1.2). As mentioned in Section 2.2, the thermal conductivity of the evaporator membrane material in SHLHPs does not affect the performance of the system. On the other hand, the condenser membrane material in a sub-saturated SHLHP should be highly conductive to minimize the thermal resistance between the condenser and the heat sink.

Figure 2.4 presents an enlarged view of Figure 2.1c, highlighting the nanoporous membrane in the evaporator. As indicated, I propose a layer of nanoporous membrane (layer I) be supported by a microporous layer (layer II) that connects to extended microchannels. The nanoporous layer allows for the generation of large ΔP_c between the liquid and vapor phases; the supporting layer with micrometer scale pores presents a high permeability to flow of the liquid and serves as a structural support of the nanoporous layer. In considering the structural stability of the membranes, I note that the large pressure difference across the membrane could cause the membrane to deform and potentially crack. As the thickness of the membrane decreases (to minimize the hydraulic resistance), the possibility of membrane collapse increases. The micropores of the layer II must be of sufficiently small radius to avoid collapse of layer I. Further, the width of microchannels on the liquid and vapor sides of the membrane should also be sufficiently small to avoid deformation of the whole membranes.

Organic gels or inorganic sol-gels are candidates for the nanoporous coating. Such gels present molecular-scale pores that can provide large capillary pressures. A successful example of using this kind of material is found in the work from Wheeler and Stroock¹⁵. In that work, an organic gel allowed for capillary pressures in excess of 200 bars. Other candidate materials include nanoporous semiconductors (e.g., porous silicon⁶⁰⁻⁶²), ceramics⁶³, and metals^{64,65}. Appropriate candidate materials should have the following properties: 1) high thermal conductivity of the condenser membrane, 2) high mechanical modulus (≥ 10 GPa), 3) tunability of pore structure to enable, for

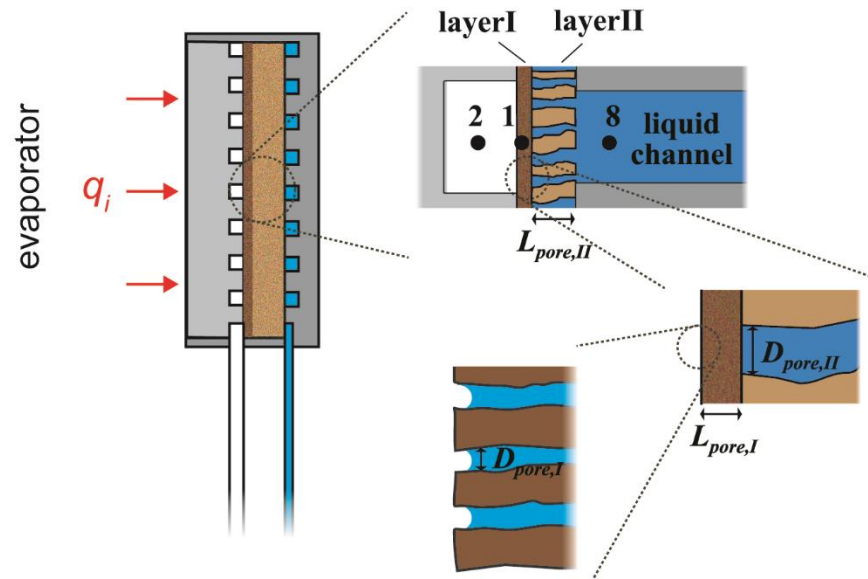


Figure 2.4: Schematic diagrams of the nanoporous membranes required in the evaporator of the saturated SHLHP and in both the evaporator and condenser of the sub-saturated SHLHP.

Expanded cross-sectional views show the wick membranes with a thin coating of a nanoporous material (layer I) connected to a microporous membrane (layer II). The nanoporous layer I has a pore diameter of $D_{pore,I}$ [m], thickness of $L_{pore,I}$ [m], and is supported by layer II with a span $D_{pore,II}$; layer II, thickness of $L_{pore,II}$ [m], supported by the connecting liquid channel. The pores in layer I hold the menisci that define the vapor-liquid interface.

example, the formation of membranes with gradients of pore diameter, 4) favorability of surface chemistry with respect to wetting by liquids for stabilization of liquid state with respect to heterogeneous cavitation of superheated liquid, and 5) compatibility with microfabrication techniques allowing for control in geometry and structure of the device and integration of elements of sensing and actuation.

2.3.2 Regulator

To avoid the presence of liquid in the vapor path and saturated liquid film in the condenser, one must regulate the quantity of fluid circulating through the system and control the chemical potential of the system. The inclusion of a regulator coupled to the SHLHP along either the vapor path or the liquid path can achieve this regulation: 1) The regulator acts as a reservoir that accommodates changes of the density of the liquid due to changes in temperature (in the absence of such a regulator, the expansion of fluid with rising temperatures during operation would lead to saturation of the vapor path, even if the system had been charged to a sub-saturated level at ambient temperature). Additionally, unlike the compensation chamber in conventional LHPs, the regulator for SHLHP would not contain a vapor-liquid interface. 2) The chemical potential of the fluid controlled by the regulator, μ_{reg} [J mole⁻¹], is maintained at a value less than the standard chemical potential, $\mu_0(T)$, thus maintaining a sub-saturated state throughout the SHLHP.

In the design shown in Figure 2.1c, the regulator is in the vapor path. By connecting the vapor path at the condenser with a pressure controller, one could adjust the vacuum level to regulate the vapor pressure, such that

$$a_{reg} = \frac{P_c}{P_s(T_c^{vap})} \sim \text{constant} < 1 \quad (2.4)$$

For $a_{reg} < 1$, $\mu_{reg} < \mu_0$. A vapor supply inlet is also located in the vapor path to allow the system to adapt to decreases of applied power.

The regulator could also be located in the liquid path at the condenser. For example, the regulation of a SHLHP with water as the working fluid may be achieved as follows: the pure liquid water in the condenser is coupled via an osmotic membrane to a solution of temperature-independent water activity, $a_{reg} \sim \text{constant} < 1$. Here, the water activity is defined as the mole fraction of water in solution:

$$a_{reg} = \frac{[water]}{[water] + [S(aq)]} \quad (2.5)$$

where the brackets represent concentration and S represents a solute. The solute should have a nearly temperature-independent solubility constant $K_s = [S(aq)]$ such that $a_{reg} \sim \text{constant}$.^{66,67} The osmotic membrane is required to be mechanically robust to large pressure differences and have high liquid permeability and high rejection coefficient. The volume of the regulator must be variable such that it is able to accommodate or to discharge the fluid in order to regulate the liquid pressure in the liquid path. The response time of this chamber should be fast compared to the transients in temperature to which it is designed to respond.

2.4 Model and Analysis for Steady-State Operation

The behavior and characteristics of conventional LHPs under steady-state operation are well known.⁵² A number of steady-state models based on one-dimensional heat and momentum balances have been presented^{50,53,68,69}. These simple models provide useful predictions of steady-state performance of LHPs. There are several more sophisticated models that focus on the evaporator element only, where the steady-state governing

equations for heat and fluid flow are solved numerically^{70,71}. However, to the best of our knowledge, no steady-state models have included the condition of local thermodynamic equilibrium between the superheated liquid and sub-saturated vapor phases. Neglect of this local equilibrium (neglecting departure from the saturation curve) is often reasonable for when the operating conditions remain near saturation throughout⁷². However, to account for the possibility of significant pressure differences between the liquid and vapor phases with nanoporous wicks, we must account explicitly for the local thermodynamic equilibrium between the phases. In this case, significant superheat may arise in the liquid due to resistance to flow, adverse acceleration, or sub-saturation; it is the goal of this study to elucidate the impact of this phenomenon on the performance of the heat pipe.

In the analysis of SHLHP, we assume that neither dry-out (entry of vapor) nor cavitation (boiling) occur in the liquid path. I discuss these assumptions in the *Results and Discussion* (Section 2.5). To model the steady state operation, we consider heat and momentum balances as in conventional analyses^{50,68,73}; unified heat and momentum balance equations for both conventional LHPs and SHLHPs are presented in Section 2.4.1. In Section 2.4.2, I highlight equations for the condition of local equilibrium; I then proceed to linearize these equations in order to extract expressions for the effective thermal resistance for SHLHPs, as presented in Section 2.4.3 and 2.4.4. The conversion of the nomenclature for temperatures and pressures at different points in the loop can be found in Figure 2.2.

2.4.1 Mass, heat and momentum balances

Mass balance. At steady state, the system is closed to mass transfer with the outside, thus the mass flow rate, Q , through the liquid and vapor paths is constant. We note that at the startup of the operation, some liquid will be displaced from the liquid path into

the vapor path due to thermal expansion as the temperature of the system rises. In the case of saturated SHLHP, we assume that this liquid will collect in the vapor cavity of the condenser; in the case of the sub-saturated SHLHP, the excess liquid volume will be evacuated by the regulator such that the vapor path remains devoid of liquid.

Heat balances. The heat input, q_i [W], comes in from the vapor side of the evaporator. We assume perfectly adiabatic liquid and vapor paths such that there is no heat exchange between the pipe lines and the surrounding environment during transportation; all heat that enters at the evaporator exits through at the condenser.

In the evaporator, most of the heat input is used for the liquid vaporization while some of the heat conducts through wick structure in the evaporator into the liquid side; the amount of the heat leakage is proportional to the temperature difference across the wick. Assuming T_{source} is the average temperature of the evaporator wall, T_e^{vap} is the average temperature in the vapor cavity in the evaporator, and T_e^{liq} is the average temperature in the liquid cavity in the evaporator, the heat balances in the evaporator vapor side are:

$$0 = q_i - \frac{(T_{source} - T_e^{vap})}{\mathbf{R}_{wall,e}} \quad (2.6)$$

and

$$0 = \frac{(T_{source} - T_e^{vap})}{\mathbf{R}_{wall,e}} - \frac{(T_e^{vap} - T_e^{liq})}{\mathbf{R}_{wick,e}} - Q(H_e^{vap} - H_e^{liq}) \quad (2.7)$$

where $\mathbf{R}_{wall,e}$ [K W⁻¹] represents the thermal resistance between the evaporator wall surface in contact with the heat source and the vapor in the evaporator, and $\mathbf{R}_{wick,e}$ represents the effective thermal resistance of the evaporator wick membrane.

The heat leak into the liquid cavity through the wick casing is neglected (i.e. all the heat leak is conducted through the wick into the liquid side in the evaporator). In the liquid cavity in the evaporator,

$$0 = \frac{(T_e^{vap} - T_e^{liq})}{R_{wick,e}} - Q(H_e^{liq} - H_c^{liq}) \quad (2.8)$$

such that the heat conducted through the wick is balanced by the sensible heat of the cold liquid returning from the condenser (this equation is essentially Eq. (2.3)). The heat exchange between the liquid cavity and ambient is neglected by assuming perfect insulation of the liquid side wall.

For the case of a SHLHP sub-saturated throughout the loop, a membrane is used in the condenser and the condensation would occur at the wick surface. An additional heat balance equation is used to describe the heat released by the fluid in the condenser via conduction through the wick in to the liquid cavity; this heat transfer can be related to the temperature difference across the wick membrane:

$$0 = Q(H_e^{vap} - H_c^{surf}) - \frac{(T_c^{vap} - T_c^{liq})}{R_{wick,c}} \quad (\text{sub-saturated SHLHP only}) \quad (2.9)$$

where T_c^{vap} is the average temperature in the vapor cavity in the condenser, and T_c^{liq} is the average temperature in the liquid cavity in the condenser. The temperature of the heat sink in contact with the condenser wall is fixed at a constant, known value T_{sink} , such that

$$0 = h_{sink} A_{sink} (T_c^{liq} - T_{sink}) - q_i \quad (2.10)$$

where h_{sink} is the overall heat transfer coefficient and A_{sink} is the heat exchange surface area between the liquid in the condenser and the heat sink. We note that for conventional design, Eq. (2.10) is a simplified version of the condenser tube energy balance; more detailed model can be found in the literature⁷³. This simplification does not affect our results or comparisons between the conventional design and the designs proposed in this paper.

Momentum balances. For the liquid phase,

$$0 = QR_{liq} + \rho_{liq} g_{total} L_{pipe} - (P_c^{liq} - P_e^{liq}) \quad (2.11)$$

where g_{total} [$m\ s^{-2}$] is the total acceleration along the pipe due to both gravity and acceleration ($g_{total} = g_0 + g_{dyn}$, where g_0 and g_{dyn} are the projections of the gravitational and dynamic acceleration onto the axis of the pipe.). For the wick membrane in the evaporator,

$$0 = QR_{wick,e} - (P_e^{liq} - P_e^{surf}) \quad (2.12)$$

For the vapor phase,

$$0 = QR_{vap} + p_c \exp\left(-\frac{MW g_{total} L_{pipe}}{R_{gas} T_e^{vap}}\right) - p_e \quad (2.13)$$

The Boltzmann factor in the exponential term accounts for the effect of acceleration, g_{total} , along the axis of the pipe on the vapor.

In the case of conventional LHPs and saturated SHLHPs, pressure losses in the condenser are usually negligible; while for a sub-saturated SHLHP, liquid overcomes hydraulic resistance flowing through the condenser wick membrane:

$$P_c^{surf} = P_c^{liq} \text{ (conventional LHP and saturated SHLHP)} \quad (2.14).a$$

or

$$0 = QR_{wick,c} - (P_c^{surf} - P_c^{liq}) \text{ (conventional LHP and saturated SHLHP)} \quad (2.14).b$$

2.4.2 Local thermodynamic equilibria

Applying the condition of local equilibrium, we set the chemical potentials equal across the interfaces at which phase change occurs: $\mu_w^{surf} = \mu_w^{vap}$. The use of this condition neglects the possibility of interfacial resistance due to, for example, contaminants adsorbed on the interface. With this condition, we can write down explicitly the thermodynamic balance equations at vapor-liquid interfaces. For the evaporator, we set the chemical potentials of the liquid and vapors equal to find:

$$\bar{v}_{liq} [P_e^{surf} - p_s(T_e^{vap})] = R_{gas} T_e^{vap} \ln \left[\frac{P_e}{p_s(T_e^{vap})} \right] \quad (2.15)$$

In deriving Eq. (2.15), we have assumed that the liquid is inextensible with molar volume, v_{liq} [$\text{m}^3 \text{mole}^{-1}$] and the vapor acts as an ideal gas⁷⁴.

For conventional LHPs and saturated SHLHPs without wick membrane in the condenser, vapor is in equilibrium with the liquid in the condenser:

$$P_c^{surf} = p_c \quad (2.16)$$

Also, there is negligible curvature of the vapor-liquid interface for conventional LHPs and saturated SHLHP without condenser membranes, such that the pressure of the liquid is simply the saturation pressure at the local temperature, so we have:

$$P_c^{surf} = p_s(T_c^{vap}) \quad (2.17).a$$

For sub-saturated SHLHPs with condenser membranes, the thermodynamic balance equations at sub-saturated vapor-liquid interfaces, similar to the one for the evaporator wick surface (Eq. (2.15)), is used:

$$\bar{v}_{liq} [P_c^{surf} - p_s(T_c^{vap})] = R_{gas} T_c^{vap} \ln \left[\frac{P_c}{p_s(T_c^{vap})} \right] \quad (2.17).b$$

Finally, in conventional LHPs, the liquid pressure in the liquid cavity in the evaporator is simply the saturation pressure of the temperature in the compensation chamber due to the coexistence of the two phases,

$$P_e^{liq} = p_s(T_e^{liq}) \quad (2.18).a$$

For SHLHPs, the activity of the fluid is controlled by the regulator. If the regulator is located in the vapor side of the condenser, we have:

$$\frac{P_c}{p_s(T_c^{vap})} = a_{reg} \quad (2.18).b$$

If the regulator is located in the liquid side of the condenser,

$$\bar{v}_{liq} \left[P_c^{liq} - p_s(T_c^{liq}) \right] = R_{gas} T_c^{liq} \ln \left[a_{reg} \right] \quad (2.18).c$$

For SHLHPs without regulator in the condenser to maintain sub-saturated condition, $a_{reg} = 1$.

Eqs. (2.6)–(2.18) can be solved numerically to find the operating temperature, T_{source} , as a function of the heat input, q_i , for a given sink temperature, T_{sink} . The numerical solutions presented in the discussion section are solved iteratively by proceeding as follows: we start with initial guesses for T_e^{vap} and Q , and then solve the rest of the unknowns, including p_e . Using this p_e , we solve Eq. (2.15) for an updated T_e^{vap} and Eq. (2.7) for an updated Q , and then solve for the rest of the unknowns. We repeat the steps until the relative change in the values of T_e^{vap} less than 10^{-2} and Q less than 10^{-6} from one iteration to the next.

2.4.3 Linear analysis and expression of LHP effective thermal resistance

The global effective thermal resistance, R_{eff} [K W⁻¹], is used to characterize the LHP performance, and can be defined as follows:

$$R_{eff} = \frac{T_{source} - T_{sink}}{q_i} \quad (2.19)$$

In conventional LHPs, experiments and existing models^{50,51,68,73} indicate that, in general, R_{eff} depends on the heat flow, q_i ; the response is non-linear. In particular, at low heat flow, the temperature difference ($\Delta T_{8.7}$) required to satisfy the sub-cooling condition (Eq. (2.3)) dominates and R_{eff} decreases with increasing q_i (“variable conductance mode”); at high heat flow, R_{eff} becomes constant (“fixed conductance mode”) as heat transfer in the condenser becomes the limiting resistance⁵⁰. In contrast, in a SHLHP, the sub-cooling condition is not constrained by pressure load and we expect R_{eff} to be constant for a small to moderate heat flows; the initial response is linear. Based on this expectation, we develop an analytical expression for this constant R_{eff} for SHLHPs. This expression helps to elucidate the effects of the distinct components of the system on the performance of a SHLHP. In the *Results and Discussion* (Section 2.5.2), we check the validity of the following linear analysis against complete solutions of Eqs. (2.6)–(2.18).

Linear response is defined as follows:

$$T_{\text{source}} - T_{\text{sink}} \propto q_i \quad (2.20)$$

When this relation holds, R_{eff} for SHLHPs can be written as a function of $(T_e^{\text{vap}} - T_c^{\text{liq}})$ as:

$$\begin{aligned} R_{\text{eff}} &= \frac{T_{\text{source}} - T_e^{\text{vap}}}{q_i} + \frac{T_e^{\text{vap}} - T_c^{\text{liq}}}{q_i} + \frac{T_c^{\text{liq}} - T_{\text{sink}}}{q_i} \\ &= R_{\text{wall,e}} + \frac{T_e^{\text{vap}} - T_c^{\text{liq}}}{q_i} + R_{\text{film}} + R_{\text{wall,c}} \end{aligned} \quad (2.21)$$

To find the expression of the second term in Eq. (2.21) for R_{eff} , I consider the limit of low heat flow and thus small temperature difference, ΔT_{tot} . I use $\Delta T_{\text{tot}} = (T_e^{\text{vap}} - T_c^{\text{liq}})$

and $T_0 = T_c^{liq}$. We begin by recasting the local equilibrium at the evaporator, Eq. (2.15), into a non-dimensional form and as an expansion in ΔT_{tot} :

$$\begin{aligned} \frac{p_e \left. \frac{dp_s}{dT} \right|_{T_0}}{p_{s,0}^2 T_0} (\Delta T_{tot})^2 + \left[\frac{1}{T_0} \left(1 - \frac{p_e}{p_{s,0}} \right) - \frac{\left. \frac{dp_s}{dT} \right|_{T_0}}{\frac{R_{gas} T_0}{\bar{v}_{liq}}} + \frac{p_e \left. \frac{dp_s}{dT} \right|_{T_0}}{p_{s,0}^2} \right] \Delta T_{tot} \\ + \left[\frac{(P_e^{surf} - p_{s,0})}{\frac{R_{gas} T_0}{\bar{v}_{liq}}} + \left(1 - \frac{p_e}{p_{s,0}} \right) \right] = 0 \end{aligned} \quad (2.22)$$

In arriving at Eq. (2.22), we have expanded $p_s(T_e^{vap})$ to first order in ΔT_{tot} about T_0 , expanded the logarithm to first order in $(1 - p_e/p_s(T_e^{vap}))$, and expanded $1/p_s(T_e^{vap})$ to first order in $(dp_s/dT|_{T_0})/p_{s,0}$. These approximations hold for the following conditions:

$$\Delta T_{tot} \ll 2 \frac{\left. \frac{dp_s}{dT} \right|_{T_0}}{\left. \frac{d^2 p_s}{dT^2} \right|_{T_0}} \quad (2.23)$$

$$\left| 1 - \frac{p_e}{p_s(T_e^{vap})} \right| \ll 1 \quad (2.24)$$

and

$$\frac{\Delta T_{tot}}{p_{s,0} \left/ \frac{dp_s}{dT} \right|_{T_0}} \ll 1 \quad (2.25)$$

If we further assume:

$$\frac{\Delta T_{tot}}{T_0} \ll 1 \quad (2.26)$$

$$\left| 1 - \frac{p_e}{p_{s,0}} \right| \ll 1 \quad (2.27)$$

and

$$\frac{\left. \frac{dp_s}{dT} \right|_{T_0}}{\frac{R_{gas}}{\bar{v}_{liq}}} \ll 1 \quad (2.28)$$

we can simplify Eq. (2.22) by neglecting terms that are the product of two small factors and solve for ΔT_{tot} :

$$\Delta T_{tot} = - \frac{p_{s,0}^2}{\left. \frac{dp_s}{dT} \right|_{T_0}} \left[\frac{(P_e^{surf} - p_{s,0})}{\frac{R_{gas} T_0}{\bar{v}_{liq}} p_e} + \left(\frac{1}{p_e} - \frac{1}{p_{s,0}} \right) \right] \quad (2.29)$$

By differentiating ΔT_{tot} with respect to q_i (i.e., looking for the dependence of p_e and P_e^{surf} on q_i) and assuming the following:

$$\frac{(P_e^{surf} - P_{s,0})}{\frac{R_{gas} T_0}{\bar{v}_{liq}}} \ll 1 \quad (2.30)$$

and

$$\frac{MWg_{total} L_{pipe}}{R_{gas} T_e^{vap}} \ll 1 \quad (2.31)$$

we find the expression of the second term in Eq. (2.21) in which we can separate out the contributions associated with the vapor flow, R_{vap} (see Eq. (2.37)), the liquid flow, R_{liq} (see Eq. (2.38)), the conduction through the wicks in the condenser, $R_{wick,c}$ (see Eq. (2.34)).

At the end of the day, we arrive at an expression for R_{eff} in which the contributions associated with all loop elements – the evaporator wall, the vapor flow, the liquid flow, the conduction through the wicks in the condenser, and the heat exchange with the heat sink – are separated out:

$$R_{eff} = R_{wall,e} + R_{vap} + R_{liq} + R_{wick,c} + R_{film} + R_{wall,c} \quad (2.32)$$

In Eq. (2.32), $R_{wall,e}$ and $R_{wall,c}$ are the conductive resistances of the evaporator and condenser walls:

$$\mathbf{R}_{\text{wall,e}} = \frac{L_{\text{wall}}}{k_{\text{wall}}A_{\text{source}}} \text{ and } \mathbf{R}_{\text{wall,c}} = \frac{L_{\text{wall}}}{k_{\text{wall}}A_{\text{sink}}} \quad (2.33)$$

where L_{wall} [m] is the thickness and k_{wall} [$\text{W m}^{-1}\text{K}^{-1}$] is the thermal conductivity of the wall in contact with the heat source or the sink. For the saturated SHLHP without a membrane in the condenser, $\mathbf{R}_{\text{wick,c}} = 0$, while for sub-saturated SHLHP,

$$\mathbf{R}_{\text{wick,c}} = \sum_{i=1}^N \frac{L_{\text{pore},i}}{k_{\text{w},i}A_{\text{w}}}, \quad i=1, 2, \dots, N \quad (2.34)$$

where N is the total number of layers of the wick membrane in the condenser (e.g., in Figure 2.1c, $N = 2$). \mathbf{R}_{film} accounts for the film condensation heat transfer in tubes:

$$\mathbf{R}_{\text{film}} = 1/h_{\text{film}}A_{\text{sink}} \quad (2.35)$$

where we take the heat transfer coefficient h_{film} from the literature^{75,76}:

$$h_{\text{film}} = 0.76 \left(\frac{2k_{\text{liq}}^3 \rho_{\text{liq}}^2 gL}{\eta_{\text{liq}} Q} \right)^{\frac{1}{3}} \quad (2.36)$$

where k_{liq} [$\text{W m}^{-1}\text{K}^{-1}$] is the thermal conductivity of the condensate and η_{liq} [$\text{kg m}^{-1} \text{s}^{-1}$] is the viscosity of the condensate. For the sub-saturated SHLHP, the condensation occurs directly on the surface of the condenser membrane (with no film), so we take $\mathbf{R}_{\text{film}} = 0$.

The important and less obvious predictions that emerge from the linearization are for the contributions of the vapor and liquid paths:

$$R_{\text{vap}} = \frac{1}{\lambda \left. \frac{dp_s}{dT} \right|_{T_0}} R_{\text{vap}} = \frac{T_0}{\lambda^2 \rho_{\text{vap},0}} R_{\text{vap}} \quad (2.37)$$

and

$$R_{\text{liq}} = \frac{\rho_{\text{vap},0}}{\rho_{\text{liq},0}} \frac{1}{\lambda \left. \frac{dp_s}{dT} \right|_{T_0}} (R_{\text{liq}} + \sum R_{\text{wick}}) = \frac{T_0}{\lambda^2 \rho_{\text{liq},0}} (R_{\text{liq}} + \sum R_{\text{wick}}) \quad (2.38)$$

where R_{vap} and R_{liq} are the hydraulic resistances of the vapor and liquid paths, and $\sum R_{\text{wick}}$ is the sum of the hydraulic resistances of the wick membranes through which the liquid flows. We have used the Clausius-Clapyeron relation (neglecting $1/\rho_{\text{liq}}$ relative to $1/\rho_{\text{vap}}$) to arrive at the second equalities in Eqs. (2.37) and (2.38). While earlier investigators derived the expression in Eq. (2.37),⁷⁷ we are unaware of a previous derivation of Eq. (2.38). These expressions clarify the importance of the latent heat, the slope of the saturation curve and the fluid viscosity (present in the hydraulic resistance terms) in defining the impact of hydraulic resistances on SHLHP performance. Comparing to the hydraulic resistance in the vapor path, we note that the impact of hydraulic resistance in the liquid path is less by a factor of $(\rho_{\text{vap}}/\rho_{\text{liq}})$ for equivalent hydraulic resistances; this factor is less than 10^{-3} for water up to 100 °C. This observation points to the opportunity to use conduits of small caliber for the liquid path as one designs heat pipes of large dimensions with nanoporous wicks.

2.4.4 Comparison between the R_{eff} of conventional LHPs and SHLHPs

For conventional LHP and saturated SHLHP which have the same condenser design, the terms $R_{\text{wall,e}}$, R_{film} and $R_{\text{wall,c}}$ are the same. The difference of the global thermal resistance of the two designs lies in the expression for R_{vap} and R_{liq} .

For the conventional design, these resistances can be identified by combining the temperature head condition (Eq. (2.2)) and the sub-cooling condition (Eq. (2.3)):

$$\begin{aligned}
 R_{\text{vap}} + R_{\text{liq}} &= \frac{T_e^{\text{vap}} - T_c^{\text{liq}}}{q} \\
 &= \frac{\Delta T_{2-8}}{q} + \frac{T_e^{\text{liq}} - T_c^{\text{liq}}}{q} \\
 &\cong \frac{\Delta P_{2-8}}{Q\lambda \frac{dp_s}{dT}} + \frac{T_e^{\text{liq}} - T_c^{\text{liq}}}{q}
 \end{aligned} \tag{2.39}$$

By further replacing $\Delta P_{2-8}/Q$ by the hydraulic resistances and using Clausius-Clapeyron equation, we can get:

$$R_{\text{vap}} + R_{\text{liq}} = \frac{T}{\lambda^2 \rho_{\text{vap}}} R_{\text{vap}} + \frac{T}{\lambda^2 \rho_{\text{vap}}} (R_{\text{liq}} + R_{\text{wick}}) + \frac{T_e^{\text{liq}} - T_c^{\text{liq}}}{q} \tag{2.40}$$

The third term from the right hand side of Eq. (2.40) is a non-linear term associated to the sub-cooling effect (Eq. (2.3)):

$$\frac{T_e^{\text{liq}} - T_c^{\text{liq}}}{q} = \frac{\Delta T_{8-7}}{q} \cong \frac{\Delta T_{2-8}}{q^2 C_p^{\text{liq}} R_{\text{wick,e}} / \lambda} \tag{2.41}$$

At small heat flux or small evaporator wick thermal resistance, this term becomes large and can even dominate the global effective thermal resistance.

For comparison to the saturated SHLHP, Eqs. (2.37) and (2.38) give us:

$$\mathbf{R}_{\text{vap}} + \mathbf{R}_{\text{liq}} = \frac{T}{\lambda^2 \rho_{\text{vap}}} R_{\text{vap}} + \frac{T}{\lambda^2 \rho_{\text{liq}}} (R_{\text{liq}} + R_{\text{wick}}) \quad (2.42)$$

The first term associated with the hydraulic resistance in the vapor path is identical to \mathbf{R}_{vap} for the conventional LHP. The second term, \mathbf{R}_{liq} associated with the hydraulic resistance in the liquid path, is different from that in conventional LHP (Eq. (2.40)) by a factor of $(\rho_{\text{liq}}/\rho_{\text{vap}})$. This difference comes from the fact that, for a conventional LHP, the vapor pressure in the evaporator must push *both* the vapor and liquid phases through their respective sections of the loop. In contrast, in the SHLHP, the reduced pressure in liquid in the evaporator drives the liquid flow; the vapor pressure is only responsible for driving the flow of the vapor phase. As we will see in the *Results and Discussion*, this distinction leads to significant differences in the responses of the LHP and the SHLHP as the pressure drop along the liquid path increases. The non-linear term accounting for sub-cooling (Eq. (2.41)) does not influence the SHLHP since the temperature across the evaporator wick, ΔT_{2-8} , is not directly coupled to the entire pressure drop in the vapor and liquid paths.

2.5 Results and Discussion

In Figure 2.5–Figure 2.9, I present the predictions of the model in Section 2.4 for the performance of conventional LHPs and SHLHPs for heat transfer over a distance of 10 meters with various operational parameters. The geometries of the systems are as depicted in Figure 2.1; we take a smaller diameter liquid conduit in the SHLHPs (350

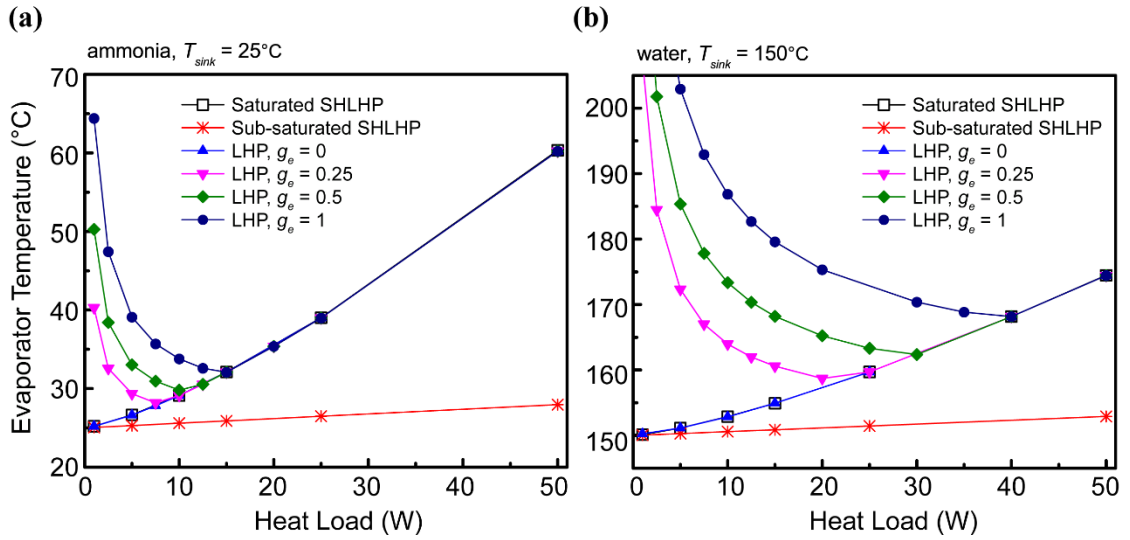


Figure 2.5: Effect of the adverse acceleration (ranging for 0 to 1 time gravity) on conventional LHP, saturated SHLHP and sub-saturated SHLHP with (a) ammonia and (b) water as working fluid.

Presented data are numerical solutions (Eqs. (2.6)–(2.19)). Sink temperature, T_{sink} , is 25°C for (a) and 150°C for (b). Varying g_{total} between 0 and 1 times gravity has no effect on the SHLHPs. The results for saturated LHP overlap with the line for conventional LHP at $0 g_e$.

For the conventional case, $D_{liq} = 1 \text{ mm}$; for the SHLHPs, $D_{liq} = 350 \mu\text{m}$.

Other operational parameters: $L_{pipe} = 10 \text{ m}$, porosity of the membrane = 0.6, thermal conductivity for the evaporator wick membrane material = 13 W/m K , $D_{vap} = 6 \text{ mm}$, $L_{pore,1} = 2 \mu\text{m}$, $D_{pore,1} = 20 \text{ nm}$, $L_{pore,2} = 3 \text{ mm}$, $D_{pore,2} = 2 \mu\text{m}$, $A_{source} = 1 \text{ cm}^2$, $L_{wall} = 1 \text{ mm}$ and $k_{wall} = 400 \text{ W/m K}$. For saturated condenser, $D_{cond} = 4 \text{ mm}$, $A_{sink} = 100 \text{ cm}^2$; for sub-saturated SHLHP, a condenser membrane with thermal conductivity = 130 W/m K , $A_w = A_{sink} = 1 \text{ cm}^2$, $L_{pore,1} = 2 \mu\text{m}$, $D_{pore,1} = 20 \text{ nm}$, $L_{pore,2} = 300 \mu\text{m}$, and $D_{pore,2} = 2 \mu\text{m}$ is added to replace the condenser tube. The vapor pressure in the sub-saturated SHLHP is controlled by the regulator and has activity, $a_{reg} = 0.99$.

μm -diameter) than in the LHPs (1 mm). All parameter values are provided in the captions. The predictions are made by solving Eqs. (2.6)–(2.18) numerically for T_e^{vap} at fixed heat flow and T_{sink} or by evaluating the expressions for effective thermal resistance in Eqs. (2.32)–(2.38).

2.5.1 Comparison of the response of conventional LHPs and SHLHPs

Figure 2.5 presents the operating curves (steady-state evaporator temperature vs. the heat input) for ammonia (Figure 2.5a) and water (Figure 2.5b) with acceleration load, g_{total} , varying from 0 to 1 times gravity ($g_{total} = 0, 0.25, 0.5, \text{ and } 1 g_e$, where $g_e = 10 \text{ m s}^{-2}$) for 10 m-long pipes. The performance of SHLHPs is essentially independent of acceleration: varying g_{total} has no effect on the performance of either the saturated SHLHP or the sub-saturated SHLHP. The operating curves of the saturated SHLHP overlaps with the curve for conventional LHP at $g_{total} = 0$. At high heat flux, the effective thermal resistances of both designs are dominated by the thermal resistance of the condenser. On the other hand, for sub-saturated SHLHP with condenser membrane design (as detailed in Figure 2.3), the effective thermal resistance is reduced to that of the condenser wick and condenser wall material, as discussed in Section 2.2 (comparison between Figure 2.2b and Figure 2.2c), and the rise in the evaporator temperature is significantly slower than in the saturated systems.

In the predictions for conventional LHP in Figure 2.5 (with the liquid path taken to be perfectly insulated), the evaporator temperature increases with increasing heat input over the entire power range when no adverse acceleration is imposed ($g_{total} = 0$). When there is adverse acceleration imposed on the system, characteristic u-shaped curves^{52,53} appear at the low heat flux. Looking at a single heat input, the higher the adverse acceleration load, the larger the liquid path hydrostatic pressure must be, as required by the temperature head condition (Eq. (2.2)) and shown schematically in Figure 2.3a. For

a fixed acceleration, the increasing heat input leads to increasing flow rate, providing more efficient cooling for the evaporator and reducing the temperature difference in the compensation chamber; as the heat input keeps increasing, the conventional LHP enters its fixed conductance mode where the impact of acceleration becomes small compared to that of the viscous pressure head, and the system is dominated by the resistance to heat transfer in the condenser. The larger the acceleration load, the later the operating curve enters the fixed conductance mode.

In summary, while the effective resistance of conventional LHPs is strongly affected by the adverse acceleration due to Eq. (2.2) and Eq. (2.3), the resistance of SHLHPs is independent of the pressure load in this range due to the absence of the saturated state in compensation chamber. Further, by eliminating the film resistance in the condenser, the global resistance of a sub-saturated SHLHP is predicted to be lower than that in either the saturated SHLHP or the conventional LHP.

Response to acceleration load. Figure 2.6a–b compare the effective thermal resistances (numerically solved Eqs. (2.6)–(2.19)) of a conventional LHP and a saturated SHLHP as a function of the adverse acceleration for ammonia (Figure 2.6a) and water (Figure 2.6b) for $q_i = 10$ W. For both fluids, the resistance of the SHLHP is small ($R_{\text{film}} \sim 0.4$ for (a) and 0.3 for (b)) and varies slowly with g_{total} . The predicted decrease in the resistance with increasing g_{total} comes from the impact of acceleration on the film resistance in the model we have used (Eq. (2.36)). As I will illustrate in Section 2.5.3, the other resistances are insensitive to acceleration. The resistance of the conventional LHP is much larger than that for the SHLHP for $g_{\text{total}} > 0$ and increases with the increasing adverse acceleration; this trend validates the schematic description provided in Figure 2.3a. At the heat input considered (10 W), the conventional design is operating below its fixed conductance regime (see Figure 2.5). We note that the

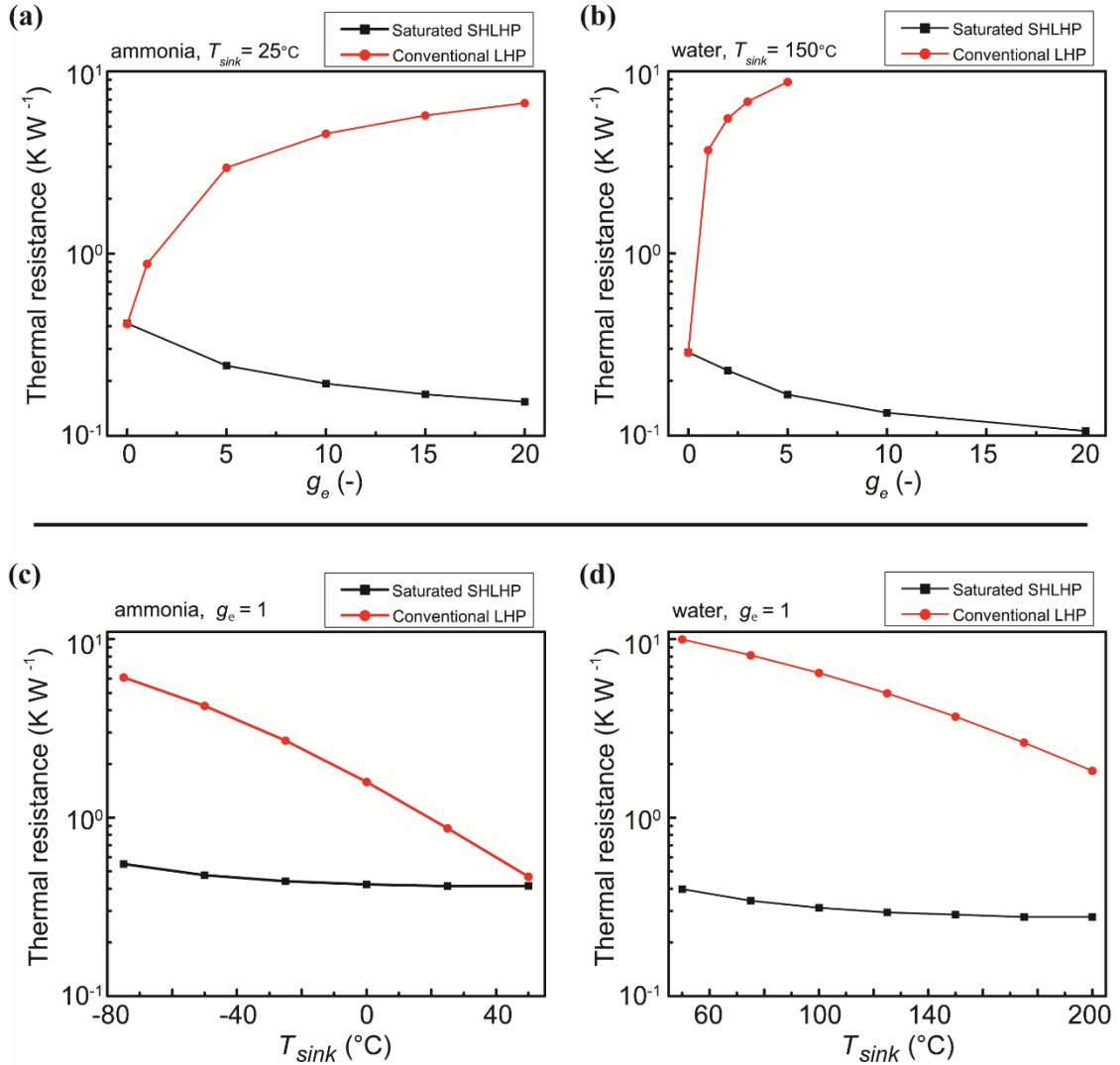


Figure 2.6: Comparison of the total effective thermal resistance for conventional LHP and saturated SHLHP varying acceleration (a-b) and sink temperature (c-d), with ammonia and water as the working fluid.

Black squares are numerical solutions (Eqs. (2.6)–(2.19)) for total effective thermal resistance for sub-saturated SHLHPs; red circles are solutions for conventional LHPs. The heat input, $q_i = 10$ W. Sink temperature, T_{sink} , is 25°C for (a) ammonia and 150°C for (b) water. $g_{total} = 1 g_e$ for both (c) and (d). $L_{pipe} = 10$ m, other operational parameters are the same as in Figure 2.5.

impact of increasing acceleration is more pronounced for water than for ammonia at the temperatures considered, due to the weaker slope of water's saturation curve.

Response to sink temperature. Figure 2.6c–d compare the effective thermal resistances of the two designs as a function of sink temperature for ammonia (Figure 2.6c) and water (Figure 2.6d) with $g_{total} = 1 g_e$ in the adverse orientation. The temperatures for each fluid were chosen to be within their most efficient ranges⁵². For both fluids, the resistance of the SHLHP is small ($R_{film} \sim 0.5$ for (c) and 0.4 for (d)) and nearly independent of T_{sink} . The slight rise at the lowest temperatures is due to the resistance to vapor flow, as we will see more clearly in Section 2.5.3. The resistance of the conventional LHP is much larger than for the SHLHP for all conditions and varies significantly over the ranges of temperature considered. The large effective thermal resistance of the LHP arises from the need to generate sufficient pressure in the vapor at the evaporator to drive the fluid around the loop and against gravity. As discussed in Section 2.2 (Eq. (2.2)) and shown schematically in Figure 2.4b, the evaporator temperature must rise until the vapor pressure is sufficiently high to drive the flow; this rise in the T_e^{vap} raises the global thermal resistance for a given, fixed T_{sink} . As T_{sink} increases, the global temperature difference decreases, and the effective resistance falls. The predictions in Figure 2.6c–d validate the schematic description provided in Figure 2.3b and illustrate the potential advantages – constant, low thermal resistance over a broad range of sink temperatures – of the SHLHP design.

2.5.2 Validity of SHLHP linear response

In order to test the predictions of our linear response treatment (Eqs. (2.32)–(2.38)) against full numerical solutions of Eqs. (2.6)–(2.19), and to elucidate the relative contributions of distinct components of the system, Figure 2.7 presents the total thermal resistance of saturated SHLHP (Figure 2.7a) and sub-saturated SHLHP (Figure 2.7b)

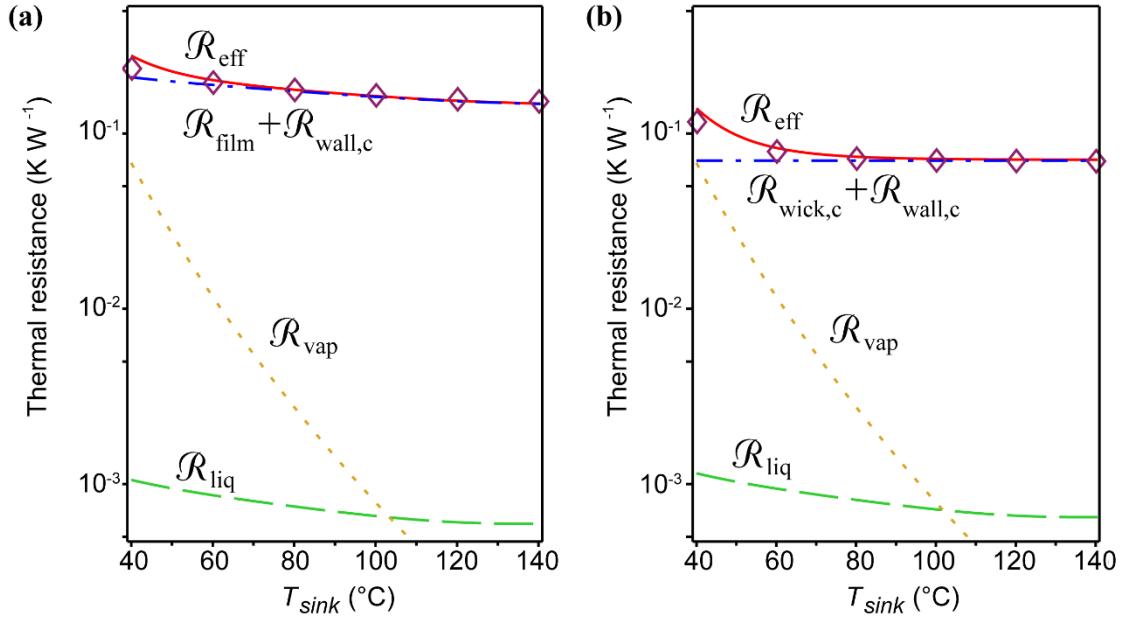


Figure 2.7: Predicted effective thermal resistances of (a) saturated SHLHP and (b) sub-saturated SHLHP as a function of the sink temperature, T_{sink} .

Water is used as the working fluid. Purple diamond symbols are numerical solutions of total effective thermal resistance (Eqs. (2.6)–(2.19)) for $q_i = 100$ W. Red solid line is the solution from linearized expression, R_{eff} (Eq. (2.32)), and dashed lines are components of R_{eff} due to different components in the loop - the vapor path is gold, dotted line (R_{vap} , Eq. (2.37)), the liquid path is green, dashed line (R_{liq} , Eq. (2.38)), and the condenser is blue, dash-dot line ($R_{wick,c} + R_{wall,c}$, Eq. (2.34) and (2.33)).

Operational parameters: $g_{total} = 10 g_e$ (100 m s^{-2}), $L_{pipe} = 10 \text{ m}$, $A_{source} = 1 \text{ cm}^2$, $D_{vap} = 6 \text{ mm}$, $D_{liq} = 350 \text{ }\mu\text{m}$, $L_{pore,1} = 2 \text{ }\mu\text{m}$, $D_{pore,1} = 20 \text{ nm}$, $L_{pore,2} = 300 \text{ }\mu\text{m}$, $D_{pore,2} = 2 \text{ }\mu\text{m}$, and $L_{wall} = 0.5 \text{ mm}$. For (a), $D_{cond} = 4 \text{ mm}$, $A_{sink} = 100 \text{ cm}^2$; for (b), $a_{reg} = 0.99$, $A_w = A_{sink} = 1 \text{ cm}^2$, $k_w = 130 \text{ W/m K}$ and $k_{wall} = 400 \text{ W/m K}$.

with an adverse acceleration of $10 g_e$ ($g_{total} = 100 \text{ m s}^{-2}$). Other operational parameters are included in the caption. The symbols in Figure 2.7 present the full numerical solution for the total effective thermal resistance, R_{eff} (Eqs. (2.6)–(2.19)), as a function of T_{sink} for $q_i = 100 \text{ W}$; the continuous lines are the predictions of the linearization, Eqs. (2.32)–(2.38). For these parameters, the predictions of the linearized equations are in good agreement with the full solutions except at the lowest temperature. We can understand the origin of the breakdown of the linearized theory by noting that among the conditions for the validity of this linearization (Eqs. (2.23)–(2.28) and (2.30)–(2.31)): Eq. (2.25) is the first to breakdown for water in the temperature range considered as the rate of heat transfer is increased. When re-expressed in terms of the effective thermal resistance, it requires that,

$$q_i \ll \frac{P_{s,0}}{R_{\text{eff}} \left. \frac{dp_s}{dT} \right|_{T_0}} \quad (2.43)$$

for the linearized solution to be valid. This condition fails as the total resistance increases due to the increasing resistance of the vapor path, R_{vap} as the saturation pressure of vapor decreases at low temperatures.

2.5.3 Contributions of loop elements to R_{eff} for SHLHPs

We return to Figure 2.7 to see the distinct contributions of the components of the SHLHP to the effective thermal resistance. The terms R_{wall} , R_{wick} and R_{film} are simply the conductive resistance of the wall material, the wick membrane in the condenser, and the heat transfer resistance for conducting the heat out to the sink. We are particularly interested in the effective thermal resistance due to the resistance to the flow of the vapor and liquid. Despite the substantial hydraulic resistance to liquid flow through a capillary

10 m-long and 350 μm in diameter, the contribution of the liquid path to the total thermal resistance is negligible. This fact allows for the design of long SHLHPs with small volumes of liquid (e.g., ~ 1 mL of liquid per cm^2 of wick for this 10 m-long pipe); the minimization of the volume of liquid is important for weight and for stability of this superheated phase. For SHLHPs, the temperature variation within the working fluid itself is small compared to the temperature drop between the condenser and the sink. The global resistance, R_{eff} is essentially R_{film} (or $R_{\text{wick,c}}$) + $R_{\text{wall,c}}$, except at low temperatures at which R_{vap} becomes of the same order and affects the total resistance; of course, the magnitude of R_{vap} could be decreased by increasing the size of the vapor conduit. As the operating temperature rises, R_{vap} decreases as the slope of the saturation line increases (Eq. (2.37)) and the total thermal resistance is dominated by the condenser resistance in most of the temperature range. As discussed in Section 2.2, the inclusion of regulator and condenser wick membrane adds the $R_{\text{wick,c}}$ term but gets rid of R_{film} term by eliminating condensate from the vapor side of the condenser; for the case studied, this change leads to a 10 fold reduction in the global thermal resistance (Figure 2.7b). The elimination of condensate in the sub-saturated SHLHP further allows us to use less condenser area compared to the saturated case. In Figure 2.7, the condenser area used in the sub-saturated case (Figure 2.7b) was 100 times smaller than in the saturated case (Figure 2.7a), yet the R_{eff} for sub-saturated SHLHP is lower.

The increasing evaporator temperature is accompanied by an increase in the slope of the saturation line, resulting into a decrease of resistance in vapor path, R_{vap} . Therefore, after the operation temperature goes up, the resistance from vapor path eventually becomes small relative to the resistances of both the liquid path and wick membranes. Given that the thermal resistances of these solid components and the liquid path have weak temperature-dependence, the effective thermal conductivity becomes nearly constant as temperature increases further, such that the total thermal resistance is

dominated by the conductive resistance of the condenser wick and heat sink, $R_{\text{wick,c}} + R_{\text{wall,c}}$. In summary, as the operational temperature rises, the performance of SHLHP shifts from the monotonically decreasing R_{eff} into higher temperature regime in which the effective thermal conductance becomes temperature-independent and controlled only by the conductive resistances of the wick and wall.

The model and expressions for effective resistance provide a unified picture that will allow us to apply our SHLHP designs to extremely broad range of conditions. For example, with appropriate choices of working fluids, we could operate the SHLHP under a wide range of temperatures (around -50°C – 100°C) with stable performance (effective thermal resistance $< 0.1 \text{ K W}^{-1}$). Ammonia is a particularly attractive candidate due to the large slope of its saturation curve around ambient temperature. Figure 2.8 compares the performances of ammonia-based and water-based sub-saturated SHLHP. The predictions indicate that using ammonia as working fluid will lead to higher effective thermal conductivities near ambient; moreover, the system will be operating in the higher temperature regime, providing approximately constant global conductance. The use of water as a working fluid is predicted to be more appropriate for higher temperatures (i.e., $T_{\text{sink}} > 70^{\circ}\text{C}$).

2.5.4 Impact of activity pinned by the regulator and negative pressures in the liquid

In the expression of R_{eff} for SHLHPs, there is no dependence on activity controlled by the regulator. Physically, a decrease in the activity of the regulator lowers the vapor pressure in the evaporator and thus lowers the temperature required to evaporate the liquid; a decrease in the activity of the regulator also lowers the pressure of the liquid, such that the temperature required to drive evaporation increases. These two effects tend to cancel each other, such that the total thermal resistances are essentially

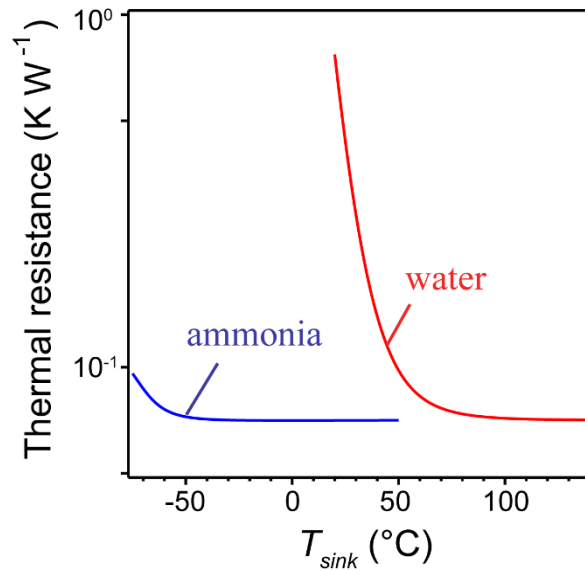


Figure 2.8: Total effective thermal resistances of sub-saturated SHLHP (Eq. (2.32)) with water (red curve) and ammonia (blue curve) as working fluid.

In the range of ambient temperature ($-30^{\circ}\text{C}\sim 50^{\circ}\text{C}$), ammonia serves as a better working fluid in that its total effective thermal resistance is constant and lower than that of water.

$g_{total} = 10 g_e$, $L_{pipe} = 10$ m, other operational parameters are the same as for Figure 2.7 (b), provided in the caption of Figure 2.7.

independent of the activity for slightly sub-saturated condition as long as the capillary pressure developed by nanoporous wick is sufficient to sustain large stress in the liquid. For example, in a 10 m-long, ammonia-operating sub-saturated SHLHP with design parameters the same as those for Figure 2.7b, variations in T_e^{vap} is less than 10^{-4} °C within the activity range of $0.95 < a_{reg} < 0.99$. As the activity goes below 0.95, the pressure difference between the vapor and liquid at the meniscus of evaporator wick membrane starts to exceed the maximum capillary pressure of 20 nm pores.

Figure 2.9 shows the variation of liquid pressure as functions of the sink temperature (Figure 2.9a) and the heat load (Figure 2.9b) in a sub-saturated SHLHP. The reduction of pressure comes from hydraulic resistances, adverse acceleration, and the regulation chamber. In this extreme operation scenario, tens of bars of tension are required to operate the SHLHP; this stress is still small compared to the maximum capillary pressure for pores of 20 nm diameter ($\Delta P_{c,max} > 100$ bars throughout the sink temperature range considered). We note that the tension required is also small compared to the largest tensions achieved with synthetic membrane (~ -70 bars)¹⁵; further, this degree of tension is of the order of stresses found in many plants. In both cases, continuous transportation of the liquid under tension has been shown.

In Figure 2.9b, a maximum evaporator heat flux of $500\text{W}/\text{cm}^2$ can be achieved while the system is still under sub-saturated condition. Under this high heat flux, the Mach number in the vapor path is 0.063, which is far from the sonic limit. Higher heat flux is possible for a SHLHP with lower activity in the regulator; as discussed above, activity controlled by the regulator has negligible effect on the total thermal resistance. Nonetheless, the higher the tension in the liquid, the more the system is prone to cavitation and drying out if defects exist in membranes, as discussed in the following sub-section.

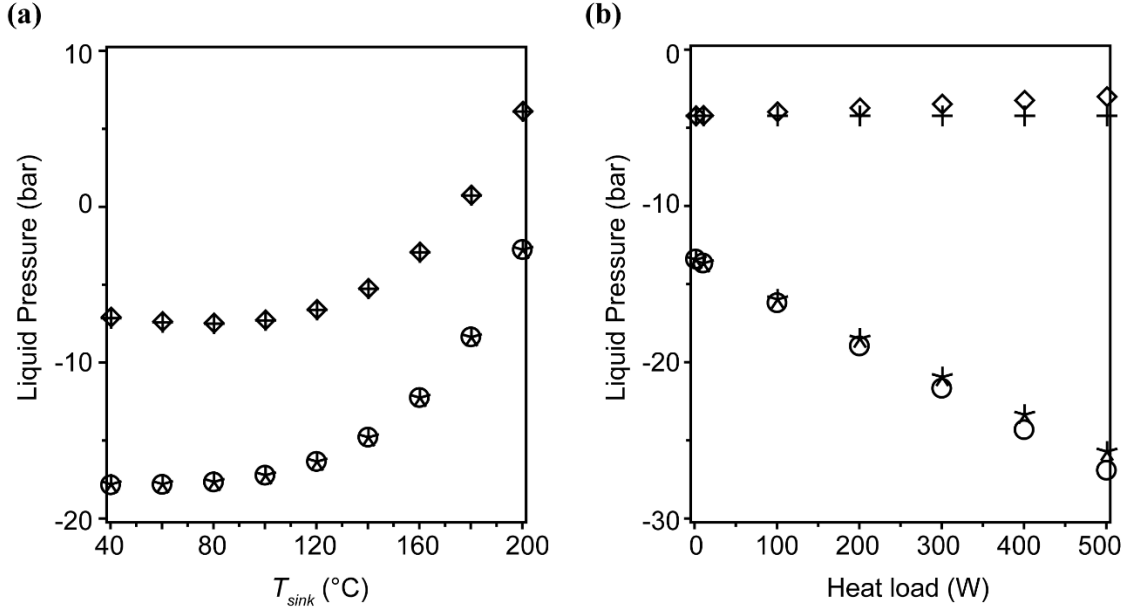


Figure 2.9: Liquid pressure profile in sub-saturated SHLHP as a function of (a) sink temperature, T_{sink} , and (b) heat load.

Diamonds represent the pressure at the condensation surface in the condenser, P_c^{surf} ; crosses represent the liquid in the condenser, P_c^{liq} ; asterisks represent the pressure in the liquid in the evaporator, P_e^{liq} ; and circles represent the pressure at the evaporation surface in the evaporator, P_e^{surf} . The pressure values are calculated from Eqs. (2.6)–(2.19) numerically. $g_{total} = 10 g_e$, $L_{pipe} = 10$ m, the working fluid is water, $q_i = 10$ W for (a) and $T_{sink} = 150^\circ\text{C}$ for (b). Note that 100 W of heat load corresponds to an evaporator heat flux of 100 W/cm^2 . Other operational parameters are the same as for Figure 2.7 (b), provided in the caption of Figure 2.7.

2.5.5 Limits of operation of SHLHP

The design of SHLHP could significantly extend the capillary limit as well as eliminate the entrainment and other negative effects of condensate film in the vapor path and the condenser. Nevertheless, the maximum heat flux of SHLHP is subject to constraints including dry-out from the membranes, boiling or cavitation along the liquid path, and choking in the vapor path. The capillary structure in SHLHP is designed to hold large pressure differences between the vapor side and the liquid side of the evaporator. Yet, the maximum capillary pressure will be defined by the largest pore that crosses between the vapor and the liquid sides of the membrane. Any defect, such as a large pore or crack, could compromise the maximum tension achievable before dry-out occurred.

Another underlying challenge is the metastability of liquid under tension¹. As observed in plants, the liquid under negative pressure is vulnerable to cavitation and the subsequent formation of gas-filled (embolized) conduits;^{78,79} such events would lead to a dramatic loss of hydraulic transport capacity of the device or even dry-out of the entire liquid path. Both homogeneous nucleation and heterogeneous nucleation of the gas phase can lead to cavitation. One strategy observed in plants to manage and control the spread of cavitation is their segmented xylem structure – a network of conduits separated by rigid plates but hydraulically connected through a large number of bordered pits that traverse the plates.²⁷ The nanoporous membranes in the center of pits serve as vapor locks that prevent vapor bubbles from expanding beyond the confines of a single conduit. This structure can be mimicked synthetically in a SHLHP, for example, by separating the liquid flow path into individual subunits by nanoporous membranes.

The SHLHP design is prone to the same limitations due to potential choking of the vapor path as in conventional HPs and LHPs.⁴⁹ As with conventional LHPs, the choking limit can be avoided by increasing the diameter of the vapor path. For the case of a 10

m-long pipe with a 6 mm-diameter vapor conduit operating with ammonia at ambient temperature, the Mach number is less than 10^{-1} for heat flows less than 1000 W.

2.6 Conclusions

I have analyzed superheated loop heat pipes in which nanoporous wick membranes and the absence of a compensation chamber allow for the transport of superheated liquid. I have further proposed the introduction of a regulator to maintain the fluid in a sub-saturated state throughout the liquid and vapor paths during operation. Comparing the working cycles of the conventional and the SHLHP designs, I have illustrated that the advantage of SHLHPs are 1) elimination of the temperature head and sub-cooling conditions that limit the conductance of conventional LHPs, and 2) improvement of the condenser thermal conductivity. Our analysis indicates that large hydraulic resistances and large adverse accelerations have negligible impact on the total resistance, such that SHLHPs could be particularly valuable in applications such as cooling of avionics and energy management in buildings in which heat must be transferred over large distances (tens of meters) and against gravity or acceleration (many time gravity). Our analytical expressions for effective resistances provide a valuable basis for the design of these systems, for example, for the choice of the size of conduits and of the working fluid.

The experimental realization of SHLHPs presents outstanding challenges. The construction of nanoporous membranes must be achieved without introducing excessive hydraulic resistance into the liquid path and in a manner that can support large pressure differences without fracture or collapse. Such structures should couple a thin and uniformly nanoporous layer to hierarchical macroporous supporting layers with increasing diameters and decreasing hydraulic resistances. Another concern about the membrane is that any trace quantities of surfactants or solvents adsorbed to the membrane surface would reduce the effective surface tension (less than the prediction

by Eq. (1.2)); suitable choices of membranes and a careful design of fabrication process are needed to minimize the possibility of contamination that may deteriorate the performance of the membranes. The robustness of SHLHP technology depends on the suppression of cavitation in the superheated liquid and the development of means to reconnect the liquid path if cavitation does occur. For the former, pipe wall materials that are hydrophilic and defect free are basic requirements; compartmentalization of the liquid path, as is found in the xylem conduits of plants⁸⁰, could help to control the spread of cavitation. For the later, integration of source of energy to drive refilling must be developed. On all of these fronts, plant physiology may continue to provide significant guidance.^{80,81}

Notation

γ	: surface tension of the liquid	[Pa m]
ΔP_c	: capillary pressure ($= 2\gamma \cos\theta_c/r_p$)	[Pa]
η_{liq}	: viscosity of the condensate	[kg m ⁻¹ s ⁻¹]
θ_c	: contact angle between the liquid meniscus and the pore wall	(-)
λ	: heat of vaporization of the working fluid	[J kg ⁻¹]
μ_w^{vap}	: chemical potential of the vapor at the vapor-liquid interface	[J mole ⁻¹]
μ_w^{surf}	: chemical potential of the liquid at the vapor-liquid interface	[J mole ⁻¹]
$\nu_{vap,0}$: kinematic viscosity of the vapor at T_0	[m ² s ⁻¹]
$\nu_{liq,0}$: kinematic viscosity of the liquid at T_0	[m ² s ⁻¹]
$\rho_{vap,0}$: density of the vapor at T_0	[kg m ⁻³]
$\rho_{liq,0}$: density of the liquid at T_0	[kg m ⁻³]
A_{source}	: area conducting heat into the evaporator	[m ²]
A_w	: area of the wick membrane	[m ²]
A_{sink}	: area conducting heat out of the condenser	[m ²]
a_{reg}	: activity of the regulator	(-)
D_{vap}	: diameter of the vapor path	[m]
D_{liq}	: diameter of the liquid path	[m]
D_{cond}	: diameter of the condenser tube (for saturated cases)	[m]
D_{pore}	: diameter of membrane pores	[m]
g_{total}	: the sum of gravitational and dynamic acceleration	[m s ⁻²]

g_e	: time of gravities ($g_e = 1$, $g_{total} = 10$ [kg m s ⁻²])	(-)
H_e^{vap}	: enthalpy of the vapor in the evaporator	[J]
H_e^{liq}	: enthalpy of the liquid in the liquid cavity in the evaporator	[J]
H_c^{surf}	: enthalpy of the liquid at the wick interface in the condenser	[J]
H_c^{liq}	: enthalpy of the liquid in the liquid cavity in the condenser	[J]
h_{sink}	: overall heat transfer coefficient conducting heat out of the condenser	[W m ⁻² K ⁻¹]
h_{film}	: heat transfer coefficient for the condensate film	[W m ⁻² K ⁻¹]
k_w	: effective thermal conductivity of the wick membrane	[W m ⁻¹ K ⁻¹]
k_{wall}	: thermal conductivity of the pipe wall material	[W m ⁻¹ K ⁻¹]
k_{liq}	: thermal conductivity of the condensate	[W m ⁻¹ K ⁻¹]
L_{pipe}	: length of the heat pipe	[m]
L_{pore}	: thickness of the wick membranes	[m]
L_{wall}	: thickness of the pipe wall material	[m]
MW	: molecular weight	[kg mole ⁻¹]
P_e^{surf}	: pressure at the surface of the wick membrane of the evaporator	[Pa]
P_e^{liq}	: pressure in the liquid cavity of the evaporator	[Pa]
P_c^{surf}	: pressure at the surface of the wick membrane of the condenser	[Pa]
P_c^{liq}	: pressure in the liquid cavity of the condenser	[Pa]
$p_s(T)$: saturation vapor pressure at a given temperature T	[Pa]
$p_{s,0}$: saturation vapor pressure at T_0	[Pa]
p_e	: vapor pressures in the vapor cavities of the evaporator	[Pa]

p_c	: vapor pressures in the vapor cavities of the condenser	[Pa]
Q	: mass flow rate of the working fluid	[kg s ⁻¹]
q_i	: heat input	[W]
q_{leak}	: heat leaked into the evaporator liquid cavity	[W]
R_{gas}	: the gas constant	[J K ⁻¹ mole ⁻¹]
R_{vap}	: hydraulic resistance of the vapor conduit	[Pa s kg ⁻¹]
R_{liq}	: hydraulic resistances of the liquid conduit	[Pa s kg ⁻¹]
$R_{wick,e}$: hydraulic resistance of the wick membrane in the evaporator	[Pa s kg ⁻¹]
$R_{wick,c}$: hydraulic resistance of the wick membrane in the condenser	[Pa s kg ⁻¹]
R_{eff}	: effective thermal resistance	[K W ⁻¹]
$R_{wall,e}$: thermal resistance of the evaporator wall	[K W ⁻¹]
$R_{wall,c}$: thermal resistance of the condenser wall	[K W ⁻¹]
$R_{wick,e}$: thermal resistance of the evaporator wick membranes	[K W ⁻¹]
$R_{wick,c}$: thermal resistance of the condenser wick membranes	[K W ⁻¹]
R_{vap}	: the contribution associated with the vapor flow within R_{eff}	[K W ⁻¹]
R_{liq}	: the contribution associated with the liquid flow within R_{eff}	[K W ⁻¹]
R_{film}	: thermal resistance of the film condensation heat transfer	[K W ⁻¹]
r_p	: radius of the pores	[m]
T_{source}	: temperatures of the vapor side wall material in the evaporator	[K]
T_e^{vap}	: temperatures in the vapor cavities in the evaporator	[K]
T_e^{liq}	: temperatures in the liquid cavities in the evaporator	[K]

T_c^{vap}	: temperatures in the vapor cavities in the condenser	[K]
$T_c^{liq} (T_0)$: temperatures in the liquid cavities in the condenser	[K]
T_{sink}	: temperature of the heat sink outside the liquid side of the condenser	[K]
\bar{v}_{liq}	: molar volume of liquid	[m ³ mole ⁻¹]

CHAPTER 3

STABILITY LIMIT OF WATER BY METASTABLE VAPOR-LIQUID EQUILIBRIUM WITH NANOPOROUS SILICON MEMBRANES

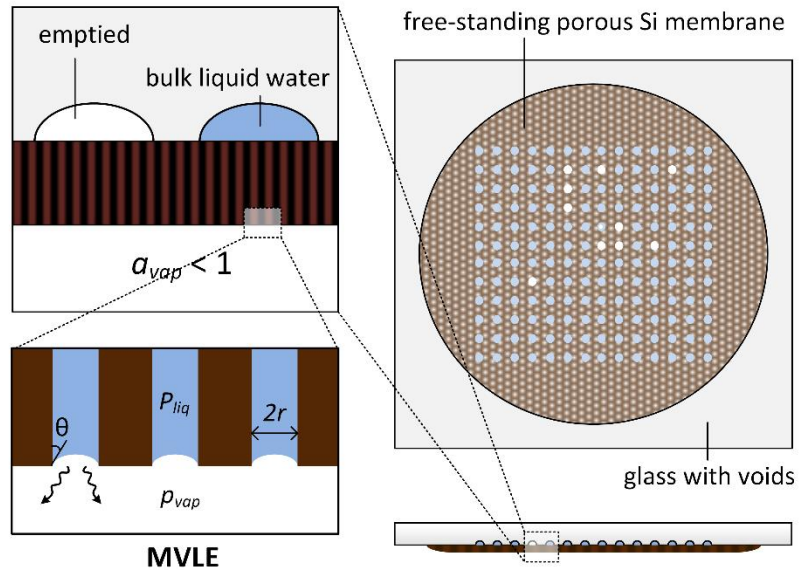
Adapted from the manuscripts submitted to *J. Phys. Chem. B*

3.1 Introduction

Liquid can sustain mechanical tension as its pressure drops below the vapor-liquid coexistence line and becomes less than zero, until it reaches the stability limit – the pressure at which cavitation (i.e. the nucleation of vapor bubbles in bulk liquid) inevitably occurs. As introduced in Chapter 1.1, for liquid water, its stability limit is still a subject of debate. The experimental measurements for water stability limits obtained with different techniques shows a large scatter, in particular at the temperature range from 50°C down to 0°C (see Figure 1.4). While the experiments in quartz inclusions^{8,17} frequently measure stabilities as low as -140 MPa, consistent with that predicted by theory or simulations^{18–20}, the majority of the experiments have observed stability limits around -20 to -30 MPa,^{10,12,13,16,21–25} a far less negative value compared to theoretical predictions. Further, among these experiments that show low stability, there are two sets of data showing contradictory temperature-dependence of the stability limit: Briggs¹⁰ reported a remarkable 10-fold decrease in the maximum tension observed between 6°C and 0°C; in contrast to this abrupt change in the stability limit, Davitt *et al.*²⁴ found a monotonic increase (more negative) trend in the stability limit as temperature approached 0°C.

In this chapter, I report on an experimental system which enables test of the temperature-dependence of the stability limit with the MVLE method (Figure 3.1). In

(A)



(B)

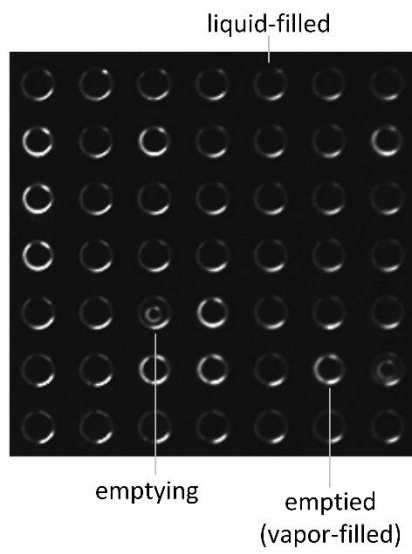


Figure 3.1: Metastable vapor-liquid equilibrium (MVLE).

(A) Schematic diagrams showing the top and cross-sectional views of a nanoporous silicon membrane bonded with glass to define the voids in the sample. The enlarged figures illustrate the MVLE method: a nanoporous silicon membrane saturated with liquid water separates the bulk liquid water within glass voids from the external sub-saturated vapor with activity, $a_{vap} < 1$. At the membrane surface, the liquid water in pores and the sub-saturated vapor satisfy the chemical potential balance, $\mu_{liq}(P_{liq}, T) = \mu_{vap}(p_{vap}, T)$. The pressure of the water under the concave meniscus is $P_{liq} = p_{vap} - 2\sigma\cos\theta/r$, where σ [N m^{-1}] is the surface tension, θ [$^\circ$] is the contact angle of liquid water with the pore wall, and r [m] is the radius of the pore. (B) An actual device image (top view) shows liquid-filled, emptying, and vapor-filled cavities.

our previous work exploiting MVLE method¹⁶, liquid water was encapsulated in vapor-coupled voids defined in hydrogel membranes. The sample reached metastable equilibrium with sub-saturated water vapor; activities of the vapor were established by the saturated salt solutions. The water remained stable with sub-saturated vapor of activity, a_{vap} down to 0.85 at room temperature, corresponding to a stability limit of -22 MPa, based on Eq. (1.1), falling into the range typically reported by other techniques.

Here, we chose to change the materials and format of our samples to overcome challenges associated with using hydrogel as the membrane material; these challenges include the long equilibration time and difficulty controlling the volume and geometry of the internal volume of liquid. We turned to anodized silicon, an alternative nanoporous membrane material, as presented in our previous works of microtensiometer⁸², cavitation-coupled drying³², and nano-confined flow³³. We chose nanoporous silicon in this study for its preferred hydrophilic surface, its tunable porosity and pore structure, as well as its compatibility with standard micro-fabrication techniques. We fabricate free-standing porous silicon membranes and anodically bond them with glass substrates patterned with voids (Figure 3.1(A)). These voids serve as vessels for water and are coupled to the water vapor through the porous silicon membrane. We also chose to control the activity of water with the pressure of pure water vapor in vacuum. This choice was made for two reasons: 1) exposing the samples to pure water vapor instead of air allowed us to minimize the dissolved gases in the bulk liquid water sample, and 2) controlling the water vapor pressure directly avoided complication of temperature-dependence of the activity of salt solutions – the suitable salts to achieve a desired series of activities becomes harder to find as the temperature approaches 0°C.

In this work, stability limit of water as a function of temperature from 15°C to 0°C is reported. We found the trend to be monotonically increasing as temperature

approaches zero; this trend contradicts with the work by Briggs¹⁰ but agrees with that observed in the study by Davitt *et al.*²⁴ Nevertheless, the observed stability limit is again less negative than the limit predicted for homogeneous nucleation from nucleation theories. A few possible mechanisms triggering heterogeneous or seeded nucleation are discussed to try to explain the low stability limit observed in this work.

3.2 Theory

3.2.1 Metastable vapor-liquid equilibrium (MVLE)

Figure 3.1(A) illustrates the MVLE method in which a macroscopic volume of liquid confined in a closed container (void etched in glass) is coupled to the external vapor through a porous medium with rigid, wettable walls (porous silicon layer). When the vapor becomes sub-saturated (the activity of the vapor, $a_{vap} < 1$), the liquid evaporates from the membrane surface and liquid is pulled out of the void of a fixed volume; the cohesion of liquid water can resist this external mechanical tension (pulling) and results in a reduction of the internal liquid pressure. The pressure within the bulk liquid drops until the liquid in the void reaches metastable equilibrium with the sub-saturated vapor or cavitates. Capillarity ensure this equilibrium at the open ends of the pores. As the equilibrium is reached, the liquid pressure, P_{liq} , must satisfy the chemical potential balance, $\mu_{vap}(p_{vap}, T) = \mu_{liq}(P_{liq}, T)$:

$$\mu_{sat}(T) + \int_{P_{sat}}^{P_{vap}} v_{vap}(P, T) dP = \mu_{sat}(T) + \int_{P_{sat}}^{P_{liq}} v_{liq}(P, T) dP \quad (3.1)$$

where $\mu_{sat}(T)$ is chemical potential of water at the saturation pressure, p_{sat} , and temperature, T , and v_{vap} and v_{liq} are the molar volumes. Eq. (3.1) forms the basis for the

approximate Kelvin equation (Eq. (1.1)). If we assume that water vapor is an ideal gas, then Eq. (3.1) can be rewritten as:

$$RT \ln(a_{vap}) = \int_{P_{sat}}^{P_{liq}} \frac{1}{\rho_{liq}(P, T)} dP \quad (3.2)$$

where $\rho_{liq}(P, T)$ [mol m⁻³] is the molar density of the liquid water that can be evaluated with an extrapolation of an equation of state (EoS). In this work, the translation between a_{vap} and P_{liq} under MVLE is done through Eq. (3.2) with an extrapolation of the IAPWS EoS^{83,84}. For a given temperature, we numerically integrated P_{liq} , starting from the saturation density ρ_{sat} to the spinodal density ρ_{min} , using trapezoid rule with a step size $\Delta\rho=0.005$. At each step, the (P_{liq}, a_{vap}) pair was recorded. The saturation vapor pressure data as a function of temperature, T from 235 to 400 K, was obtained from [Murphy & Koop, 2005]⁸⁵ (235–273.15 K) and NIST⁸⁶ (273.16–400 K), and interpolated for any desired temperature within the range.

A pressure difference, $\Delta P = p_{vap} - P_{liq}$, arises as the two phases – sub-saturated vapor and metastable liquid – come to equilibrium. The ΔP can be calculated from the chemical potential balance described above. For example, for a 1% reduction in vapor activity from saturation ($a_{vap} = 0.99$) at room temperature, there exists a difference of pressure, $\Delta P \sim 1.3$ MPa. Such a co-existence of a liquid and its vapor at different pressures deviating from the binodal can be mediated with a porous medium with sufficiently small pore, based on capillarity. The Young-Laplace equation predicts that the pressure difference (the Laplace pressure) across a curved meniscus within a cylindrical pore,

$$P_{vap} - P_{liq} = \Delta P = \frac{2\sigma \cos \theta}{r_{pore}} \quad (3.3)$$

where σ [N m⁻¹] is the surface tension, θ [°] is the contact angle of liquid water with the pore wall, and r_{pore} [m] is the radius of the pore (see schematics for enlarged pore surface in Figure 3.1(A)). The porous medium with its associated menisci thus acts as a “membrane”, in that it separates the bulk liquid and the bulk vapor phases while allowing equilibrium between them. The liquid water can pass through the membrane as a Darcy flow and transfer to and from the vapor phase via evaporation and condensation at the menisci; on the contrary, the vapor phase cannot penetrate the membrane as long as the menisci remain pinned within the pores based on the mechanical balance in Eq. (3.3). The larger degree of sub-saturation in the vapor is (and the larger the reduction in pressure in the liquid is), the higher this Laplace pressure must be to sustain the pressure difference between the liquid and vapor phases, and the smaller the pore size must be. When the pressure difference required for equilibrium exceeds the Laplace pressure for the receding contact angle in any larger pores, these menisci will recede into the membrane and eventually allow vapor bubbles to enter the void ((a) in Figure 3.2(A) and (B) – meniscus invasion); the existence of a single path between the internal volume of liquid and the external vapor with pore size larger than a critical value ($r_{pore} > 2\sigma \cos \theta / \Delta P$) would result in the release of the metastability in the bulk liquid. For example, at $\Delta P = 20$ MPa (corresponding to $a_{vap} \sim 0.86$ at room temperature), the largest pore size within the membrane is required to be no larger than $r_{pore} \sim 7$ nm.

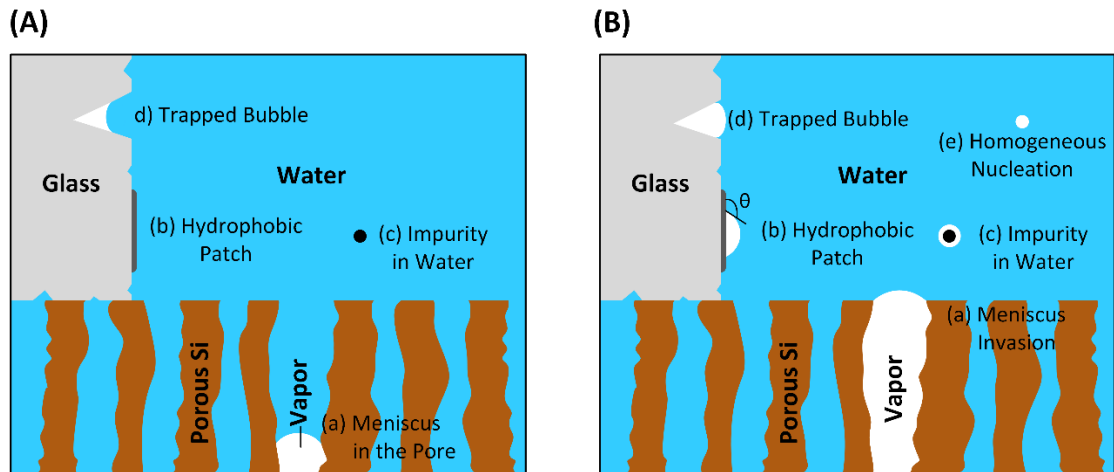


Figure 3.2: Mechanisms of cavitation.

(A) Illustration of features in a glass void bonded to porous silicon membrane that potentially lead to cavitation thresholds above the kinetic stability limit imposed by homogeneous nucleation, including (a) invasion of meniscus in a large pore, (b) heterogeneous nucleation on a hydrophobic patch on the surface of the void, (c) heterogeneous nucleation on a dissolved or dispersed impurity, and (d) pre-nucleation by a bubble trapped in a crevice on the void wall. (B) As the bulk water in the void is placed at sufficiently reduced pressures, cavitation may occur due to (a) meniscus receding into the void, or features (b)-(d), or (e) homogeneous nucleation.

3.2.2 Kinetic theory of the homogeneous nucleation

In the absence of a pre-existing pocket of gas in the liquid volume (e.g., in a structural defect – see below) or of invasion of gas through pore in the membrane, the metastable liquid may relax toward stable state via the formation (nucleation) of new vapor bubble within the bulk liquid (Figure 3.2(B)-(e) – homogeneous nucleation). This nucleation event is an activated process that occurs when a thermal fluctuation overcomes the free energy barrier to form a bubble of the critical size (above which the bubble grows spontaneously).

Classical nucleation theory (CNT) lays the foundation of theoretical treatments of nucleation processes¹ – for droplet condensation from supercooled vapor, for crystallization in supercooled liquid, as well as for bubble nucleation in superheated liquid. Consider a liquid been put under tension at constant T to a pressure P_{liq} , the energy associated with creation of a vapor bubble of radius R [m] is given by:⁸⁷

$$E(R) = \frac{4}{3} \pi R^3 (P_{liq} - p_{vap}) + 4\pi R^2 \sigma \quad (3.4)$$

where p_{vap} is the pressure of the vapor at the same chemical potential as the liquid at P_{liq} . The first term on the right hand side gives the energy gain through forming a volume of the stable phase, and the second term accounts for the energy cost of creating an interface with surface tension, σ [N m^{-1}]. The maximum of the energy profile in Eq. (3.4) gives an energy barrier,

$$E_b(P_{liq}) = \frac{16\pi\sigma^3}{3(P_{liq} - p_{vap})^2} \quad (3.5)$$

associated with the critical bubble of radius $r_c = 2\sigma / (p_{vap} - P_{liq})$. Thermal fluctuations of the system trigger the nucleation at a rate k_{cav} [s^{-1}], which can be expressed as

$$k_{cav} = \Gamma_0 V \exp\left(-\frac{E_b}{k_B T}\right) \quad (3.6)$$

where Γ_0 [$m^{-3} s^{-1}$] is a kinetic prefactor, V [m^3] is the volume of the bulk liquid, and k_B [$J K^{-1}$] is Boltzmann's constant. The probability that no cavitation event will occur during an experiment over time τ is:⁵

$$\Sigma = \exp(-k_{cav} \cdot \tau) \quad (3.7)$$

The cavitation pressure P_{cav} at a given temperature T is defined as the liquid pressure at which the cavitation probability reaches 1/2,

$$P_{cav} = p_{vap} - \left(\frac{16\pi\sigma^3}{3k_B T \ln\left(\frac{\Gamma_0 V \tau}{\ln 2}\right)} \right)^{1/2} \quad (3.8)$$

In this study, we compare the survival probability of voids in the sample against this theory to test the compatibility of our work with a thermally activated cavitation mechanism.

3.2.3 Other mechanisms of cavitation

One possibility for cavitation occurring before reaching the kinetic stability limit predicted by homogeneous nucleation theory is heterogeneous nucleation.

Heterogeneous nucleation happens when the surface of the container in contact with the liquid (see Figure 3.2-(b) – hydrophobic patch) or an impurity within the liquid (see Figure 3.2-(c) – impurity in water, such as suspended particles or dissolved solutes) provide a favorable nucleation site on which the formation of vapor starts. In many practical circumstances, cavitation events will be heterogeneous instead of homogeneous, due to the difficulty in avoiding any imperfectly wetted moieties or impurities within liquid. Heterogeneous nucleation can be described using the same formalism as described above for homogeneous nucleation, however it can have a lower energy barrier. For example, consider a hydrophobic surface in contact with the bulk liquid water as in Figure 3.2-(b), the energy barrier to form a vapor bubble of critical size is given by:⁸⁸

$$E_{het,b}(P_{liq}) = \frac{16\pi\sigma^3 F}{3(P_{liq} - p_{vap})^2} \quad (3.9)$$

where $F = (2 + 3\cos\theta - \cos^3\theta)/4$ and θ [°] is the equilibrium contact angle of water on the bulk solid surface. This expression differs from the one for the homogeneous nucleation only by the factor F , a function of contact angle, θ .

Another possibility for cavitation occurring before reaching the homogeneous stability limit is pre-nucleation due to the presence of gas bubbles trapped in the wall of the liquid container during the filling process (see Figure 3.2-(d) – trapped bubble). As the liquid pressure drops, these bubbles can expand and result in a macroscopic vapor phase. Apfel's model^{89,90} predicts the threshold pressure in the liquid, P_T , required to cause cavitation by the expansion of gas pockets trapped in idealized, conical crevices (as depicted in Figure 3.2-(d)); this treatment is reasonable for the MVLE experiments exploiting a quasi-static application of tension. Depending on the crevice geometry

(e.g. radius at the opening and apex angle), wettability of the liquid inside crevices (e.g. advancing and receding contact angle), and pressure history of the sample, different functional forms of the threshold pressure were predicted. For sufficiently large crevices, the gas content in the liquid and the application of elevated pressure during the preparation of the samples affect the threshold pressure. There can also exist crevices of arbitrarily small size that lead to a threshold pressure that is independently of the pre-pressurization, and can be anywhere in the range between p_{vap} and $-2\sigma/r_0$. A detailed discussion exploring criteria of trapped bubbles effecting stability limit in MVLE can be found in [Wheeler & Stroock, 2009].¹⁶

3.3 Experimental Methods

3.3.1 Sample fabrication

Figure 3.1(A) shows the schematics of the porous silicon-glass void sample. The free-standing porous silicon membranes were anodically bonded to glass substrates patterned with voids; these voids served as vessels for water and are independently coupled to the water vapor through the porous silicon membrane.

Porous silicon was formed by anodization of silicon substrate in an HF-based electrolyte.⁶⁰ A partial dissolution of silicon occurs due to the electrochemical reaction at its surface. The porosified portion can be released from the substrate to form a free-standing layer with pores passing through its thickness.⁹¹ Techniques of fabricating this free-standing silicon membrane have been described by many researchers.⁹²⁻⁹⁶ These samples have mainly served for studying the optical and optoelectronic properties of porous silicon. A few different methods can be found in the literature, including a two-stage method^{92,93} involving sharply raising the current density to the electropolishing region, a single-stage technique⁹⁴ in which porous layer is spontaneously detached, and a new two-step approach⁹⁶ consisting of gradually ramping the current density at a

certain rate. We used the latter approach for its simplicity and its good control over the thickness and the porosity of the membrane.

Nanoporous silicon membranes were prepared by electrochemical anodic etching of highly doped, p-type, <100> oriented silicon wafers with a resistivity of 0.01 Ω -cm. Silicon wafers were mounted, one at a time, between a Teflon cell and an Aluminum bottom electrode with one side of the silicon wafer in contact with the electrolyte, a 70:30 (v/v) solution of 49% hydrofluoric acid and 99% acetic acid in the Teflon cell. Figure 3.3 shows the profiles of typical current density (Figure 3.3(A)-left) and voltage (Figure 3.3(A)-right) across the electrochemical etch cell, as well as schematic cross-section views of the silicon substrate during the etch process (Figure 3.3(B)). With a Hewlett Packard DC power supply (Model 6634B), silicon substrate was etched at a constant current density of 13 mA cm⁻² for 150 minutes, until the required thickness of porous layer was reached as assessed by total current passed per etched area; in our work, the etch rate = 1.18 [$\mu\text{m} (\text{C}/\text{cm}^2)^{-1}$]. Then, the current density was gradually ramped up at a constant rate of 90 mA minute⁻¹, to detach the porous layer from the substrate. As soon as the sign of membrane fully detaching was observed, etching was stopped. In Figure 3.3(A)-right, the sudden drop of the voltage during the ramp reflects the full detachment of the porous layer into a free-standing membrane. The membrane taken out of the electrochemical cell was immersed in isopropanol for 5 minutes and then pentane for 5 minutes to reduce the stress during membrane drying. The final membrane thickness of the sample used in experiments reported here was measured by a Mitutoyo digital micrometer to be 138 μm .

BOROFLOAT[®] 33 float borosilicate glass wafers were used to define voids that we coupled to the porous silicon membrane. These voids were formed as follows: An amorphous silicon layer was deposited (Oxford PlasmaPro 100 PECVD) onto the glass wafer to a thickness of ~200 nm and then annealed to reduce the residual stress⁹⁷. This

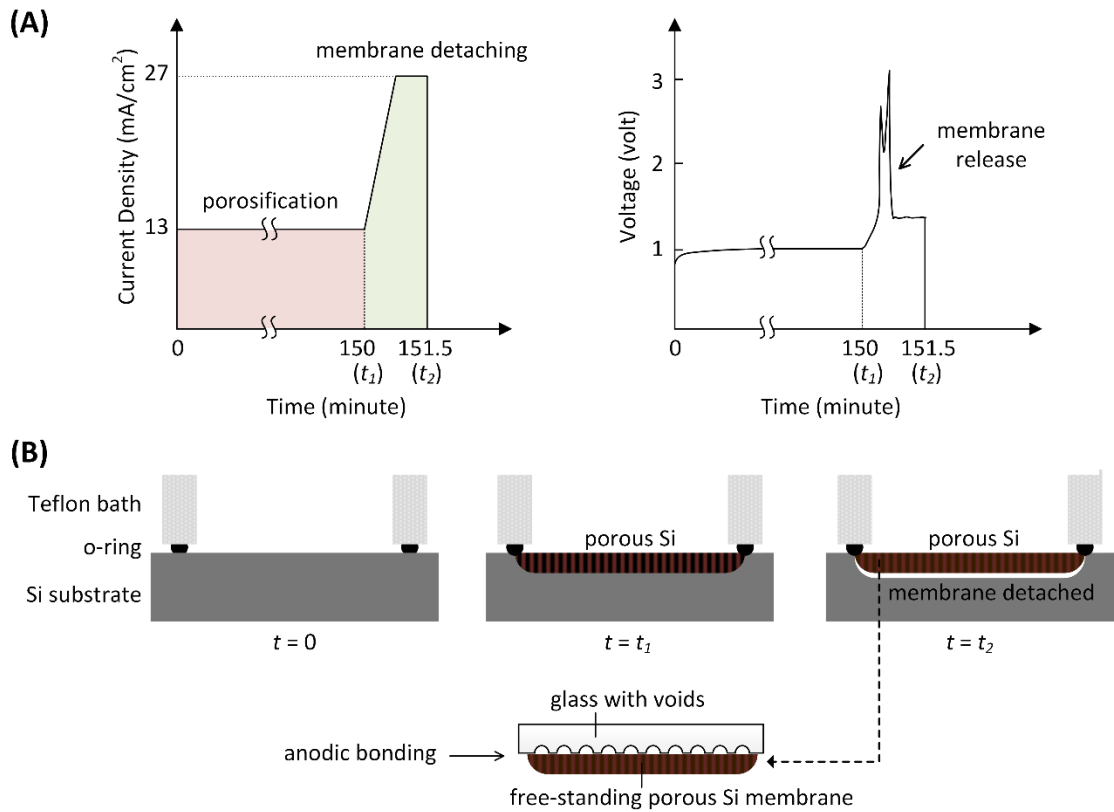


Figure 3.3: Fabrication of free-standing porous silicon membrane and membrane-coupled voids.

(A) The temporal profile of imposed current density (left) and an example of a typical measured voltage profile (right) during the phases of the porosification and the ramping of current density to detach the porous layer. (B) Cross-sectional view of silicon wafer under electrochemical etch cell at corresponding time points and the subsequent bonding with etched glass.

layer served as the mask for the glass etch, and was patterned via standard lithography into a pattern of circular voids (200 μm in diameter) arranged in a square array of 25×25 , with a distance of 400 μm between successive voids (Figure 3.1(A) shows an array of 12×12 for the purpose of clarity). The voids were etched with 49% hydrofluoric acid to reach a depth of 25 μm ; the etch rate was 7 $\mu\text{m minute}^{-1}$. We then bonded the glass and silicon anodically (400°C, 800V) to couple each voids to the outside environment via the nanopores of the silicon membrane.

The bonded samples were submerged in water and left in the vacuum oven for 12 hours to remove air from the voids; this step was performed in order to avoid the large supersaturation with air in the liquid that would occur if one atmosphere of air were forced to dissolve in an equal volume of liquid. The samples were then filled with degassed water in a pressure bomb with 35 MPa of pressure to minimize residual gases in trapped bubbles.

3.3.2 Vapor control system

Figure 3.4(A) shows the schematic diagram of the vapor control system. The custom sample stage was connected between the water vapor source and the vacuum pump, with needle valves on either side. As shown in the enlarged figure in Figure 3.4(A), this aluminum stage consisted of a sample chamber on top of a cooling base. Two important features of the stage were: 1) the micro-grooves on the floor within the sample chamber in contact with the membrane-side of the sample; these grooves ensures good thermal contact between the silicon membrane and the sample chamber floor, and at the same time provide a macroscopic path way for the vapor to be equilibrated with the water in the membrane pore. 2) A recessed area in the ceiling of the cooling fluid cavity minimized the distance between the sample chamber floor and the cooling fluid; keeping a larger distance between the rest of the sample chamber and the cooling fluid

(A)

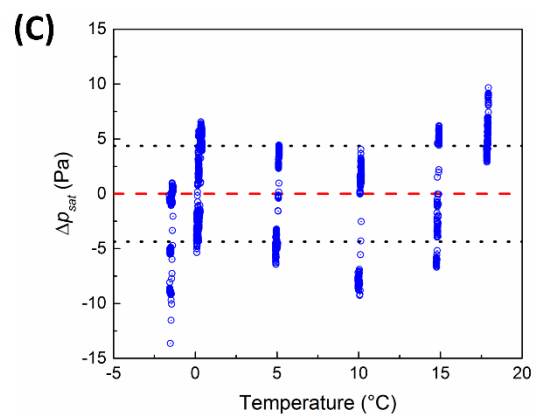
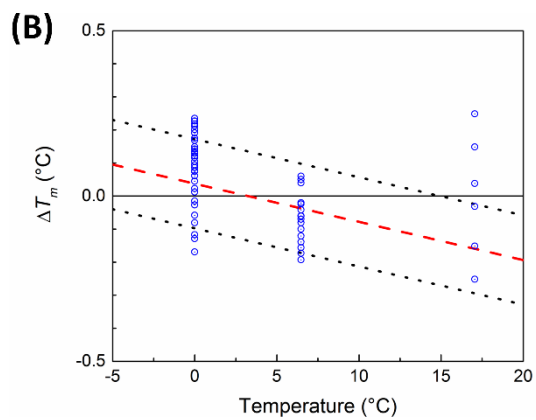
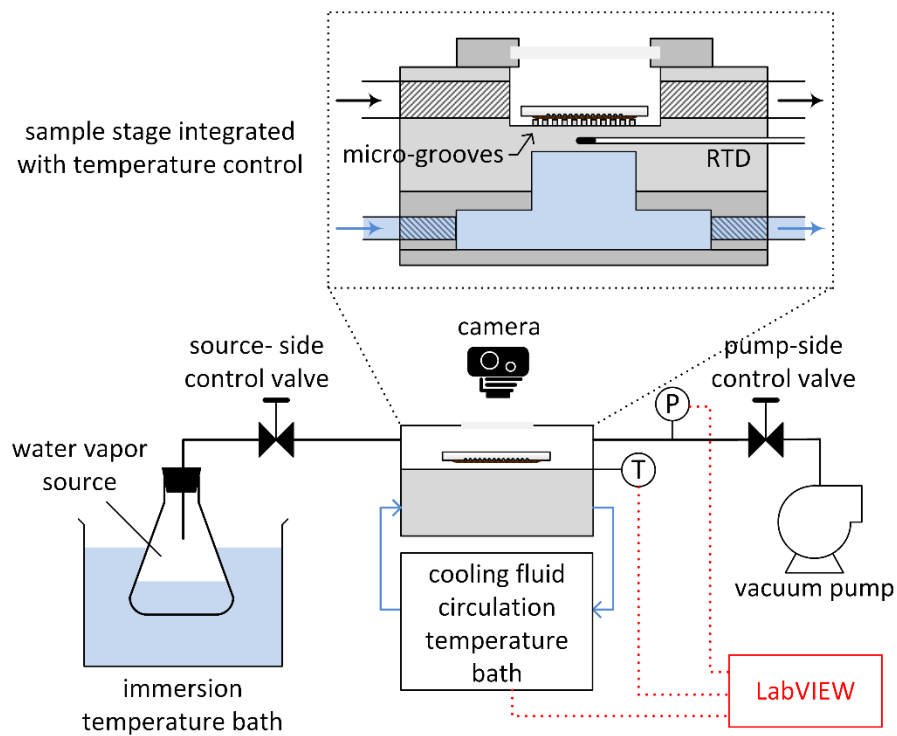


Figure 3.4: Vapor control system.

(A) Schematic diagrams of the experimental system. The temperature and pressure within the chamber were automated to record every 2 seconds using LabVIEW. The expanded view (top) shows the detail of a custom-built sample stage. (B) Temperature calibration data. Blue circles represent the differences in measured melting temperatures relative to literature values, $\Delta T_m = (\text{measured melting points} - T_m)$, for three liquids – water ($T_m = 0^\circ\text{C}$), cyclohexane ($T_m = 6.7^\circ\text{C}$), and hexadecane ($T_m = 18.08^\circ\text{C}$). The red dash line presents the calibration line obtained from the data and the black dot line shows the standard deviation of the data from the calibration line. This calibration line was used to calibrate all temperature measurements in this work; $T_{actual} = 0.992 \times T_{measured} + 0.0567$. (C) Pressure calibration data. Blue circles represent the differences in measured saturation pressures from literature values, $\Delta p_{sat} = (\text{measured saturation pressure}(T) - p_{sat}(T))$; the temperature corresponding to each data point is calibrated using the temperature calibration line.

also minimized condensation around the sample that could affect the vapor pressure. By adjusting the position of the two needle valves, one placed upstream and one placed downstream, we could control the vapor pressure within the sample chamber. The vapor pressure was measured with a capacitance pressure gauge (Adixen ASD2002). Water in the vapor source flask was degassed prior to the experiment to avoid abrupt boiling. The temperature of the vapor source immersion bath (Lauda Brinkmann Ecoline100) was fixed at a value higher than that within the chamber to enable precise control of the vapor activity at values near saturation (relative humidity close to 100%) at the temperature of the sample. Cooling fluid to the stage was connected to an external temperature control bath (Thermo Scientific RTE 740) and circulated through the base of the stage to control the temperature at the sample. A resistance temperature detector (RTD) was inserted into a hole in the aluminum plate between the cooling fluid chamber and the sample chamber to measure the chamber floor temperature in real time. The sample was viewed using a stereoscope placed above the sample chamber's viewing window to observe the glass-side of the sample and the images were recorded over the duration of each experiment. To reduce condensation on the outer surface of the sample chamber, it was wrapped in insulating material and dry air was blown across the viewing window.

Figure 3.4(B) and (C) show the temperature and pressure calibration data for the vapor control system. The temperature measurement was calibrated by observing the melting point, T_m , of pure liquids under atmospheric pressure on a piece of silicon wafer placed on the floor of the stage, as within our sample during experiments. Three different liquids were used – water ($T_m = 0^\circ\text{C}$), cyclohexane ($T_m = 6.7^\circ\text{C}$) and hexadecane ($T_m = 18.08^\circ\text{C}$). As shown in Figure 3.4(B), the measured melting points were compared with the known values of T_m to establish a temperature calibration line (the red dash line). The standard deviation of the temperature offsets from the

calibration line was 0.14°C; this standard deviation was treated as uncertainty and was propagated to the uncertainty in vapor activity. The vapor pressure measurement was calibrated by observing the saturation pressure across the temperature range $T = -1.5$ – 18°C : the stage temperature was held at a constant value while the vapor pressure was gradually increased by adjusting the valves until liquid droplets emerged on the sample stage; we identified the pressure at the onset of condensation as the saturation vapor pressure at the set temperature, $p_{sat}(T)$. Figure 3.4(C) compares the measured pressures with the saturation pressures from the literature ([Murphy & Koop, 2005]⁸⁵ and NIST⁸⁶). We found no systematic offset of the measured pressures and hence we used no calibration line for pressure measurement; the standard deviation of pressure offsets was 4.4 Pa. For all the experiment data points ($T_{measured}, p_{vap}$), we calibrate $T_{measured}$ using the temperature calibration line to obtain T_{actual} , and used p_{vap} as it is. The standard deviations of both temperature and pressure were treated as uncertainties and propagated to the uncertainty in vapor activity and liquid pressure (Figure 3.7 and Figure 3.9).

The experimental protocol for investigating stability limit was as follows: The temperature of the base of the chamber was set at a constant temperature prior to loading the sample. The bonded sample filled with liquid water was placed membrane-side down onto the floor of the chamber in the stage; a macroscopic film of liquid water was maintained near the sample to keep it hydrated during the assembly of the chamber. As the chamber was assembled and sealed, the vacuum pump was turned on to evacuate any air left in the chamber and start pulling pure water vapor into the system. The valves were adjusted to maintain the desired vapor pressure according to the activity set point. The duration for each activity was at least 3 hours before adjusting the valve to step down vapor pressure to a new set point; this duration was selected based on the observation that most cavitation events after a pressure step change happened within the

first 90 minutes or less (see Figure 3.6(A) and *Results and Discussion* (Section 3.4) – cavitation event history and survival probability curve). The cavitation events within glass voids and the subsequent emptying of liquid water were observed and recorded every 10 minute. We continued lowering the vapor pressure in step increments until all voids were cavitated and emptied.

3.3.3 Determination of probability of cavitation

Figure 3.1(B) shows a snapshot of the sample top view during the course of the experiment. As shown, different states of the void are easily identifiable in these images: filled voids are almost entirely dark, emptied voids show a bright ring around the perimeter of the etched circle, and voids undergoing emptying have meniscus of the vapor bubble evolving in the center of the void. The time evolution of the number of the voids at each state (filled/emptying/emptied) was calculated with standard image analysis procedure using ImageJ and MATLAB. This cavitation history was then synchronized with the corresponding temperature and pressure data (an example of the cavitation history is shown in Figure 3.6(A), see *Results and Discussion* – cavitation event history and survival probability curve). The synchronized data were used to produce the survival probability curve as a function of the water pressure (survival probability, $\Sigma = \text{number of filled voids}/\text{total number of voids}$), at each temperature.

3.4 Results and Discussion

3.4.1 Characterization of free-standing porous silicon membrane

The pore structure of the freestanding silicon membrane was observed with scanning electron microscopy (Figure 3.5). The top view of the nanoporous silicon shows the opening of pores at the surface (dark spots) with diameters ranging from 3–8 nm; this range of pore size was confirmed by nitrogen adsorption porosimetry (data not shown).

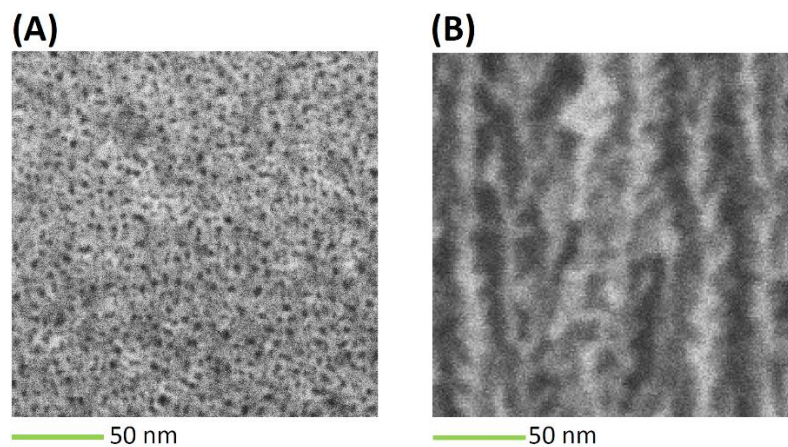


Figure 3.5: Top (A) and cross-sectional (B) views of the free-standing porous silicon membrane taken by scanning electron microscopy (SEM).

The pore size observed from the top view is at the 5 nm-diameter range; this side of the porous silicon membrane is bonded to the glass. From the cross-sectional view, the channels have variable pore diameters ranging from ~5–20 nm.

The cross-sectional view shows the typical pore structure obtained in highly-doped, <100> oriented substrate – independent vertical pores with side branching. Assuming Darcy flow through the porous silicon membrane during the emptying of the voids, we estimated the hydraulic permeability, κ [$\text{m}^2 (\text{Pa}\cdot\text{s})^{-1}$], of the membrane based on Darcy's law,

$$Q = \frac{\Delta P}{R_{liq}} = \frac{-\kappa A (P_{liq} - P_{vap})}{L} \quad (3.10)$$

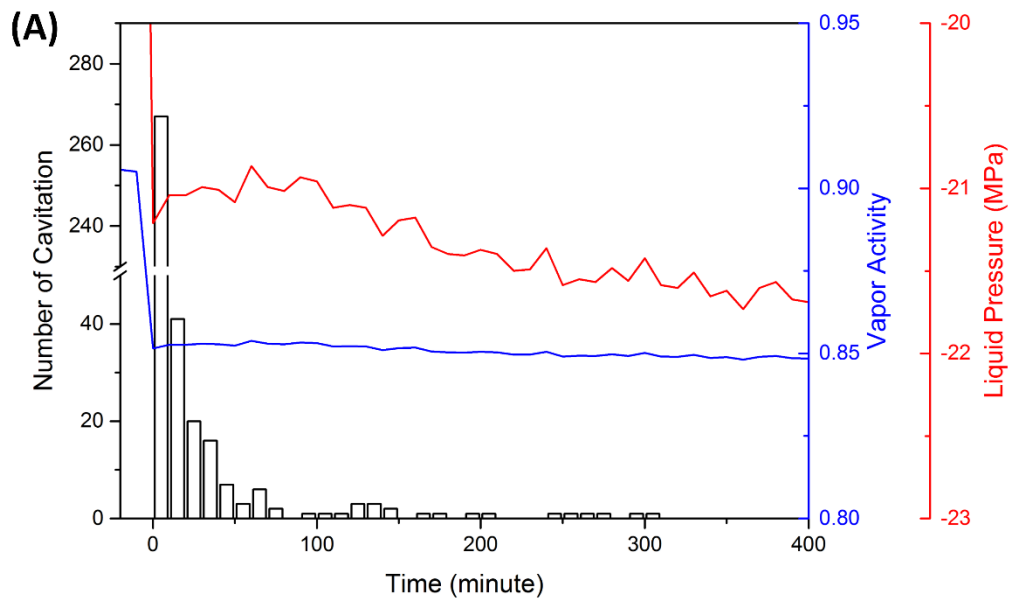
where Q [$\text{m}^3 \text{s}^{-1}$] is the volumetric flow rate, R_{liq} [Pa s m^{-3}] is the hydraulic resistance of the membrane saturated with liquid water, A [m^2] is the cross-sectional area to flow, and L [m] is the thickness of the porous membrane. The emptying time was not measured in detail in this work but has an upper bound of 10 minutes – the time frame between two consecutive images; once cavitated voids always emptied within one image frame. Due to this lack of temporal resolution, we can only estimate the hydraulic permeability of the membrane to be on the order of $10^{-18} \text{ m}^2 (\text{Pa}\cdot\text{s})^{-1}$. In our previous work³², the permeability for porous silicon was reported to be $1.44 \times 10^{-17} \text{ m}^2 (\text{Pa}\cdot\text{s})^{-1}$.

3.4.2 Cavitation event history and survival probability curve

After each step change in vapor pressure, new cavitation events started immediately and showed a decay in the number of events over time (Figure 3.6(A)). We extracted a characteristic time for this decay by fitting to an exponential:

$$N(t) = N_0 \cdot \exp(-t / \tau_c) \quad (3.11)$$

where N is the number of cavitation events happened over a certain time frame (10 minutes) at time t , N_0 is the total number of cavitation events within the entire duration



(B)

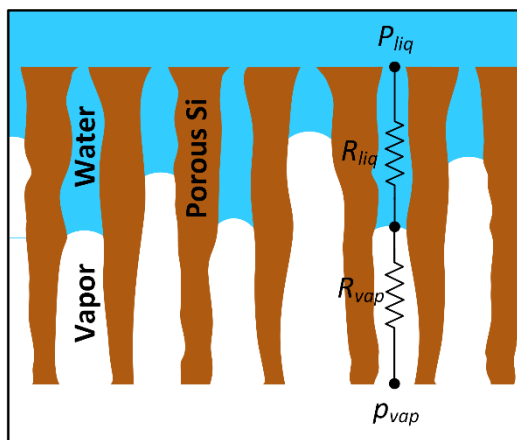


Figure 3.6: Temporal evolution of cavitation events.

(A) Part of the cavitation history at $T = 14.5^\circ\text{C}$ showing the evolution of cavitation events (counted every 10 minutes) after a step change in the vapor pressure from $a_{vap} = \sim 0.9$ to ~ 0.85 . The blue axis (right) is the vapor activity calculated from the vapor pressure data acquired in real time. The red axis (right) is the corresponding liquid pressure P_{liq} (Eq. (3.2)). (B) Schematic diagram illustrating menisci receding from the porous silicon membrane edge in a membrane with irregular shape pores. The liquid water and vapor phases within the pores contribute to the overall hydraulic resistance, R_{total} , with R_{liq} and R_{vap} , respectively. The aspect ratio of the pores is exaggerated in this diagram.

of one pressure step, and τ_c is characteristic time of decay. The average τ_c for all pressure steps was 92 minutes; therefore the time we allowed for equilibration in each pressure step (3 hours) was sufficient to ensure that the system was equilibrated and that the pressures within the voids were fully developed. This time scale of 92 minutes may be related to the pressure equilibration time, τ_{void} , of the bulk water in the voids to be in equilibrium with the external vapor,

$$\tau_{void} = R_{mem} \frac{V}{B} \quad (3.12)$$

where R_{mem} [Pa s m⁻³] is the hydraulic resistance of the membrane and B [Pa] is the bulk modulus of liquid water. If we assumed the membrane to be entirely filled with liquid during the experiment, then $R_{mem} = R_{liq}$ and we could estimate τ_{void} based on the hydraulic permeability (as in the previous section, Eq. (3.10)). However, such estimation gives an equilibration time, τ_{void} on the order of seconds, in contrast to the tens of minutes observed for τ_c in Figure 3.6(A). One hypothesis to explain this long equilibration time is that $R_{mem} = R_{liq} + R_{vap}$; while R_{liq} is the hydraulic resistance associated with the liquid water in pores, R_{vap} is the hydraulic resistance associated with the vapor in pores (see Figure 3.6(B)) and can be estimated from Knudsen diffusion. The pores can be partially filled with vapor during the experiments; e.g., for pores of conical shape with the end of larger openings in contact with the external vapor, the menisci would gradually retreat deeper into the membrane to reach equilibrium at a smaller pore diameter as a_{vap} goes down (see Figure 3.6(B)). This possibility is supported by the SEM images observing the top and cross sectional view of the membrane (Figure 3.5) – the membrane is asymmetrical: the pores are larger at the vapor side and are smallest at the top surface (bonded to the glass). Compare a single

pore filled entirely with liquid or vapor, the ratio of R_{vap} / R_{liq} is estimated to be on the order of 10^3 .³³ The time scale of τ_{void} considering the effect of vapor is on the order of tens of minutes, a value that is compatible with the scale of τ_c .

We note that a few cavitation events did continue to happen along the span of experiment. The small fluctuations in vapor activity (blue curve and the first vertical axis to the right) corresponds to non-negligible fluctuations in liquid pressure of ~ 1 MPa (red curve and the second vertical axis to the right) and may have provoked the continued cavitation at long times. Other cavitation mechanisms are also possible, and are discussed in the section – other mechanisms of cavitation.

At each temperature, we recorded the cavitation pressures of a total of 573 voids and plotted the survival probability, $\Sigma(P_{liq})$ – the probability that cavitation did not occur after the vapor activity was lowered to a given value. Figure 3.7 shows the survival probability as a function of liquid pressure (calculated with Eq. (3.2)) for four different temperatures. The 52 voids under bonding defects were excluded in the analysis (see Figure 3.8(A), these defect voids are marked with cavitation threshold $P_{liq} = 0$). We found that the lower the temperature, the higher the survival probability at a given P_{liq} . The lowest pressure in the liquid was observed at 0.3 °C and fell within the range of -25 to -30 MPa.

To analyze these survival curves further, we compared them to the predictions of CNT. According to CNT, the probability for survival (no cavitation), $\Sigma = \exp(-k_{cav} \cdot \tau)$ (Eq. (3.7)), during an observation time τ in a cavity of volume V at pressure P_{liq} , where k_{cav} [s^{-1}] is the rate of nucleation:

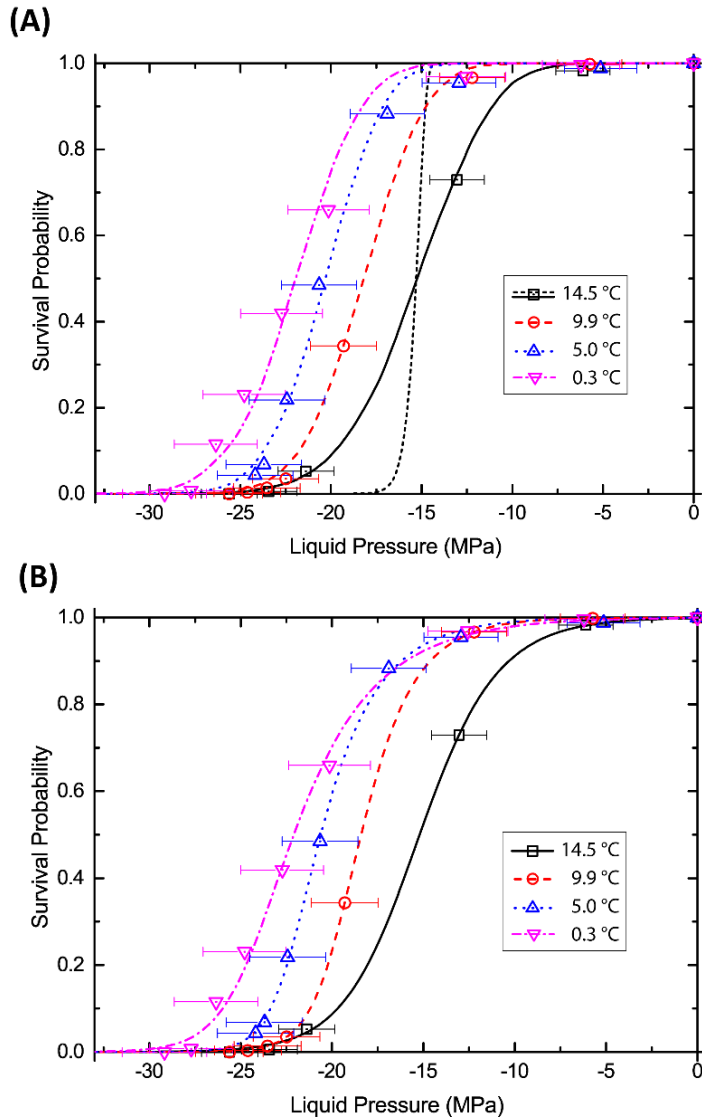


Figure 3.7: Survival probability (Σ) for water in porous silicon/glass sample as a function of the liquid pressure (P_{liq}).

The pressure was translated from vapor activity (a_{vap}) using IAPWS EoS (Eq. (3.2)).

(A) The dashed, black curve shows the prediction of CNT (Eq. (3.7)) with σ as the only adjustable parameter. The other trend lines for all four temperatures are fits with the modified CNT with adjusted σ and $\Delta\sigma$. (B) Survival probability with trend lines that are least-squares fits to the survival probability data at each temperatures using the standard logistic regression (Eq. (3.14)).

$$\begin{aligned}
k_{cav} &= \Gamma_0 V \exp\left(-\frac{E_b(P_{liq})}{k_B T}\right) \\
&= \Gamma_0 V \exp\left(-\frac{16\pi\sigma^3}{3(P_{liq} - p_{vap})^2 k_B T}\right)
\end{aligned}
\tag{3.13}$$

In Figure 3.7(A), the dashed, black curve shows this prediction with the surface tension, σ , adjusted to match approximately the P_{cav} at 14.5°C. Clearly, the dependence on pressure predicted by CNT is dramatically more abrupt than observed in our system. This incompatibility with CNT differs from what was reported by Wheeler and Stroock¹⁶ for analogous experiments in which a hydrogel served as the membrane: in those experiments, the shape of the transition was consistent with the prediction of the kinetic model of thermally activated nucleation. Such compatibility with CNT was also reported by for cavitation of liquid water with focused acoustic waves.²⁴ In work by our laboratory with a sample based on a porous silicon membrane with a distinct geometry from that used here, we did observe similarly broad transitions.³² The samples in that study were distinct from those used here in having much thicker (72 fold) membrane between the voids and the external vapor. In that work, we successfully accounted for the breadth of the transition with a modified CNT model in which we allowed the effective surface tension to vary from void to void to account for spatial heterogeneities³². We hypothesized that the effective surface tensions vary across the population of voids within a narrow Gaussian distribution of mean value σ [N m⁻¹] and standard deviation $\Delta\sigma$. With this hypothesis, we built a survival probability by convolving the prediction of CNT with this Gaussian distribution. The trend lines in Figure 3.7(A) show, for each temperature, fits with this modified CNT with adjusted σ and $\Delta\sigma$. The surface tension σ and the ratio ($\Delta\sigma / \sigma$) we obtained at 4 different temperatures are summarized in Table 3.1. These values of surface tension are of the

Table 3.1: Fitting parameters for survival probability curves at different temperatures

T [°C]	14.5	9.9	5.0	0.3
σ [N m ⁻¹]	0.0161	0.0178	0.0191	0.0200
$\Delta\sigma/\sigma$	15%	10%	9%	9%
σ/σ_{bulk}	0.217	0.240	0.255	0.264
P_{cav} [MPa]	-15.3	-18.5	-20.7	-22.1

same order of magnitude as those used to match the observed kinetics of cavitation of water by acoustic excitation: they found an average $(\sigma / \sigma_{bulk}) = 0.237$ for temperatures ranging from 0 to 190°C, whereas the average value we find is 0.244.²⁴ This value is also similar to that found by us previously for MVLE with porous silicon (0.256). The decrease of the distribution of surface tensions ($\Delta\sigma / \sigma$, Table 3.1) as temperature approaches zero is most likely due to the artifact that fewer data points were obtained during experiments at higher temperature.

We note, though, that the curves obtained with this model fail to capture the asymmetric shape of the data in our experiments – a smoother transition at lower tension and a steeper slope towards the more negative pressures. This observation suggests that the cavitation events in this work were not purely due to thermally activated nucleation, but rather to a mixture of the mechanisms. Hence, we choose to present in Figure 3.7(B) the fits of the data with the standard logistic regression, to better represent the experimental data and to estimate more accurately the P_{cav} (the liquid pressure at which the survival probability $\Sigma = 0.5$) at each temperature:

$$\Sigma = 1 - \frac{1}{\left[1 + \left(\frac{e^{P_{liq}}}{e^{P_{cav}}} \right)^b \right]^c} \quad (3.14)$$

where b is the slope factor and c is the asymmetric factor. P_{cav} , b , and c were adjusted for each temperatures to obtain the trend lines. The values of P_{cav} for 4 different temperatures are reported in Table 3.1.

3.4.3 Spatial heterogeneity

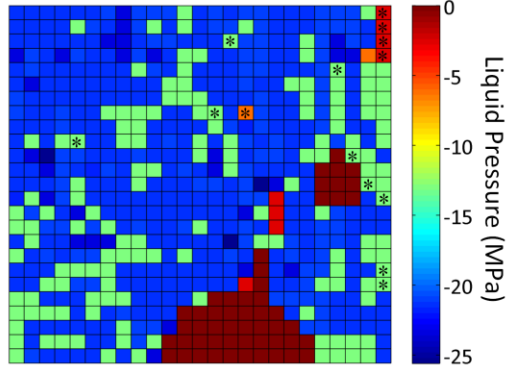
The survival probability curves across different temperatures show similar shape, however, the breadth of the transition and its asymmetric shape suggest distinct

mechanisms of cavitation may play a role in setting the observed threshold activity or liquid pressure for cavitation in different the voids across the sample. To explore this phenomenon, in Figure 3.8(A) we present color maps showing the distribution of cavitation thresholds across the sample for experiments at different temperatures. We see in the pattern of threshold values that some voids repeatedly cavitated in the same range of tension; examples of a few such voids are marked with asterisks (*) in each frame in Figure 3.8(A). The consistency in the threshold of these voids suggests that they contain persistent defects that render the cavitation deterministic. On the other hand the majority of the voids demonstrate apparently random changes in their thresholds from one run to another. To quantify this assessment, we analyze the correlation of cavitation thresholds for each voids between runs at different temperatures. The analysis consists in comparing the spatial maps of cavitation status for different runs at the same cavitated fraction, x (x = number of cavitated voids/total number of voids); the cavitation map records the status – either filled or cavitated (including emptying and emptied) – of each void at a given x . Two randomness indexes, α and β are used to compare the cavitation maps.

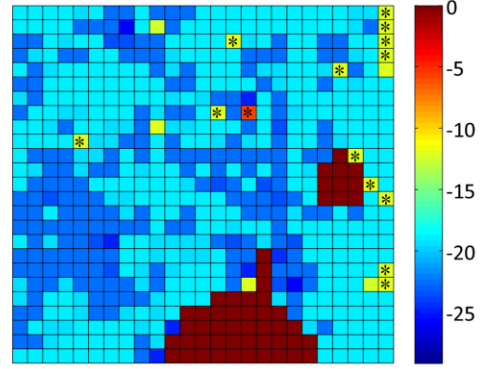
1) The α -index calculates the average correlation between two cavitation maps of the same cavitated fraction, x : if a void had the same status between two runs, it is assigned 1; if different, it is assigned 0. By averaging the assigned numbers over all voids we get the value of α (can be anywhere between 0 and 1), as a function of x . For comparison, the form of α -index for purely stochastic processes, $\alpha_{stoch} = x^2 + (1 - x)^2$; α_{stoch} is parabolic in x with a minimum of 0.5 at $x = 0.5$. Data points located above α_{stoch} indicate a positive correlation between the two cavitation matrixes; below α_{stoch} , anti-correlation. The further away a point is from the $\alpha_{stoch}(x)$ at a given x , the more deterministic the process is.

(A)

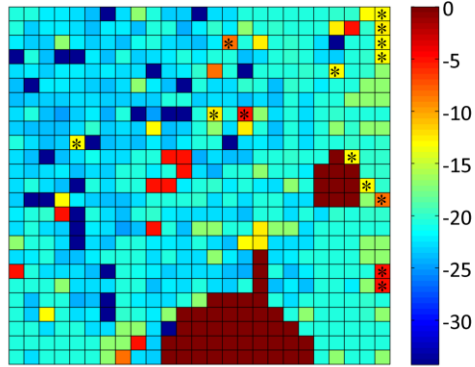
$T = 14.5^\circ\text{C}$



$T = 9.9^\circ\text{C}$



$T = 5.0^\circ\text{C}$



$T = 0.3^\circ\text{C}$

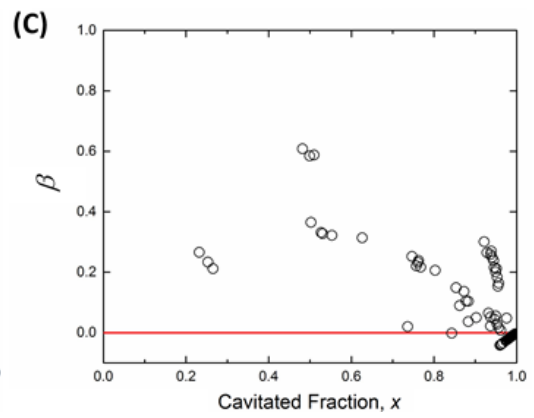
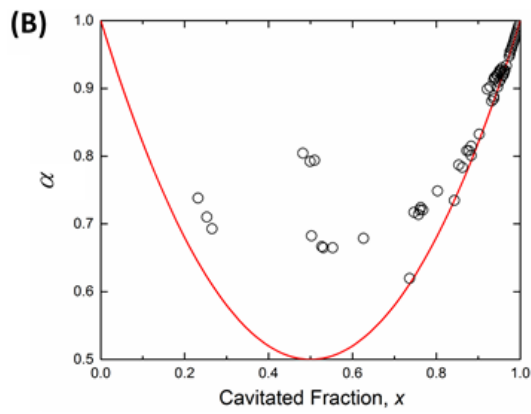
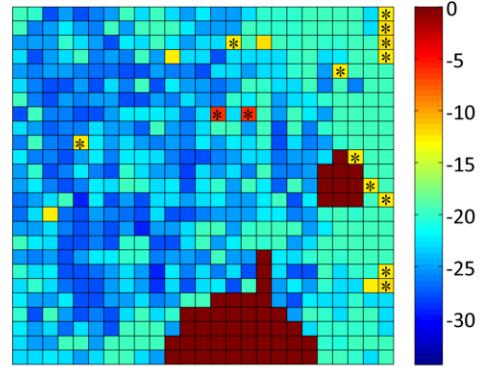


Figure 3.8: Variations in cavitation threshold.

(A) Spatial color maps showing cavitation threshold for each voids at $T = 14.5^\circ\text{C}$, 9.9°C , 5.0°C , and 0.3°C . Two areas of voids (near middle right and near bottom center) were defective due to bonding, and were excluded during data analysis. The color of each voids corresponds to the value of P_{liq} at which cavitation initiated. The color bars represent the liquid pressure, P_{liq} over the range from p_{sat} ($a_{vap} = 1$) to $2 \times P_{cav}$. The voids marked with asterisks (*) were voids that repeatedly cavitated at the same range of relatively low tensions in each run. (B-C) Correlation indices (α -index in (B) and β -index in (C) – see text) for thresholds across the four runs as a function of the cavitated fraction, x .

2) The β -index is proposed to remove the dependency of randomness index on x , as in α -index; it is calculated using the equation $\beta = (\alpha(x) - \alpha_{stoch}(x)) / (1 - \alpha_{stoch}(x))$. For a process with a given degree of correlation, β is a constant value not dependent on x . The value of β is 0 for purely stochastic process and 1 for purely deterministic process. $\beta > 0$ indicates a positive correlation; $\beta < 0$, anti-correlation.

The α -index and β -index calculated for this work are compared to that for a purely stochastic process (solid red curves), and shown in Figure 3.8(B) and (C); the data points shown summarize all comparisons between any two temperatures (a total of 6 pairs from 4 temperatures). As the cavitated fraction gets closer to 1, both the α and β indexes tend toward their values for a random process. This tendency is more apparent for β -index (Figure 3.8(C)) as it flattens the dependence of α -index to x . These observations confirm the assertions above that, far from the cavitation threshold (lower tensions), the cavitation process occurs in a more deterministic manner whereas, as the experiment approaches the cavitation limit, the cavitation events become more random. We interpret the less random process as occurring due to structural defects in certain voids such as large pores that allow cavitation to occur by invasion of the meniscus (Figure 3.2(B)-(a)). The more random behavior is compatible with a thermally-activated nucleation process. The shape of the survival probability curves also agrees with this interpretation: a steeper transition near the cavitation limit corresponds to thermally-activated process, and a less abrupt transition at lower tension correspond to cavitation induced by structural defects of varying concentrations or sizes.

3.4.4 Comparison of temperature-dependence of cavitation threshold across different methods

In Figure 3.9, we report the largest tension (the most negative liquid pressure) observed at each temperature in the experiments presented here along with the results

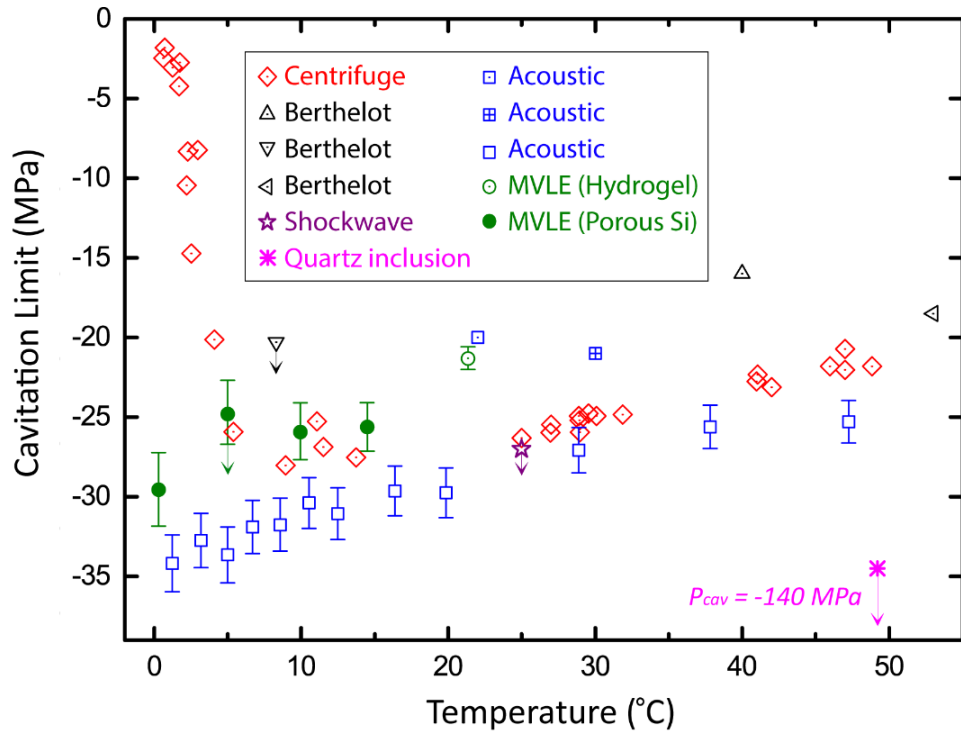


Figure 3.9: Comparison of the largest tension (the most negative pressure) of liquid water as a function of temperature obtained with different techniques

This figure is adapted from [Caupin *et al.*, 2012]²⁶, added data points from this work for comparison: z-tube centrifuge (red diamonds); Berthelot-Bourdon tubes (triangle up and triangle down); metal Berthelot tube with pressure transducer (triangle facing left); shock wave (purple star); acoustic (blue squares); and MVLE in synthetic trees (green circle) and in free-standing porous Si sample (green solid circles). A short arrow on data points means that the cavitation limit in that specific experiment was not yet reached. Result from one Quartz inclusion experiment (pink asterisk) is indicated on the graph with a long arrow pointing the observed cavitation limit of -140 MPa. On the data points for porous silicon (green solid circles), the uncertainty of temperature calibration were smaller than the symbol width; the vertical error bars represent the uncertainty based on the propagation of the standard deviation of both the temperature and the pressure calibration.

obtained with other techniques.²⁶ The stability limit we obtained falls in the same range with all other experiments (except the quartz inclusion experiments of -140 MPa) and it varies monotonically as temperature approaches zero. This trend suggests again that the rapid loss of stability for temperatures below 10°C observed by Briggs¹⁰ (red diamonds) was an artifact. The general trend of our work agrees with that of the work by Davitt *et al.*²⁴ (blue squares), with our thresholds occurring at ~3 MPa higher pressure (less negative) than found by the acoustic technique. This discrepancy is small compared to the discrepancy with respect to the quartz experiments, and may be due to the different physics of the methods and some inherent systematic errors associated with different techniques used to evaluate the liquid pressure.

The large discrepancy between the results from MVLE experiments and from quartz experiments may be due to a nearly ubiquitous cavitation mechanism(s) that imposes the highly reproducible values of stability limit between -20 to -30 MPa found with a variety of different techniques. Detailed discussions and analysis regarding the origin of this discrepancy can be found in several papers and reviews^{4,16,17,98}. In brief, among the few mechanisms described in Figure 3.2, mechanisms involving structural defects (e.g. hydrophobic patches – Figure 3.2-(b), or bubbles trapped in the walls – Figure 3.2-(d)) can be excluded, considering that 1) the absence of walls/boundaries in contact with the water sample in acoustic experiments, and 2) these mechanisms impose dependence of cavitation pressure on the distribution of defects and would result in a less abrupt transition in probability curve, in contradiction to the results obtained by Wheeler & Stroock¹⁶. Menisci invasion (Figure 3.2-(a)) is not applicable to acoustic and shockwave experiments. One possible mechanism left to explain the discrepancy is the presence of dissolved or dispersed impurities in bulk water (Figure 3.2-(c)). These floating impurities are unlikely to be dissolved gases, in that 1) carefully degassed ultrapure water samples were used in the acoustic experiments and in this work, and 2)

water samples saturated with various gases exhibit minor changes in the cavitation pressure.⁵ In this work, the vacuum environment in which the experiments were performed further minimized the presence of dissolved gases in the samples. Nevertheless, there may be other destabilizing impurities present in the water used in all experiments that are eliminated in quartz inclusions during sample fabrication, or that are absorbed onto the walls of quartz and are deactivated. Potential candidates for this ubiquitous impurity have been proposed (e.g., hydronium ions)^{4,9}; nevertheless, more experiments and simulations are required to further investigate this mechanism.

While some of the aforementioned mechanisms – Figure 3.2-(a), (b) and (d) – are unlikely to be the mechanism(s) governing the low stability limits found with different techniques, we note that we cannot exclude the possibility that these mechanisms play some role in our experiments and affect the shape of the stability probability curves; discussion regarding the roles of these mechanisms in this specific work can be found in the next section (other mechanisms of cavitation).

3.4.5 Other mechanisms of cavitation

In this section we consider the mechanisms that could possibly explain the low stability limit and the shape of the survival possibility curves (Figure 3.7) observed in this work, including menisci invasion (Figure 3.2-(a)), heterogeneous nucleation (Figure 3.2-(b) and (c)) and pre-nucleated bubbles (Figure 3.2-(d)).

As described in Theory – metastable vapor-liquid equilibrium (MVLE), the largest, continuously connected pore coupling a void to the outside vapor would determine the maximum tension sustainable in the liquid within the void. Once the water meniscus in the pore walls reaches its receding contact angle, the pore water begins to retract and eventually the void starts to dry out once the meniscus reaches the inner end of the pore. Although the pore size and the pore structure of nanoporous silicon membranes are

fairly uniform (as shown in the SEM images, Figure 3.5, and porosimetry results), a few larger pores may exist across the membrane surface and govern the stability limit of the voids coupled to them. For example, water within a pore with a smallest effective pore diameter $r_{pore} = 10$ nm would recede into the void at $P_{liq} \sim -13.3$ MPa for a receding contact angle, $\theta = 25^\circ$.³³ Structural defects inherent in the porous silicon membrane most likely contribute to the few voids that repeatedly cavitared at lower tensions, and hence resulted in the gentle decrease observed in survival probability curves at pressures far above (less negative) than the stability limit.

To consider the possibility that heterogeneous nucleation occurs on hydrophobic patches, it is essential to gain knowledge regarding the hydrophobicity of the materials used to fabricate the sample. Both the borosilicate glass and the porous silicon are considered to be hydrophilic; however, only the macroscopic contact angle of water on the bulk surface of these materials were reported to be from 0–40°.^{33,99,100} The contact angle of water at the pore walls within the porous silicon is difficult to characterize; while the wetting behavior of water and other liquids is consistent with the bulk contact angle, we cannot exclude the possibility that there exist highly hydrophobic patches on the membrane side walls – e.g., hydrogen bond terminated Si surface instead of oxide – that are small enough and at sufficiently low density to have had a weak impact on the macroscopic contact angle or wetting behavior. Heterogeneous nucleation can also occur on impurities floating in the bulk liquid; we cannot exclude the possibility that some impurities inevitably dissolved into the water and affect the shape of the stability curves.

The possibility of pre-nucleated vapor bubbles trapped in large crevices and affect the stability limit is unlikely. Our previous experiments suggested that the cavitation threshold would be equal or larger in magnitude than the pre-pressure; the pre-pressurization of samples in this work was done at 35 MPa. The magnitude of this pre-

pressure is larger than that of the cavitation threshold for the most stable void observed (~-30 MPa). Any bubbles trapped in large crevice within the samples should either be completely dissolved into the water or reside in the crevices and would not attain the critical size to cause cavitation at the tensions observed. However, as discussed in the Theory section, there may be “calibrated” crevices of arbitrarily small sizes that could lead to a threshold pressure only depending on the geometry of the crevices and the wetting properties, and be independent of the pre-pressure.¹⁶

All the aforementioned defects or impurities may have a non-uniform size or concentration distribution across the voids and may enter the voids in a random manner during each refilling, and hence result in a relatively broad probability curve. To confirm or exclude any of these mechanisms, further experiments are needed. We note however that the cavitation pressures observed on most stable voids at different temperatures are most likely due to the dominate mechanism that is the same in various experiments, and the general trend of the stability limit as a function of temperature presented in this work is probably not affected by these other mechanisms for nucleation.

3.5 Conclusions

We used the metastable vapor-liquid equilibrium method with a nanoporous silicon membrane to investigate the stability limit of liquid water as a function of temperature from 15°C to 0°C. We found the stability limit to be monotonically increasing (more negative) as temperature approached 0°C; this trend contradicts the famous results of Briggs but agrees with the experiments by acoustic cavitation. Nonetheless, our results lie within the range of -20 MPa to -30 MPa; this limit is far less negative than the limit predicted for homogeneous nucleation.

The vapor control system introduced in this work opens up the possibility of studying stability limit of water at temperatures further down below zero, into the doubly metastable region on water's phase diagram (supercooled and negative pressure). Experiments investigating water properties in this region can potentially shed light on water's anomalies.³ Also, the porous silicon membrane provides a practical platform to reliably place a static, bulk volume of liquid into metastable region that can be studied, manipulated and coupled to existing technologies – e.g., MEMS-based loop heat pipes³⁹ for the transfer of heat with liquids at negative pressures, and tensiometers⁸² for measuring water potentials in plants and soils.

CHAPTER 4

SUPERHEATED LOOP HEAT PIPE PROTOTYPE – DESIGN OF POROUS SILICON WICK STRUCTURE AND EXPERIMENTAL SYSTEM

4.1 Introduction

Superheated loop heat pipes (SHLHPs), as presented in Chapter 2, are promising heat transfer devices in particular for applications regarding heat transfer over long distance or with liquid motion against gravity or acceleration field. The operating principles of SHLHPs differ from conventional designs in 1) the un-coupling of the working fluid from its saturation curve to eliminate limitations associated with temperature head and sub-cooling conditions and 2) the possibility of maintaining sub-saturation throughout the device to eliminate film condensation and improve the condenser thermal conductivity. This chapter presents the design and analysis of a prototype SHLHP.

The experimental realization of SHLHPs presents outstanding challenges. One of the major challenges is associated with the reduced wick membrane pore size to transport liquid under tension and hence the potential for increased hydraulic resistance relative to conventional wicks. Therefore, the fabrication of appropriate membrane with desired functionalities is essential. A desired membrane should meet the following criteria: 1) uniform pores with sub-micrometer diameters; the failure of one single large pore will cause dry-out in all hydraulically connected paths, 2) optimal pore size which provides a sufficient capillarity stress and sufficient permeability to avoid generating excessive tension in the liquid, and 3) ability to sustain high pressure difference without fracture or collapse of the conduits. Such membrane structures should couple a thin and

uniformly nanoporous layer for large capillary stress to hierarchical macroporous supporting layers with increasing diameters for low hydraulic resistance. Another major challenge to realize a SHLHP is the increased proneness to dry-out due to boiling of the superheated liquid. The robustness of a SHLHP depends on the suppression of cavitation in the superheated liquid and the design to ensure the continuing operation of a SHLHP after dry-out or boiling events. For the former, liquid path wall and wick membrane materials that are hydrophilic and defect free are basic requirements; hydraulically independent, redundant liquid paths, as is found in the compartmented xylem conduits of plants, could help to control the spread of cavitation. For the later, cavitation sensing and refilling techniques must be developed and to be integrated with SHLHPs.

As a proof-of-principle demonstration, I proposed MEMS-based, microscale SHLHP designs, fabricated completely on silicon and glass wafers. The opportunities with the MEMS-based (silicon-based) design include: 1) well-defined patterning techniques for flexible structure design, 2) tunable porosity and pore structure of porous silicon and its preferred hydrophilic surface, and 3) possibilities of integration with other materials and standard microfabrication packaging techniques. Porous silicon has proven useful as a nanoporous material in many projects in our lab: study of stability limit of water (as presented in Chapter 3), microtensiometer⁸², cavitation-coupled drying³², and nano-confined flows³³. Here, to successfully exploit porous silicon to achieve the desire SHLHP membrane functionality, a thorough understanding of the fabrication parameters and the subsequent microstructure of porous silicon is required. In the next section (4.2), I briefly review the effects of substrate properties and anodization conditions on the formation and the structure of both nanoporous and macroporous silicon; this review lays the foundation of the three different designs of SHLHP prototype structures, which are discussed in Section 4.3 and Section 4.4; the

three designs are: 1) the potassium hydroxide (KOH)-etched cavities coupled with nanoporous silicon membrane, 2) the multilayer porous silicon membrane and 3) the two-layer porous silicon membrane.

Preliminary characterizations of the KOH cavities and the multilayer designs revealed foreseeable challenges and complexities associated with realizing a SHLHP prototype of these two designs, therefore I chose to proceed with the two-layer design and fabricated the first SHLHP prototype. Characterizations and modeling results of this SHLHP prototype are presented in Section 4.4. In Section 4.5, I introduce the experimental system designed to study the performance of a SHLHP. To further improve the performance of the SHLHP membranes and to extend its functionalities to a broader range of applications, a few nanoporous materials are proposed to be incorporated with SHLHPs; discussions and preliminary experimental results are presented in Section 4.6.

4.2 A Review – Formation and Structural Properties of Porous Silicon

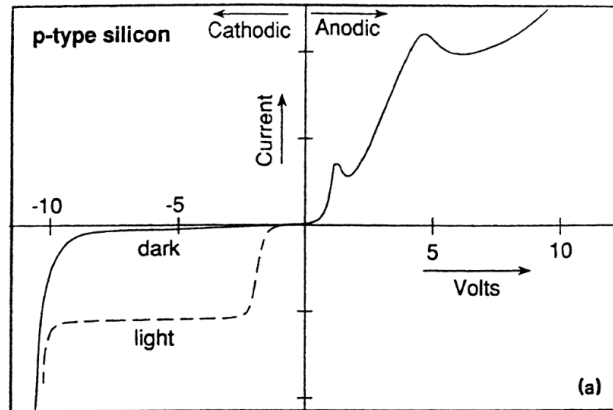
Porous silicon has been investigated since it was first reported half a century ago.⁹¹ Since the discovery of its photoluminescence properties in 1990, porous silicon has attracted considerable research interest world-wide and a large number of studies have been directed towards the understanding of the structural, optical and electronic characteristics of porous silicon.^{61,62} The better understanding of various kinds of porous silicon structures and properties inspired the use of this porous material in an array of technological applications⁶², such as optoelectronics¹⁰¹ (e.g., light-emitting diodes (LEDs)¹⁰² and waveguides¹⁰³), solar cells¹⁰⁴, wafer technologies (e.g. silicon on insulator (SOI) structures¹⁰⁵), microelectronics¹⁰⁶, biosensors^{107,108}, etc. For comprehensive reviews on the fabrication, properties, characterizations and applications of porous silicon, one can refer to the work by Canham *et al.*⁶⁰, Cullis *et al.*⁶¹ and Bisi

*et al.*⁶² Here I focus on the formation and the effects of substrate properties and anodization conditions on the structure of both nanoporous and macroporous silicon, which are relevant to the development of a SHLHP prototype.

The generally preferred approach to form porous silicon is by the anodic conversion of crystalline silicon in hydrofluoric acid (HF) solutions under galvanostatic conditions; this approach reproducibly gives wide ranges of pore structure and thickness. Figure 4.1(A) shows the typical *I-V* curve of p-type silicon. Under anodic polarizations, silicon dissolution occurs. Depending upon the magnitude of the anodic potential, different surface morphologies result – at high anodic overpotentials, the silicon surface undergoes electropolishing; at low anodic overpotentials, partial dissolution of silicon occurs at the surface and forms porous structure that can penetrate deep into the bulk of the silicon substrate. The anodic current-potential characteristics of four types of silicon substrate (p, p⁺, n, and n⁺) with different HF concentrations were reported by Zhang *et al.*¹⁰⁹

The formation mechanisms of porous silicon are still in dispute. Various models have been proposed to try and explain the dissolution chemistries, pore initiation and pore propagation mechanisms. It is generally accepted that holes are prerequisite for both electropolishing and pores formation. Figure 4.1(B) presents a silicon dissolution scheme proposed by Lehmann and Gösele¹¹⁰ – holes are supplied to the surface of silicon, fluoride ions attack, electrons inject into the substrate, HF then attacks Si-Si bond which leads to the divalent Si oxidization state. Pore initiation/nucleation is controlled by the supply of holes and has been described by different models, such as the morphological instability of the silicon-electrolyte interface to linear perturbations¹¹¹, the evolution of point defects in the near-surface region of semiconductors¹¹², and hydrogen-induced microdefects in the near-surface region being selectively etched¹¹³. After the initiation, pores grow directionally and dissolution

(A)



(B)

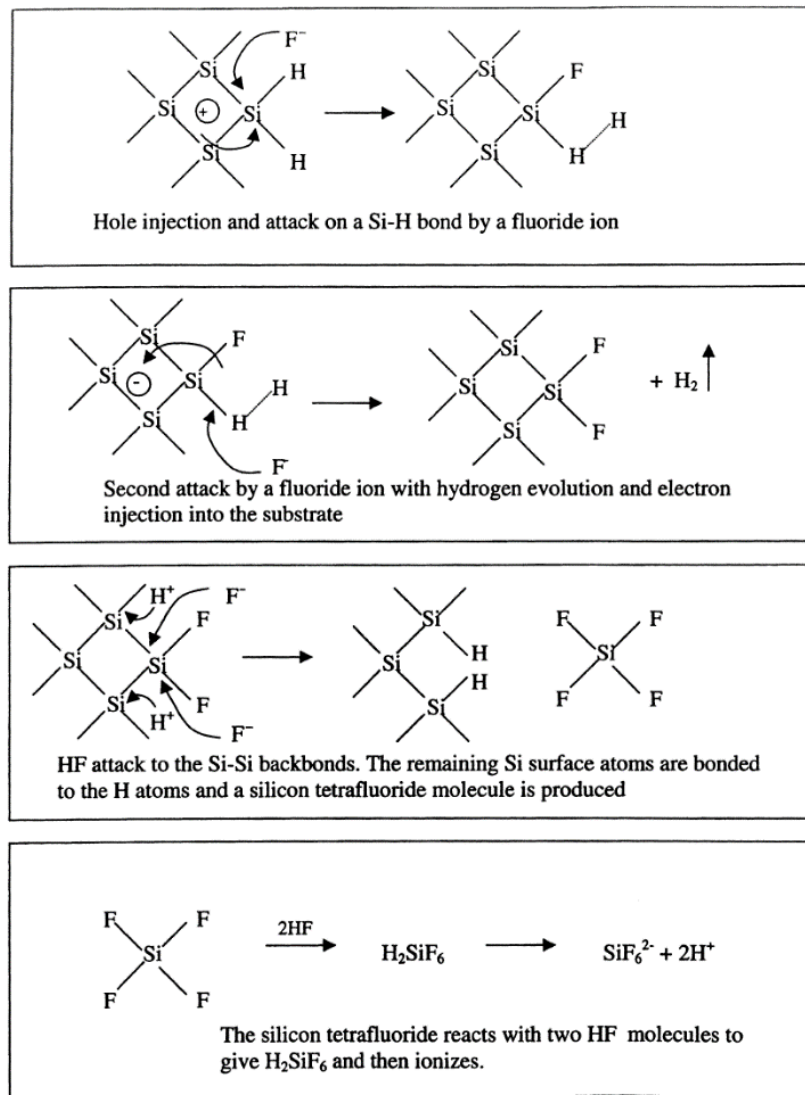


Figure 4.1: (A) Typical I - V curve for p-type silicon. (B) Silicon dissolution scheme propose by Lehmann and Gösele¹¹⁰.

(A) The first (small, sharp) peak on the anodic side of the curve is the electropolishing peak. Pore formation occurs only in the initial rising part of the curve, where the potential is below the potential of the electropolishing peak. The quantitative values of the I - V curves, as well as the values corresponding to the electropolishing peak, depend on etching parameters and wafer doping. The I - V curve for n-type silicon is not shown; it is basically symmetric to the one for p-type and anodization is carried under back illumination. Due to this added complexity of illumination with n-type substrate, I used only p-type silicon in all the works presented in this dissertation.

(A) adapted from: Smith, R. L.; Collins, S. D. Porous Silicon Formation Mechanisms. *J. Appl. Phys.* **1992**, *71* (8), R1–R22.

(B) adapted from: Lehmann, V.; Gösele, U. Porous Silicon Formation: A Quantum Wire Effect. *Appl. Phys. Lett.* **1991**, *58* (8), 856–858.

advances only at the pore tips. Proposed pore propagation and side wall passivation mechanisms include the increased band gap forming depletion layers¹¹⁴, holes diffusion-limited growth rate at the pore tips^{115,116}, charge transfer dominated by tunneling of the carriers¹¹⁷, hindrance layers on the wall composed of the silicic acid¹¹⁸ or silicon fluoride and silicon oxide¹¹⁹. In each of these mechanisms, the pore diameter and density emerge as length scales that are specific to the silicon-electrolyte system employed.¹²⁰

The porosity, geometries (pore size, inter-pore distance, and layer thickness) and morphologies (pore direction, shape, topological distribution, etc.) of the porous silicon depend on the substrate properties (type of dopant, doping level, surface roughness, etc.) and etching parameters (electrolyte composition, HF concentration, anodization duration, current density, etc.) For the porosity of p-type silicon substrate, observed trends are:^{60,62,121,122} 1) at a given HF concentration the larger the current density the larger the porosity, 2) at a fixed current density, the lower the HF concentration the larger the porosity, and 3) with fixed HF concentration and current density, the porosity increases with layer thickness.

Porous silicon pore diameter can range from a few or tens of nanometers to the classical macroporous range of a few to tens of micrometer (according to the IUPAC standard, pores with geometries < 2 nm are micropores; 2–50 nm, mesopores; > 50 nm, macropores.¹²³ In this study, nanoporous refers to pore geometries < 50 nm; macroporous, pore geometries on the order of 1 μm). When designing SHLHP prototype, the nanoporous silicon layer is essential to provide the Laplace pressure required to sustain liquid under tension. The pore size of nanoporous silicon shows general trends the same as of the porosity – increasing with increasing current density and decreasing HF concentration. Further, with a p-type substrate, the pore size tends to increase with increasing doping density.¹²⁴ In the KOH and the multilayer design, silicon substrates with doping level of p (1–10 $\Omega\text{-cm}$) and p⁻ (> 30 $\Omega\text{-cm}$), respectively,

were used to provide the highest maximum Laplace pressure; in the two-layer design, p^+ silicon wafers were used to provide optimal hydraulic resistance (see Section 4.3.4). The pore network in low or moderately doped substrate (p^- and p) looks homogeneous and interconnected; as the dopant concentration increases (p^+), the structure becomes more anisotropic, with long pores running perpendicular to the surface.⁶²

Macroporous silicon, with pore geometries 3 orders of magnitude larger than those of the nanoporous silicon, can be made via electrochemical etch with HF solutions. Formation of macropores in p-type silicon substrates was first reported in 1994,¹²⁵ with moderately doped substrate and organic electrolyte. Later researchers found that macropores can be formed in various levels of boron doping,^{126–128} and both organic and aqueous electrolytes are suitable.¹²⁹ In macroporous silicon, two types of pores often coexist: nanoporous nucleation layer on top of the macropores filled with nanoporous structure; during the anodization the nanoporous parts may be dissolved, leaving filled macropores without nucleation top layer, or further, hollow macropores cleared of fillings. To explain the onset of macropores after the initial nucleation of nanopores, researchers extended the models proposed for nanoporous silicon formation and proposed more complete models of the electrochemistry of silicon^{129–131} (e.g., the current burst model). For details on the formation of macroporous silicon, one can refer to the review by Föll *et al.*¹²⁰

The major parameter to achieve desired pore structure is the proper choice of electrolyte. A few general guidelines for the design of macropore etching conditions include:¹²⁷ 1) optimized hydrogen termination defines the anisotropy of the pore growth, 2) presence of oxygen clears the filling in macropores, and 3) highly doped substrates produce sub-micrometer pores. In the multilayer design for SHLHP prototype, a layer of nanoporous silicon is required to serve as the active layer while macropores underneath serve as the structural support and mediate the hydraulic resistance across

the membrane. Therefore a low-resistivity substrate with oxygen free organic electrolyte is preferred to keep the nanoporous structure while forming the macropores of a few μm in diameter. A subsequent step is required to clear the pore filling while leaving the nucleation layer or a thin layer of nanoporous fillings as the active nanoporous membrane (see Section 4.3.3).

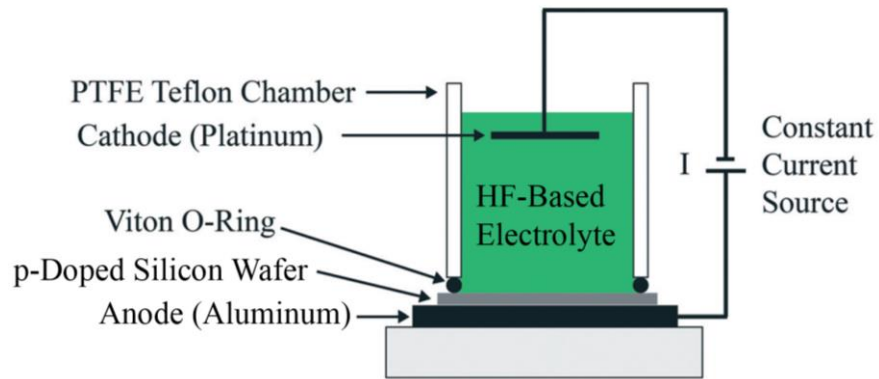
4.3 Porous Silicon Wick Design and Fabrication

4.3.1 Materials and methods

Substrates. Silicon wafers used in all three designs were 4-inch diameter, <100> orientation, p-type doping wafers. Wafers of different resistivity were used for different designs to achieve the desired pore size and morphology. KOH-etched cavities coupled with porous silicon: $1\text{--}10\ \Omega\text{-cm}$, 300 ± 25 thickness, double-side polished (DSP) (University Wafer, <http://www.universitywafer.com>). Multilayer silicon membrane: $30\text{--}45\ \Omega\text{-cm}$, $525 \pm 25\ \mu\text{m}$ thickness, DSP (WRS Materials, www.wrsmaterials.com). Two-layer silicon membrane: $6 \times 10^{-4}\text{--}5 \times 10^{-3}\ \Omega\text{-cm}$, $300 \pm 25\ \mu\text{m}$ thickness, DSP (WRS Materials); some wafers were bought as single-side polished or with larger thickness and then were ground and thinned to $300\ \mu\text{m}$ (GDSI, <http://www.wafergrind.com>). Glass pieces for stability tests or liquid paths were BOROFLOAT[®] 33 (4-inch diameter, $500\ \mu\text{m}$ thickness, DSP, prime grade) float borosilicate glass wafers (University Wafer).

Anodization. Figure 4.2 illustrates the setup for the electrochemical porosification of silicon. Both nanoporous and macroporous silicon was formed by anodization of silicon substrate in an HF-based electrolyte; the electrolyte was contained in a custom-built electrochemical etch cell made of polytetrafluoroethylene (PTFE or Teflon). Silicon wafers were mounted, one at a time, between the etch cell and an aluminum bottom electrode with one side of the silicon wafer in contact with the electrolyte in the etch cell, as shown in Figure 4.2(A). For wafers with resistivity $> 10^{-1}\ \Omega\text{-cm}$, an

(A)



(B)

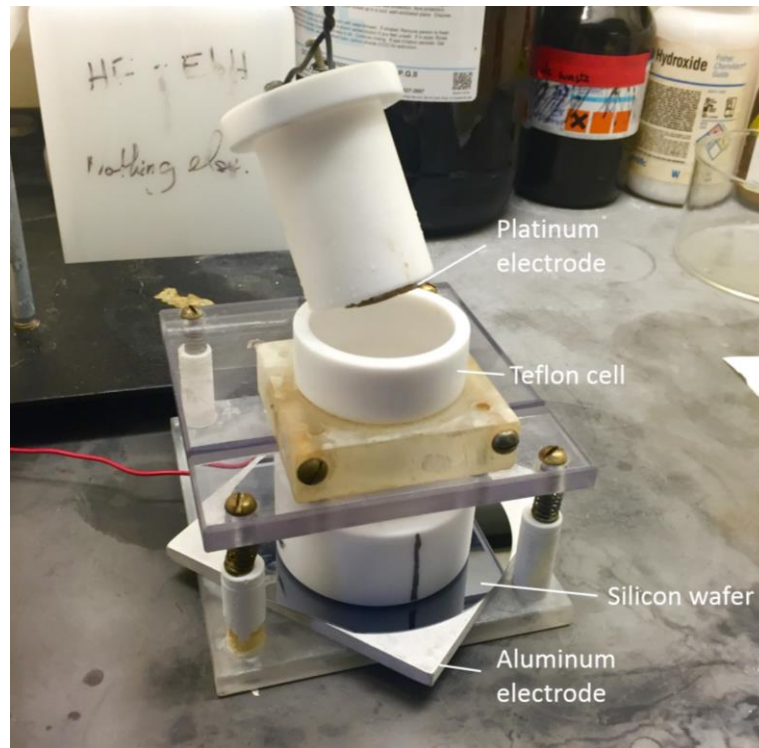


Figure 4.2: (A) Schematic diagram showing the cross-sectional view of the electrochemical etch cell. (B) Picture of the actual setup.

(A) adapted from: Pagay, V.; Santiago, M.; Sessoms, D. A.; Huber, E. J.; Vincent, O.; Pharkya, A.; Corso, T. N.; Lakso, A. N.; Stroock, A. D. A Microtensiometer Capable of Measuring Water Potentials below -10 MPa. *Lab Chip* **2014**, *14* (15), 2806–2817.

aluminum layer of ~ 200 nm was deposited (SC4500 evaporator) on the backside to serve as the electrical contact to the aluminum electrode. The Al film was annealed with forming gas (N₂/H₂) at 400°C for 30 minutes (metal anneal furnace C1) to achieve Ohmic contact between the film and the silicon wafer.

The choices of HF-based electrolytes and etching conditions were catered to the different designs. KOH-etched cavities coupled with porous silicon: 70:30 (v/v) solution of 48% HF and 95% ethanol, constant current density of 4 mA/cm². Multilayer silicon membrane: 70:30 (v/v) solution of 48% HF and 98% acetic acid (AA), constant current density of 10 mA/cm² for the nanoporous layer; 2:88:10 (v/v/v) or 4:86:10 (v/v/v) solution of 48% HF, acetonitrile and 98% AA, constant current density of 6 mA/cm² for the macroporous layer. Two-layer silicon membrane: 60:40 (v/v) solution of 48% HF and 98% ethanol, constant current density of 15 mA/cm² for wafers with resistivity $< 2 \times 10^{-3}$ Ω-cm; 40:60 (v/v) solution of 48% HF and 98% ethanol, constant current density of 30 mA/cm² for wafers with resistivity $> 2 \times 10^{-3}$ Ω-cm.

4.3.2 KOH-etched cavities coupled with porous silicon membrane

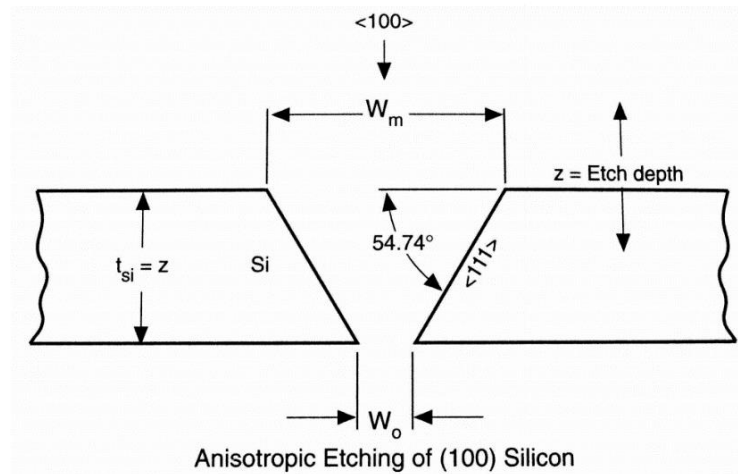
The general form of a MEMS-based SHLHP prototype is similar to a micro-columnated loop heat pipe,¹³² consisting of stack of wafers bonded together to define different components in the loop – the evaporator, the liquid paths and the condenser. On a single silicon wafer piece both the evaporator and condenser wick membranes are etched vertically through the wafer, independent of each other; this membrane layer is bonded to the liquid path layer made of a glass substrate etched with liquid paths running laterally to connect the evaporator membrane and the condenser membrane. The other side of the membrane layer is in contact with the structure defining the vapor side evaporator cavity and is connect to the vapor path. The essential part of designing a

SHLHP is to fabricate the vias through the silicon substrate that couple the nanoporous silicon to the liquid paths in the glass.

Figure 4.3 presents the first design I proposed to connect the nanoporous silicon membrane to the back side of the wafer; this design utilized the anisotropic wet etch of silicon in KOH solutions. Heated KOH-water system is commonly used for preferential etching of silicon along crystal planes. KOH etch on <100> oriented silicon wafer produces uniform and bright side wall and bottom surfaces with a side wall angle of 54.74°, as illustrated in Figure 4.3(A). Figure 4.3(B) shows the process flow for fabricating KOH-etched cavities coupled with porous silicon membranes. The process consists of 1) KOH etch of the backside pit, 2) front side porosification of silicon membrane, 3) opening the bottom of the pits to complete the continuous membrane flow path, and 4) anodic bonding with glass to form a stability test device or a prototype SHLHP.

Silicon wafers were MOS cleaned and then deposited with thin-film masking layers: ~ 200 nm of thermal silicon dioxide (oxide furnace B2) followed by ~ 100 nm of silicon nitride (PECVD nitride furnace B4). The oxide film served as a dielectric layer in the anodization step and the nitride film served as a hard mask for the KOH wet etch. The nitride and oxide layer on the backside were then patterned with standard photolithographic techniques to open up the KOH pits – solvent clean wafers on spinner with acetone and isopropyl alcohol (IPA), spin primer P20 at 3000 RPM for 30 s, spin S1827 photoresist at 3000 RPM for 30 s, soft bake at 115°C on contact hotplate for 150 s, expose the photoresist with EV620 (soft contact, 9 s @ 12 mW/cm²) or other contact aligners, and develop in Hamatech-Steag Wafer Processors (program 2, 726MIF 120s DP). Nitride and Oxide layers were opened with dry etch (Oxford 81/82) and then the photoresist layer was stripped. KOH etch of the cavities was done in 33% aqueous KOH, 75°C, and constant stirring; the etch rate: ~ 60 µm/hr. After KOH etch, remaining

(A)



(B)

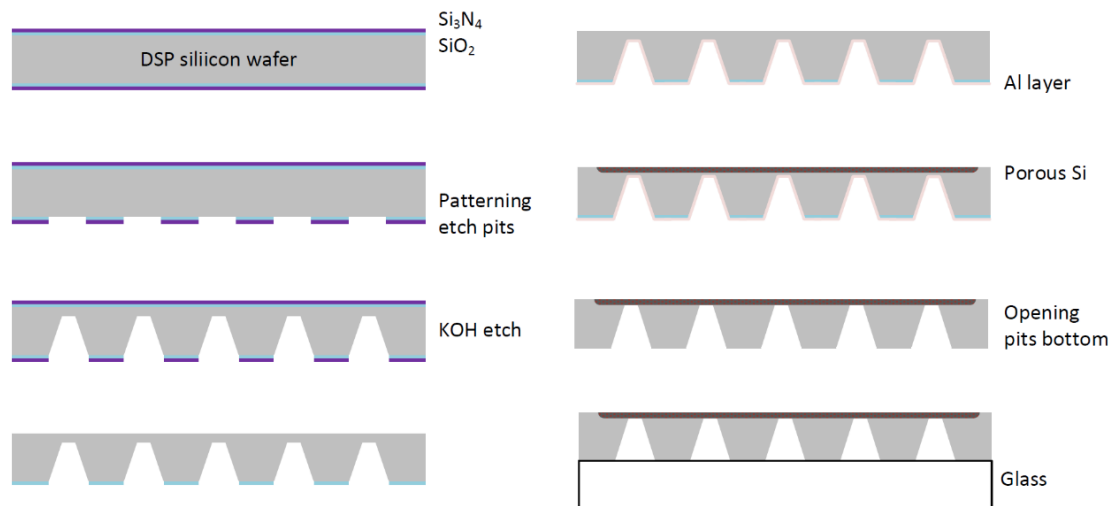


Figure 4.3: (A) Relation of KOH-etched cavity opening width with mask opening width. (B) Process flow for the KOH-etched cavities coupled with porous Si membrane.

W_m : the mask opening. W_o : the width of the rectangular or square cavity on bottom plane.

(A) adapted from: Madou, M. J. Fundamentals of Microfabrication: The Science of Miniaturization; CRC Press, 2002.

thin films on the front side and the nitride on the back side were stripped with dry etch. An aluminum layer of $\sim 200 \mu\text{m}$ was then deposited (SC4500 evaporator) on the backside to serve as the electrical contact for the electrochemical porosification. Silicon substrate was anodized from the front side to a depth that $\sim 5 \mu\text{m}$ of silicon was left between the porous silicon and the bottom of KOH pits. The membrane taken out of the electrochemical cell was immersed in isopropanol for 5 minutes and then pentane for 5 minutes to reduce the stress during membrane drying. Aluminum contact layer was stripped with Piranha solution (sulfuric acid : hydrogen peroxide $\sim 50:1$, 50°C). The bottom of the KOH cavities was opened with dry etch (Oxford 82, SF_6/O_2 silicon etch) and the remaining oxide was stripped. Finally the anodic bonding of silicon and glass substrates was done at -1200 V and 400°C until current falls to 5% of max value (Suss SB8e Substrate Bonder).

4.3.3 Multilayer porous silicon membrane

Figure 4.4 presents the design I proposed to replace the KOH pits and to improve the membrane permeability. This design consisted in a hierarchical multilayer of silicon structures with different pore sizes all etched in one silicon wafer – nanoporous silicon membrane on top of hollow silicon macropores connected to the back-etched DRIE (deep reactive ion etching) channels. The average pore sizes in each layers are $\sim 5 \text{ nm}$, $\sim 2 \mu\text{m}$ and $\sim 50 \mu\text{m}$, respectively. DRIE is a standard microfabrication technique to build high-aspect-ratio micromachines with dry-etching. High etch rate DRIE features the Bosch process of alternating repeatedly between different modes: 1) a standard, nearly isotropic plasma etch, 2) the deposition of a chemically inert passivation layer over the entire surface, and 3) a directional etch attack the passivation layer at the bottom of the trench but not along the side walls; these three steps are repeated many times to result high aspect ratio vertical channels deep into the silicon substrate.

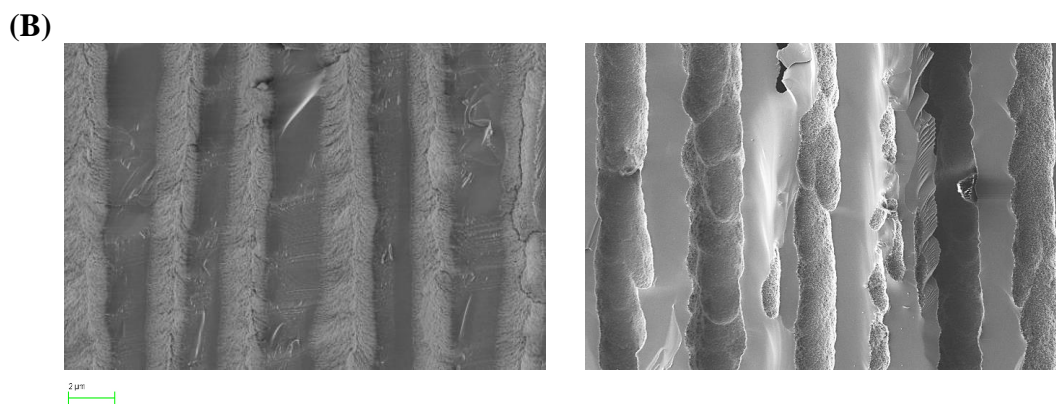
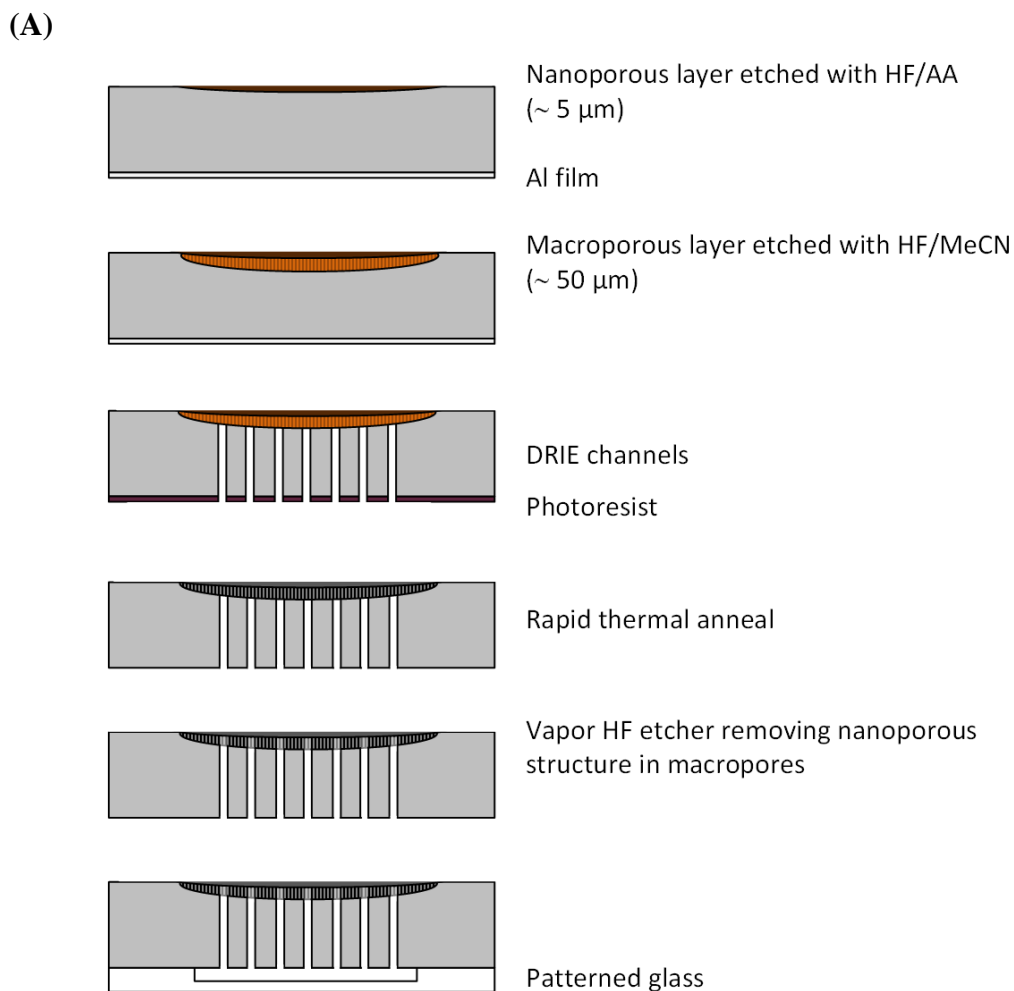


Figure 4.4: (A) Process flow for the multilayer porous silicon membrane. (B) Macropores filled with nanoporous structure (left) or hollow (right).

The magnification of the two images in (B) was the same. The scale bar: 2 μm .

Figure 4.4(A) shows the process flow for the multilayer porous silicon membrane. In the KOH cavities design, considering that the wet etch step (KOH etch) would attack porous silicon, the anodization was done after the KOH pits were etched. On the other hand, DRIE is a dry etch process which will not affect the features on the opposite side of the wafer, such that the anodization step can be done first to achieve as uniform as possible porous silicon membranes. The process consists of 1) front side porosification of nanoporous/macroporous silicon membrane, 2) fabrication of back side DRIE channels, 3) removal of nanoporous fillings in macropores (see Figure 4.4(B)) while leaving a thin nanoporous layer intact, and 4) anodic bonding with glass to form a stability test device or a prototype SHLHP.

Silicon wafers were MOS cleaned and then anodized at the front side to form a thin layer ($\sim 5 \mu\text{m}$) of nanoporous silicon membrane which serves as the active porous layer to provide capillarity. The electrolyte in the Teflon etch cell was then changed to anodize the macroporous silicon layer of $\sim 100 \mu\text{m}$. The membrane taken out of the electrochemical cell was immersed in isopropanol for 5 minutes and then pentane for 5 minutes to reduce the stress during membrane drying. The backside of the wafer was patterned with standard photolithographic techniques to define DRIE channel openings – solvent clean wafers on spinner with acetone, prime wafers with YES Vapor Prime Oven, spin SPR220.7 photoresist at 1000 RPM for 60 s, soft bake ramping from 95°C to 115°C (10 minutes) and then ramp down to 95°C (10 minutes) on proximity hotplate, expose the photoresist with Suss MA6 or other contact aligners (soft contact, 5 cycles with $9 \text{ s @ } 10 \text{ mW/cm}^2$ each cycle and 10 s wait time in between cycles), leave wafers to rehydrate in yellow light zone for at least 3 hours. Developing the photoresist was done by pipetting 726 MIF on top of the pattern for 10 minutes; doing development by hand was to avoid developer attacking porous silicon. The photoresist-patterned wafers were descummed (Branson Asher) and etched with DRIE tool (Unaxis UN770) until

channels reaches the bottom of the porous silicon membrane. DRIE etch rate varies from run to run, and a characterization run is recommended on dummy wafers right before etching on devices. After DRIE, the remaining photoresist was stripped. The wafers were annealed (RTA AG610) to fully oxidize the nanoporous silicon so that it can be dry-etched in the following step. Vapor HF etcher (Primaxx) was used to clear the nanoporous filling in the macropore from the DRIE side; the etch rate was controlled to leave the nanoporous top layer intact. Finally the anodic bonding of multilayer silicon membrane and glass substrates was done at -800 V and 400°C until current falls to 5% of max value (home-made bonder in Olin 212).

4.3.4 Two-layer porous silicon membrane

The two-layer porous silicon membrane design features two modifications of the multilayer design to achieve the desired SHLHP functionality: 1) fabricating a single nanoporous layer instead of two porous silicon layers (nanoporous active layer and macroporous supporting layer) to avoid the complexities associated with the process to etch away the porous filling, and 2) increasing the pore size of the nanoporous layer while reducing the DRIE channel dimensions to provide structural support and achieve optimal hydraulic resistance while eliminating the macroporous supporting layer. Figure 4.5 shows the process flow for fabricating SHLHP prototype with two-layer porous silicon membranes. The process is similar to that of the multilayer design but eliminate the anodization of macroporous layer. Silicon wafers were MOS cleaned and then patterned with alignment marks on the front side. The wafers were then porosified to form nanoporous membranes of $\sim 25 \mu\text{m}$. The membrane taken out of the electrochemical cell was immersed in ethanol for 5 minutes to reduce the stress during membrane drying. The membranes were then annealed (RTA AG610) to partially oxidize the nanoporous silicon so that the oxidized structure served as an etch stop to

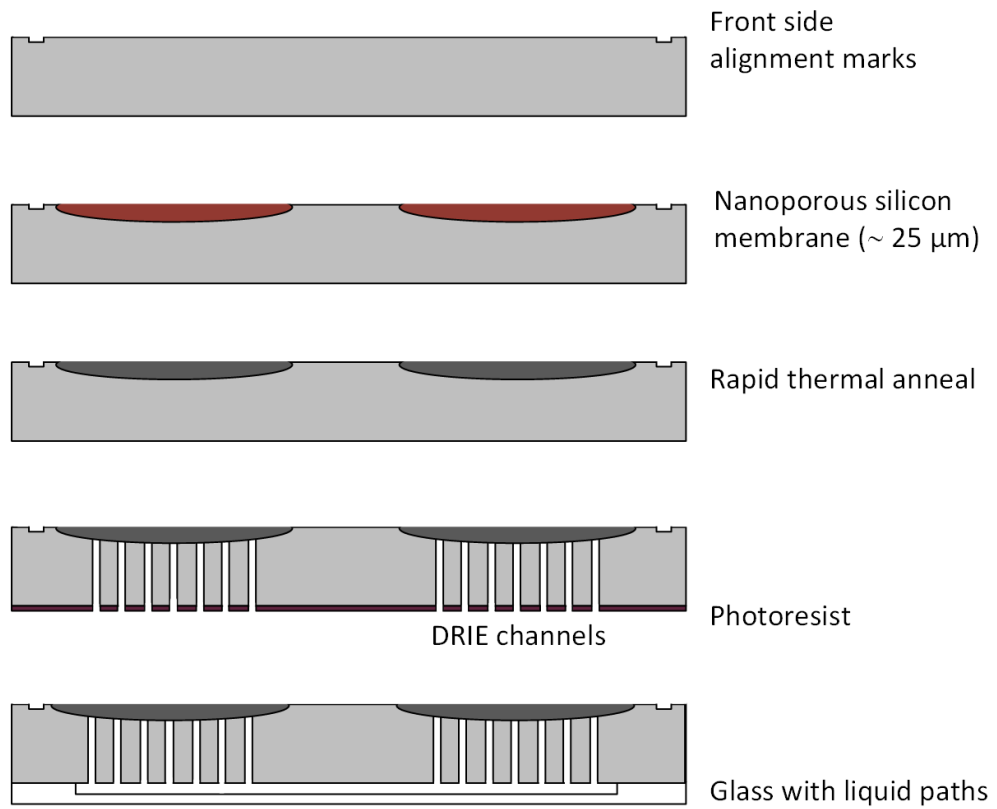


Figure 4.5: Process flow for SHLHP prototype with two-layer porous silicon membranes.

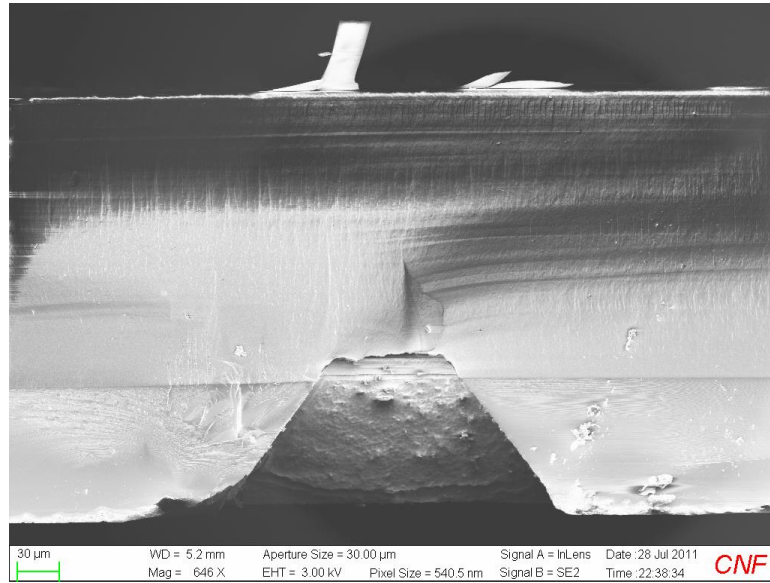
DRIE. The backside of the wafers were patterned to define DRIE channel openings – solvent clean wafers on spinner with acetone and IPA, prime wafers with YES Vapor Prime Oven, spin SPR220.7 photoresist at 2000 RPM for 45 s, soft bake at 115°C for 6 minutes on proximity hotplate, expose the photoresist with Suss MA6 or other contact aligners (soft contact, 2 cycles with 10 s @ 10 mW/cm² each cycle and 10 s wait time in between cycles), leave wafers to rehydrate in yellow light zone for at least 2 hours. Developing the photoresist was done by pipetting 726 MIF on top of the pattern for 10 minutes. The photoresist-patterned wafers were descummed (Oxford 81) and etched with DRIE tool (Unaxis UN770) until channels reaches the bottom of the porous silicon membrane. Finally the anodic bonding of the silicon and glass substrates was done at - 800 V and 400°C until current falls to 5% of max value (home-made bonder in Olin 212).

4.4 Results and Discussion

4.4.1 Challenges with the KOH-cavity and the multilayer designs

Figure 4.6 shows the microscopy images taken from KOH-cavity devices. In Figure 4.6(A), the nanoporous membrane thickness ~ 200 μm; with this thickness, the stress built in the porous membrane during anodization would be too large such that in the subsequent bonding step the membrane would crack and flake off. To tackle this problem, the KOH cavities were re-designed to be etched deeper (~ 250 μm) into the substrate to decrease the porous membrane thickness required to connect with the KOH pits. Considering the side wall angle (54.74°, as illustrated in Figure 4.3(A)) of the anisotropic KOH etch, the KOH pit opening was increased from 250×250 μm² to 400×400 μm² to maintain the final open area of the porous membrane. Figure 4.6(B) shows the bottom view of the porous silicon membrane after the KOH pit bottom was opened. This structure improved the stability of the porous silicon membrane, yet the

(A)



(B)

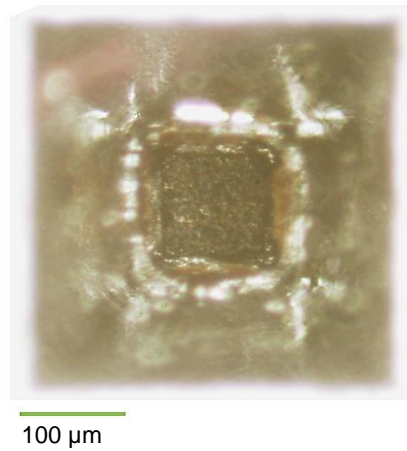
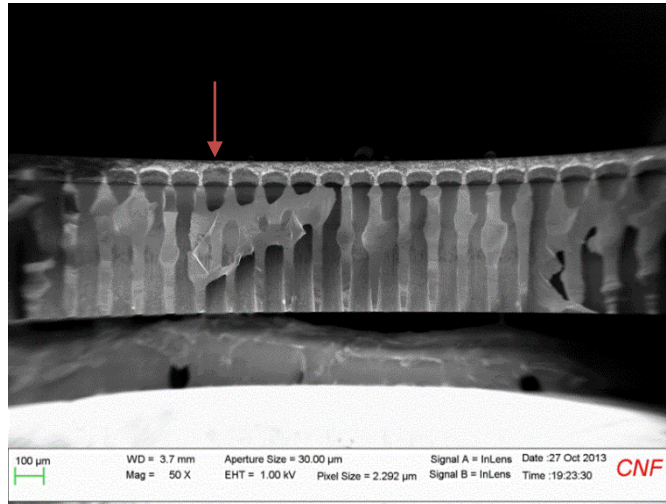


Figure 4.6: (A) Cross-sectional view of the KOH-etched cavities and porous silicon membrane taken by scanning electron microscopy (SEM). (B) Bottom view of nanoporous membrane from the KOH-etched side taken by optical microscope.

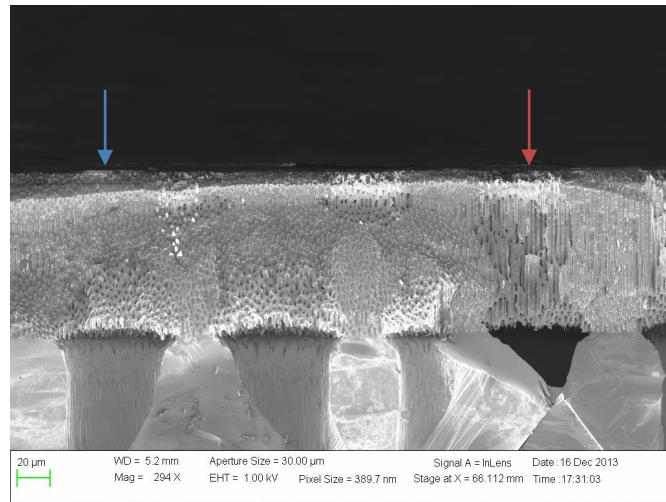
bonding was not successful due to the leaking of electrolyte during anodization; this leakage occurred at the corners of the KOH cavities due to the concentrated electric field. The leaked HF etched away the protective oxide layer on the back side of the wafer, roughened the silicon surface and reduced bonding quality. To solve this problem, one can replace the aluminum conductive layer with other metal resistant to HF; however I chose to stop proceeding with KOH-cavity design, considering the geometry of KOH cavities largely limited the open area of the membrane – to etch deeper into the substrate, membrane open area was sacrificed that there was only 0.4% of the membrane area over total device area. Improving the bonding quality of the KOH-cavity membrane would allow it to serve as a device for stability test but it would not be appropriate as a SHLHP prototype.

Figure 4.7 shows the cross-sectional views of the multilayer porous silicon membrane. As shown in the first and second images, the vapor HF etch to remove the nanoporous fillings was not horizontally uniform; affected by the DRIE channel geometry and the vapor HF chamber conditions, the depth of the clearance varied within one channel and across channels. This non-uniformity limited the maximum depth of the clearance and always left some channels with thicker nanoporous fillings (and hence larger hydraulic resistance) than others. Further, the HF vapor tended to penetrate faster along the wall and created through holes which undermined the cavitation limit of the membrane. As shown in Figure 4.7(C), while there is $\sim 8 \mu\text{m}$ of the nanoporous structure left in the macropores, along the pore walls there are a few defects that might cause air invasion later on. In summary, this “subtraction” to clear the nanoporous structure requires extremely precise control of the etch rate and uniformity, as well as some serendipity depending on the tool conditions. Therefore, this design was not bought to next step to realize a SHLHP prototype.

(A)



(B)



(C)

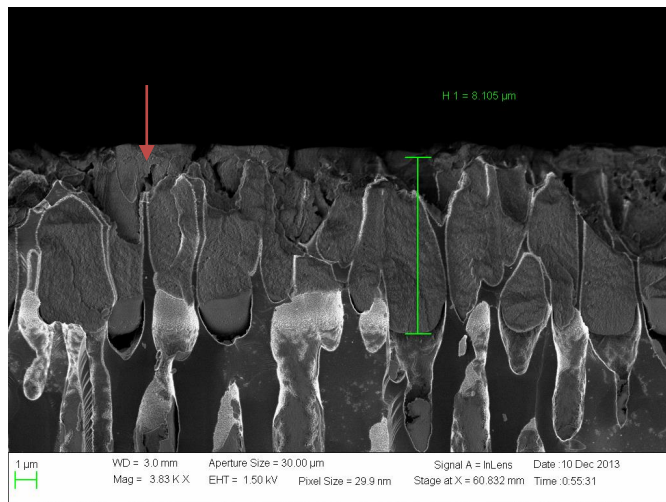


Figure 4.7: Cross-sectional views of the multilayer porous silicon membrane taken by scanning electron microscopy (SEM).

In (A), the vapor HF etch rate is non-uniform from channel to channel: for the majority of the channels, HF has etched half way through the macropores; in some channels (e.g., the one pointed by the red arrow) the filling is almost cleared. Similarly, in (B), membrane area under the red arrow is etched all the way while there is $\sim 10 \mu\text{m}$ of the nanoporous structure left in the area under the blue arrow. In (C), there is $\sim 8 \mu\text{m}$ of the nanoporous filling preserved across the span of this image, however there are some defects (e.g., the one pointed by the red arrow) creating though holes due to a higher vapor HF etch rate along the macropore walls.

4.4.2 Effect of etching parameters on the structure of porous silicon

As reviewed in Section 4.2, the general trend of the porosity and the pore size of nanoporous silicon on p-type silicon substrates is that they increase with increasing current density and decreasing HF concentration. In this work, various etching parameters were used on substrates of different doping levels to achieve the desired device structure for each designs. Hence, the purpose of this sub-section is to report the trends observed according to all experiments done in this study, and to provide reference and guidance for future works.

Table 4.1 reports the pore sizes and the etch rates of nanoporous silicon samples obtained from anodization of silicon substrates of different substrate resistivity (measured with CDE ResMap 4-point Probe). For p or p⁺ substrate, the pore size increases with the doping level; this trend is consistent with the data reported by Lehmann *et al.*¹²⁴ As the doping level enters p⁻ regime, the pore size decreases slightly with the increasing resistivity. Also, as observed in Table 4.1, the etch rate decreases with increasing doping level. Note that the etch rates reported in this study were normalized by the current density [mA/cm²]. Table 4.2 shows the variations of the pore size and the etch rate with electrolyte composition and current density. The pore diameter of nanoporous silicon was found to increase with a decrease of the HF concentration. As HF concentration is lower than a critical value, the porosity of the porous layer would become too large and the layer would collapse and break upon drying or transferring; some examples of this situation are listed in Table 4.2. Similarly, when the forming current density is increased, the pore sizes widen and the pore size distributions broaden. These trends are in consistent with the data summarized in the book edited by Canham.⁶⁰ In general, about the same pore size range is obtained for the same porosity, whatever the experimental forming conditions; the increasing of current density and the increasing of HF concentration cancel the effects of each other, and vice

Table 4.1: Variations of the pore diameter and the etch rate of nanoporous silicon with silicon substrate resistivity

Wafer Resistivity [Ω/cm]	Electrolyte Composition (-)	Current Density [mA/cm^2]	Pore Diameter* [nm]	Etch Rate* [$\frac{\mu\text{m}}{\text{hr}(\text{mA}/\text{cm}^2)}$]
37	35% HF in AA**	4	3–5	(-)***
24	35% HF in AA	10	2–5	4.2
1.0×10^{-2}	35% HF in ethanol	(-)	4–8	(-)
3.3×10^{-3}	25% HF in ethanol	30	4–9	2.6
1.2×10^{-3}	25% HF in ethanol	30	4–10	(-)
6.3×10^{-4}	30% HF in ethanol	20	8–16	1.7

* Pore diameter range reported and the etch rate of the sample were estimated from SEM images.

** HF comes from 48% HF in water. AA = 98% acetic acid. “35% HF in AA” = 7:3 v/v, 48% HF : AA.

*** Etch rate was not measured for that sample.

Table 4.2: Variations of the pore diameter of nanoporous silicon with electrolyte composition and current density

Wafer Resistivity [Ω/cm]	Electrolyte Composition (-)	Current Density [mA/cm^2]	Pore Diameter [nm]	Etch Rate [$\frac{\mu\text{m}}{\text{hr}(\text{mA}/\text{cm}^2)}$]
3.3×10^{-3}	25% HF in ethanol	30	4–9	2.6
3.3×10^{-3}	22.5% HF in ethanol	30	5–11	(-)
3.3×10^{-3}	20% HF in ethanol	30	6–14	2.3
3.3×10^{-3}	6% aqueous HF + Mirasol	3	8–16	2.2
1.2×10^{-3}	30% HF in ethanol	20	4–13	2.3
1.2×10^{-3}	25% HF in ethanol	30	4–14	(-)
1.2×10^{-3}	25% HF in ethanol	15	4–10	2.0
1.2×10^{-3}	20% HF in ethanol	30	N/A*	(-)
6.3×10^{-4}	30% HF in ethanol	20	8–16	1.7
6.3×10^{-4}	25% HF in ethanol	7.5	7–14	1.7
6.3×10^{-4}	20% HF in ethanol	10	N/A*	(-)

* The porous layer collapsed and flaked off upon drying.

versa. Figure 4.8 presents SEM images of nanoporous silicon samples formed on substrates of two different doping levels with different current densities and electrolytes of different HF concentrations. Porous silicon samples formed on the substrate with lower resistivity show clearly larger pores size and porosity. On the other hand, on both substrates, decreasing the HF concentration by 5% while decreasing the current density produce samples of similar pore morphology.

Figure 4.9 shows the variation of the etch rate of macroporous silicon samples with current density and silicon substrate resistivity. The etch rate reported in the graphs was normalized by current density, and only the thickness of macroporous layer was counted (i.e. excluding the thickness of the top nucleation layer). As illustrated in Figure 4.9(A), the etch rate varies almost linearly with the current density but shows a slight drop as the current density increases. Unlike observed on nanoporous silicon, the etch rate of macroporous silicon layer does not strongly depend on the substrate resistivity (within the range of 30–45 Ω -cm) or the electrolyte composition, as shown in Figure 4.9(B).

4.4.3 Two-layer porous silicon membrane characterizations

Figure 4.10(A) shows the cross-sectional views of the two-layer porous silicon membrane. The two distinct layers of the nanoporous silicon membrane and the DRIE channels are clearly illustrated; the interface between the two layers is shown in Figure 4.10(B). The DRIE mask pattern consists square pits ($50 \times 50 \mu\text{m}^2$) arranged in a square array of 100×100 , with a distance of $100 \mu\text{m}$ between successive pits, covering an area of $\sim 1 \text{ cm}^2$. During the DRIE, the channel opening gradually widened due to the non-ideal side wall etching, forming channels of funnel shape as shown in Figure 4.10(A). The nanoporous silicon membrane in this particular device was formed on a silicon substrate of $3.3 \times 10^{-3} \Omega$ -cm, with 22.5% HF in ethanol, current density 30 mA/cm^2 .

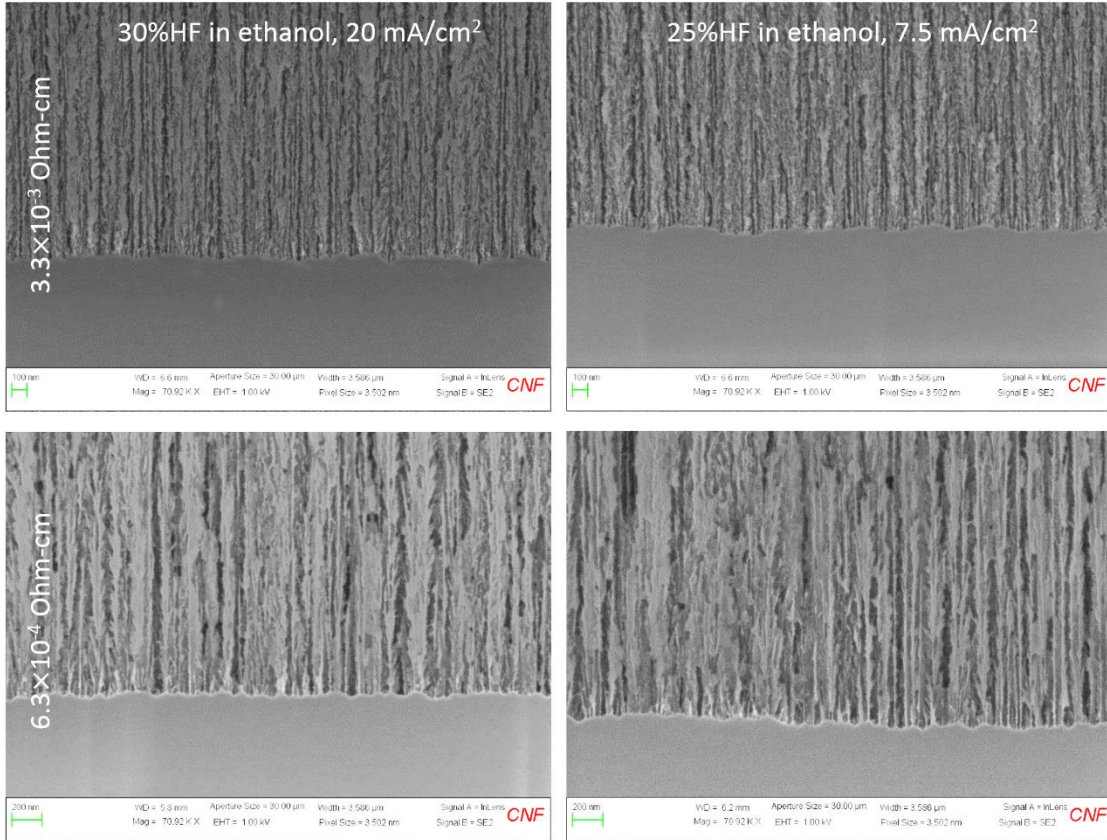
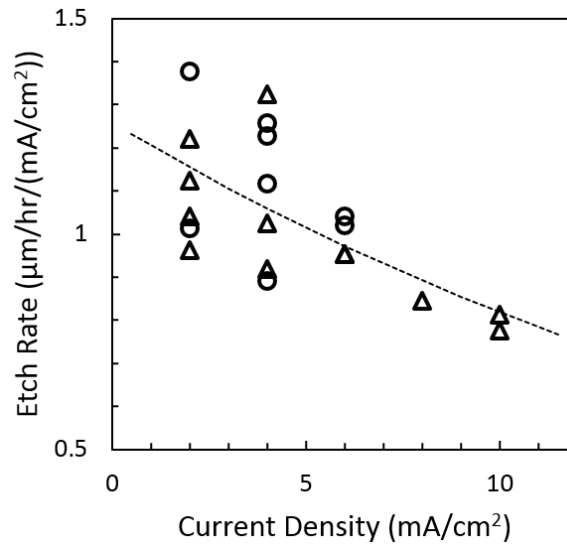


Figure 4.8: Scanning electron micrographs of the interface between bulk and porous silicon for p-type silicon substrates of different doping levels with different anodization conditions.

The magnification in all 4 images was the same.

(A)



(B)

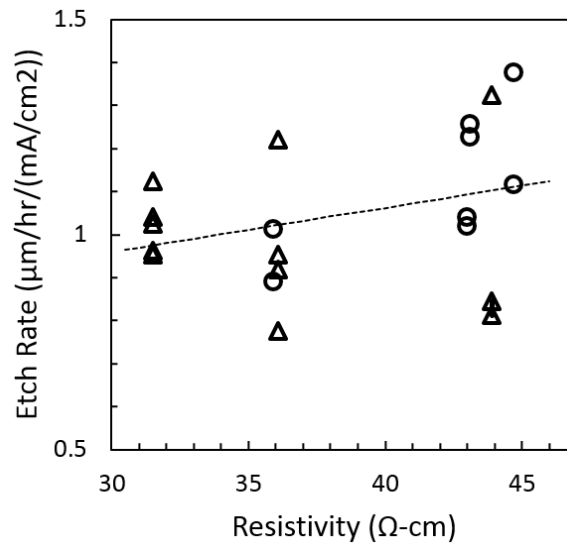
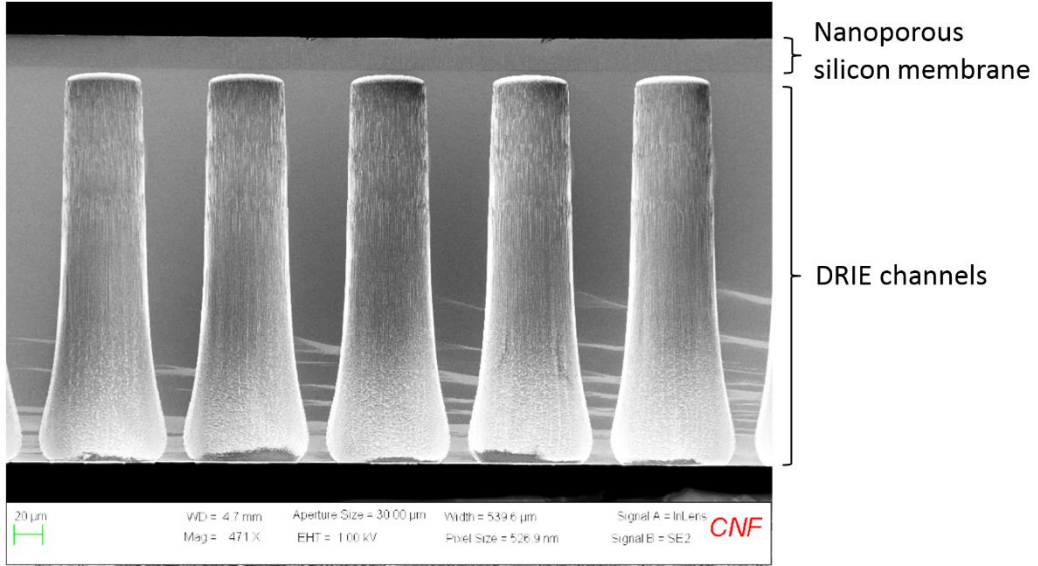


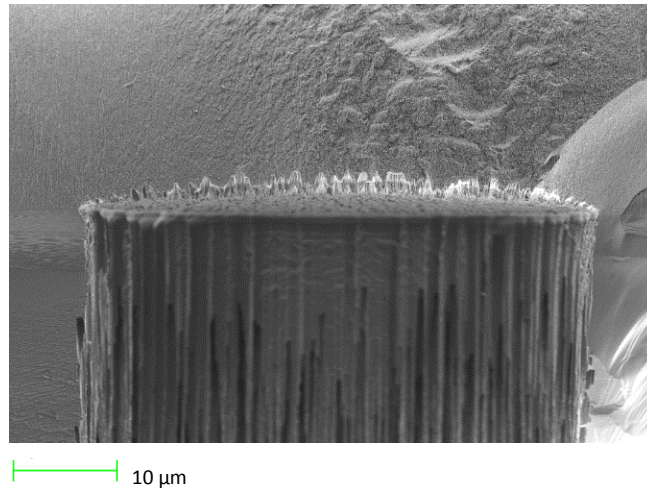
Figure 4.9: Variation of the etch rate of macroporous silicon layers with (A) current density and (B) silicon substrate resistivity.

Legends: triangles – 4:86:10 (v/v/v) solution of 48% HF, acetonitrile and 98% AA; circles – 2:88:10 (v/v/v) solution of 48% HF, acetonitrile and 98% AA.

(A)



(B)



(C)

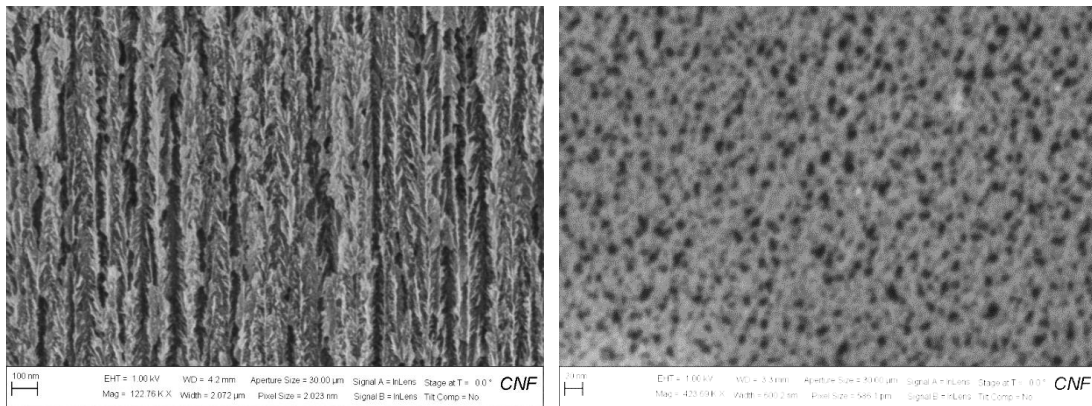


Figure 4.10: Scanning electron microscopy (SEM) images of the two-layer silicon membrane. (A-B) Cross-sectional views of the two-layer structure; (C) cross-sectional (left) and top (right) views of the nanoporous silicon layer.

In (A), the DRIE channels are almost but yet connected to the nanoporous membrane. A few more loops of DRIE connected the channels to the bottom of the nanoporous membrane, as shown in (B).

Figure 4.10(C) presents the cross-sectional and top views of this nanoporous layer; the pore diameter is $\sim 5\text{--}11$ nm, membrane thickness ~ 25 μm .

The unified model for steady state operation of both the conventional and superheated LHP designs is presented in Chapter 2 (see Section 2.4); this model can predict and compare the performances of a SHLHP prototype and a conventional LHP with the same form factors. By numerically solving the coupled heat and momentum balances and local thermodynamic equilibria (Eqs. (2.6)–(2.18)), we can model the steady-state evaporator temperature as a function of the heat load at a fixed heat sink temperature, T_{sink} . Figure 4.11 shows the operating curves for both conventional and saturated SHLHP designs with geometric parameters identical to the two-layer membrane prototype; evaporator was placed above the condenser in the modeling (i.e. $g_e = 1$ g). The evaporator temperatures of the SHLHP are more than 100°C lower than those of the conventional case.

The insert in Figure 4.11 shows the liquid profile at the evaporator membrane surface as a function of the heat load. For a SHLHP prototype with saturated condenser, a tension of larger than 3 MPa would be generated in the liquid at the membrane surface during steady state operation at 50 W/cm^2 (nanopore diameter: 10 nm). For a device with smaller effective nanopore diameter, the resulted hydraulic resistance of the membrane would be larger and high tension would be generated. Further, for a SHLHP operated with sub-saturated condenser, the pressure drop across the condenser membrane would add to this tension at the evaporator. Hence, the ability of the two-layer silicon membrane to hold tension is essential. To test the stability of water with MVLE methods and two-layer silicon membrane, I implemented an experimental set-up similar to the one for the free-standing membrane stability test (as presented in Chapter 3).

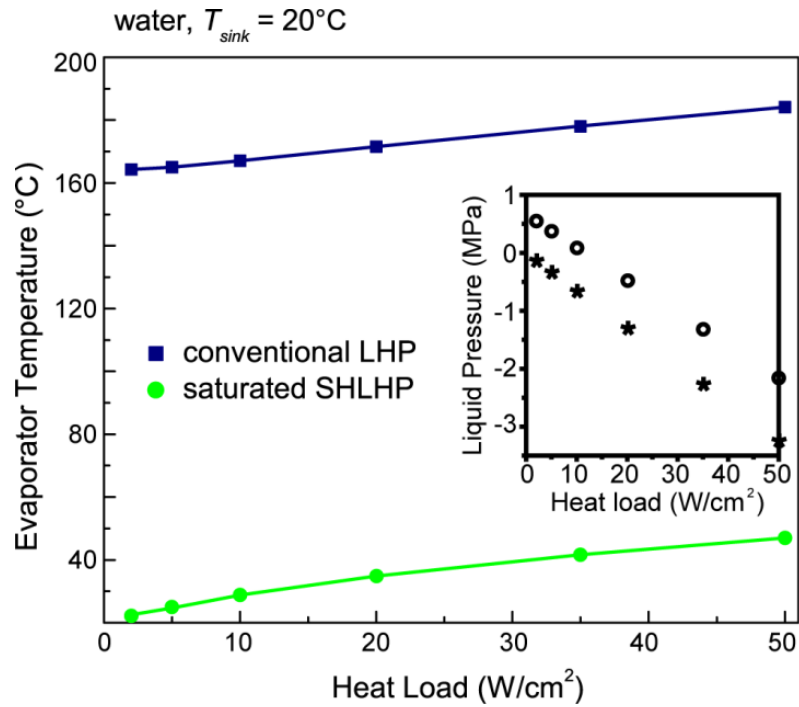


Figure 4.11: Operating curves and liquid pressures at the membrane surface (insert) for conventional and saturated SHLHP designs with MEMS-based form factor.

Working fluid: water. Sink temperature: 20°C . Length, diameter and number of liquid paths: 6 cm, $30\ \mu\text{m}$ and 100, respectively. Thickness and diameter of channels of the DRIE layer: $280\ \mu\text{m}$ and $50\ \mu\text{m}$. Thickness and diameter of pores of the nanoporous layer: $20\ \mu\text{m}$ and 10 nm. Legends in the insert: open circles are of conventional LHP; asterisks, saturated SHLHP.

Figure 4.12 (A) shows the top and cross-sectional views of a stability test device – the two-layer membrane was bonded on the DRIE side to the glass with etched voids. This device was placed in the vapor control system to be subjected to sub-saturated vapor of activity < 1 . As shown in the snapshot of an actual device top view during the course of the experiment, different states of the void are easily identifiable in these images: filled voids are almost entirely dark, emptied voids show a bright ring around the perimeter of the etched circle, and voids undergoing emptying have meniscus of the vapor bubble evolving in of the void. The openings of the DRIE pits can be seen clearly in this image. Figure 4.12(B) presents the survival probability curve for a two-layer membrane etch from a silicon wafer of $3 \times 10^{-3} \Omega\text{-cm}$ resistivity. Etching conditions for this sample: 22.5% HF in ethanol, 30 mA/cm². The device sustained a cavitation pressure (liquid pressure corresponding to a probability of 1/2) of $\sim -27\text{MPa}$ at 15°C; 100% of the voids survived tension up to -16MPa , much larger compared to the predicted tensions in Figure 4.11.

From the emptying of the voids, I estimated the hydraulic permeability, $\kappa [\text{m}^2 (\text{Pa} \cdot \text{s})^{-1}]$, of the membrane based on Darcy's law (Eq. (3.10)). The observed emptying time varied across voids, ranging from ~ 10 s to slightly over 1 minute. This observation may be due to the interrupted emptying of liquid by potentially existing vapor plugs in DRIE channels. Unlike in the free-standing membrane devices the liquid in the voids directly in contact with the nanoporous membrane, in the two-layer membrane device liquid in the voids flows through narrow DRIE channels to reach the membrane. Cavitation might start in the DRIE channel, form vapor plugs, and hence hinder the emptying of the liquid in the void. Using the shortest emptying time for the estimation, the hydraulic permeability of the membrane was on the order of $10^{-16} \text{m}^2 (\text{Pa} \cdot \text{s})^{-1}$. In our previous work, the permeability for porous silicon was reported to be $1.44 \times 10^{-17} \text{m}^2 (\text{Pa} \cdot \text{s})^{-1}$.³²

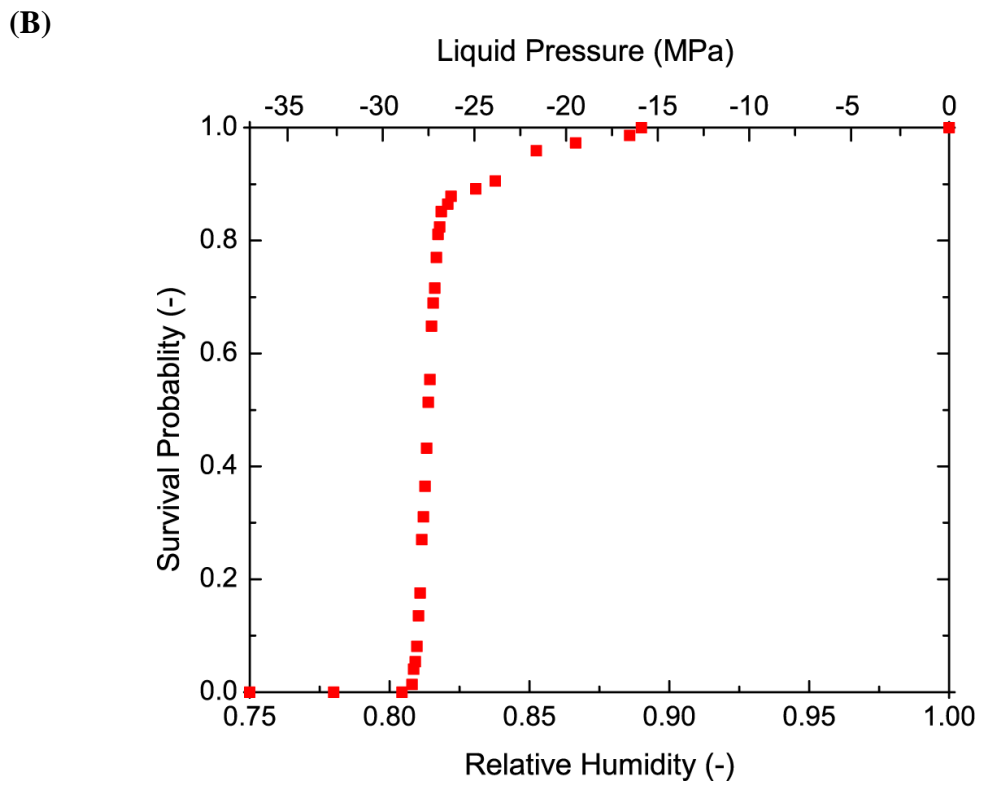
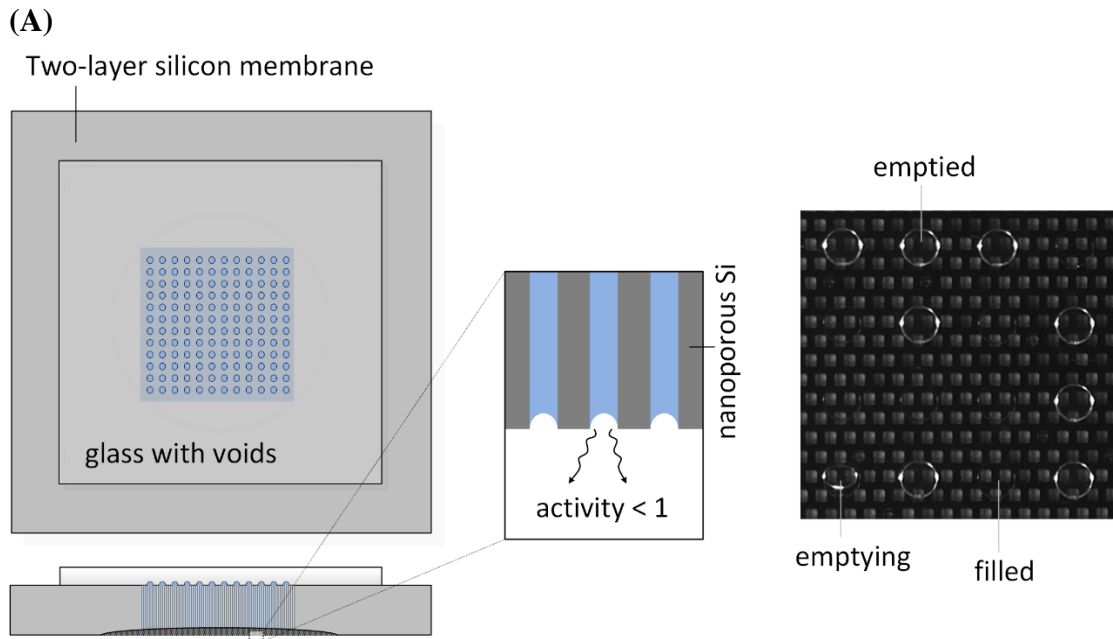


Figure 4.12: Two-layer silicon membrane stability test.

(A) Schematic diagrams (left) showing the top and cross-sectional views of a two-layer silicon membrane bonded to void-patterned glass substrate for stability tests. (Right) An actual device image (top view) shows liquid-filled, emptying, and emptied (vapor-filled) voids. (B) Survival probability for water in the two-layer membrane device at 15°C.

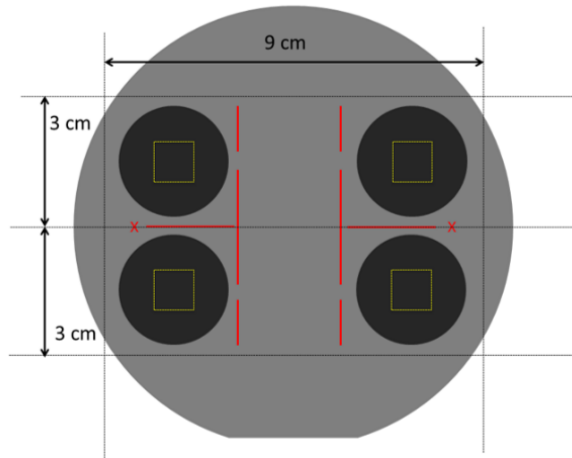
This increase in the membrane permeability can be attributed to the higher doping and the larger current density creating pores of larger diameter.

4.5 Experimental System Studying SHLHP Performance

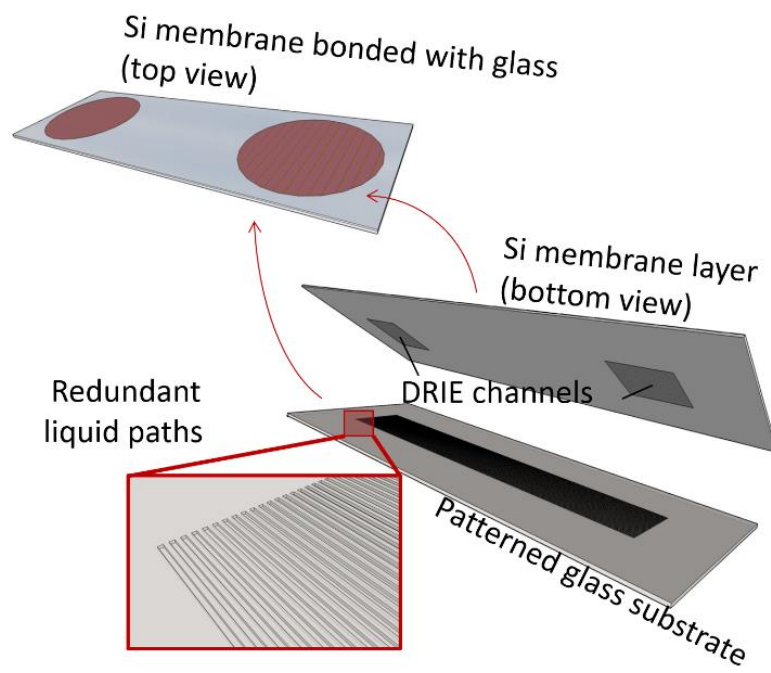
Figure 4.13 shows the design of a prototype MEMS-based SHLHP. The size of a device is roughly $3 \times 9 \text{ cm}^2$, as illustrated in Figure 4.13(A). The device consists of a piece of silicon substrate with silicon membranes etched on both ends and a glass substrate patterned with liquid paths. The two membranes serve as the evaporator and the condenser membrane of a SHLHP; the pore structures of the two membranes can be designed and fabricated independently. The DRIE side of the silicon piece is bonded to the glass so that the liquid paths in glass connect the evaporator and the condenser membranes. The liquid paths are designed to be independent channels etched into the glass; such hydraulically independent, redundant liquid paths provide passive robustness to cavitation – when a liquid path cavitates, the others are not affected and continues to transport liquid. The liquid path pattern consists of 100 rectangular channels of $20 \mu\text{m} \times 7 \text{ cm}$ each, $100 \mu\text{m}$ pitch between successive channels. The channels was etched until the depth reaching $\sim 17 \mu\text{m}$. Due to the isotropic nature of the wet etch, the final cross section of a channel was $\sim 50 \mu\text{m}$ wide. Figure 4.13(C) demonstrates the connection between the liquid paths and the DRIE channels. One liquid path is connected to all DRIE channels in the same row.

In Figure 4.14 is shown the custom-made jig for studying operation characteristics of the prototype SHLHP. This jig consists of the sample stage, the evaporator assembly and the condenser assembly. The sample stage and the insulation layers in the evaporator assembly were made of MACOR[®] Machinable Ceramic; this material has the ability to withstand high temperatures, possesses low thermal conductivity, has no outgassing and is radiation resistant. The SHLHP device can fit in the shallow cavity

(A)



(B)



(C)

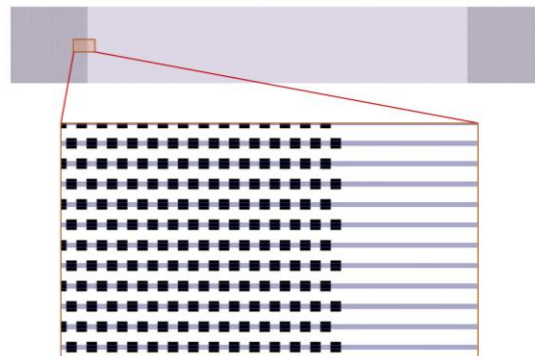
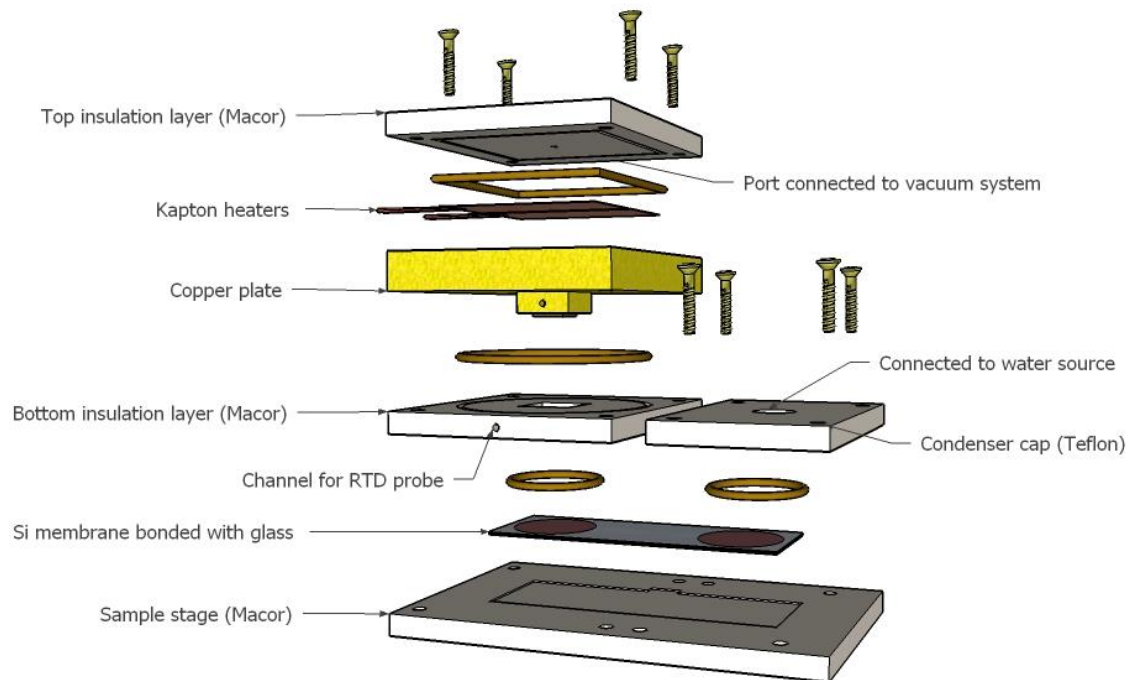


Figure 4.13: Design schematics for a prototype MEMS-based SHLHP with two-layer silicon membranes.

(A) The size of the device is $3 \times 9 \text{ cm}^2$; a 4-inch silicon wafer can fit 2 pieces. The yellow squares indicate the DRIE channels on the backside. (B) Silicon substrate with porous silicon membranes and DRIE channels is bonded to glass substrate with redundant liquid paths. (C) The mask pattern for the DRIE channel pits arrays (black squares) and liquid paths (purple). One liquid path is connected to 100 DRIE pits at each end.

(A)



(B)

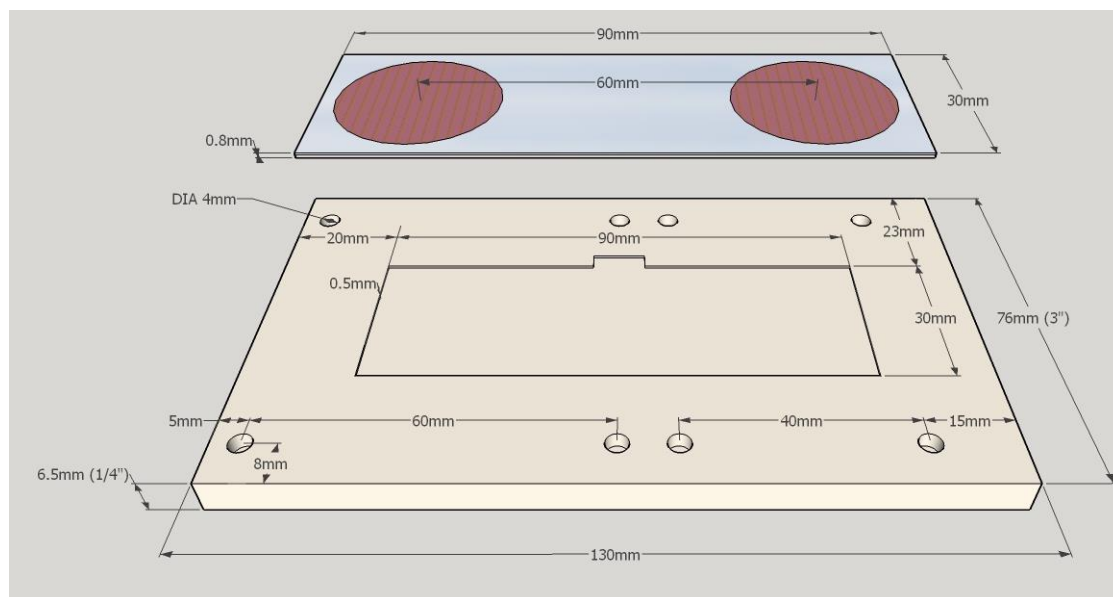
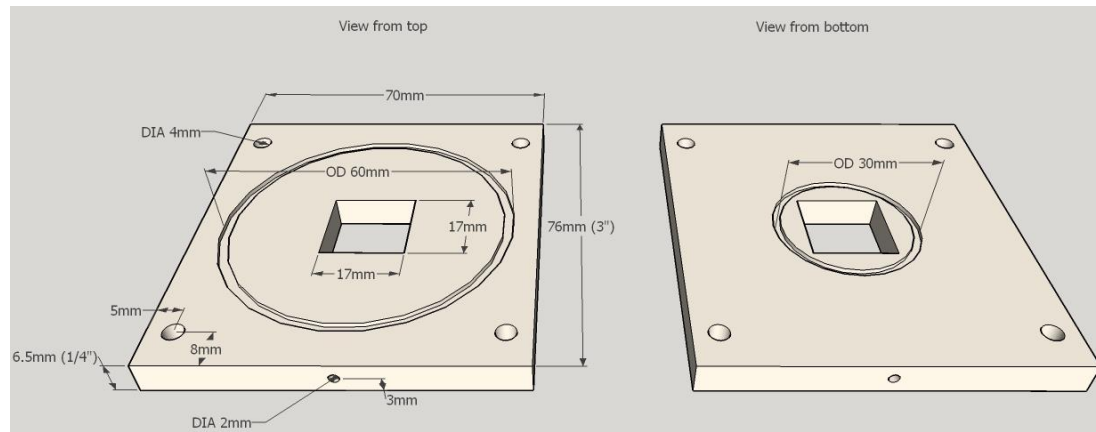


Figure 4.14 (Continued)

(C)



(D)

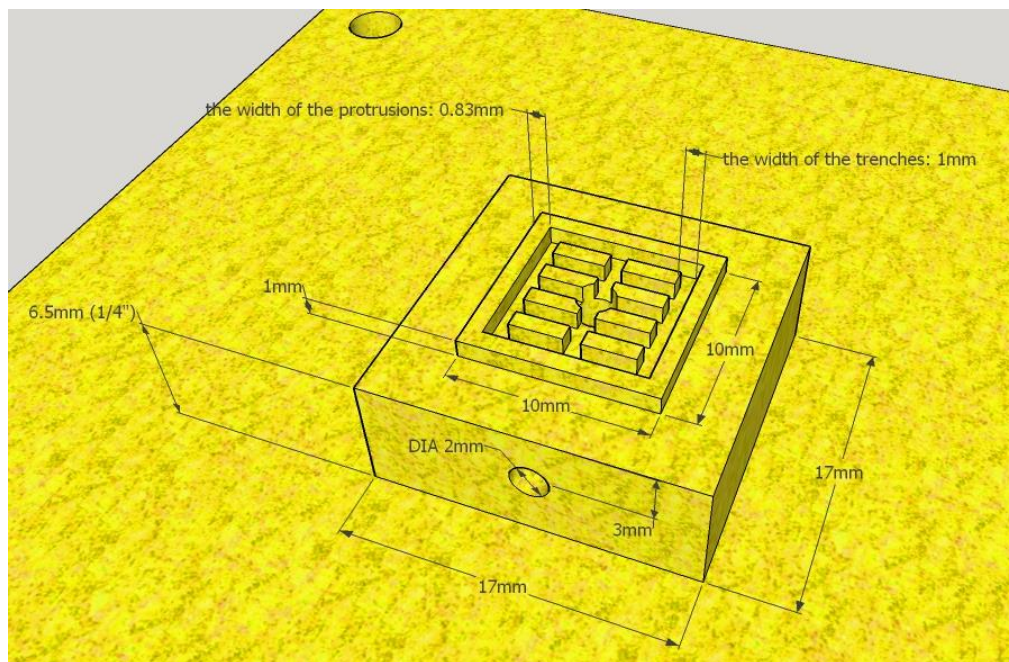


Figure 4.14: Custom-made SHLHP assembly to study SHLHP prototype performance.

(A) The overview of the entire experiment jig. The left side is the evaporator, including the heat supply, the temperature measurement spot, and the vapor outlet connected to the vapor control. The right side is the condenser. (B-D) Detailed designs of the sample stage (B), insulation later (C), and copper finger (D).

machined in the center of the stage (see Figure 4.14(B)). In the evaporator assembly, a copper plate is sandwiched between two MACOR[®] insulation layers; the center of this copper plate intrudes through the bottom insulation layer to reach the evaporator membrane surface and provide a concentrated heat flux. On the tip of the copper finger, pillars and grooves were machined at the center 1 cm^2 ; the pillars define the evaporator contact area, while the grooves serve as the vapor paths and direct the vapor to the center vapor outlet (see Figure 4.14(D)). The heat is supplied by the thin film heaters attached to the copper plate (e.g., Kapton[®] heater). The heaters are held in place by an o-ring under the top insulation layer. A temperature detector inlet is drilled through the bottom insulation layer and part of the copper finger to reach the center of the copper finger and measure the temperature, T_{source} . To efficiently deliver the heat to the evaporator membrane surface without losing much heat to the surrounding, the entire evaporator assembly can be wrapped with fiberglass insulation materials.

A major challenge is to reduce the contact thermal resistance between the copper finger tips and the evaporator membrane surface to minimize the temperature raise in the evaporator assembly as the heat is applied. For a heat load of 30 W/cm^2 , direct contact between the copper finger tips and the porous silicon membrane would produce a temperature difference of $\sim 70^\circ\text{C}$ across the contact plane. Two methods were tested to reduce the contact thermal resistance: 1) applying a thin layer of thermal compound (Arctic Silver AS5) between the copper tips and the membrane, and 2) filling the gap between the copper tips and the membrane with copper powders (Sigma Aldrich, spheroidal, $14\text{--}25 \text{ }\mu\text{m}$, 99%). Table 4.3 provides the preliminary test results of the thermal resistance measurements. The data show that applying thermal compound reduced the contact resistance by up to 3-fold compared to direct contact. On the other hand, using copper powders increased the contact thermal resistance by 50%, possibly due to the air gap introduced between the copper powders. However, using thermal

Table 4.3: Comparing the contact thermal resistance between the copper finger tips and the silicon membrane

	Resistance [K/W]	Capacitance [J/K]	Temperature Difference* [K]
Copper Plate	0.048	217.3	1.4
Direct Contact	0.857	(-)	69.4
Thermal Compound	2.315	(-)	25.7
Copper Powders	3.429	(-)	102.9

* Temperature differences were calculated with a heat flux of 30 W/cm².

compound would potentially contaminate the working fluid in the long run. Cleaner alternative methods to reduce the contact thermal resistance or alternative heat delivery methods (e.g., radiative heat) should be further investigated.

Figure 4.15 shows the schematic diagrams of the experimental setups for studying the SHLHP prototype performance. A vapor control system similar to the one used for stability tests was built to serve as the regulator that controls the vapor pressure in the vapor path. By adjusting the position of the two needle valves between the water vapor source and the pump, one could control the vapor pressure between the valves (see Section 3.3.2 for more details). The applied heat flux is controlled by adjusting the input voltage on Kapton heaters. The temperature in the evaporator wall (copper plate) is measured by a resistance temperature detector (RTD) inserted into the copper finger.

An open loop test may be performed first to characterize the evaporator wick performance: by independently controlling the vapor cavities above the condenser and the evaporator, the transport limitations of phase change on vapor-liquid interfaces in both wick membranes can be isolated. Figure 4.15(A) presents the setup for an open-loop evaporator test. The evaporator vapor outlet is connected to the vapor control system to be pinned at a constant vapor activity according to the evaporator temperature measured. The condenser is connected to a water reservoir maintain at a constant temperature to supply the evaporator liquid cavity with a constant temperature working fluid. In summary, parameters controlled in an open-loop evaporator test include the heater input power (q_i), the vapor cavity pressure (p_e), and the liquid cavity temperature (T_e^{liq}), and the parameters measured include the working fluid flow rate (Q) and the evaporator wall temperature (T_{source}). Also, the cavitation phenomenon in liquid paths and the maximum heat flux before dry-out can be studied with an open-loop characterization.

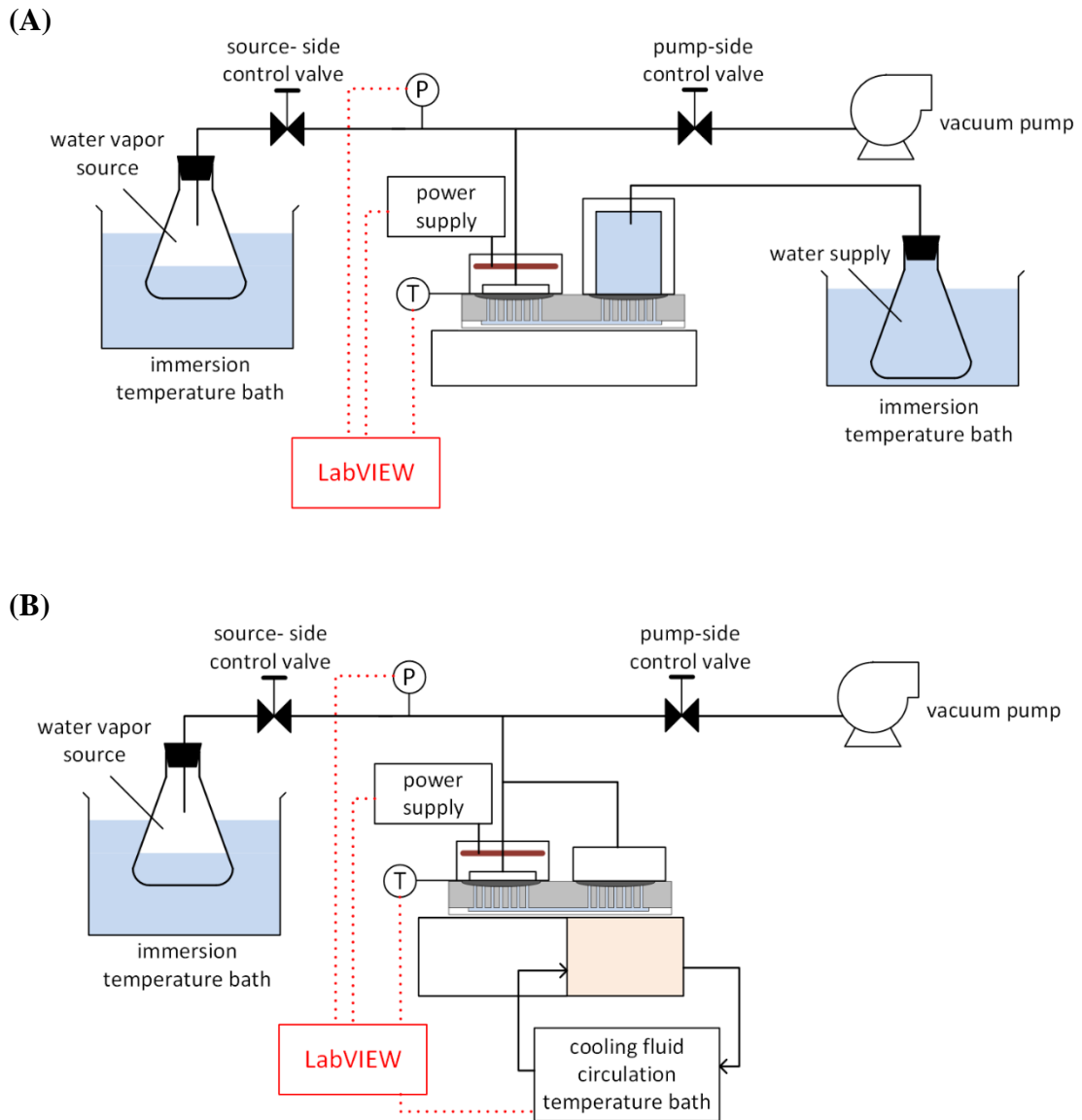


Figure 4.15: Schematic diagrams for the experimental setups: (A) open-loop design; (B) closed-loop design.

After the open-loop experiments, we can turn to characterize the closed-loop operation. Figure 4.15(B) shows the experimental setup for the close-loop tests. By connecting the condenser vapor cavity to the vapor control system, a closed vapor path is formed and the vapor control system serves as the regulation chamber connected to the vapor path. Cooling fluid to the stage is connected to an external temperature control bath and circulated through the base of the condenser to control the heat sink temperature, T_0 . Steady state functions of a SHLHP prototype (e.g. operating curves as functions of the regulator activity and/or the heat sink temperature) can be demonstrated and compared to the results of model simulations and of conventional LHPs.

4.6 Integration of Nanoporous Materials onto Porous Silicon Membrane and SHLHP Prototype

Reported in Section 4.4.3, the ability of the two-layer membrane to sustain tension was tested by anodically bonding the membrane to a glass substrate etched with independent voids and exerting tension on liquid in voids with MVLE method (see Figure 4.12). With this device configuration, a two-layer membrane was able to sustain a cavitation pressure, $P_{cav} \sim -27\text{MPa}$ at 15°C (Figure 4.12(B)). Nevertheless, it is essential to characterize the stability limit of water in SHLHP prototype devices with the same two-layer membranes one both ends bonded to glass channels. Instead of the vapor control system, the stability experiments for SHLHP prototype were done with unsaturated salt solutions controlling the relative humidity experienced by the device. The experimental procedure consists of 1) submerging the device in water and left in the vacuum chamber for 12 hours to remove air from the channels, 2) filling the samples with degassed water in a pressure bomb with 35 MPa of pressure for > 12 hours, 3) placing the device in the petri-dish filled with salt solution corresponding to the relative humidity of interest (the device was supported to hang over the solution liquid surface)

and sealing the petri-dish, 4) observing the glass side from top with camera to obtain cavitation history, and 5) moving the device to the next petri-dish of lower relative humidity. For SHLHP prototype, survival probability = number of filled liquid paths/total number of liquid paths.

In Figure 4.16 is summarized the survival probability of water in three SHLHP prototypes. SHLHP devices were not able to sustain as high tension as in membrane bonded with independent voids, even though the membranes were fabricated following the same recipe and procedure. This observation is related likely to the following two facts: 1) The silicon substrates used for fabricating SHLHP devices exhibit a slightly lower resistivity compared to those for the two-layer membranes bonded to glass with individual voids; $1 \times 10^{-4} \Omega\text{-cm}$ and $3.3 \times 10^{-3} \Omega\text{-cm}$, respectively. The increased pore size and porosity of the porous silicon on lower resistivity substrates may be accompanied with more defects (e.g., large pores causing invasion of menisci). 2) In the SHLHP prototype design, one liquid path connects a total of 200 DRIE pits (100 pits at each end); this configuration largely increase the probability that a liquid path is exposed to any defect in the porous silicon membrane. Figure 4.17 shows the top views of the two-layer membranes in the two device configurations after equilibrating with a relative humidity of ~97.5% for 5 days. For the membrane bonded to glass etched with liquid paths, water showed a survival probability of 18%; the membrane bonded to individual voids, 90%. However, for the latter, if the individual voids in the same column were connected, only 5 out of 19 channels would have survived (i.e. survival probability = 26%).

While porous silicon presents a versatile base material with predictable trends of average pore size and porosity as well as tightly-distributed pore size ranges, the design target for membranes in a SHLHP – defect free over macroscopic dimensions – is challenging to meet; fabricating porous silicon membranes capable of sustaining a

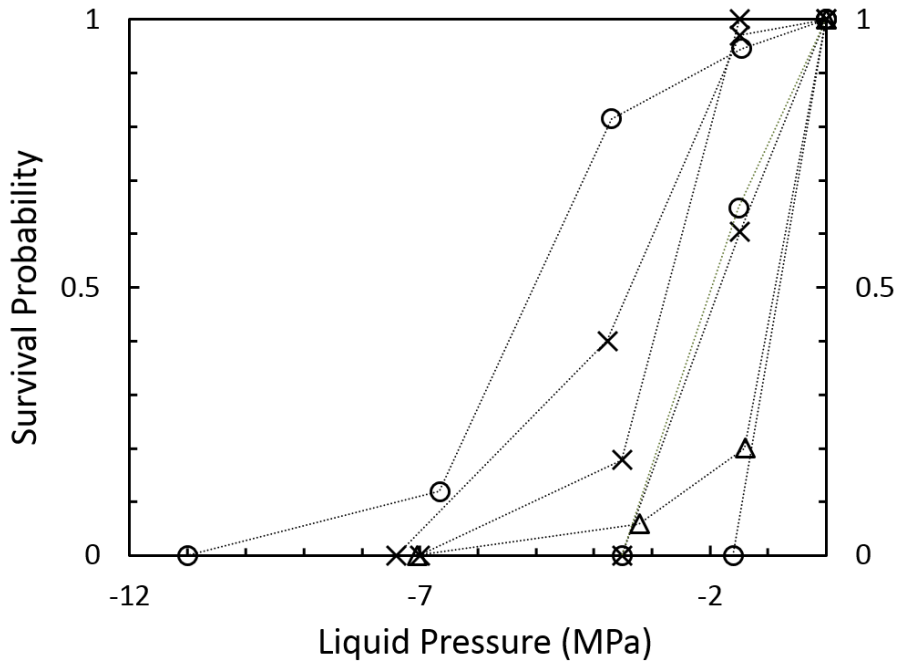


Figure 4.16: Survival probability for water in SHLHP prototypes as a function of the liquid pressure at room temperature.

The data points were obtained from three SHLHP devices; data points from the same device were marked with the same legend.

Circle: $8.9 \times 10^{-3} \Omega\text{-cm}$, ground, 6:4 HF : ethanol, 15 mA/cm²

Cross: $9.2 \times 10^{-4} \Omega\text{-cm}$, ground, 6:4 HF : ethanol, 15 mA/cm²

Triangle: $4.3 \times 10^{-3} \Omega\text{-cm}$, polished, 4:6 HF : ethanol, 30 mA/cm²

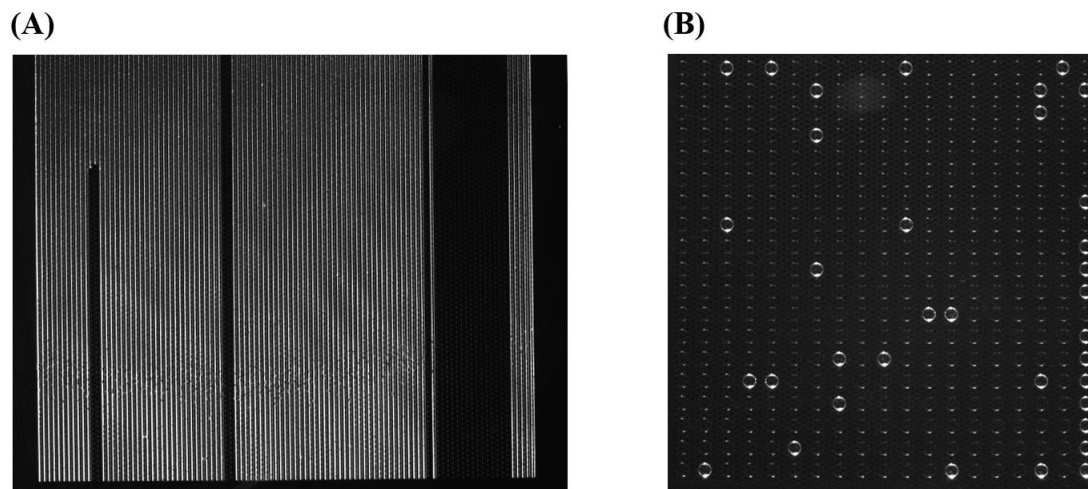


Figure 4.17: Device images (top view) during stability tests of the two-layer membranes bonded to glass substrates etch with SHLHP liquid paths (A) and individual voids (B).

The devices were subjected to a relative humidity of $\sim 97.4\%$ ($P_{liq} \sim -3.5$ MPa) at room temperature for 5 days. The silicon membranes in these two device were fabricated on the same silicon substrate using the same recipe and procedures.

survival probability of 1 at -16 MPa (as illustrated in Figure 4.12) depends not only on the choice of silicon substrates but also the distribution of defects (pores of larger radii). Hence, to “amend” an already-made silicon membrane and improve the maximum tension it can sustain, it is helpful to look into nanomaterials that can potentially be combined with silicon membrane structures. In this section, a few nanoporous materials were proposed to be incorporated with the SHLHP prototype to increase the stability and enable potential applications of this device beyond heat pipe functionalities. Among these nanoporous materials, anodic aluminum oxide and graphene oxide were explored with experiments; the preliminary results are presented in Section 4.6.1 and Section 4.6.2. Other potential materials including polyelectrolyte multilayer, zeolite and porous carbon membranes are discussed in Section 4.6.3.

I note that other effects may have contributed to the low stability observed in SHLHP prototype, including: 1) The anodic bonding between the silicon substrate and the glass was not perfectly sealed. In some devices, the DRIE side silicon surface (the side bonded to the glass) was ground instead of polished. Although the surface roughness of ground wafers were $50\text{--}75\text{\AA}$, well within the range for obtaining quality anodic bond¹³³, it was observed that in some ground-surface devices, cavitation events seemed to propagate from channel to channel, resulting in blocks of cavitating channels (as shown in Figure 4.17(A)). Nevertheless, the stability limit was similar obtained with SHLHP with polished silicon surface. There is also possibility that the bonding defects were not due to surface roughness being too large, but due to the narrow bonded width between paths ($\sim 40\ \mu\text{m}$) allowing air to seed through these separations. 2) The narrow, elongated geometry of liquid path channels may render the device more susceptible to mechanical disturbances. This hypothesis comes from observation that in some devices cavitation events were triggered by moving around the sealed petri-dish.

4.6.1 Porous anodic aluminum oxide

Porous anodic aluminum oxide (AAO) film, or anodic porous alumina, similar to nanoporous silicon, is a self-organized nanostructured material formed by electrochemical oxidization of aluminum substrate in an acidic electrolyte. Porous AAO film is composed of a porous oxide layer containing parallel nanopores and a barrier oxide layer (non-porous) at pore bottom in conformal contact with aluminum substrate. Under proper anodization conditions, self-ordered honeycomb-like structure can be obtained in porous AAO;¹³⁴ this characteristic of AAO has attracted attention of the researchers worldwide and properties of AAO has been extensively studied, especially AAO fabricated with bulk aluminum foils. Figure 4.18 shows an idealized structure of porous AAO – a packed array of columnar hexagonal cells with central, cylindrical, uniformly sized pores ranging from 4 to 500 nm in diameter.

The thickness of the porous AAO layer is proportional to the total charge involved in the anodization. Hence, by controlling anodization time, the depth of the pore is tunable from a few tens of nanometers up to hundreds of micrometers. Dependence of other structural parameters (see Figure 4.18(b)) of porous AAO on the anodizing conditions has been investigated and discussed in detail; for comprehensive reviews on this matter, one can refer to the work by Lee and Park¹³⁵ and the work by Sulka¹³⁶. In brief, morphology of porous AAO depends most strongly on anodizing potential and type of electrolyte. The interpore distance and pore size of porous AAO were observed to be directly proportional to the anodizing potential.^{137,138} The pore size is also affected by the pH value in the solution¹³⁹ – pore size decreases with decreasing pH (or increasing electrolyte concentration). Further, elevated temperature and/or increased anodization time tend to increase the pore diameter due to enhanced chemical dissolution of oxide.¹⁴⁰ By selecting the appropriate anodizing potential and electrolyte, self-ordered hexagonal pore arrays with pore size ranging from ~ 20–400 nm can be obtained

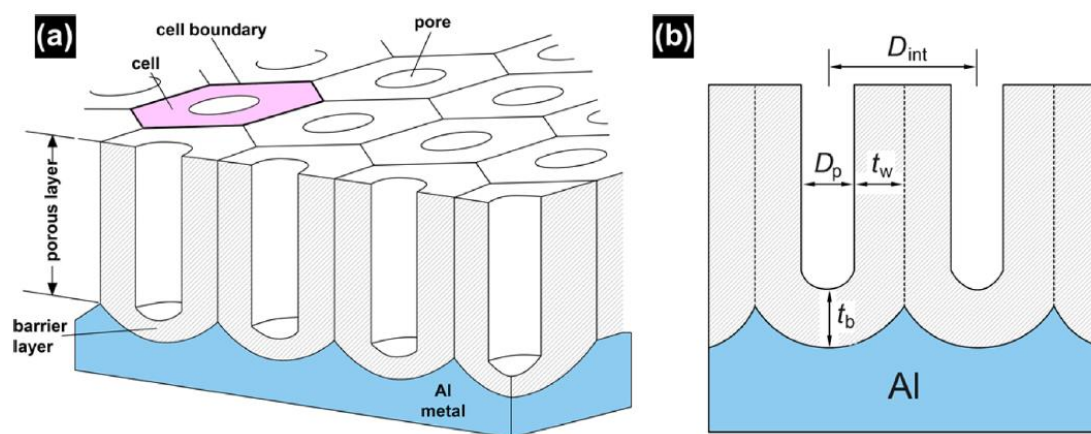


Figure 4.18: Schematic diagrams showing idealized structure of (a) porous anodic aluminum oxide (AAO) on Al foil and (b) cross-sectional view.

Porous AAO consists of a large number of mutually parallel pores forming a honeycomb-like structure. Each cylindrical nanopore and its surrounding oxide constitute a hexagonal cell aligned normal to the substrate surface. Each nanopore at the metal/oxide interface is closed by a thin barrier oxide layer with an approximately hemispherical morphology. The structure of porous AAO is often defined by several structural parameters illustrated in (b): inter-pore distance, D_{int} , pore diameter, D_p , pore wall thickness, t_w , and barrier layer thickness, t_b .

This figure adapted from: Lee, W.; Park, S.-J. S. S. Porous Anodic Aluminum Oxide: Anodization and Templated Synthesis of Functional Nanostructures. *Chem. Rev.* **2014**, *114* (15), 7487–7556.

by anodizing aluminum in various acidic solutions, including sulfuric, phosphoric, oxalic, and chromic acid.¹⁴¹⁻¹⁴³

The tunable and tightly-distributed pore size of AAO make it an attractive material to be incorporated with SHLHP to improve the performance. There are porous AAO films commercially available as filter membranes (e.g. Whatman Anodisc) with a variety of pore sizes. However, these commercial membranes are not suitable for integration with the device because 1) they exhibit large thickness values and show relatively non-uniform pore sizes and irregular geometries,¹⁴⁴ and 2) they come in a free-standing, well-packaged format which makes the bonding challenging. Fabricating porous AAO on bulk aluminum foils according to the conventional technique provides excellent flexibility and reliability of pore geometries, yet great care needs to be exercised in the manipulation of the free-standing AAO film^{145,146} and the subsequent bonding to the substrate¹⁴⁷, in particular with thin AAO film of thickness $\sim 1 \mu\text{m}$. Porous AAO grown with aluminum films that are deposited on foreign substrates (such as silicon or glass) would be appropriate to be incorporated with SHLHP. This convenient and practical method of fabricating an ordered, porous AAO thin film has been used by researchers to achieve a range of applications including pattern transfer¹⁴⁸, templated synthesis of nanowires¹⁴⁹, and biomolecule separation¹⁴⁴.

Process flow. Here, I report a viable method to fabricate thin porous AAO membrane directly on top of the silicon membrane either to reinforce the nanoporous layer and improve the performance of existing silicon membrane, or to replace the nanoporous silicon layer and serve as the active layer for SHLHP membranes. Figure 4.19 shows the process flow for the porous AAO-integrated SHLHP device. Note that shown here is AAO fabricated on multilayer porous silicon membranes and replacing the nanoporous silicon top layer, yet porous AAO can potentially be integrated onto devices of other silicon membrane geometries. The process is similar to that of the

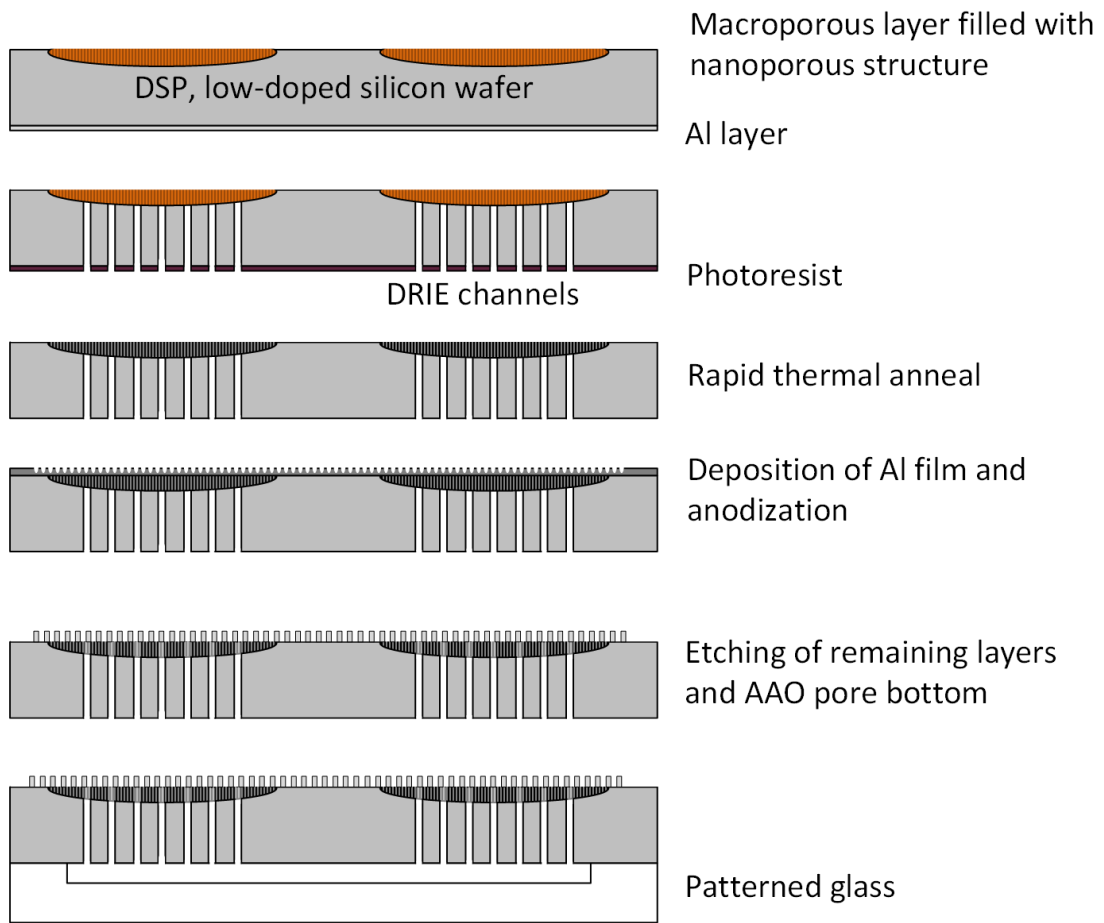


Figure 4.19: Process flow for AAO-integrated SHLHP prototype with multi-layer porous silicon membranes.

multilayer membrane, except for adding the Al deposition and anodization, and removal of the AAO barrier layer.

Silicon wafers were MOS cleaned and then anodized at the front side to anodize the macroporous silicon layer of $\sim 100 \mu\text{m}$ with 3:87:10 (v/v/v) solution of 48% HF, acetonitrile and 98% AA, constant current density of 6 mA/cm^2 . The backside of the wafer was patterned with standard photolithographic techniques to define DRIE channel openings and then etched with DRIE tool (Unaxis UN770) until channels reaches the bottom of the porous silicon membrane (please refer to Section 4.3.3 for more details). After DRIE, the remaining photoresist was stripped. The wafers were annealed (RTA AG610) to fully oxidize the nanoporous silicon. The front side of the silicon was oxygen-cleaned (Yes Asher) and deposited with silicon oxide insulation layer of $\sim 800 \text{ nm}$ (Oxford PECVD). Titanium and aluminum films of $\sim 20 \text{ nm}$ and $1.2 \mu\text{m}$ respectively were then sputtered on the front side; the titanium film was deposited to enhance the adhesion between the aluminum film and the silicon oxide surface.¹⁴⁴ The aluminum film was anodized using the home-made electrochemical cell (Figure 4.2(A)) with an alligator clip connecting the aluminum film to the power supply. Anodization was done with H_2SO_4 20 wt% in water, constant voltage of 19 V for 5 minutes. Vapor HF etcher (Primaxx) was used to cleared the nanoporous filling in the macropore from the DRIE side. A plasma etch¹⁴⁴ or ion-milling¹⁵⁰ can be used to remove the silicon oxide layer and AAO pore bottom.

Results and discussion. In Figure 4.20(A) and (B) are shown SEM images of the top and cross-sectional views of the porous AAO membrane. From the top view, the pore diameter is $\sim 10\text{--}25 \text{ nm}$; compared to the top view of nanoporous silicon, pore in AAO exhibits a more circular and smooth shape. From the cross-sectional view, the porous AAO shows distinct, parallel pore channels of width $\sim 20\text{--}25 \text{ nm}$. Figure 4.20(C) illustrates the stacking of the porous AAO, the silicon oxide insulation layer and the

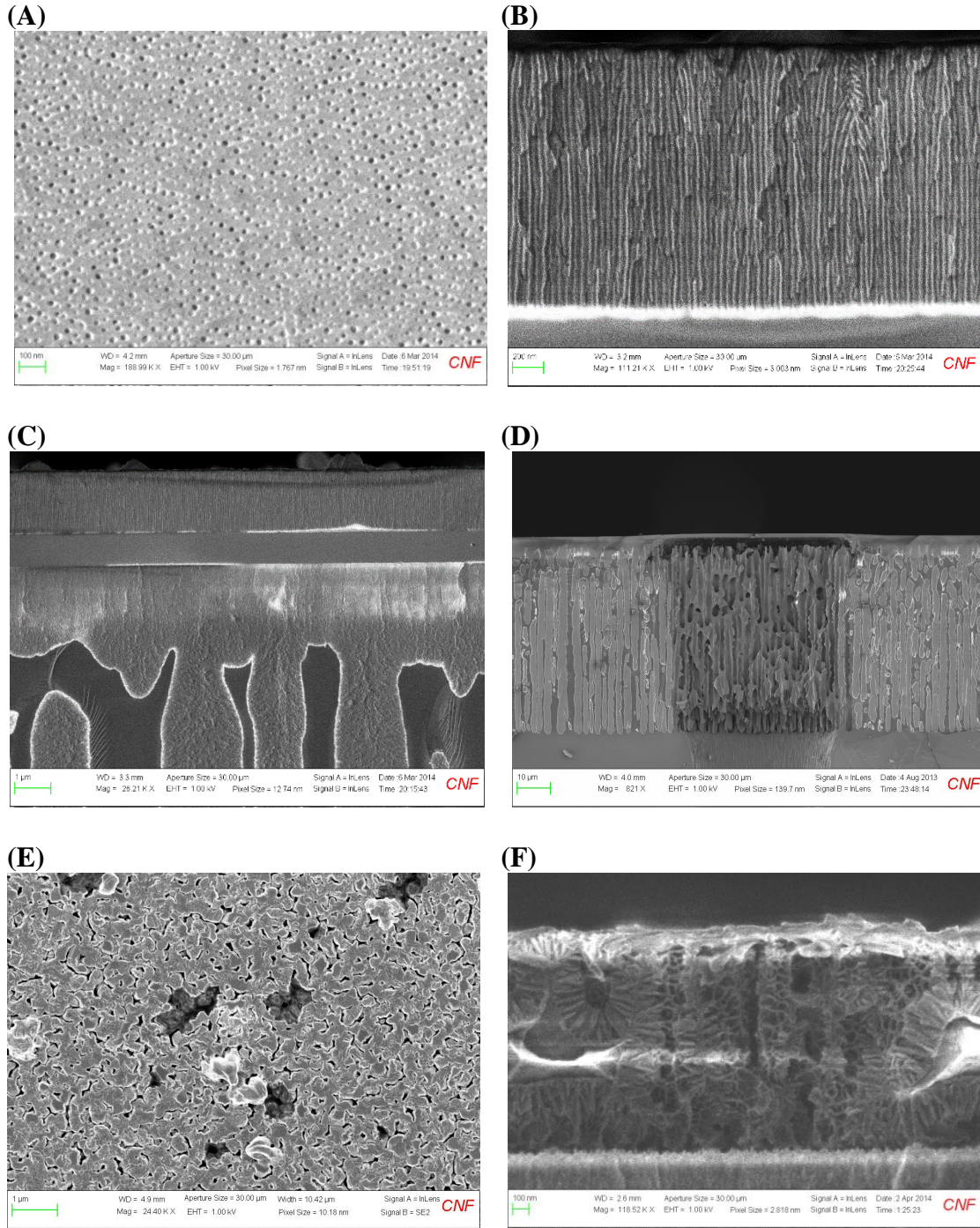


Figure 4.20: Top (A) and cross-sectional views (B-D) of the porous AAO-integrated multilayer silicon membranes taken by scanning electron microscopy (SEM). (E) Top view of a sputtered aluminum film with large grain size and the porous AAO membrane formed with it (F).

macroporous silicon layer (starting from top). The AAO thickness increased from ~ 1 μm of as-sputtered aluminum to ~ 1.7 μm due to the density difference between aluminum and alumina. There was no nanoporous layer anodized during the process, however, as shown in Figure 4.20(C), the silicon macropore layer exhibits a nucleation layer of ~ 1 μm .

While porous AAO membrane provides more orderly arranged pores and tightly-distributed channel width, there are challenges associated with AAO-integrated SHLHP device. For devices fabricated using the process flow presented in Figure 4.19, in order to open up the AAO channel bottom, the nucleation layer and the silicon oxide layer were entirely removed. The thin porous AAO layer is suspended over the macropore layer with a gap of ~ 3 μm in between, as shown in Figure 4.20(D). When the liquid in the device is placed tension, this unsupported configuration of the AAO potentially results in deformation and breakdown of the film. To mitigate this problem, the substrate underneath the AAO film has to stay intact; alternative methods¹⁴⁹ to remove the barrier layer should be further investigated.

Another challenge is that the AAO film with ordered, vertical, parallel pore arrays is formed pending good aluminum film quality. Figure 4.20(E) shows the top view of an as-sputtered aluminum film; this particular sample exhibits a rough surface with hills and valleys of length scale \sim film thickness. AAO membrane anodized from such film shows irregular pore initiation and channel clusters, as well as some un-etched aluminum islands enclosed in the membrane, as shown in Figure 4.20(F). To improve the aluminum film quality, one should go for depositing a thicker aluminum film and electrochemically polishing the film before anodization¹⁴⁹. Further, to achieve a better degree of AAO pore ordering, a conventional two-step anodization may be performed; this procedure has been shown to improve the self-organization of the pore channels in AAO and increase the permeability of the membrane.¹⁵¹ Thin film aluminum can also

be holographically patterned to manipulate and guide the initial pore nucleation,¹⁵² and hence achieving a better ordered pore array.

In conclusion, while porous AAO membrane provides a better membrane quality and requires not as much precise control of the etch rate and uniformity as for multilayer silicon membrane, there are challenges to be resolved before it can be exploited in a SHLHP. Nevertheless, porous AAO is a versatile thin film porous material that can be utilized in a range of study, such as nucleation phenomenon of supercooled liquid in porous materials, a topic currently pursued in our laboratory.

4.6.2 Graphene oxide membrane

Graphene-based materials have attracted significant attention over the past two decades due to the excellent physical, electrical, mechanical and transport properties that people predicted them to possess.^{153,154} Among graphene derivatives, graphene oxide (GO) membrane, a paper-like material consisting of layers of individual graphene oxide sheets of micron-size^{155,156}, is reported to exhibit great stiffness, strength, flexibility, biocompatibility, as well as chemical tenability.^{155–158} Hence, this free-standing, laminate material presents a versatile and promising candidate for an array of applications, including barrier films¹⁵⁹, dielectric materials¹⁶⁰, and nanoelectromechanical (NEMS) systems¹⁶¹.

Our proposal to integrate GO membranes with SHLHP was inspired by the reported “unimpeded” permeation of water through GO membrane: the GO membranes studied by Nair *et al.*¹⁵⁹ were observed to be impermeable to liquids, vapors and gases, yet allow water to wick through at a rate 10^{10} times faster than helium gas; permeability measurements through their GO membranes are shown in Figure 4.21(A). Nair *et al.*¹⁵⁹ attributed this observation to the two-dimensional nanocapillary network formed between stacked platelets of graphene oxide sheets (see Figure 4.21(B)), through which

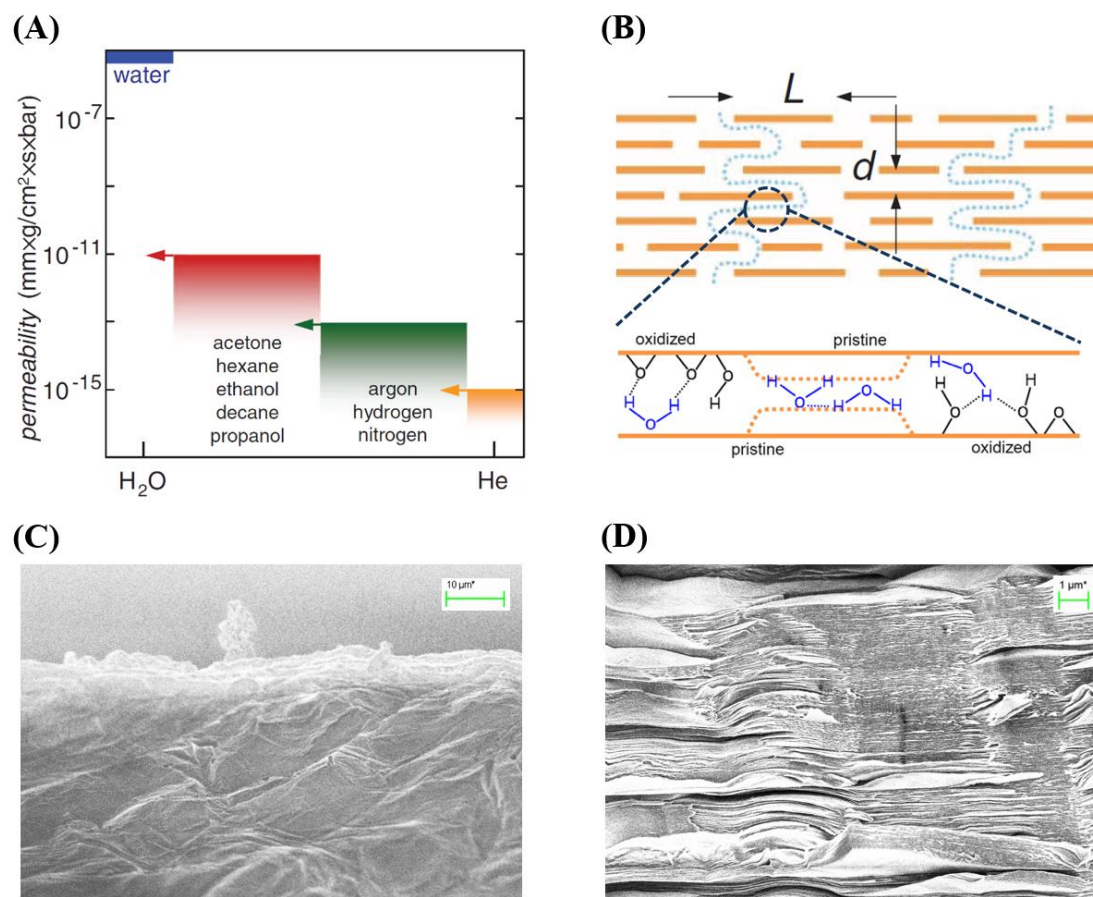


Figure 4.21: (A) Permeability of GO membrane with respect to water and various small molecules. (B) Schematic view for possible permeation of water molecules through the laminates. (C-D) Top and cross-sectional views of the GO membrane taken by scanning electron microscopy (SEM).

(A) and (B) adapted from: Nair, R. R.; Wu, H. a.; Jayaram, P. N.; Grigorieva, I. V.; Geim, a. K. Unimpeded Permeation of Water Through Helium-Leak-Tight Graphene-Based Membranes. *Science* **2012**, 335 (6067), 442–444.

monolayers of water can flow with low friction. The spacing between two adjacent parallel graphene oxide sheets, $d \sim 0.5\text{--}1$ nm, is kept by the oxidized region with functional groups attached to graphene sheets serving as spacers. This remarkably high permeability of GO membrane to liquid water, combined with its strength and flexibility, could potentially make GO membrane an excellent candidate to be incorporated with SHLHP to provide the required Laplace pressure while creating minimal pressure drop across the wick.

To assess the feasibility of GO membranes integrated with SHLHP prototype, I performed preliminary experiments to estimate the permeability of GO membrane and its bonding characteristics. Hummers method¹⁶², a chemical conversion from graphite, was employed to synthesize graphitic oxide that was dispersed in water or methanol, followed by sonication and centrifugation to obtain the supernatant – stable colloidal suspension of individual graphene oxide sheets. GO membrane was then produced by filtration of the supernatant through an Anodisc filter (Whatman, 47 mm in diameter, 0.2 μm pore size), followed by drying in air and peeling from the filter membrane. The thickness of the GO membrane was controlled by adjusting the volume of supernatant to be filtered. Figure 4.21(C) and (D) show the SEM images of our GO membrane; the membrane cross-sectional view reveals the well-packed, layered structure while top view shows the wavy skin layer.

First, the weight loss experiment conducted by Nair *et al.*¹⁵⁹ was repeated in our lab to evaluate the GO membrane as barrier for water and for ethanol; the results were qualitatively comparable – while no weight loss was observed with ethanol, the evaporation rate of water through the GO membrane was practically the same as in free evaporation through open aperture. When immersed in water, GO membranes would readily dissolve; to cross-link the graphene oxide platelets and prevent dissolution, branched polyethylenimine (bPEI, Sigma Aldrich, $M_w \sim 25000$) coupled with EDC-

NHS solution (EDC, 1-ethyl-3-(3-dimethylaminopropyl) carbodiimide, 30mg/mL; NHS, N-hydroxysuccinimide, 5 mg/mL) in phosphate buffer was used to modify premade GO membranes. The solution was passed through the still wet GO membrane following the initial filtration of graphene oxide supernatant. After drying, these bPEI-modified GO membranes exhibited increased thickness of ~ two fold compared to the original membranes, and the SEM images of the side view showed the maintenance of the stacked laminate structure. However, while this treatment did render the GO membrane to become insoluble and stable in water, the permeability of the membrane dropped dramatically.

To practically exploit GO membrane on a SHLHP, a further investigation on chemical modifications of GO must be performed to develop cross-linked GO membrane that is stable in solvent while possesses the high permeability to water as of its parent GO membrane. A potential cross-linking procedure may be adding the crosslinker (e.g., PEI¹⁶³, polyallylamine¹⁶⁴, or metal ions¹⁶⁵) to the supernatant of graphene oxide sheets and creating a uniform colloidal suspension for filtration; a challenge of this procedure would be to reduce the flocculation of graphene oxide sheets.¹⁶⁴ Further, one may consider depositing large area GO films directly onto the device surface to mitigate the complexities associated with bonding premade GO membranes to the substrate¹⁶¹.

4.6.3 Other potential candidates

Polyelectrolyte multilayer membrane. Polyelectrolyte multilayer (PEM) membranes are thin films composed of many bi-layers of oppositely charged polyelectrolytes – polymers with charged or chargeable groups within their monomer repeat units. PEM membranes formed by layer-by-layer (LBL) assembly has been studied extensively over the last two decades due to its simplicity, the versatility of

choosing over a variety of polyelectrolyte pairs, and the nanometer range thickness control.^{166,167} LBL method involves alternating adsorption of polycations and polyanions on a charged surface, followed by a rinsing step after each adsorption to remove excess polymer chains. LBL can be done under static (dip coating) or dynamic (filtrating the polyanion and polycation alternatively) conditions^{168,169}; the process to form one bi-layer of polyelectrolyte pair is illustrated in Figure 4.22.

PEM membranes have been exploited in a number of different material systems, such as solid-state electrolytes^{170,171}, nanomechanical thin films¹⁷², as well as separation science, including nanofiltration¹⁷³, forward osmosis¹⁷⁴, reverse osmosis¹⁷⁵ and pervaporation^{176,177}. Both the versatile thickness control and the successful application of PEM as perm-selective membranes make this material seem promising to be incorporated with SHLHPs to improve its ability to hold tension. To evaluate the feasibility of PEM modification of porous silicon membrane, I performed preliminary tests. Figure 4.23 compares the survival probabilities of a device bonded to glass etched with individual voids before and after PEM coating. The PEM membrane used in the tests consisted of 5 bilayers of PAA/bPEI (PAA, polyacrylicacid, Sigma Aldrich, $M_v \sim 450000$, 0.05 wt% in water; bPEI, Sigma Aldrich, $M_w \sim 25000$, 0.25 wt% in ethanol). Dipping time of the porous silicon membrane in the individual solutions was 20 minutes; between each dip, the membrane surface was rinsed with water for 3 minutes. After the deposition of the 5 polyelectrolyte bilayers, the membrane was dried with air. As shown in Figure 4.23, after PEM coating the survival probability of the device increased from $\sim 80\%$ to $\sim 89\%$. Similar results were obtained with SHLHP devices: PEM coated devices exhibited higher survival probabilities compared to the devices before coating subjected to the same vapor activity for the same amount of time. However, the maximum tension a device could sustain did not improve given the equilibration time

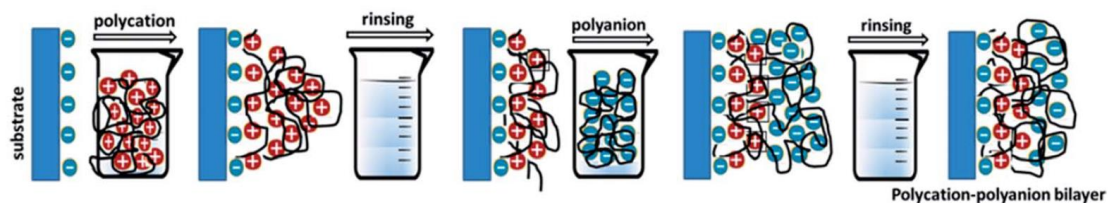


Figure 4.22: Static layer by layer assembly method to form polyelectrolyte multilayer membranes.

The LBL method involves alternating sequential adsorption of polycations and polyanions on a charged surface, followed by a rinsing step after each adsorption to remove weakly associated polymer chains.

This figure adapted from: Joseph, N.; Ahmadiannamini, P.; Hoogenboom, R.; Vankelecom, I. F. J. Layer-by-Layer Preparation of Polyelectrolyte Multilayer Membranes for Separation. *Polym. Chem.* **2014**, 5 (6), 1817–1831.

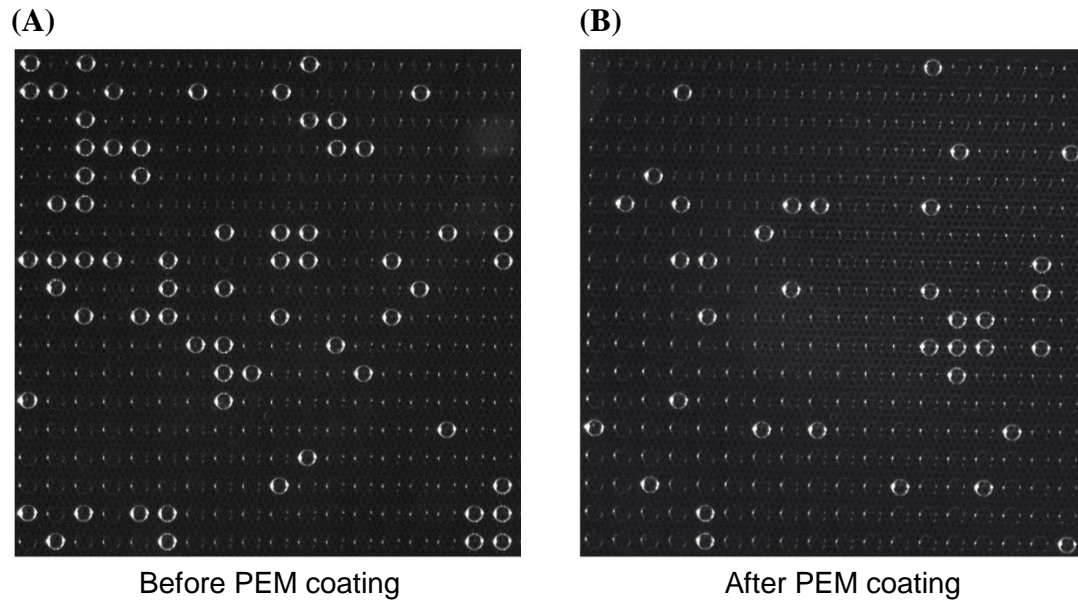


Figure 4.23: Device images (top view) during stability tests of the two-layer membrane bonded to glass substrate etched with individual voids before (A) and after (B) PEM coating.

The device was subjected to a relative humidity of $\sim 94.9\%$ ($P_{liq} \sim -7.2$ MPa) at room temperature for ~ 5 days. The survival probability before PEM coating (A) was 79.6%; after coating (B), 88.9%.

was long enough. With only 5 bilayers, the tests to evaluate the ability of PEM membrane improving the membrane performance were not clear and inconclusive.

In brief, the preliminary tests showed that PEM membrane is compatible with porous silicon devices: good adhesion, stable in water, robust enough for bonding and filling process (pressurization). Nevertheless, PEM membrane with more bilayers may be required to fully amend the defects and to improve the stability. In addition, by carefully choosing the polyelectrolyte pair, PEM membrane can be utilized to achieve selective ion transport;^{178,179} this characteristic coupled with SHLHP functionalities may allow the device to transport mass when subjected to different osmolalities.

Nanoporous carbon/zeolite membrane. Carbide-derived nanoporous carbon^{180,181} and zeolite^{182,183} are both nanomaterials that have been shown to be able to form continuous thin film active layers after coated or deposited onto macroscopic supports. The advantage of these materials include the temperature stability compared to polymer membranes, and that the pore size in these materials can be fine-tuned with sub-nanometer precision. These advantages render the nanoporous carbon and zeolite potential candidates to be integrated with macroporous silicon structure or as ultrathin films covering defected nanoporous silicon to achieve maximum Laplace pressure of the wick membrane.

4.7 Conclusions

In this chapter, three designs are proposed for MEMS-based, microscale SHLHP prototypes. As preliminary characterizations of the KOH cavities and the multilayer designs revealed foreseeable challenges and complexities, the first SHLHP prototype was fabricated based on the two-layer silicon membrane design. Model analysis and experiments were carried out to characterize the two-layer membrane; the membrane

was able to sustain a cavitation pressure, $P_{cav} \sim -27$ MPa at 15°C when bonded to individual voids etched in glass.

Based on the two-layer membrane prototype form factor, an experimental system to study SHLHP performances is designed and introduced. This system enables both the open-loop evaporator characterizations and the closed loop SHLHP realization. This system can potentially be utilized for studying other applications, including thin film evaporation¹⁸⁴ and osmotic membrane processes¹⁸⁵. These directions are currently being pursued in our laboratory.

CHAPTER 5

SUMMARY AND CONCLUSIONS

As discussed in Chapter 1, while plants exploit liquid water at negative pressure to remain hydrated in their daily lives, the properties of such metastable state of water are largely unknown to us, and the use of water at significant negative pressure is not found in current human technologies. “If plants can do it, why don’t we?” This dissertation aims at answering part of this question by dealing with both the open questions regarding fundamental thermodynamics of water at negative pressure, and the development of its application in heat transfer – the design, modeling, fabrication, and experimental testing of plant-mimetic loop heat pipes exploiting working fluid at negative pressure. In Section 5.1, I summarize the study regarding the stability limit of water, including the report on a new experimental system and the results of temperature-dependence of the stability limit with the metastable vapor-liquid equilibrium (MVLE) method. Paralleled to the fundamental study, the efforts on the development – both theoretical models and experimental platforms – of superheated loop heat pipe are summarized in Section 5.2. Finally, in Section 5.3, I conclude the dissertation with a discussion on the outlook of technologies exploiting plant-mimetic generation of liquid at negative pressure.

5.1 Summary of Study Regarding Stability Limits of Water under Tension

Among many open questions regarding water at negative pressure, recent experiments have questioned the exact value of the stability limit of water, as well as its temperature-dependence; I described this stability limit debate in details in Section 1.1

and Chapter 3. Studying the stability limit of water is not only of fundamental science interest, but also essential to the developments of technological applications of negative pressure water. In Chapter 3, I reported the experimental platform which combines free-standing porous silicon-glass void samples and a vacuum control system to overcome the challenges encountered in the previous system in our lab (hydrogel/salt solution), enabling the study of temperature-dependence of stability limit of water with MVLE in silicon-based devices. The stability limit measured lies within the range of -20 MPa to -30 MPa, and is monotonically increasing (more negative) as temperature approaches 0°C; this trend contradicts the famous results of Briggs¹⁰ but agrees with the experiments by acoustic cavitation²⁴. This result confirms that a static method (i.e. MVLE) can reach stability values similar to the dynamic stretching technique (i.e. the acoustic method), even close to 0°C. I also note that, our synthetic experimental platform seems to provide accurate description of the mechanism by which cavitation happens in tree; both value and the temperature-dependence of the stability limit are compatible with those record in tree species.²⁵

Nevertheless, the measured stability limit (maximum tension) by MVLE in a porous silicon sample is far less negative than the limit predicted by both thermodynamic and kinetic calculations and measurements with Berthelot-tube like methods. A nearly ubiquitous cavitation mechanism is yet to be identified that imposes the highly reproducible values of stability limit stuck at -20 to -30 MPa found with a variety of different techniques. Indeed, our current experimental system involves many uncertainties and complexities in terms of interpreting the cavitation mechanisms. Greater care should be taken to avoid or identify sources of heterogeneous nucleation, especially the presence of hydrophobic patches, to provide a more convincing report of cavitation mechanisms and potentially extend the maximum tension achievable in

MVLE systems. Also, further study should be pursued to understand the physics and dynamics involved in the MVLE systems, such as the Kelvin limit to tension at the vapor-liquid menisci³³ and the effects of metastability in porous media¹⁸⁶.

5.2 Summary of Modeling and Experimental Work for Superheated Loop Heat Pipe

While passive liquid phase change-based heat transport systems (heat pipes and loop heat pipes) have found widespread use in many fields, limitations on their operations constrains their performance in particular on larger format platforms, e.g. cooling of avionics and energy management in buildings. As I detailed in Section 1.3 and 2.2, the phase change diagram of the two-phase working fluid in the device flow loop imposes two important operational requirements – the motive temperature head condition and the subcooling condition; these conditions result from the two coupled vapor-liquid menisci at (or close to) saturation and the parasitic heat flow from the heat source to the liquid compensation chamber. To mitigate the limitations imposed by these requirements, I proposed a superheated loop heat pipe (SHLHP). Inspired by trees, the design concept of SHLHP consists in utilizing the negative pressure in liquid to cycle the fluid in the loop, instead of building up high saturation pressure difference (and hence the coupled temperature head) to drive the fluid motion, as in conventional LHPs.

In Chapter 2, I presented a detailed theoretical analysis of the coupled transport and thermodynamic phenomena in SHLHPs. The unified numerical steady-state model proposed for both conventional LHP and SHLHP can predict and compare the operational characteristics of the two devices, and the analytical expressions for effective resistances provide a valuable basis for the design of these systems. My analysis indicates that large hydraulic resistances and large adverse accelerations have negligible impact on the total resistance, such that SHLHPs could be particularly

valuable where heat must be transferred over large distances and against gravity or acceleration. Further, without the subcooling condition, SHLHP design could be valuable where parasitic heat flow is the main hindrance to device operation, e.g. high-heat-flux thermal management in electronic systems¹³². For future works, a dynamic model for SHLHP is needed to understand the behavior of startup and shutdown periods and its reaction to abrupt power changes during operation. The lumped parameter analysis as described in Appendix A.1 is able to predict the time constant for the system to reach its steady state, yet a more comprehensive model including all pipe elements and the essential physical processes is required to capture the complex heat and mass transfer coupling between loop elements (e.g. the dynamics of menisci within the wick), as well as cavitation or other events that lead to dry-out.

In Chapter 4, I presented silicon-based designs of a microscale SHLHP to pursue proof-of-concept experiments. These SHLHP prototypes exploit porous silicon; this versatile nanoporous material is compatible with standard microfabrication techniques, possessing preferred hydrophilic surface and tunable porosity and pore structure, and allows for integration with other materials and packaging techniques. I reviewed the formation and structural properties of porous silicon as well as experimental results on the effect of etching parameters on porous silicon in Section 4.2 and Section 4.4, respectively. The essential part of designing a SHLHP is the configuration coupling the nanoporous silicon to the liquid paths; I dealt with the fabrication processes and experimental characterizations of several prototype configurations in Section 4.3 and 4.4. Based on the two-layer membrane prototype form factor, I designed an experimental system to study SHLHP performances. As introduced in Section 4.5, this system performs open-loop tests to characterize the startup and steady state evaporation characteristics and the dry-out criteria, and the closed-loop operation to demonstrate

steady state functions of a SHLHP prototype (e.g. operating curves as functions of the regulator activity and/or the heat sink temperature).

The experimental realization of SHLHPs encountered several challenges. First of all, due to DRIE etching limitations (e.g., etch rate, resist selectivity, etc.) the current fabrication process is lengthy and exhibits variations from batch to batch. A simplified standard operation procedure should be developed to achieve better yield and reproducible device structure. A more critical challenge (and the most frustrating part) is that, once integrated into wick structures, membranes fabricated following the same recipe and procedure were not able to sustain as high tension as in membrane bonded with independent voids. A few directions may be looked into to solve this problem: 1) modifying the device configuration to further branch the liquid path network (see Appendix A.4 for an example) and, again by following the example of plants, adding compartments within liquid paths to isolate cavitation from single membrane defect, 2) investigating the correlation between cavitation events and the geometry of liquid paths to identify and minimize potential causes of cavitation in SHLHP devices, e.g. mechanical disturbances, bonding qualities, etc., and 3) improving the nanoporous membrane functionalities (i.e., tighter pore size distribution, lower hydraulic resistance, better mechanical strength, etc.) by optimizing anodization parameters for porous silicon or incorporating other nanoporous materials. For the latter, a few promising candidate materials were tested and discussed in Section 4.6, yet further work is needed to finalize the integration of these nanomaterials with SHLHP devices.

5.3 Speculation on the Future of Technologies Exploiting Liquid at Negative Pressure

Above all, to exploit liquid at negative pressure in technologies, it is essential to improve our understanding of metastable liquids and our ability to manipulate them. Let aside the debate over the origin of water anomalies, being able to better answer outstanding questions related to the kinetic stability limit of water would be the basis of developing technologies exploiting water and/or other liquids under tension. Exploring the phase diagram of water is not only a fundamental science interest, but also helps us to gain access to parts of the phase diagram never exploited by human.

The theoretical analysis strongly suggests that the SHLHP could be a promising heat transfer system especially in electronics cooling, building-scale heat management or military vehicles and space mission, yet there are certainly technological challenges to realize this technology. As I addressed in this dissertation, optimization of transport properties of loop elements (in particular the wick membranes) and the suppression of cavitation in the superheated liquid are the first steps for a functional SHLHP. On top of that, the development of means to reconnect the transport paths if cavitation does occur would be a more critical step towards a high-performance and robust SHLHP. While plant physiology can surely provide significant insight into the development of refilling techniques, inspirations based on other physics may be equally important to discover effective and practical refilling mechanisms (e.g. electroosmotic refilling). Beyond proof-of-concept experiments, the scaling up of SHLHP technology is a whole new story and may present even more challenges and pitfalls – device filling and packaging, integration with existing infrastructure, etc. The choice of suitable materials (e.g. porous glass) and the invention of new designs would pave the road for realization

of this application in our daily lives. Lastly, perhaps the most difficult part in the future of SHLHP technology would be to convince people to attempt (or just to consider) this proposal; providing the world with exceptionally rigorous and detailed study to communicate effectively and clearly our ideas is the key.

In the review by Stroock *et al.* in 2014³⁴, the authors asked two questions provoked by the dramatically progressed understanding of the vascular physiology of plants over the past few decades: *Why do human technologies not use liquids under tension? Why do humans not exploit differences in osmolality to manage local differences in pressure within materials and transport systems?* For the former, the SHLHP could be the first step with respect to heat transfer technologies. Extended from here lie opportunities with respect to mass transfer technologies – open loop SHLHP configuration is essentially a synthetic tree-in-a-pipe, with relevance to applications such as irrigation system management¹⁸⁷ or water extraction and long-term transportation for arid environments. For the latter, nanoporous membrane integrated with selective functionalizations (e.g. functional polyelectrolyte multilayer or block copolymer-derived membranes) may allow for studies on osmotically generated tension in transport systems, and subsequently manipulation of chemical properties of solvents under tension and passively controlled transportation between local regions subjected to different osmolalities. A simplest experiment to start can be measuring solvent mass transport between salt solutions of different osmolalities. These studies may provide new insight in to applications such as long-term drug delivery, nano-liquid chromatography, forward osmosis in water purification or desalination, conversion enhancement in reactors, and so on. Undoubtedly, tremendous efforts is required before we can transform these ideas from interesting and intriguing ones to critical and practical ones, nevertheless I am confident that the concepts and building tools

presented in this dissertation (as well as in other works of our laboratory) are serving as the step stones.

APPENDIX

A.1 Lumped Parameter Analysis for SHLHP Startup Response

Chapter 2 presents a mathematical model which analyzes the steady state operation of SHLHPs – the model is constructed by accessing heat and momentum balances and the condition of local equilibrium between the liquid and vapor phases, and then applying the limit of small rates of heat transfer that the system has linear responses to obtain effective thermal resistances. In this section, a simple approach is proposed to study the non-steady state performance of SHLHPs. Based on the steady state model, lumped capacitance analysis is used to approximate the non-steady state behavior by defining effective thermal capacitances and further describe the whole system by an analogous circuit. The time required for the system to reach its steady state can then be estimated.

A.1.1 Mathematical model

For non-steady state analysis, we assume that before operation, the temperature throughout the SHPHP is uniform and is set by the temperature in the liquid cavities in the condenser, T_0 ; the pressure in the liquid path is controlled by the regulation chamber and the vapor pressure in the vapor path is in equilibrium with the liquid over wick membrane menisci. A heat source is suddenly applied to the evaporator and starts to increase the temperatures and alter the pressures of the system.

An overall heat balance of the liquid cavity in evaporator yields:

$$0 = q_i - \frac{(T_e^{liq} - T_e^{vap})}{R_{wick,e}} - QC_p^{liq} (T_e^{liq} - T_c^{liq}) - \sum^{e,liq} (\rho CV) \frac{dT_e^{liq}}{dt} \quad (A.1)$$

an overall heat balance of the vapor cavity in evaporator yields:

$$0 = \frac{(T_e^{liq} - T_e^{vap})}{R_{wick,e}} - Q\lambda - \sum^{e,vap} (\rho CV) \frac{dT_e^{vap}}{dt} \quad (A.2)$$

and an overall heat balance of the vapor cavity in condenser yields:

$$0 = Q\lambda + QC_p^{vap} (T_e^{vap} - T_c^{vap}) - \frac{(T_c^{vap} - T_0)}{R_{wick,c}} - \sum^{c,vap} (\rho CV) \frac{dT_c^{vap}}{dt} \quad (A.3)$$

The temperature in the liquid cavity in condenser is always kept at a constant, T_0 ; therefore, there is no additional balance equation required for it.

A.1.2 Results and discussion

Effective thermal capacitances. In the loop system of SHPHPs, the temperatures of various components do not change uniformly, so we should complete transient lumped analyses for each component separately⁴⁹. Neglecting sensible heat in Eq. (A.1) and Eq. (A.3), we can find that all the governing equations for non-steady state heat balances (Eq. (A.1), (A.2), and (A.3)) are analogous to a RC circuit in which the resistor and the capacitor are in parallel and the input signal is fed by a current source,

$$I = C \frac{dV}{dt} + \frac{V}{R} \quad (\text{A.4})$$

Accordingly, we can simply define the effective thermal capacitance of the evaporator,

$$C_e = \sum^{e,liq} (\rho CV) = \frac{1}{2} \rho_{liq} C_p^{liq} V_{liq} + \frac{1}{2} \rho_{liq} C_p^{liq} V_{wick} \phi + \frac{1}{2} \rho_{si} C_{si} V_{wick} (1-\phi) \quad (\text{A.5})$$

the effective thermal capacitance of the vapor path,

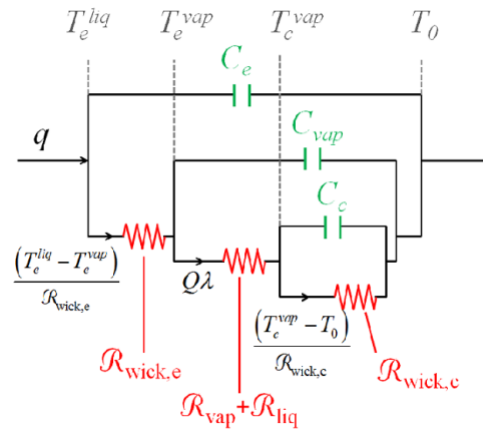
$$C_{vap} = \sum^{e,vap} (\rho CV) = \frac{1}{2} \rho_{vap} C_p^{vap} V_{vap} + \frac{1}{2} \rho_{liq} C_p^{liq} V_{wick} \phi + \frac{1}{2} \rho_{si} C_{si} V_{wick} (1-\phi) \quad (\text{A.6})$$

and the effective thermal capacitance of the condenser,

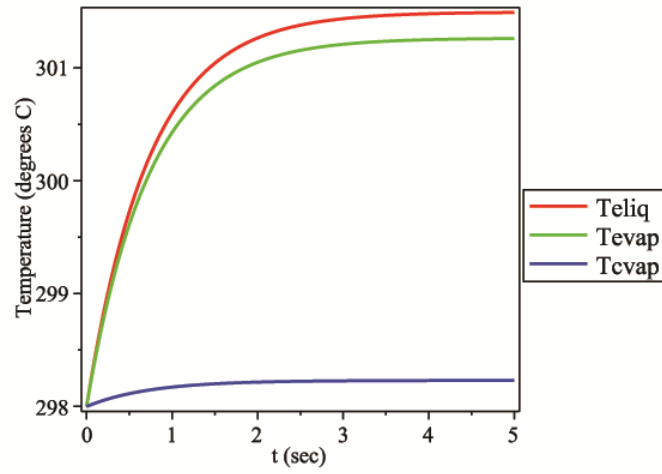
$$C_c = \sum^{c,vap} (\rho CV) = \frac{1}{2} \rho_{vap} C_p^{vap} V_{vap} + \frac{1}{2} \rho_{liq} C_p^{liq} V_{wick} \phi + \frac{1}{2} \rho_{si} C_{si} V_{wick} (1-\phi) \quad (\text{A.7})$$

Figure A.1(a) is the schematic diagram of an analogous circuit of a SHLHP. By substituting the values of R_{eff} 's and C_{eff} 's into the analogous circuit and solving the nonhomogeneous linear ODEs, we can get the temperature profiles at the startup period of a SHPHP. Figure A.1(b) and (c) presents the transient variations of temperatures of a SHPHP operating with water and $T_0 = 298$ K. Transient temperature variation shows an exponential trend and reaches the steady state very fast.

(a)



(b)



(c)

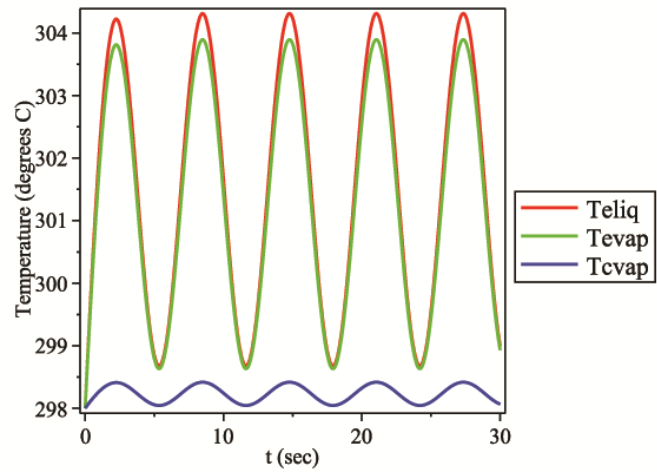


Figure A.1: (a) Analogous circuit of a SHPHP. (b-c) Transient temperature profiles for SHPHP as a function of time.

The heat applied to the SHPHP through the wall of the liquid side of evaporator builds up temperature rise of the evaporator and conducts through the wick to the vapor side, evaporating the working fluid into vapor. The vapor carrying heat gradually builds up the pressure variation (which reflecting in circuit is actually the temperature difference), and translates to the condenser, condensing and releasing latent heat. This latent heat builds up the temperature rise in the condenser and conducts through the wick, being taken away by the heat sink.

Parameters used in calculation were: 10 m-long, 5 nm-diameter pores in the wicks, and 10 g of the acceleration. In (b), a step input of $q_i=10 \text{ W/cm}^2$ was applied; in (c), a sinusoidal input of $q_i = 10[1 + \sin(t)] \text{ W/cm}^2$.

A.1.3 Conclusions

Using lumped parameter analysis we are able to model the non-steady state operations of a SHPHP. The results show that normal operation of the SHPHP could be achieved very fast after the heat input to the evaporator is suddenly applied (less than 5 seconds for parameters used). We should note that this method is effective under the limit of small heat flow (Eq. (2.43)) and small dependence of the density of working fluid on temperature. Nevertheless, under moderate operation temperature (around room temperature) and by choosing appropriate working fluid (such as water), we can conclude that the analytical expressions for effective thermal resistances and effective thermal capacitances presented here provide a valuable basis for the design of SHPHP systems.

A.2 Maple and Mathematica Scripts Used for SHLHP Modeling

This section publishes the original Maple and Mathematica scripts used for steady state calculations and the linear analysis presented in Chapter 2 (Maple), lumped parameter analysis presented in Section A.1 (Maple), as well as predicting steady state performance of SHLHP prototype presented in Section 4.4.3 (Mathematica).

A.2.1 Steady state calculations for conventional LHPs and SHLHPs (Maple)

```
> restart; with(plots); with(Statistics); with(RealDomain);

# Antoine's constants and material properties (SI units) for water

# Antoine parameters extracted from fit of saturation curve from NIST at 33 values between
273.16 and 593.16 K

> C0:=23.1953647696257 : C1:=3816.99213575208 : C2:=45.9240851812291 :

#p[sat]=e^(((C0-C1)/(T-C2)))

> ps0:=exp(C0-C1/(T0-C2)): dpdT0 := diff(exp(C0-C1/(T0-C2)), T0):
d2pdT20:=diff(diff(exp(C0-C1/(T0-C2)), T0),T0):

> p[esatTev]:= exp(C0-C1/((Tevap-C2))): # saturation pressure at evaporator
> p[csatTcv]:= exp(C0-C1/((Tcvap-C2))): # saturation pressure at condenser
> p[esatTel]:= exp(C0-C1/((Teliq-C2))): # saturation pressure at compensation chamber

# Temperature dependences of properties are based on data from NIST at 21 values between
273.16 and 473.16 . Fits over this range provide R-squared values >= 0.999.

> g:=10: # gravitational acceleration, m/(s^(2))
> R[gas]:=8.314472: # gas constant, J/(K.mol)
> MW:=18.015268*10^(-3): # molecular weight, kg/mole
```

> lambda:=(-1.65302E-05*T0^(3)+ 1.49098E-02 *T0^(2) - 6.86262E+00*T0^(1) +
 3.60026E+03)*10^(3): # latent heat of vaporization of water from difference in enthalpies of
 liquid at vapor, J/kg
 > Cpliq:=(4.12059E-14 *T0^(6) - 9.60454E-11 *T0^(5)+ 9.29777E-08*T0^(4)- 4.77994E-
 05*T0^(3) + 1.37625E-02*T0^(2) - 2.10454E+00 *T0^(1) + 1.37737E+02)*10^(3): # specific
 heat capacity of water, J/ (Kg*K)
 > rho[liq]:= -3.89737E-08 *T0^(4) + 6.26585E-05 *T0^(3) - 3.97984E-02*T0^(2) +
 1.09057E+01*T0^(1) - 6.95342E+01: # density of water, (kg)/(m^(3))
 > mu[liq]:= 4.11031790E-16*T0^(6) - 9.68082253E-13*T0^(5) + 9.47109629E-10*T0^(4) -
 4.92836995E-07*T0^(3) + 1.43938246E-04*T0^(2) - 2.23898176E-02*T0^(1) +
 1.45116063E+00: # viscosity of water, kg/(m.s) =Pa*s
 > vkin :=(mu[liq])/(rho[liq]): # kinematic viscosity of liquid water, m ^(2)/s
 > Vmolarliq:=MW/(rho[liq]): # molar volume of liquid, m ^(3)/mole
 > sigma:= -2.25306E-07*T0^(2) - 2.27104E-05*T0^(1) + 9.87545E-02: # surface tension of
 liquid water at RT, N/(m)
 > kw:= -5.70043E-13 *T0^(4) + 1.81825E-08*T0^(3) - 2.66229E-05*T0^(2) + 1.27391E-
 02*T0^(1) - 1.30089E+00: # thermal conductivity of water, W/(m.K)
 > Cpvap := (5.15950E-15*T0^(6) - 1.35114E-11*T0^(5) + 1.43051E-08*T0^(4) - 7.73466E-
 06*T0^(3) + 2.26362E-03 *T0^(2) - 3.41539E-01*T0^(1) + 2.26856E+01)*10^(3):
 # heat capacity of vapor, J/ (Kg*K)
 > rho[vap]:= 6.23591E-09*T0^(4)- 7.36047E-06 *T0^(3) + 3.30094E-03*T0^(2) - 6.65126E-01
 *T0^(1) + 5.06961E+01: # density of vapor, (kg)/(m^(3))
 > mu[vap]:= -1.67553E-13*T0^(3) + 2.06613E-10 *T0^(2) - 5.00277E-08*T0^(1) + 1.08661E-
 05:
 # viscosity of vapor, kg/(m.s)

```

> vsoundvap:= -3.46923E-06*T0^(3) + 2.31016E-03*T0^(2) + 2.34201E-01 *T0^(1) +
2.43375E+02: # speed of sound in saturated vapor; (m)/(s)
> ksi:=130: # thermal conductivity of Silicon, W/(m.K)

```

Antoine's constants and material properties for ammonia

```

# Antoine parameters extracted from fit of saturation curve from NIST at 14 values between
273 and 403 K for ammonia

```

```

> C0:=22.1003576: C1:=2185.987641: C2:=34.14474466: #p[sat]=e^(((C0-C1)/(T-C2)))
> ps0:=exp(C0-C1/(T0-C2)): dpdT0 := diff(exp(C0-C1/(T0-C2)), T0):
d2pdT2:=diff(diff(exp(C0-C1/(T0-C2)), T0),T0):
> p[esatTev]:= exp(C0-C1/((Tevap-C2))): # saturation pressure at evaporator
> p[csatTcv]:= exp(C0-C1/((Tcvap-C2))): # saturation pressure at condenser
> p[esatTel]:= exp(C0-C1/((Teliq-C2))): # saturation pressure at compensation chamber

```

```

# Temperature dependences of properties are based on data from NIST at 13 values between
273 and 393K for ammonia. Fits over this range provide R-squared values >= 0.999. (Cpliq
and Cpvap diverge as it comes close to the critical point. So only fits the curve up to 383K)

```

```

> g:=10:
> R[gas]:=8.314472:
> MW:=17.031*10^(-3): > lambda:=(-3.69071E-08*T0^(5) + 5.83378E-05*T0^(4) - 3.69036E-
02*T0^(3) + 1.16575E+01*T0^(2) - 1.84050E+03*T0^1 + 1.17675E+05)*10^(3):
> Cpliq:=(3.53998E-12*T0^(6) - 5.58078E-09*T0^(5) + 3.51552E-06*T0^(4) - 1.10557E-
03*T0^(3) + 1.73502E-01*T0^(2) - 1.08569E+01*T0^1 + 2.00000E+00)*10^(3):
> rho[liq]:= -9.43567E-07*T0^(4) + 1.16998E-03*T0^(3) - 5.46724E-01*T0^(2) +
1.12488E+02*T0^1 - 7.88787E+03:

```

```

> mu[liq]:= -3.64607E-11*T0^(3)+ 4.05351E-08*T0^(2) - 1.57502E-05*T0^ + 2.19076E-03:
> vkin :=(mu[liq])/(rho[liq]):
> Vmolarliq:=MW/(rho[liq]):
> sigma:= 6.96336E-07 *T0^(2) - 7.27677E-04*T0^ + 1.79811E-01:
> kw:= 1.56668E-06*T0^(2) - 3.75267E-03*T0^ + 1.46601E+00:
> Cpvap := ( 3.81196E-11*T0^(6) - 7.23404E-08*T0^(5) + 5.71332E-05*T0^(4) - 2.40330E-
02*T0^(3) + 5.67821E+00 *T0^(2) - 7.14390E+02*T0^ + 3.73900E+04)*10^(3):
> rho[vap]:= 9.58410E-07*T0^(4) - 1.19131E-03*T0^(3) + 5.57563E-01 *T0^(2) -
1.16101E+02 *T0^+ 9.06023E+03:
> mu[vap]:= 1.04541E-15 *T0^(5) - 1.65878E-12*T0^(4) + 1.05184E-09 *T0^(3) - 3.33042E-07
*T0^(2) + 5.26674E-05*T0^ - 3.32058E-03:
> vsoundvap:= -2.89481E-07*T0^(4) + 3.50685E-04 *T0^(3) - 1.65041E-01 *T0^(2) +
3.55991E+01 *T0^ - 2.54480E+03:
> ksi:=130:

```

Geometric parameters

```

> Pi:=3.14159265:
> A:=1e-4:           # area of porous wick = area of evaporator and condenser, m2
> phi:=0.6:         # pore fraction of porous wicks.
> Lcond:=10^(-2):   # length of condenser, m
> Dia[vap]:=6e-3:   # diameter of vapor path, m
> Dia[liq]:=1e-3:   # diameter of the liquid path, m
> Dia[pore1]:=2e-6: # diameter of pores in microporous layer 1, m
> L[pore1]:=3e-3:   # thickness of microporous layer 1, m
> Dia[pore2]:=20e-9: # diameter of pores in nano-porous layer 2, m

```

```

> L[pore2]:=2*10^(-6); # thickness of nano-porous layer 2, m
> Lsi:=L[pore1]+L[pore2]: # thickness of Silicon wafer m
> n[vap]:=1: # number of vapor conduits
> n[liq] :=1: # number of liquid conduits

# Hydraulic resistances
> R[vap]:=(128. L[pipe].mu[vap])/((PI.rho[vap].(Dia[vap])^(4))):
# resistance of vapor path, Pa/(kg/(s))
> R[liq ]:=(128. L[pipe].mu[liq])/((PI. rho[liq].(Dia[liq])^(4))):
# the resistance of the liquid path, Pa/(kg/(s))

# Calculating the wick section resistance. Two layers are in series. Layer 1 is the support
layer with larger pores and larger thickness. Layer 2 contains the pores that must support the
tension. The former terms are the number of pores.
> R[layer1 ]:=((phi.A)/(0.25* PI.(Dia[pore1])^(2)))^(-1).(128.
L[pore1]*mu[liq])/((PI.rho[liq].(Dia[pore1])^(4))):
# resistance of microporous wick structure, Pa/(kg/(s))
> R[layer2 ]:=((phi.A)/(0.25* PI.(Dia[pore2])^(2)))^(-1).(128.
L[pore2]*mu[liq])/((PI.rho[liq].(Dia[pore2])^(4))):
# resistance of nano-porous wick structure, Pa/(kg/(s))
> R[wick]:=R[layer1]+R[layer2]: # Maximum capillary pressure

> unassign('T0');
> Pmax[pore2]:=(4. sigma)/(Dia[pore2]*(1e5));
# maximum Laplace pressure the nano pore can sustain, bars
> Pmax[pore1]:=(4. sigma)/(Dia[pore1]*(1e5));

```

maximum Laplace pressure the micro pore can sustain, bars

Operational parameters for LHP

```
> qi := 10; Tsink := 273.15+25; L[pipe] := 10; ng := 1;
> T0 := Tsink; Dia[cond] := 4*10^(-3); W[F] := qi/lambda;
> if ng < 1 then gcond := 1 else gcond := ng end if;
> h := .76*(Dia[cond]^3*rho[liq]^2*gcond*(2*100*A/(PI*Dia[cond]))/(mu[liq]*W[F]))^(1/3);
> 100*A/(PI*Dia[cond]);           #condenser tube length
> T0 := qi/(100*h*A)+Tsink;       #estimated temperature of condensation (Tcvap)
> (. `(1/n[vap], R[vap]), qi)/lambda; # hydraulic pressure drop along vapor path
> R[liq]*qi/(n[liq]*lambda);     # hydraulic pressure drop along liquid path
> rho[liq]*ng*g*L[pipe];         # hydrostatic pressure drop along liquid path
> R[wick]*qi/lambda;             # hydraulic pressure drop through wick
> kwick := 13;
> Rw := Lsi/(A*((1-phi)*kwick+phi*kw));
> Rw*qi*Cpliq/lambda;
> (lambda/(Rw*qi*Cpliq+1))*(C1/(C0-
ln(ps0+R[liq]*qi/(n[liq]*lambda)+rho[liq]*ng*g*L[pipe]))+C2-T0); # approx. (Tevap-T0)
> 1/(100*h*A);                   # thermal resistance of condenser heat transfer
> unassign('T0');
298.15
Dia[cond] := 1/250
W[F] := 0.00000860225749825954
gcond :=1
h := 242.895712595936
```

```

0.795774716368782
302.266993212077
2.99211598212315
755.167695184853
59639.1128239900
5683.94516569140
R[w] := 5.47320309418381
0.229470723447633
9.14599909223037
0.411699321207669

```

Coupled heat, momentum and thermodynamic balances for LHP

```

> Digits := 15; Tcvap := qi/(100*h*A)+Tsink; Tcvap := Tcvap; T0 := Tsink; Q := qi/lambda;
> p[cond] := p[csatTcv]; P[cond1] := p[cond]; P[cond] := P[cond1]; P[evap] := P[cond]-
R[liq]*Q/n[liq]-rho[liq]*ng*g*L[pipe];
> Teliq := C1/(C0-ln(P[evap]))+C2;
> P[evap1] := -R[wick]*Q+P[evap]; p[evap] := `(`(1/n[vap], R[vap]), Q)+p[cond]*exp(-
MW*ng*g*L[pipe]/(R[gas]*Tevap));
> fEe := P[evap1]-exp(C0-C1/(Tevap1-C2))-R[gas]*Tevap1*ln(p[evap]/exp(C0-C1/(Tevap1-
C2)))/Vmolarliq;
> s2 := solve({fEe}, {Tevap1}); assign(s2);
> Tevap := Tevap1; unassign('Tevap1');
> T01 := Teliq-(Tevap-Teliq)/(Rw*Q*Cpliq);

# if T01 > Tsink

```

```

> T0 := T01;
> fEe := qi-Q0*(lambda+Cpliq(Tevap-T0));
> s1 := solve({fEe}, {Q0}); assign(s1);
> Q := Q0; unassign('Q0');
> check := 0; while check = 0 do
p[cond] := p[csatTcv]; P[cond1] := p[cond]; P[cond] := P[cond1]; P[evap] := P[cond]-
R[liq]*Q/n[liq]-rho[liq]*ng*g*L[pipe]; Teliq := C1/(C0-ln(P[evap]))+C2; P[evap1] := -
R[wick]*Q+P[evap]; p[evap] := `(`(1/n[vap], R[vap]), Q)+p[cond]*exp(-
MW*ng*g*L[pipe]/(R[gas]*Tevap)); fEe := P[evap1]-exp(C0-C1/(Tevap1-C2))-
R[gas]*Tevap1*ln(p[evap]/exp(C0-C1/(Tevap1-C2)))/Vmolarliq; s2 := solve({fEe}, {Tevap1});
assign(s2);

if abs(Tevap1-Tevap) < 0.5e-3 then check := 1 elif abs(Tevap1) <> Tevap1 then check := 2
elif Tevap > 400 then check := 3 end if;

Tevap := Tevap1; unassign('Tevap1'); fEe := qi-Q0*(lambda+Cpliq(Tevap-T0)); s1 :=
solve({fEe}, {Q0}); assign(s1);

if abs((Q0-Q)/Q0) > 0.25e-2 then check := 0 end if;
Q := Q0; unassign('Q0');
end do;

# if T01 < Tsink
> Digits := 15;
> T0 := Tsink; Tevap := Tcvap; Q := qi/lambda; Teliq := T0; check := 0;

```

```

> while check = 0 do
P[evap] := p[esatTel]; P[evap1] := -R[wick]*Q+P[evap]; P[cond] :=
P[evap]+R[liq]*Q/n[liq]+rho[liq]*ng*g*L[pipe]; P[cond1] := P[cond]; p[cond] := P[cond1];
Tcvap := C1/(C0-ln(p[cond]))+C2; p[evap] := `(`(1/n[vap], R[vap]), Q)+p[cond]*exp(-
MW*ng*g*L[pipe]/(R[gas]*Tevap)); fEe := P[evap1]-exp(C0-C1/(Tevap1-C2))-
R[gas]*Tevap1*ln(p[evap]/exp(C0-C1/(Tevap1-C2)))/Vmolarliq; s2 := solve({fEe}, {Tevap1});
assign(s2);

if abs(Tevap1-Tevap) < 0.1e-1 then check := 1 elif abs(Tevap1) <> Tevap1 then check := 2
elif Tevap > 593 then check := 3 end if;

Tevap := Tevap1; unassign('Tevap1'); Q := qi/(lambda+Cpliq(Tevap-T0)); Teliq :=
(Tevap/Rw+Q*Cpliq*T0)/(1/Rw+Q*Cpliq)
end do;

# Operational parameters for SHLHP
> qi := 50; a0[comp] := .99; T0 := 273.15+150; L[pipe] := 10; ng := 0; kwick := 13;
> Rwe := Lsi/(A*((1-phi)*kwick+phi*kw));
> Rwc := Lsi/(A*((1-phi)*ksi+phi*kw));

# Coupled heat, momentum and thermodynamic balances for SHLHP
> Digits := 15;
> q[senl0] := 0;
> Q := qi/lambda; Teliq := T0; Tevap := Teliq; check := 0;

```

```

while check = 0 do
Tcvap := (Q*(lambda+Cpvap*Tevap)+T0/Rwc)/(1/Rwc+Q*Cpvap); p[cond] :=
a0[comp]*p[csatTcv]; P[cond1] := ln(a0[comp])*R[gas]*Tcvap/Vmolarliq+p[csatTcv]; P[cond] :=
P[cond1]-R[wick]*Q; P[evap] := -R[liq]*Q/n[liq]-rho[liq]*ng*g*L[pipe]+P[cond]; P[evap1] := -
R[wick]*Q+P[evap]; p[evap] := `(`(1/n[vap], R[vap]), Q)+p[cond]*exp(-
MW*ng*g*L[pipe]/(R[gas]*Tevap));
fEe := P[evap1]-exp(C0-C1/(Tevap1-C2))-R[gas]*Tevap1*ln(p[evap]/exp(C0-C1/(Tevap1-
C2)))/Vmolarliq; s1 := solve({fEe}, {Tevap1}); assign(s1);
Tevap := Tevap1; Teliq := (Tevap1/Rwe+Q*Cpliq*T0)/(1/Rwe+Q*Cpliq); unassign('Teliq1');
unassign('Tevap1'); q[senl] := Q*Cpliq*(Tevap-T0);

if abs(q[senl]-q[senl0]) < 0.1e-4 then check := 1 elif abs(q[senl]) <> q[senl] then check := 2
end if;
q[senl0] := q[senl]; unassign('q[senl]');
Q := (qi-q[senl0])/lambda
end do;

if ng = 0 then glist := [ng]; T0list := [T0]; Tcvaplist := [Tcvap]; Teliqlist := [Teliq]; Tevaplist :=
[Tevap]; Refflist := [(Tevap-Tsink)/qi]; pevaplist := [p[evap]]; pcondlist := [p[cond]];
Pcondsurflist := [P[cond1]]; Pcondlist := [P[cond]]; Pevaplist := [P[evap]]; Pevapsurflist :=
[P[evap1]]; Pcaplist := [p[evap]-P[evap1]] else glist := [op(glist), ng]; T0list := [op(T0list), T0];
Tcvaplist := [op(Tcvaplist), Tcvap]; Teliqlist := [op(Teliqlist), Teliq]; Tevaplist := [op(Tevaplist),
Tevap]; Refflist := [op(Refflist), (Tevap-Tsink)/qi]; pevaplist := [op(pevaplist), p[evap]];
pcondlist := [op(pcondlist), p[cond]]; Pcondsurflist := [op(Pcondsurflist), P[cond1]]; Pcondlist :=

```

```

[op(Pcondlist), P[cond]]; Pevaplist := [op(Pevaplist), P[evap]]; Pevapsurflist :=
[op(Pevapsurflist), P[evap1]]; Pcaplist := [op(Pcaplist), p[evap]-P[evap1]] end if;

> unassign('Q', 'Tevap', 'Teliq', 'Tcvap', 'P[evap]', 'P[evap1]', 'P[cond]', 'P[cond1]', 'p[cond]',
'p[evap]', 'P[comp]', 'Tevap1', 'Q0');

```

A.2.2 Linear analysis and expression of SHLHP effective thermal resistance (Maple)

```

> restart; with(plots); with(Statistics);

# Antoine's constants

# Antoine parameters extracted from fit of saturation curve of water from NIST at 10 values
between 273.16 and 373.16 K.

> C0 := 23.1963; C1 := 3816.7; C2 := 46.062;

> ps0 := exp(C0-C1/(T0-C2));

> dpdT0 := diff(exp(C0-C1/(T0-C2)), T0);

> d2pdT20 := diff(diff(exp(C0-C1/(T0-C2)), T0), T0);

> p[esatTev] := exp(C0-C1/(Tevap-C2));

> p[csatTcv] := exp(C0-C1/(Tcvap-C2));

# Material properties (SI units)

# temperature dependences of properties are based on data from NIST at 10 values between
273.16 and 373.16K. Fits over this range provide R-squared values >= 0.999.

```

```

> g := 10; R[gas] := 8.314472; lambda := (3171.5-2.4467*T0)*10^3; MW := 18.015268*10^(-3);
Cpliq := 4.1825*10^3; rho[liq] := 233.64+6.7583*T0-0.18749e-1*T0^2+1.5659*10^(-5)*T0^3;
mu[liq] := .46522-5.3813*10^(-3)*T0+2.345*10^(-5)*T0^2-4.5534*10^(-8)*T0^3+3.3206*10^(-
11)*T0^4; Cpvap := 1918.; vkin := mu[liq]/rho[liq]; Vmolarliq := MW/rho[liq]; rho[vap] :=
ps0*MW/(R[gas]*T0); mu[vap] := 0.59348e-5-0.18137e-8*T0+0.50436e-10*T0^2;
vsoundvap := 128.86+1.3114*T0-0.10479e-2*T0^2; sigma := 0.94327e-1+0.42358e-5*T0-
0.26576e-6*T0^2; kw := -.51486+0.53182e-2*T0-0.33539e-5*T0^2-0.62337e-8*T0^3; ksi :=
130;

```

Geometric parameters

```

> PI := 3.14159265; A := 0.1e-3; phi := .6; L[pipe] := 10; Dia[pore1] := 0.200e-6; L[pore1] :=
0.300e-3; Dia[pore2] := 0.5e-8; Dia[comp] := 0.30e-7; Lsi := 3*10^(-4); L[pipe] := 10;

```

Hydraulic resistances

```

> R[vap] := (.^(128.*L[pipe], mu[vap]))/(.^(PI, rho[vap], Dia[vap]^4));
> R[liq] := (.^(128.*L[pipe], mu[liq]))/(.^(PI, rho[liq], Dia[liq]^4));
> R[layer1] := .^(((.^(phi, A))/(.^(.25*PI, Dia[pore1]^2)))^(-1), 128.*L[pore1]*mu[liq]/(.^(PI,
rho[liq], Dia[pore1]^4)));
> R[layer2] := .^(((.^(phi, A))/(.^(.25*PI, Dia[pore2]^2)))^(-1), 128.*L[pore2]*mu[liq]/(.^(PI,
rho[liq], Dia[pore2]^4)));
> R[wick] := R[layer1]+R[layer2];

```

Operational parameters

```

> T0 := 298; qi := 20; a0[comp] := .995; ng := 10; n[vap] := 1; n[liq] := 1; Dia[liq] := 350*10^(-6);
Dia[vap] := 6*10^(-3); L[pore2] := 2*10^(-6); unassign('Q', 'Tevap', 'Teliq', 'Tcvap', 'P[evap]',
'P[evap1]', 'P[cond]', 'P[cond1]', 'p[cond]', 'p[evap]', 'P[comp]');

```

Coupled heat, momentum and thermodynamic balances

heat balances

```

> Q := qi/lambda;
> Te1iq := ((k(A)/Lsi)^(-1)*qi+Tevap;
> Tcvap := ((k(A)/Lsi)^(-1)*qi+T0;

```

momentum balances

```

> P[evap] := -R[liq]*Q/n[liq]-rho[liq]*ng*g*L[pipe]+P[cond];
> P[evap1] := -R[wick]*Q+P[evap];
> p[cond] := p[csatTcv]*exp((P[cond1]-p[csatTcv])*Vmolarliq/(R[gas]*Tcvap));

```

local equilibria

```

> P[cond1] := R[wick]*Q+P[cond];
> P[cond] := P[comp];

```

coupled equations, solved iteratively.

```

> Tevap0 := T0;
> p[evap] := ((1/n[vap], R[vap], Q)+p[cond]*exp(-MW*ng*g*L[pipe]/(R[gas]*Tevap0));
> fEe := P[evap1]-exp(C0-C1/(Tevap1-C2))-R[gas]*Tevap1*ln(p[evap]/exp(C0-C1/(Tevap1-
C2)))/Vmolarliq;
> s1 := solve({fEe}, {Tevap1}); assign(s1); Tevap0 := Tevap1; unassign('Tevap1');
> Tevap := Tevap0;
> T0List := [op(T0List), T0]; CondList := [op(CondList), qi/(Te1iq-T0)];

```

```
> print(T0, qi, a0[comp], Q, Te1iq-T0, Tevap-T0, Tcvap-T0, 10^(-5)*P[evap], 10^(-5)*P[evap1],
10^(-5)*P[cond], p[evap], p[cond], ps0, qi/(Te1iq-T0), R[vap]/n[vap], R[liq]/n[liq], ng);
298, 20, 0.995, 0.000008188722540, 6.1666171, 5.7050786, 0.4615385, -18.86554046, -22.39446964, -
6.842169431, 4299.866935, 3204.156452, 3124.213530, 3.243269312, 1.366419701 108, 2.507308198 1010, 10
```

```
# Test criteria for linearization using parameter values from above
```

```
> p[evap]/ps0; (Tevap-T0)*dpdT0/ps0; MW*ng*g*L[pipe]/(R[gas]*T0);
```

```
1.376303794
```

```
0.3430538536
```

```
0.007270927060
```

```
> a := p[evap]*dpdT0/(ps0^2*T0); b := -Vmolarliq*dpdT0/(R[gas]*T0)+(1-
```

```
p[evap]/ps0)/T0+p[evap]*dpdT0/ps0^2; c := Vmolarliq*(P[evap1]-ps0)/(R[gas]*T0)+1-
```

```
p[evap]/ps0;
```

```
0.0002777146006
```

```
0.08149481656
```

```
-0.3926580916
```

```
# Check solution to linearized equation and further approximations
```

```
> -4*a*c/b^2; -c/b; (-b+sqrt(b^2-4*a*c))/(2*a); Tevap-T0;
```

```
0.06567699636
```

```
4.818197134
```

```
4.741581869
```

```
5.7050786
```

```
> (Tevap-T0)/T0; Vmolarliq*dpdT0/(R[gas]*T0);
```

```
0.01914455906
```

```
0.000001370020416
```

> -c/b; -ps0^2*(Vmolarliq*(P[evap1]-ps0)/(R[gas]*T0*p[evap]+1/p[evap]-1/ps0)/dpdT0;

4.818197134

4.744599668

Find approximate form for d/(dqi)(DeltaTevap)

Note that all dependence on qi comes in through p[evap] and P[evap1]

> # d/(dqi)(DeltaTevap) ~ -(((ps0)^2)/(dpdT0))*(Vmolarliq)/(R[gas]*T0)*d/(dqi)((P[evap1]-ps0)/(p[evap])) - (((ps0)^2)/(dpdT0)) *d/(dqi)(1/(p[evap])-1/(ps0))

> # d/(dqi)(DeltaTevap) ~ -(((ps0)^2)/(dpdT0))*(Vmolarliq)/(R[gas]*T0)*(-(P[evap1]-ps0)/(p[evap]^2))*(dp[evap]/(dqi)+1/(p[evap])*(dP[evap1]/(dqi)) + (((ps0)^2)/(dpdT0)) * (1/(p[evap]^2))(dp[evap]/(dqi))

> # d/(dqi)(DeltaTevap) ~ -

(((ps0)^2)/(dpdT0*p[evap]))*(Vmolarliq)/(R[gas]*T0)*((dP[evap1]/(dqi)) +

((ps0^2)/(dpdT0*p[evap]^2))) * (1+(Vmolarliq)/(R[gas]*T0)*(P[evap1]-ps0))*(dp[evap]/(dqi)

> # d/(dqi)(DeltaTevap) ~ -((ps0)/(dpdT0))*(Vmolarliq)/(R[gas]*T0)*((dP[evap1]/(dqi)) + ((1)/(dpdT0)) * (dp[evap]/(dqi)

> # (In this last step, we have used p[evap] ~ ps0 and (Vmolarliq)/(R[gas]*T0)*(P[evap1]-ps0)<<1

> # p[evap] = (R[vap]*qi)/(lambda)+p[cond] ;

> # Ignoring dependence of p[cond] on T[evap], i.e., ignoring Boltzmann factor with MW*g*L[pipe].

> # p[cond] = ps(T[cvap])*exp((P[cond1]-ps(T[cvap]))/((RT[cvap])/(Vmolarliq))) ~ ps(T[cvap])*(1+(P[cond1]-ps(T[cvap]))/((RT[cvap])/(Vmolarliq)))

> # ~ (ps0+dpdT0*(T[cvap]-T0))*(1+(Vmolarliq)/(R)*((P[cond]+qi/(lambda))*R[wick])-(ps0+dpdT0*(T[cvap]-T0)))/(T[cvap])

> # = (ps0+dpdT0*(Lsi/(ksi*A))qi)*(1+(Vmolarliq)/(R)((P[cond]+qi/(lambda)*R[wick])-(ps0+dpdT0*(Lsi/(ksi*A))qi))/(T[cvap]))

> # = (ps0+dpdT0*(Lsi/(ksi*A))qi)*(1+(Vmolarliq)/(R)((P[cond]-ps0)+((R[wick])/(lambda)-dpdT0*(Lsi/(ksi*A))qi))/(T[cvap]))

> #

=(ps0+dpdT0*(Lsi/(ksi*A))qi)*(1+(Vmolarliq)/(R)((R*T0)/(Vmolarliq)*ln(a0[comp])+((R[wick])/(lambda)-dpdT0*(Lsi/(ksi*A))qi))/(T[cvap]))

> #

=(ps0+dpdT0*(Lsi/(ksi*A))qi)*(1+(T0)/(T[cvap])*ln(a0[comp])+(Vmolarliq)/(R*T[cvap]))((R[wick])/(lambda)-dpdT0*(Lsi/(ksi*A))qi))

> # ~ ps0+ps0*((T0)/(T[cvap])*ln(a0[comp])+(Vmolarliq)/(R*T[cvap]))((R[wick])/(lambda)-dpdT0*(Lsi/(ksi*A))qi)+dpdT0*(Lsi/(ksi*A))qi

> # neglecting terms that are the product of two small factors

> # = ps0+ps0*((T0)/(T[cvap])*ln(a0[comp])+(Vmolarliq)/(R*T0)*(R[wick])/(lambda)qi)+(1-ps0*(Vmolarliq)/(R*T[cvap]))*dpdT0*(Lsi/(ksi*A))*qi

> # ~

ps0*(1+(1+(qi*R[wick])/(T[cvap]))*ln(a0[comp]))+(1+(qi*R[wick])/(T[cvap]))*ps0*(Vmolarliq)/(R*T0)*(R[wick])/(lambda)*qi+dpdT0*(Lsi/(ksi*A))*qi

> # d/(dqi)(p[evap]) ~

(R[vap])/(lambda)+ps0*(Vmolarliq)/(R*T0)(R[wick])/(lambda)+dpdT0*(Lsi/(ksi*A))

> # P[evap1] = P[cond]-(qi)/(lambda)(R[liq]+R[wick])- rho[liq]gL[pipe]

> # d/(dqi)(P[evap1])= -((R[liq]+R[wick]))/(lambda)

> # d/(dqi)(DeltaTevap) ~ ((ps0)/(dpdT0))*(Vmolarliq)/(R[gas]*T0)*(((R[liq]+2*R[wick])/(lambda)) + ((1)/(dpdT0)) *(R[vap])/(lambda)+(Lsi/(ksi*A))

> # d/(dqi)(DeltaTevap) ~ ResLiq+ResVap+ResWick;

A.2.3 Lumped parameter analysis (Maple)

```
> restart; with(plots); with(Statistics); with(linalg); with(Units);
```

Antoine's constants

```
# Antoine parameters extracted from fit of saturation curve of water from NIST at 10 values  
between 273.16 and 373.16 K.
```

```
> C0:=23.1963; C1:=3816.7; C2:=46.062; ps0:=exp(C0-C1/(T0-C2)); dpdT0 := diff(exp(C0-  
C1/(T0-C2)), T0); d2pdT20:=diff(diff(exp(C0-C1/(T0-C2)), T0),T0):
```

```
> p[esatTev]:= exp(C0-C1/((Tevap-C2))): #saturation pressure at evaporator
```

```
> p[csatTcv]:= exp(C0-C1/((Tcvap-C2))): #saturation pressure at condenser
```

Material properties (SI units)

```
# Temperature dependences of properties are based on data from NIST at 10 values between  
273.16 and 373.16K. Fits over this range provide R-squared values>=0.999.
```

```
> g := 10; R[gas] := 8.314472; lambda := (3171.5-2.4467*T0)*10^3; MW := 18.015268*10^(-3);
```

```
Cpliq := 4.1825*10^3; rho[liq] := 233.64+6.7583*T0-0.18749e-1*T0^2+1.5659*10^(-5)*T0^3;
```

```
mu[liq] := .46522-5.3813*10^(-3)*T0+2.345*10^(-5)*T0^2-4.5534*10^(-8)*T0^3+3.3206*10^(-
```

```
11)*T0^4; Cpvap := 1918.; vkin := mu[liq]/rho[liq]; Vmolarliq := MW/rho[liq]; rho[vap] :=
```

```
ps0*MW/(R[gas]*T0); mu[vap] := 0.59348e-5-0.18137e-8*T0+0.50436e-10*T0^2;
```

```
vsoundvap := 128.86+1.3114*T0-0.10479e-2*T0^2; sigma := 0.94327e-1+0.42358e-5*T0-
```

```
0.26576e-6*T0^2; kw := -.51486+0.53182e-2*T0-0.33539e-5*T0^2-0.62337e-8*T0^3; ksi :=
```

```
130; Cpsi := 19.789/(28.0855)*1000; rho[si] := 2.3290*10^3;
```

Geometric parameters

```
> PI := 3.14159265; A := 0.1e-3; phi := .6; L[pipe] := 10; Dia[pore1] := 0.200e-6; L[pore1] :=
0.300e-3; Dia[pore2] := 0.5e-8; Dia[comp] := 0.30e-7; Lsi := 3*10^(-4);
```

Heat capacities and hydraulic resistances

```
> C1 := rho[sj]*Cpsi*A*Lsi*(1-phi);
```

```
> C2 := MW*lambda*dpdT0*Dia[vap]^2*PI*L[pipe]/(4*R[gas]*T0);
```

```
> C3 := rho[sj]*Cpsi*A*Lsi*(1-phi);
```

```
> R[vap]:=(128. L[pipe].mu[vap])/((PI.rho[vap].(Dia[vap])^(4))); #` resistance of vapor path,
`Pa/(kg/(s))
```

```
> R[liq ]:=(128. L[pipe].mu[liq])/((PI. rho[liq].(Dia[liq])^(4))); #` the resistance of the liquid
path, `Pa/(kg/(s))
```

```
> R[layer1 ]:=((phi.A)/(0.25* PI.(Dia[pore1])^(2)))^(-1).(128.
```

```
L[pore1]*mu[liq])/((PI.rho[liq].(Dia[pore1])^(4))); #` resistance of porous wick structure,
`Pa/(kg/(s))
```

```
> R[layer2 ]:=((phi.A)/(0.25* PI.(Dia[pore2])^(2)))^(-1).(128.
```

```
L[pore2]*mu[liq])/((PI.rho[liq].(Dia[pore2])^(4))); #` resistance of porous wick structure,
`Pa/(kg/(s))
```

```
> R[wick]:=R[layer1]+R[layer2];
```

Effective resistances (from s.s. equations)

```
> ResLiq := ps0*Vmolarliq*R[liq]/(dpdT0*R[gas]*T0*n[liq]*lambda);
```

```
> ResLiqwick := ps0*Vmolarliq*R[wick]/(dpdT0*R[gas]*T0*lambda);
```

```
> ResVap := R[vap]/(dpdT0*n[vap]*lambda);
```

```
> esWick := Lsi/(ksi*A);
```

```

> ResTotalEvap := ResLiq+2*ResLiqwick+ResVap+ResWick;
> ResTotalEliq := ResTotalEvap+ResWick;
> R1 := ResWick;
> R2 := ResLiq+2*ResLiqwick+ResVap;

```

Operational parameters;

```

> T0 := 298; a0[comp] := .995; ng := 10; n[vap] := 1; n[liq] := 1; Dia[liq] := 350*10^(-6);
Dia[vap] := 6*10^(-3); L[pore2] := 2*10^(-6);

```

Transient temperature profile

```

> unassign('t');
> eq[1] := diff(T3(t), t) = -T3(t)/(R1*C3)+T2(t)/(R2*C3); eq[2] := diff(T2(t), t) = T3(t)/(R1*C3)-
T2(t)/(R2*C3)-T2(t)/(R2*C2)+T1(t)/(R1*C2); eq[3] := diff(T1(t), t) = -(T3(t)/(R1*C3)-
T2(t)/(R2*C3)-T2(t)/(R2*C2))-T1(t)/(R1*C2)-T1(t)/(R1*C1)+qi/C1; pars := {qi =
10*(1+sin(20*t))};
> vars := [T3(t), T2(t), T1(t)]; eqs := [seq(rhs(eq[i]), i = 1 .. 3)];
> eqs := subs(pars, eqs); A := genmatrix(eqs, vars, 'B'); b := matrix(3, 1);
> for i to 3 do b[i, 1] := -B[i] end do;
> mat := exponential(A, t); Y0 := matrix(3, 1, [0, 0, 0]); b2 := subs(t = t1, evalm(b)); mat2 :=
subs(t = t-t1, evalm(mat)); mat3 := evalm(`&*(mat2, b2)); mat4 := map(int, mat3, t1 = 0 .. t);
sol := evalm(`&*(mat, Y0)+mat4);
> dT3 := sol[1, 1]; dT2 := sol[2, 1]; dT1 := sol[3, 1]; tf := 5;
> p[1] := plot(dT1+dT2+dT3+T0, t = 0 .. tf, thickness = 2, linestyle = 1, legend = "Teliq"); p[2] :=
plot(dT1+dT2+T0, t = 0 .. tf, thickness = 2, linestyle = 1, color = green, legend = "Tevap");
p[3] := plot(dT3+T0, t = 0 .. tf, thickness = 2, linestyle = 1, color = blue, legend = "Tcvap");

```

```

> display({seq(p[i], i = 1 .. 3)}, axes = boxed, labels = ["t (sec)", "Temperature (degrees C)"],
labeldirections = [HORIZONTAL, VERTICAL]);

> plot(dT1+dT2+dT3, t = 0 .. tf, axes = boxed, thickness = 2, linestyle = 1, color = gold, legend
= "&Delta;Ttotal", labels = ["t(sec)", "Temperature(degreesC)"], labeldirections =
[HORIZONTAL, VERTICAL]);

> unassign('t');

> eq[1] := diff(T3(t), t) = -T3(t)/(R1*C3)+T2(t)/(R2*C3); eq[2] := diff(T2(t), t) = T3(t)/(R1*C3)-
T2(t)/(R2*C3)-T2(t)/(R2*C2)+T1(t)/(R1*C2); eq[3] := diff(T1(t), t) = -(T3(t)/(R1*C3)-
T2(t)/(R2*C3)-T2(t)/(R2*C2))-T1(t)/(R1*C2)-T1(t)/(R1*C1)+qi/C1;

> vars := [T3(t), T2(t), T1(t)];

> eqs := [seq(rhs(eq[i]), i = 1 .. 3)]; A := genmatrix(eqs, vars, 'B'); b := matrix(3, 1);

> for i to 3 do b[i, 1] := -B[i] end do;

> mat := exponential(A, t); Y0 := matrix(3, 1, [0, 0, 0]); s1 := evalm(Y0+`&^*(inverse(A), b));
sol := evalm(`&^*(mat, s1)-`&^*(inverse(A), b));

> dT3 := sol[1, 1]; dT2 := sol[2, 1]; dT1 := sol[3, 1];

> p[1] := plot(dT1+dT2+dT3+T0, t = 0 .. 3, thickness = 2, linestyle = 1, legend = "Teliq"); p[2] :=
plot(dT1+dT2+T0, t = 0 .. 3, thickness = 2, linestyle = 1, color = green, legend = "Tevap");
p[3] := plot(dT3+T0, t = 0 .. 3, thickness = 2, linestyle = 1, color = blue, legend = "Tcvap");

> display({seq(p[i], i = 1 .. 3)}, axes = boxed, labels = ["t (sec)", "Temperature (degrees C)"],
labeldirections = [HORIZONTAL, VERTICAL]);

> dTsteadystate := limit(dT1+dT2+dT3, t = infinity);

> eqss := .99*dTsteadystate = dT1+dT2+dT3;

> Timereqd := fsolve(eqss, t);

> t := Timereqd; evalf(dT1); evalf(dT2); evalf(dT3);

```

A.2.4 Steady state calculations for conventional LHP, saturated and unsaturated MEMS-based SHLHPs (Mathematica)

```
ClearAll["Global`*"]
```

Antoine's constants, Material properties (SI units) and Hydraulic Resistances

(* Antoine parameters extracted from fit of saturation curve from NIST at 33 values between 273.16 and 593.16 K *)

```
C0=23.1953647696257;
```

```
C1=3816.99213575208;
```

```
C2=45.9240851812291;
```

```
ps[T0_]:=Exp[C0-C1/(T0-C2)];
```

```
ps0:=ps[T0]
```

```
dpsdT0:=ps'[T0];
```

```
d2psdT20:=ps''[T0];
```

```
pesatTev:=Exp[C0-C1/(Tevap-C2)];
```

```
pcsatTcv:=Exp[C0-C1/(Tcvap-C2)];
```

```
pesatTel:=Exp[C0-C1/(Teliq-C2)];
```

(* temperature dependences of properties are based on data from NIST at 21 values between 273.16 and 473.16. Fits over this range provide R-squared values ≥ 0.999 . *)

```
g=10;
```

```
Rgas=8.314472;
```

```
MW=18.015268*10^-3;
```

$\text{lambdaf}[T0_]=(-0.165302*10^{-4}*T0^3+0.149098*10^{-1}*T0^2-6.86262*T0+3600.26)*10^3;$
 $\text{Cpliqf}[T0_]=(0.412059*10^{-13}*T0^6-0.960454*10^{-10}*T0^5+0.929777*10^{-7}*T0^4-$
 $0.477994*10^{-4}*T0^3+0.137625*10^{-1}*T0^2-2.10454*T0+137.737)*10^3;$ $\text{rholiqf}[T0_]=-$
 $0.389737*10^{-7}*T0^4+0.626585*10^{-4}*T0^3-0.397984*10^{-1}*T0^2+10.9057*T0-$
 $69.5342;$ $\text{muliqf}[T0_]=0.411031790*10^{-15}*T0^6-0.968082253*10^{-}$
 $12*T0^5+0.947109629*10^{-9}*T0^4-0.492836995*10^{-6}*T0^3+0.143938246*10^{-3}*T0^2-$
 $0.223898176*10^{-1}*T0+1.45116063;$
 $\text{Vmolarliqf}[T0_]=\text{MW}*(-0.389737*10^{-7}*T0^4+0.626585*10^{-4}*T0^3-0.397984*10^{-}$
 $1*T0^2+10.9057*T0-69.5342)^{-1};$
 $\text{sigmaf}[T0_]=-0.225306*10^{-6}*T0^2-0.227104*10^{-4}*T0+0.987545*10^{-1};$ $\text{kwf}[T0_]=-$
 $0.570043*10^{-12}*T0^4+0.181825*10^{-7}*T0^3-0.266229*10^{-4}*T0^2+0.127391*10^{-1}*T0-$
 $1.30089;$ $\text{Cpvapf}[T0_]=(0.515950*10^{-14}*T0^6-0.135114*10^{-10}*T0^5+0.143051*10^{-7}*T0^4-$
 $0.773466*10^{-5}*T0^3+0.226362*10^{-2}*T0^2-.341539*T0+22.6856)*10^3;$
 $\text{rhovapf}[T0_]=0.623591*10^{-8}*T0^4-0.736047*10^{-5}*T0^3+0.330094*10^{-}$
 $2*T0^2-.665126*T0+50.6961;$
 $\text{muvapf}[T0_]=-0.167553*10^{-12}*T0^3+0.206613*10^{-9}*T0^2-0.500277*10^{-}$
 $7*T0+0.108661*10^{-4};$ $\text{vsoundvapf}[T0_]=-0.346923*10^{-5}*T0^3+0.231016*10^{-}$
 $2*T0^2+.234201*T0+243.375$

$\text{lambda}:=\text{lambdaf}[T0];$

$\text{Cpliq}:=\text{Cpliqf}[T0];$

$\text{rholiq}:=\text{rholiqf}[T0];$

$\text{muliq}:=\text{muliqf}[T0];$

$\text{Vmolarliq}:=\text{Vmolarliqf}[T0];$

$\text{sigma}:=\text{sigmaf}[T0];$

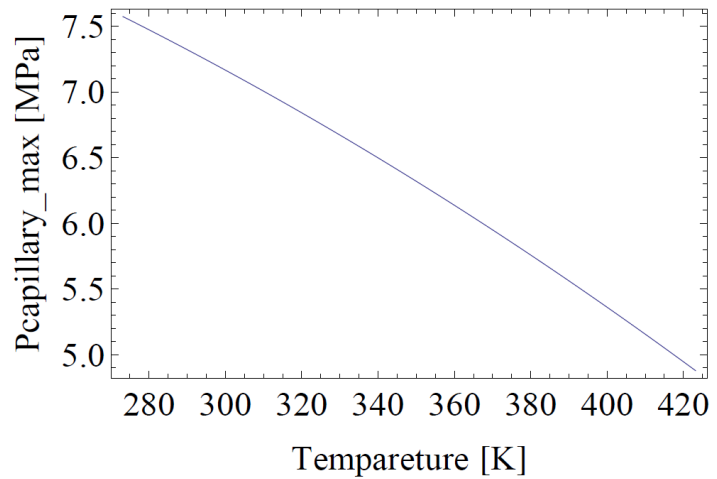
```

kw:=kwf[T0];
Cpvap:=Cpvapf[T0];
rhovap:=rhovapf[T0];
muvap:=muvapf[T0];
vsoundvap:=vsoundvapf[T0];

(* hydraulic resistances *)
Rvap:=128*Lpipev*muvapf[Tevap]*(Pi*rhovapf[Tevap]*Diavap^4)^-1;
Rliq:=128*Lpipel*muliq*(Pi*rholiq*Dialiq^4)^-1;
Rlayer1:=128*Lpore1*muliqf[Teliq]*(Pi*rholiqf[Teliq]*Diapore1^4)^-
1*(phi*A/(Pi*Diapore1^2/4))^-1;
Rlayer2:=128*Lpore2*muliqf[Teliq]*(Pi*rholiqf[Teliq]*Diapore2^4)^-
1*(phi*A/(Pi*Diapore2^2/4))^-1;
Rwick:=Rlayer1+Rlayer2;

T0=.
Diapore1:=50*10^-6;
Diapore2:=40*10^-9;
Pmaxpore2:=(4*sigma/Diapore2)*10^-6;
Plot[Pmaxpore2,{T0,273.16,423.16},Frame->True, LabelStyle->Directive[18],FrameLabel-
>{"Temperature [K]", "Pcapillary_max [MPa]"}]

```



Geometric Parameters and Operational Parameters

(* Geometric parameters *)

A:=1*10⁻⁴;

nvap:=1;

nliq:=101;

Diavap:=0.8*10⁻³;

Dialiq:=30*10⁻⁶;

Lpipe:=10*10⁻²;

Lpipev:=1*10⁻²;

Lpipel:=6*10⁻²;

phi:=0.5;

Diapore1:=50*10⁻⁶;

Lpore1:=270*10⁻⁶;

Diapore2:=3*10⁻⁹;

Lpore2:=30*10⁻⁶;

Lsi:=300*10⁻⁶;

(* Operational parameters *)

qi:=10;

Tsink:=273.15+20;

ng:=1;

(* Estimating pressure drops and thermal resistivities *)

Tevap:=Tsink;

Teliq:=Tsink;

T0:=Tsink;

Pvap:=Rvap*qi*(lambdaf[Tevap]^-1)*nvap^-1;

Pliq:=Rliq*qi*(lambdaf[Tevap]^-1)*nliq^-1;

Phydrostatic:=rho_liq*ng*g*Lpipe;

Pwick:=Rwick*qi*(lambdaf[Tevap]^-1);

kporousSi:=1.3;

ksi=130;

Rwe=Lpore2/(A*((1-phi)*kporousSi+phi*kw))+Lpore1/(A*((1-phi)*ksi+phi*kw));

T0=.

Tevap=.

Coupled heat, momentum, and thermodynamic balances (SHLHP, saturated condenser)

T0=Tsink;

Tcvap=Tsink;

Tevap=Tcvap;

```

Teliq=T0;
Q=qi/lambdaf[Tevap];

check=0;
While[check==0,
pcond=pcsatTcv; (* pcond=vapor pressure in the condenser*)
Pcond1=pcond; (* Pcond=liquid pressure in the condenser*)
Pcond=Pcond1; (* Pcond1=liquid pressure at the v-l interface in the condenser*)
Pevap=Pcond-Rliq/nliq*Q-rholiq*ng*g*Lpipe; (* Pevap=liquid pressure in the evaporator*)
Pevap1=Pevap-Rwick*Q; (* Pevap1=liquid pressure at the v-l interface in the evaporator*)
pevap=Rvap/nvap*Q+pcond*Exp[-MW*ng*g*Lpipe/Rgas/Tevap]; (* pevap=vapor pressure in
the evaporator*)

fEe:=(Pevap1-Exp[C0-C1/(Tevap1-C2)])-Rgas*Tevap1/Vmolarliq*Log[pevap/Exp[C0-
C1/(Tevap1-C2)]];

Temp=Tevap1/.FindRoot[fEe ==0,{Tevap1, Tevap}];
If[ Abs[Temp-Tevap]<10^-2, check=1,If[ Abs[Temp]!=Temp, check=2,
If[ Tevap>473.15 ,check=3] ]];
Tevap=Temp;
Temp=.;
Q=qi/(lambdaf[Tevap]+Cpliq*(Tevap-T0));
Teliq=(Tevap/Rwe+Q*Cpliq*T0)/(1/ Rwe+Q*Cpliq);

```

Coupled heat, momentum, and, thermodynamic balances (conventional LHP)

$R_{we} = L_{si} / (A * ((1 - \phi) * k_{porousSi} + \phi * k_w))$; (* use a larger resistivity in the evaporater for conventional case *)

$T_0 = T_{sink}$;

$T_{cvap} = T_{sink}$;

$T_{evap} = T_{cvap}$;

$T_{elq} = T_0$;

$Q = q_i / \lambda_{daf}[T_{evap}]$;

check=0;

While[check==0,

$P_{evap} = p_{sat}(T_{el})$;

$P_{evap1} = P_{evap} - R_{wick} * Q$;

$P_{cond} = P_{evap} + R_{liq} / n_{liq} * Q + \rho_{holiq} * n_g * g * L_{pipe}$;

$P_{cond1} = P_{cond}$;

$p_{cond} = P_{cond1}$;

$p_{evap} = R_{vap} / n_{vap} * Q + p_{cond} * \exp[-MW * n_g * g * L_{pipe} / R_{gas} / T_{evap}]$;

$T_{cvap} = C_1 / (C_0 - \log[p_{cond}]) + C_2$;

$f_{Ee} = (P_{evap1} - \exp[C_0 - C_1 / (T_{evap1} - C_2)]) - R_{gas} * T_{evap1} / V_{molarliq} * \log[p_{evap} / \exp[C_0 - C_1 / (T_{evap1} - C_2)]]$;

Temp=Tevap1/.FindRoot[fEe ==0,{Tevap1, Tcvap}];

```

If[ Abs[Temp-Tevap]<10^-2, check=1,If[ Abs[Temp]!=Temp, check=2,
If[ Tevap>473.15 ,check=3]] ];
Tevap=Temp;
Temp=.;
Q=qi/(lambdaf[Tevap]+Cpliq*(Tevap-T0));
Teliq=(Tevap/Rwe+Q*Cpliq*T0)/(1/ Rwe+Q*Cpliq);

```

Coupled heat, momentum, and thermodynamic balances (SHLHP, sub-saturated condenser)

```

a0comp:=.995;
Rwc=Lpore2/(A*((1-phi)*kporousSi+phi*kw))+Lpore1/(A*((1-phi)*ksi+phi*kw));

qsenl0:=0;
T0=Tsink;
Teliq=T0;
Tevap=Teliq;
Q=qi/lambdaf[Tevap];

check:=0;
While[check == 0,
Tcvap=(Q*(lambda+Cpvap*Tevap)+T0/Rwc)/(1/Rwc+Q*Cpvap);
pcond=pcsatTcv*a0comp;
Pcond1:=Rgas*Tcvap/Vmolarliq*Log[pcond/pcsatTcv]+pcsatTcv;
Pcond:=-Rwick*Q+Pcond1;
Pevap=Pcond-Rliq/nliq*Q-rholiq*ng*g*Lpipe;

```

Pevap1=Pevap-Rwick*Q;

pevap=Rvap/nvap*Q+pcond*Exp[-MW*ng*g*Lpipe/Rgas/Tevap];

fEe:=(Pevap1-Exp[C0-C1/(Tevap1-C2)])-Rgas*Tevap1/Vmolarliq*Log[pevap/Exp[C0-C1/(Tevap1-C2)]];

Temp=Tevap1/.FindRoot[fEe ==0,{Tevap1, Tcvap}];

Tevap=Temp;

Temp=.;

Teliq=(Tevap/Rwe+Q*Cpliq*T0)/(1/ Rwe+Q*Cpliq);

qsenl=Q*Cpliq*(Tevap-T0);

If[Abs[qsenl-qsenl0]<10^-5, check=1, If[Abs[qsenl]! =qsenl, check=2]];

qsenl0=qsenl;

qsenl=.;

Q:=(qi-qsenl0)/lambdaf[Tevap];

A.3 MATLAB Scripts

This section publishes the original MATLAB scripts used for cavitation data analysis presented in Chapter 3, including image processing, cavitation history and colormap generating, survival probability curves fitting and randomness analysis.

A.3.1 Image processing and cavitation history analysis

```
%%% Imaging processing, modified from Dave's code -----

clear all;
close all;
clc;

path=' ';
fileprefix=' '; % without "_##.avi"

% PARAMETRES TO CHANGE
outfilm=' .avi';
thresh=0.025; % intensity threshold for
binarization ( 0-1 )
cavities=25; % cavities in one dimension (i.e.,
total cavities = cavities^2)
min_object_size=4; % reject "bright" binary objects
smaller than min_object_size
quant_gas=89; % number of "on"/"bright" pixels in
binary image required to register as gas filled

stop=1; % number of frames to use for intensity averaging

%%-----
nomfilm=strcat(fileprefix, '.avi');

film=[path, nomfilm];
info=aviinfo(film);
hauteur=info.Height;
largeur=info.Width;
numframes=info.NumFrames;

% AVERAGE INTENSITY OVER ALL PIXELS
moyint=0;
mov=aviread(film, (1:stop));
for im=1:stop;
    B1=double(mov(im).cdata(:,:,1));
```

```

cmap=mov(im).colormap(:,:,1);

int(im)=0;
for k=(1:largeur)
    for j=(1:hauteur)
        int(im)=int(im)+B1(j,k);
    end
end
int(im)=int(im)/(largeur*hauteur);
moyint=moyint+int(im);
end
moyint=moyint/stop;

% AVERAGE INTENSITY FOR EACH PIXEL
pixmoy = zeros(hauteur,largeur);
for k=(1:largeur)
    for j=(1:hauteur)
        intpix(j,k)=0.;
    end
end

for im=(1:stop)
    B1=double(mov(im).cdata(:,:,1));
for k=(1:largeur)
    for j=(1:hauteur)
        intpix(j,k)=intpix(j,k)+B1(j,k);
    end
end
end

for k=(1:largeur)
    for j=(1:hauteur)
        pixmoy(j,k)=intpix(j,k)/stop;
    end
end

%%-----

hh=waitbar(0, 'image');

stop=numframes; % reset number of frames to read
largeur_crop=largeur; % cropped width
hauteur_crop=hauteur; % cropped height
cmap=colormap(gray(256)); % colormap for movie
cav_film_mat(1:numframes)=struct('cdata',zeros(cavities,'uint8'),'colormap',cmap); % preallocate matrix for the output movie
vapor_pix=cell(cavities);

cavitated=zeros(cavities);

% recording the image# when a cavity just begin cavitating;

```

```

% default = 0, means not assigned
rhmap=zeros(cavities);

count=zeros(stop,1);

film=strcat(path,fileprefix,'.avi'); % read each input .avi in turn
mov=aviread(film,(1:stop));

xdum=[1:10:hauteur]; % for display lines separating cavity
quadrants
ydum=[1:10:largeur]; % for display lines separating cavity
quadrants
xbound=floor(hauteur_crop/cavities*[1:cavities]); xbound=[1
xbound]; % for display lines separating cavity quadrants
ybound=floor(largeur_crop/cavities*[1:cavities]); ybound=[1
ybound]; % for display lines separating cavity quadrants

for im=1:stop
    waitbar(im/(stop),hh);

    Borig=double(mov(im).cdata(:,:,1)); % original image

    moyinte=0;
    for k=(1:largeur)
        for j=(1:hauteur)
            moyinte=moyinte+Borig(j,k);
        end
    end
    moyinte=moyinte/(largeur*hauteur);
    rec_moyinte(im)=moyinte;

    % intensity corrected image
    if moyinte<moyint
        Bcorr=uint8(Borig-pixmoy+moyint);
    else
        Bcorr=uint8(Borig*moyint/moyinte-pixmoy+moyint);
    end

    Bbin=im2bw(Bcorr,thresh); % transform into binary
    according to threshold "thresh"
    Bout=bwareaopen(Bbin,min_object_size,4); % eliminate
    bright objects smaller than a certain size (index #2) with
    connectivity (4 or 8, index #3)
    for y=1:cavities
        for x=1:cavities
            gas=find(Bout(ceil((x-
1)*largeur_crop/cavities+0.01):floor(x*largeur_crop/cavities),ceil((y
-1)*hauteur_crop/cavities+0.01):floor(y*hauteur_crop/cavities))==1);
            % look to see if there are bright pixels in each cavity
            % quadrant
            if length(gas)>quant_gas

```

```

        cavitated(x,y)=cavitated(x,y)+255; % bright white if
cavitated
        vapor_pix{x,y}(im)=length(gas);
    end

        if rhmap(x,y)==0 && cavitated(x,y)>0 % record the image#
if this cavity starts cavitating at this moment
        rhmap(x,y)=im;
    end

    end
    count(im)=length(find(~~cavitated & ~bad_cavities));
end
cav_film_mat(im).cdata(:)=uint8(cavitated);

%% PLOTTING IMAGE ANALYSIS

    subplot(2,2,1)
    %%% the following subroutine expands the plots to increase
visibility
    h=subplot(2,2,1); % set call variable
    ax=get(h,'Position'); % get plot position info
    ax(1:2)=ax(1:2)-0.05;ax(3:4)=ax(3:4)+.1; % shift location and
expand
    set(h,'Position',ax); % write new position info
    %%%
    imshow(mov(im).cdata(:,:,1)) % original movie

    subplot(2,2,2)
    h=subplot(2,2,2); % set call variable
    ax=get(h,'Position'); % get plot position info
    ax(1:2)=ax(1:2)-0.05;ax(3:4)=ax(3:4)+.1; % shift location and
expand
    set(h,'Position',ax); % write new position info
    imshow(Bcorr)
    hold on
    for tt=xbound
        x = [1 hauteur_crop];
        y = [tt tt];
        plot(x,y,'Color','r','LineStyle','-');
    end
    for tt=ybound
        x = [tt tt];
        y = [1 largeur_crop];
        plot(x,y,'Color','r','LineStyle','-');
    end
    hold off

    %plot([1:1:100,1:1:500]);

    subplot(2,2,3)

```

```

h=subplot(2,2,3);
ax=get(h,'Position'); % get plot position info
ax(1:2)=ax(1:2)-0.05;ax(3:4)=ax(3:4)+.1; % shift location and
expand
set(h,'Position',ax);
imshow(Bout)
hold on
for tt=xbound
    x = [1 hauteur_crop];
    y = [tt tt];
    plot(x,y,'Color','r','LineStyle','-');
end
for tt=ybound
    x = [tt tt];
    y = [1 largeur_crop];
    plot(x,y,'Color','r','LineStyle','-');
end
hold off

h=subplot(2,2,4);
ax=get(h,'Position'); % get plot position info
ax(1:2)=ax(1:2)-0.05;ax(3:4)=ax(3:4)+.1; % shift location and
expand
set(h,'Position',ax);
imshow(cavitated)

% mm=waitforbuttonpress;
count(im)=length(find(cavitated));

end

close(figure(1));
close(hh);

fichsauv=[path, outfilm];
movie2avi(cav_film_mat,fichsauv,'fps',30,'compression','none'); %
write the output

loci=find(cavitated);

% assign "cavitated before the movie" image# 0
rhmap([])=0;

% assign "bad cavities" image# -1
rhmap([])= -1;

rh=[];

```

```

% replacing image# with corresponding RH

for x=1:cavities
    for y=1:cavities
        if rhmap(x,y)==0
            rhmap(x,y)=0.98;
        elseif rhmap(x,y)== -1
            rhmap(x,y)= 1;
        else
            rhmap(x,y)=rh(rhmap(x,y));
        end
    end
end
rhmap(:,26)=0.98;
rhmap(26,:)=0.98;

for x=1:25
    rhmap_f(26-x,:)=rhmap(x,:);
end

% adjusting color bar min using the Pcav from fitting curve:
% 1-(1-Pcav)*2*0.8
rhmap_f(26,:)=1;
rhmap_f(26,26)=0.8296;

close(hh);
pcolor(rhmap_f);hold on; colorbar

```

A.3.2 Survival probability curves fitting (CNT, modified CNT with surface tension distribution, and five-point logistic regression)

```

%%% CNT, Herbert Equation-----
% fs_a7, 15degC

clear
clc

T = 287.6363566;
Pcav=-15.3;

V=(250*10^-6)^2*pi/4*25*10^-6;
tau=3*60*60;

Pliq=0:-0.1:-35;
for i=1:length(Pliq)
    Rc(i)=2*0.073564*(1649-Pliq(i));
    gamma(i)=(4/3*pi*Rc(i)^3)^-1*1.38064852*10^-23/(T*6.62607004*10^-34);
end

```

```

Prob(i) = exp(-log(2)*exp(2*log(gamma(i)*V*tau)*(Pliq(i)/Pcav-1)));
end

%%% CNT with distribution of surface tension, modified from
Olivier's code-----
% fs_a7, 0degC

clear
clc

%% adjustable parameters

sigma0 = 0.020; % effective surface tension
dsigma = 0.09*sigma0; % 0.001505; % standard deviation of surface
tension

n=600; % total number of cavities (each one has a its own surface
tension)

V=pi*(250e-6)^2/4*25e-6; %individual cavity volume
T=273.15+ 0.26; % temperature
dT=0.5; % uncertainty on temperature

tau=12*3600; % duration of experiment (for S-curve)

%% constant parameters

Gamma0 = 1e39;
R=8.314;
kB=R/6.02e23;
v=1.8e-5;

%% Experimental data

RH = [0.99 0.95191 0.90496 0.85173 0.83429 0.82058 0.81035 0.80147
0.79219]; % relative humidity

dRH = [0.24 0.24 0.24 0.24 0.24 0.240 0.24 0.24
0.33] % uncertainty on RH
dRH=dRH+0.2;

P_exp =[0 0.00349 0.03141 0.34031 0.58115 0.76963 0.88482 0.99302
1]; % proba of cavitation
dP_exp = [0.002 0.002 0.002 0.002 0.002 0.002 0.002 0.002
0.02] % uncertainty

p_exp=R*T./v.*log(RH); % calculated pressure

```

```

dp_exp=R*T./v.*dRH./RH + R./v.*log(RH)*dT;    % uncertainty

%% PROGRAM

sigmas = sigma0 + dsigma*randn(n,1); % random generation of surface
tension for all cavities

%% S-curve in pressure
pp=(0:-.1:-40)*1e6; % pressure axis for S-curve
probas=zeros(n,length(pp));

for i=1:n

    probas(i,:)=1-exp(-Gamma0*V*tau*exp(-
16*pi*sigmas(i)^3./(3*kB*T*pp.^2)));

end

probatot=sum(probas,1)/n;

figure(1)
hold on

plot(pp/1e6,probatot)
plot(p_exp/1e6,P_exp,'ok')

grid on

xlabel('pressure (MPa)')
ylabel('cavitation probability')

%% S-curve in activity

aa=exp(pp*v/(R*T)); % activity axis for S-curve

figure(2)
hold on

plot(aa,probatot)
plot(RH,P_exp,'ok')

grid on

xlabel('p_v / p_{sat}')
ylabel('cavitation probability')

```

```

%% Fitting S-Curves with 5 Parameter Logistic Curve -----

clear
clc

% ( y = min + (max-min)/(1+(x/P_cav)^b)^c )
% fs_a7, 15degC

%% adjustable parameters

P_cav = -15.80236683; % MPa
b = 0.506943292 ; % slope factor
c = 0.810103184 ; % asymmetric factor

T=273.15+ 14.49; % temperature

%% Experimental data

RH = [0.99 0.95492 0.90599 0.85038 0.83719 0.82343]; % relative
humidity
p_exp = [-1.32937793154724,-6.10655882080845,-13.0499849005941,-
21.3828071529539,-23.4341281541926,-25.6074382017946]; % MPa, P_liq
translated from RH via IAPWS
P_exp =[0 0.01745 0.27051 0.94764 0.99476 1]; % corresponding proba
of cavitation

%% S-curve in pressure

pp=(0:-.1:-40); % pressure axis for S-curve
Probatot=(1+(exp(pp)./exp(P_cav)).^b)).^(-c);

figure(1)
hold on

plot(pp,Probatot)
plot(p_exp,P_exp,'ok')

grid on

xlabel('pressure (MPa)')
ylabel('cavitation probability')

%% S-curve in activity

R=8.314;
v=1.8e-5;

aa=exp(pp*10^6*v/(R*T)); % activity axis for S-curve

```

```

figure(2)
hold on

plot(aa,Probatot)
plot(RH,P_exp,'ok')

grid on

xlabel('p_vap / p_sat')
ylabel('cavitation probability')

```

A.3.3 Randomness index analysis

```

% cavitation data were from "###_recordmatrix.m" files
% "loc#_" matrixes record the cavitation fractions recorded in both
temperatures # and %
% with ###_recordmatrix.m, "cavitated" matrixes for the fractions
listed where record in deg0/deg5/deg10/deg15 matrixes
% deg0/deg5/deg10/deg15 format: (x,y,z), x: loc, [y,x]: cavitated
matrix.

load matrixdata.mat

% Compare 0degC and 5degC
for i=1:length(loc0_5)
    for x=1:25
        for y=1:25
            A_cav(x,y)=deg0(loc0_5(i),x,y);
            B_cav(x,y)=deg5(loc0_5(i),x,y);
        end
    end

    for j=1:25*25
        if A_cav(j)>0
            A_cav(j)=1;
        end

        if B_cav(j)>0
            B_cav(j)=1;
        end
    end

    sum=0;
    for xx=1:25
        for yy=1:25

```

```

        if A_cav(xx,yy)==B_cav(xx,yy)
            sum = sum+1;
        end
    end
end
F_loc0_5(i)=(sum-52)/573;
frac_loc0_5(i)=loc0_5(i)/573;

F_rand=2*(frac_loc0_5(i))^2-2*frac_loc0_5(i)+1;
G_loc0_5(i)=(F_loc0_5(i)-F_rand)/(1-F_rand);

end

fraction = 0:0.01:1;
F_eqn=2*fraction.^2-2*fraction+1;
G_eqn=zeros(1,length(fraction));

```

A.4 Modified Liquid Path Pattern for a SHLHP Prototype

As discussed in Section 4.6, in the SHLHP prototype design (Figure 4.13(C)) one liquid path connects a total of 200 DRIE pits (100 pits at each end); this configuration largely increase the probability that a liquid path is exposed to any defect in the porous silicon membrane. To increase the stability limit in a device, one way would be to modify the device configuration to further branch the liquid path network. For example, Figure A.2 shows a mask design in which one liquid path connects a total of 50 DRIE pits.

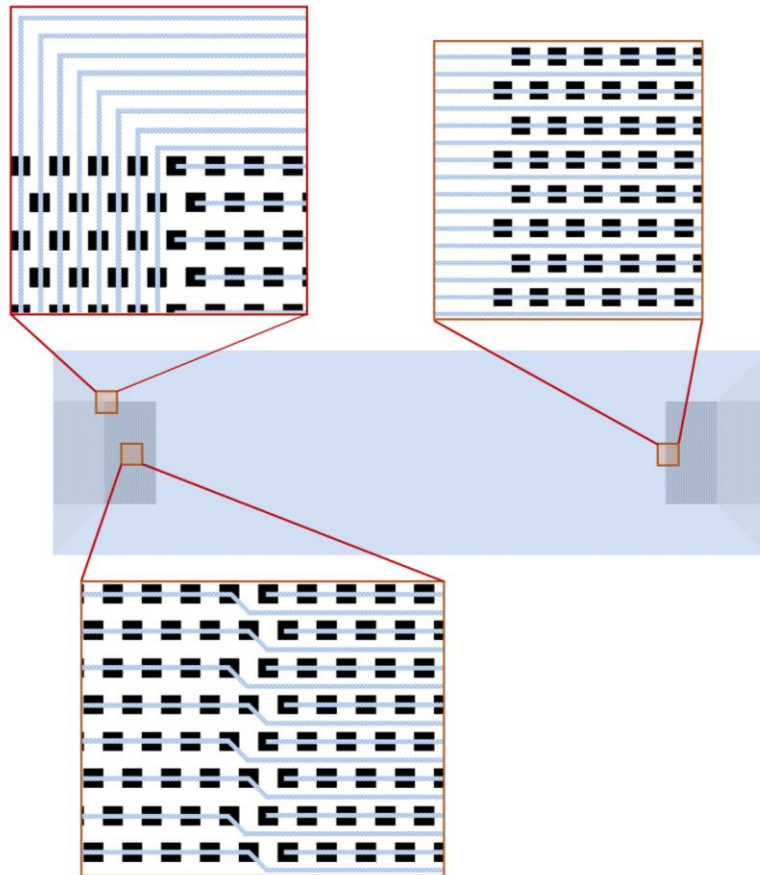


Figure A.2: Modified mask design to branch the liquid path network in a SHLHP.

REFERENCES

- (1) Debenedetti, P. G. *Metastable Liquids: Concepts and Principles*; Princeton University Press, 1996.
- (2) Debenedetti, P. G. Supercooled and Glassy Water. *J. Phys. Condens. Matter* **2003**, *15* (45), 1669–1726.
- (3) Pallares, G.; Azouzi, M. E. M.; Gonzalez, M. A.; Aragonés, J. L.; Abascal, J. L. F.; Valeriani, C.; Caupin, F. Anomalies in Bulk Supercooled Water at Negative Pressure. *Proc. Natl. Acad. Sci.* **2014**, *111* (22), 7936–7941.
- (4) Caupin, F.; Stroock, A. D. The Stability Limit and Other Open Questions on Water at Negative Pressure. *Liq. Polymorph. Adv. Chem. Phys.* **2013**, *152*, 51–80.
- (5) Herbert, E.; Balibar, S.; Caupin, F. Cavitation Pressure in Water. *Phys. Rev. E - Stat. Nonlinear, Soft Matter Phys.* **2006**, *74* (4), 1–22.
- (6) Alvarenga, A. D.; Grimsditch, M.; Bodnar, R. J. Elastic Properties of Water under Negative Pressures. *J. Chem. Phys.* **1993**, *98*, 8392–8396.
- (7) Berthelot, M. Sur Quelques Phénomènes de Dilatation Forcée Des Liquides. *Ann. Chim. Phys.* **1850**, *30*, 232–237.
- (8) Zheng, Q.; Durben, D. J.; Wolf, G. H.; Angell, C. A. Liquids at Large Negative Pressures: Water at the Homogeneous Nucleation Limit. *Science* **1991**, *254* (5033), 829–832.
- (9) Shmulovich, K. I.; Mercury, L.; Thiéry, R.; Ramboz, C.; El Mekki, M. Experimental Superheating of Water and Aqueous Solutions. *Geochim. Cosmochim. Acta* **2009**, *73* (9), 2457–2470.
- (10) Briggs, L. J. Limiting Negative Pressure of Water. *J. Appl. Phys.* **1950**, *21* (7), 721–722.
- (11) Cochard, H.; Barigah, T.; Herbert, E.; Caupin, F. Cavitation in Plants at Low Temperature: Is Sap Transport Limited by the Tensile Strength of Water as Expected from Briggs' Z-Tube Experiment? *New Phytol.* **2007**, *173* (3), 571–575.
- (12) Galloway, W. J. An Experimental Study of Acoustically Induced Cavitation in

- Liquids. *J. Acoust. Soc. Am.* **1954**, 26 (5), 849–857.
- (13) Greenspan, M.; Tschiegg, C. E. Radiation-Induced Acoustic Cavitation; Apparatus and Some Results. *J. Res. Natl. Bur. Stand., Sect. C* **1967**, 71, 299.
- (14) Machin, W. D.; Stuckless, J. T. Capillary-Condensed Water in Silica Gel. *J. Chem. Soc. Faraday Trans. 1* **1985**, 81 (3), 597.
- (15) Wheeler, T. D.; Stroock, A. D. The Transpiration of Water at Negative Pressures in a Synthetic Tree. *Nature* **2008**, 455 (7210), 208–212.
- (16) Wheeler, T. D.; Stroock, A. D. Stability Limit of Liquid Water in Metastable Equilibrium with Subsaturated Vapors. *Langmuir* **2009**, 25 (13), 7609–7622.
- (17) Azouzi, M. E. M.; Ramboz, C.; Lenain, J.-F.; Caupin, F. A Coherent Picture of Water at Extreme Negative Pressure. *Nat. Phys.* **2013**, 9 (1), 38–41.
- (18) Haar, L.; Gallagher, J. S.; Kell, G. S. *National Bureau of Standards-National Research Council Steam Tables*; CRC Press, 1984.
- (19) Poole, P. H.; Sciortino, F.; Essmann, U.; Stanley, H. E. Phase Behaviour of Metastable Water. *Nature* **1992**, 360 (6402), 324–328.
- (20) Yamada, M.; Mossa, S.; Stanley, H. E.; Sciortino, F. Interplay between Time-Temperature Transformation and the Liquid-Liquid Phase Transition in Water. *Phys. Rev. Lett.* **2002**, 88 (19), 195701.
- (21) Henderson, S. J.; Speedy, R. J. A Berthelot-Bourdon Tube Method for Studying Water under Tension. *J. Phys. E.* **1980**, 13 (7), 778–782.
- (22) Henderson, S. J.; Speedy, R. J. Temperature of Maximum Density in Water at Negative Pressure. *J. Phys. Chem.* **1987**, 17 (6), 3062–3068.
- (23) Hiro, K.; Ohde, Y.; Tanzawa, Y. Stagnations of Increasing Trends in Negative Pressure with Repeated Cavitation in Water/Metal Berthelot Tubes as a Result of Mechanical Sealing. *J. Phys. D. Appl. Phys.* **2003**, 36, 592–597.
- (24) Davitt, K.; Arvengas, A.; Caupin, F. Water at the Cavitation Limit: Density of the Metastable Liquid and Size of the Critical Bubble. *EPL (Europhysics Lett.)* **2010**, 90, 16002.
- (25) Larter, M.; Brodribb, Timothy, J.; Pfautsch, S.; Burlett, R.; Cochard, H.; Delzon, S. Extreme Aridity Pushes Trees to Their Physical Limits. *Plant Physiol.* **2015**, 168 (July), pp.00223.2015.

- (26) Caupin, F.; Arvengas, A.; Davitt, K.; Azouzi, M. E. M.; Shmulovich, K. I.; Ramboz, C.; Sessoms, D. A.; Stroock, A. D. Exploring Water and Other Liquids at Negative Pressure. *J. Phys. Condens. Matter* **2012**, *24* (28), 284110.
- (27) Nobel, P. S. *Physicochemical and Environmental Plant Physiology*, Third Edit.; Academic Press, 2005.
- (28) Arvengas, A.; Davitt, K.; Caupin, F. Fiber Optic Probe Hydrophone for the Study of Acoustic Cavitation in Water. *Rev. Sci. Instrum.* **2011**, *82* (3), 034904.
- (29) Wurster, C.; Köhler, M.; Pecha, R.; Eisenmenger, W.; Suhr, D.; Irmer, U.; Brümmer, F.; Hülser, D. Negative Pressure Measurements of Water Using the Glass Fiber Optic Hydrophone. In *1st World Congress on Ultrasonics*; Berlin, 1995; pp 635–638.
- (30) Balling, A.; Zimmermann, U. Comparative Measurements of the Xylem Pressure of Nicotiana Plants by Means of the Pressure Bomb and Pressure Probe. *Planta* **1990**, *182* (3), 325–338.
- (31) Smith, A. M. Negative Pressure Generated By Octopus Suckers: A Study of the Tensile Strength of Water in Nature. *J. Exp. Biol.* **1991**, *157* (1), 257–271.
- (32) Vincent, O.; Sessoms, D. A.; Huber, E. J.; Guioth, J.; Stroock, A. D. Drying by Cavitation and Poroelastic Relaxations in Porous Media with Macroscopic Pores Connected by Nanoscale Throats. *Phys. Rev. Lett.* **2014**, *113* (3), 1–5.
- (33) Vincent, O.; Szenicer, A.; Stroock, A. D. Capillarity-Driven Flows at the Continuum Limit. *Prepr. arXiv1510.00411* **2015**, 1–5.
- (34) Stroock, A. D.; Pagay, V. V.; Zwieniecki, M. A.; Michele Holbrook, N. The Physicochemical Hydrodynamics of Vascular Plants. *Annu. Rev. Fluid Mech.* **2014**, *46* (1), 615–642.
- (35) Brinker, C. J.; Scherer, G. W. *Sol- Gel Science: The Physics and Chemistry of Sol-Gel Processing*; Academic press, 1990.
- (36) Arndt, R. E. A. Cavitation in Fluid Machinery and Hydraulic Structures. *Annu. Rev. Fluid Mech.* **1981**, *13* (1), 273–328.
- (37) Franc, J.-P.; Michel, J.-M. *Fundamentals of Cavitation*; Springer Science & Business Media, 2006.
- (38) Hayward, A. T. J. Mechanical Pump with a Suction Lift of 17 Metres. *Nature* **1970**.

- (39) Chen, I.-T.; Pharkya, A.; Stroock, A. D. Analysis of Superheated Loop Heat Pipes Exploiting Nanoporous Wick Membranes. *AIChE J.* **2014**, *60* (2), 762–777.
- (40) Wu, M. S.; Liu, K. H.; Wang, Y. Y.; Wan, C. C. Heat Dissipation Design for Lithium-Ion Batteries. *J. Power Sources* **2002**, *109* (1), 160–166.
- (41) Zalba, B.; Marín, J. M.; Cabeza, L. F.; Mehling, H. *Review on Thermal Energy Storage with Phase Change: Materials, Heat Transfer Analysis and Applications*; 2003; Vol. 23.
- (42) Sharma, A.; Tyagi, V. V.; Chen, C. R.; Buddhi, D. Review on Thermal Energy Storage with Phase Change Materials and Applications. *Renew. Sustain. Energy Rev.* **2009**, *13* (2), 318–345.
- (43) Pastukhov, V. G.; Maidanik, Y. F.; Vershinin, C. V.; Korukov, M. A. Miniature Loop Heat Pipes for Electronics Cooling. *Appl. Therm. Eng.* **2003**, *23* (9 SPEC.), 1125–1135.
- (44) Garimella, S. V. Advances in Mesoscale Thermal Management Technologies for Microelectronics. *Microelectronics J.* **2006**, *37* (11), 1165–1185.
- (45) Pistoia, G. *Battery Operated Devices and Systems: From Portable Electronics to Industrial Products*; Elsevier, 2009.
- (46) McCabe, W. L.; Smith, J. C.; Harriot, P. *Unit Operations of Chemical Engineering*; McGraw-Hill Education, 2005.
- (47) Wang, G.; Mishkinis, D.; Nikanpour, D. Capillary Heat Loop Technology: Space Applications and Recent Canadian Activities. *Appl. Therm. Eng.* **2008**, *28* (4), 284–303.
- (48) Ball, P. Computer Engineering: Feeling the Heat. *Nature* **2012**, *492* (7428), 174–176.
- (49) Faghri, A. *Heat Pipe Science and Technology*; Taylor & Francis Group: New York, 1995.
- (50) Ku, J. Operating Characteristics of Loop Heat Pipes. *29 th Int. Conf. Environ. Syst.* **1999**, 16.
- (51) Maydanik, Y. F. Loop Heat Pipes. *Appl. Therm. Eng.* **2005**, *25* (5-6), 635–657.
- (52) Launay, S.; Sartre, V.; Bonjour, J. Parametric Analysis of Loop Heat Pipe Operation: A Literature Review. *Int. J. Therm. Sci.* **2007**, *46* (7), 621–636.

- (53) Chuang, P.-Y. A. An Improved Steady-State Model of Loop Heat Pipe Based on Experimental and Theoretical Analyses, 2003.
- (54) Pouzet, E.; Joly, J. L.; Platel, V.; Grandpeix, J. Y.; Butto, C. Dynamic Response of a Capillary Pumped Loop Subjected to Various Heat Load Transients. *Int. J. Heat Mass Transf.* **2004**, *47* (10-11), 2293–2316.
- (55) Boure, J. A.; Bergles, A. E.; Tong, L. S. Review of Two-Phase Flow Instability. *Nucl. Eng. Des.* **1973**, *25*, 165–192.
- (56) Li, J.; Wang, D.; Peterson, G. P. Experimental Studies on a High Performance Compact Loop Heat Pipe with a Square Flat Evaporator. *Appl. Therm. Eng.* **2010**, *30* (6-7), 741–752.
- (57) Scholander, P. F.; Hammel, H. T.; Bradstreet, E. D.; Hemmingsen, E. A. Sap Pressure in Vascular Plants: Negative Hydrostatic Pressure Can Be Measured in Plants. *Science* **1965**, *148* (3668), 339–346.
- (58) Choat, B.; Jansen, S.; Brodribb, T. J.; Cochard, H.; Delzon, S.; Bhaskar, R.; Bucci, S. J.; Feild, T. S.; Gleason, S. M.; Hacke, U. G.; et al. Global Convergence in the Vulnerability of Forests to Drought. *Nature* **2012**, *491* (7426), 752–755.
- (59) Kim, B.; Peterson, G. P. Experimental Study of a Reversible Loop Heat Pipe. *J. Thermophys. Heat Transf.* **2005**, *19* (4), 519–526.
- (60) *Handbook of Porous Silicon*; Canham, L., Ed.; Springer International Publishing, 2014.
- (61) Cullis, A. G.; Canham, L. T.; Calcott, P. D. J. The Structural and Luminescence Properties of Porous Silicon. *J. Appl. Phys.* **1997**, *82* (August), 909–965.
- (62) Bisi, O.; Ossicini, S.; Pavesi, L. Porous Silicon: A Quantum Sponge Structure for Silicon Based Optoelectronics. *Surf. Sci. Rep.* **2000**, *38* (1), 1–126.
- (63) Guan, Y.; Fredlund, D. G. Use of the Tensile Strength of Water for the Direct Measurement of High Soil Suction. *Can. Geotech. J.* **1997**, *34* (4), 604–614.
- (64) Kalsin, A. M. Electrostatic Self-Assembly of Binary Nanoparticle Crystals with a Diamond-Like Lattice. *Science* **2006**, *312* (5772), 420–424.
- (65) Arora, H.; Li, Z.; Sai, H.; Kamperman, M.; Warren, S. C.; Wiesner, U. Block Copolymer Directed Nanoporous Metal Thin Films. *Macromol. Rapid Commun.* **2010**, *31* (22), 1960–1964.
- (66) Paulo W. Winston, D. H. B. Saturated Solutions for the Control of Humidity in

- Biological Research. *Ecology* **1960**, *41* (1), 232–237.
- (67) Rockland, L. Saturated Salt Solutions for Static Control of Relative Humidity between 5 and 40 C. *Anal. Chem.* **1960**, *32* (10), 1375–1376.
- (68) Kaya, T.; Hoang, T. T. Mathematical Modeling of Loop Heat Pipes and Experimental Validation. *J. Thermophys. Heat Transf.* **1999**, *13* (3), 314–320.
- (69) Hamdan, M. Loop Heat Pipe (LHP) Modeling and Development by Utilizing Coherent Porous Silicon (CPS) Wicks, 2003.
- (70) Demidov, A. S.; Yatsenko, E. S. Investigation of Heat and Mass Transfer in the Evaporation Zone of a Heat Pipe Operating by the “inverted Meniscus” Principle. *Int. J. Heat Mass Transf.* **1994**, *37* (14), 2155–2163.
- (71) Cao, Y.; Faghri, A. Conjugate Analysis of a Flat-Plate Type Evaporator for Capillary Pumped Loops with Three-Dimensional Vapor Flow in the Groove. *Int. J. Heat Mass Transf.* **1994**, *37* (3), 401–409.
- (72) Cotter, T. P. Theory of Heat Pipes. **1965**.
- (73) Launay, S.; Sartre, V.; Bonjour, J. Analytical Model for Characterization of Loop Heat Pipes. *J. Thermophys. Heat Transf.* **2008**, *22* (4), 623–631.
- (74) Atkins, P.; Paula, J. de. *Physical Chemistry*, 9th ed.; Oxford University Press, 2009.
- (75) Green, D. W.; Perry, R. H. *Perry’s Chemical Engineer’s Handbook*, 8th ed.; McGraw-Hill Book Company, 2008.
- (76) Incropera, F. P.; DeWitt, D. P.; Bergman, T. L.; Lavine, A. S. *Fundamentals of Heat and Mass Transfer*; Incropera, F. P., Incropera, F. P. F. O. H. A. M. T., Eds.; Dekker Mechanical Engineering; John Wiley & Sons, 2007; Vol. 6th.
- (77) Brennan, P. J.; Krolczek, E. J. Heat Pipe Design Handbook. **1979**, *1*.
- (78) Tyree, M. T.; Sperry, J. S. Vulnerability of Xylem to Cavitation and Embolism. *Annu. Rev. Plant Physiol. Plant Mol. Biol.* **1989**, *40* (1), 19–36.
- (79) Borghetti, M. *Water Transport in Plants under Climatic Stress*; Cambridge University Press, 1993.
- (80) Tyree, M. T.; Zimmermann, M. H. *Xylem Structure and the Ascent of Sap*; Springer Science & Business Media, 2013; Vol. 12.

- (81) Zwieniecki, M. A.; Holbrook, N. M. Confronting Maxwell's Demon: Biophysics of Xylem Embolism Repair. *Trends Plant Sci.* **2009**, *14* (10), 530–534.
- (82) Pagay, V.; Santiago, M.; Sessoms, D. A.; Huber, E. J.; Vincent, O.; Pharkya, A.; Corso, T. N.; Lakso, A. N.; Stroock, A. D. A Microtensiometer Capable of Measuring Water Potentials below -10 MPa. *Lab Chip* **2014**, *14* (15), 2806–2817.
- (83) Wagner, W.; Pruß, A. The IAPWS Formulation 1995 for the Thermodynamic Properties of Ordinary Water Substance for General and Scientific Use. *J. Phys. Chem. Ref. Data* **1999**, *31* (2), 387.
- (84) The International Association for the Properties of Water and Steam. Revised Release on the IAPWS Formulation 1995 for the Thermodynamic Properties of Ordinary Water Substance for General and Scientific Use, September 2009.
- (85) Murphy, D. M.; Koop, T. Review of the Vapour Pressures of Ice and Supercooled Water for Atmospheric Applications. *Q. J. R. Meteorol. Soc.* **2005**, *131* (608), 1539–1565.
- (86) Lemmon, E. W.; McLinden, M. O.; Friend, D. G. Thermophysical Properties of Fluid Systems. In *NIST Chemistry WebBook, NIST Standard Reference Database Number 69*, Eds. P.J. Linstrom and W.G. Mallard; National Institute of Standards and Technology: Gaithersburg MD, 20899.
- (87) Fisher, J. C. The Fracture of Liquids. *J. Appl. Phys.* **1948**, *19* (11), 1062–1067.
- (88) Blander, M.; Katz, J. L. Bubble Nucleation in Liquids. *AIChE J.* **1975**, *21* (5), 833–848.
- (89) Apfel, R. E. The Role of Impurities in Cavitation-Threshold Determination. *J. Acoust. Soc. Am.* **1970**, *48* (5B), 1179.
- (90) Atchley, A. A.; Prosperetti, A. The Crevice Model of Bubble Nucleation. *J. Acoust. Soc. Am.* **1989**, *86* (3), 1065–1084.
- (91) Turner, D. R. Electropolishing Silicon in Hydrofluoric Acid Solutions. *J. Electrochem. Soc.* **1958**, *105* (7), 402–408.
- (92) Mauckner, G.; Rebitzer, W.; Thonke, K.; Sauer, R. Quantum Confinement Effects in Absorption and Emission of Freestanding Porous Silicon. *Solid State Commun.* **1994**, *91* (9), 717–720.
- (93) Ghulinyan, M.; Oton, C. J.; Bonetti, G.; Gaburro, Z.; Pavese, L. Free-Standing Porous Silicon Single and Multiple Optical Cavities. *J. Appl. Phys.* **2003**, *93* (12), 9724.

- (94) Solanki, C. S.; Bilyalov, R. R.; Bender, H.; Poortmans, J. New Approach for the Formation and Separation of a Thin Porous Silicon Layer. *Phys. Status Solidi* **2000**, *182* (1), 97–101.
- (95) Solanki, C.; Bilyalov, R. Self-Standing Porous Silicon Films by One-Step Anodizing. *J. Electrochem. Soc.* **2004**, *151* (5), C307–C314.
- (96) Goryachev, D. N.; Belyakov, L. V.; Sreseli, O. M. Free-Standing Luminescent Layers of Porous Silicon. *Semiconductors* **2010**, *44* (12), 1588–1591.
- (97) Iliescu, C.; Jing, J.; Tay, F. E. H.; Miao, J.; Sun, T. Characterization of Masking Layers for Deep Wet Etching of Glass in an Improved HF/HCl Solution. *Surf. Coatings Technol.* **2005**, *198* (1-3 SPEC. ISS.), 314–318.
- (98) Caupin, F.; Herbert, E. Cavitation in Water: A Review. *Comptes Rendus Phys.* **2006**, *7* (9-10), 1000–1017.
- (99) Sumner, A. L.; Menke, E. J.; Dubowski, Y.; Newberg, J. T.; Penner, R. M.; Hemminger, J. C.; Wingen, L. M.; Brauers, T.; Finlayson-Pitts, B. J. The Nature of Water on Surfaces of Laboratory Systems and Implications for Heterogeneous Chemistry in the Troposphere. *Phys. Chem. Chem. Phys.* **2004**, *6* (3), 604.
- (100) Cao, L.; Price, T. P.; Weiss, M.; Gao, D. Super Water- and Oil-Repellent Surfaces on Intrinsically Hydrophilic and Oleophilic Porous Silicon Films. *Langmuir* **2008**, *24* (5), 1640–1643.
- (101) Canham, L. T.; Cox, T. I.; Loni, A.; Simons, A. J. Progress towards Silicon Optoelectronics Using Porous Silicon Technology. *Appl. Surf. Sci.* **1996**, *102*, 436–441.
- (102) Richter, A.; Steiner, P.; Kozlowski, F.; Lang, W. Current-Induced Light Emission from a Porous Silicon Device. *IEEE Electron Device Lett.* **1991**, *12* (12), 691–692.
- (103) Loni, A.; Canham, L. T.; Berger, M. G.; Arens-Fischer, R.; Munder, H.; Luth, H.; Arrand, H. F.; Benson, T. M. Porous Silicon Multilayer Optical Waveguides. *Thin Solid Films* **1996**, *276* (1-2), 143–146.
- (104) Smestad, G.; Kunst, M.; Vial, C. Photovoltaic Response in Electrochemically Prepared Photoluminescent Porous Silicon. *Sol. Energy Mater. Sol. Cells* **1992**, *26* (4), 277–283.
- (105) Holmstrom, R. P.; Chi, J. Y. Complete Dielectric Isolation by Highly Selective and Self-stopping Formation of Oxidized Porous Silicon. *Appl. Phys. Lett.* **1983**, *42* (4), 386–388.

- (106) Oakes, L.; Westover, A.; Mares, J. W.; Chatterjee, S.; Erwin, W. R.; Bardhan, R.; Weiss, S. M.; Pint, C. L. Surface Engineered Porous Silicon for Stable, High Performance Electrochemical Supercapacitors. *Sci. Rep.* **2013**, *3*, 3020.
- (107) Janshoff, A.; Dancil, K. P. S.; Steinem, C.; Greiner, D. P.; Lin, V. S. Y.; Gurtner, C.; Motesharei, K.; Sailor, M. J.; Reza Ghadiri, M. Macroporous P-Type Silicon Fabry-Perot Layers. Fabrication, Characterization, and Applications in Biosensing. *J. Am. Chem. Soc.* **1998**, *120* (46), 12108–12116.
- (108) Schöning, M. J.; Kurowski, A.; Thust, M.; Kordos, P.; Schultze, J. W.; Lüth, H. Capacitive Microsensors for Biochemical Sensing Based on Porous Silicon Technology. *Sensors Actuators B* **2000**, *64* (1-3), 59–64.
- (109) Zhang, X. G. Porous Silicon Formation and Electropolishing of Silicon by Anodic Polarization in HF Solution. *J. Electrochem. Soc.* **1989**, *136* (5), 1561.
- (110) Lehmann, V.; Gösele, U. Porous Silicon Formation: A Quantum Wire Effect. *Appl. Phys. Lett.* **1991**, *58* (8), 856–858.
- (111) Kang, Y.; Jorné, J. Morphological Stability Analysis of Porous Silicon Formation. *J. Electrochem. Soc.* **1993**, *140* (8), 2258.
- (112) Corbett, J. W.; Shereshevskii, D. I.; Verner, I. V. Changes in the Creation of Point Defects Related to the Formation of Porous Silicon. *Phys. Status Solidi* **1995**, *147* (1), 81–89.
- (113) Allongue, P.; De Villeneuve, C. H.; Pinsard, L.; Bernard, M. C. Evidence for Hydrogen Incorporation during Porous Silicon Formation. *Appl. Phys. Lett.* **1995**, *67* (1995), 941.
- (114) Beale, M. I. J.; Chew, N. G.; Uren, M. J.; Cullis, A. G.; Benjamin, J. D. Microstructure and Formation Mechanism of Porous Silicon. *Appl. Phys. Lett.* **1985**, *46* (1), 86–88.
- (115) Smith, R. L.; Collins, S. D. Porous Silicon Formation Mechanisms. *J. Appl. Phys.* **1992**, *71* (8), R1–R22.
- (116) Smith, R. L.; Chuang, S. F.; Collins, S. D. A Theoretical Model of the Formation Morphologies of Porous Silicon. *J. Electron. Mater.* **1988**, *17* (6), 533–541.
- (117) Lehmann, V.; Gösele, U. Porous Silicon: Quantum Sponge Structures Grown via a Self-Adjusting Etching Process. *Adv. Mater.* **1992**, *4* (2), 114–116.
- (118) Unagami, T. Formation Mechanism of Porous Silicon Layer by Anodization in HF Solution. *J. Electrochem. Soc.* **1980**, *127* (5), 1211.

- (119) Parkhutik, V. P.; Glinenko, L. K.; Labunov, V. A. Kinetics and Mechanism of Porous Layer Growth during N-Type Silicon Anodization in HF Solution. *Surf. Technol.* **1983**, *20* (3), 265–277.
- (120) Föll, H.; Christophersen, M.; Carstensen, J.; Hasse, G. Formation and Application of Porous Silicon. *Mater. Sci. Eng. R Reports* **2002**, *39* (4), 93–141.
- (121) Pavesi, L. Porous Silicon Dielectric Multilayers and Microcavities. *La Riv. del Nuovo Cim.* **1997**, *20* (10), 1–76.
- (122) Kumar, P.; Huber, P. Effect of Etching Parameter on Pore Size and Porosity of Electrochemically Formed Nanoporous Silicon. *J. Nanomater.* **2007**, *2007*, 1–4.
- (123) Rouquerol, J.; Avnir, D.; Fairbridge, C. W.; D. H. Everett; Haynes, J. H.; Pernicone, N.; Ramsay, J. D. F.; Sing, K. S. W.; Unger, K. K. Recommendations for the Characterization of Porous Solids. *Pure Appl. Chem.* **1994**, *66* (8), 1739–1758.
- (124) Lehmann, V.; Stengl, R.; Luigart, A. On the Morphology and the Electrochemical Formation Mechanism of Mesoporous Silicon. *Mater. Sci. Eng. B Solid-State Mater. Adv. Technol.* **2000**, *69*, 11–22.
- (125) Propst, E. K.; Kohl, P. A. The Electrochemical Oxidation of Silicon and Formation of Porous Silicon in Acetonitrile. *J. Electrochem. Soc.* **1994**, *141* (4), 1006–1013.
- (126) Wehrspohn, R. B.; Chazalviel, J.-N.; Ozanam, F. Macropore Formation in Highly Resistive P-Type Crystalline Silicon. *J. Electrochem. Soc.* **1998**, *145* (8), 2958–2961.
- (127) Christophersen, M.; Carstensen, J.; Feuerhake, A.; Föll, H. Crystal Orientation and Electrolyte Dependence for Macropore Nucleation and Stable Growth on P-Type Si. *Mater. Sci. Eng. B* **2000**, *69-70*, 194–198.
- (128) Ponomarev, E. A.; Levy-Clement, C. Macropore Formation on P-Type Si in Fluoride Containing Organic Electrolytes. *Electrochem. Solid-State Lett.* **1998**, *1* (1), 42.
- (129) Lehmann, V.; Rönnebeck, S. The Physics of Macropore Formation in Low-Doped P-Type Silicon. *J. Electrochem. Soc.* **1999**, *146* (8), 2968–2975.
- (130) Chazalviel, J.-N.; Ozanam, F.; Gabouze, N.; Fellah, S.; Wehrspohn, R. B. Quantitative Analysis of the Morphology of Macropores on Low-Doped P-Si. *J. Electrochem. Soc.* **2002**, *149* (10), C511.

- (131) Carstensen, J.; Christophersen, M.; Föll, H. Pore Formation Mechanisms for the Si-HF System. *Mater. Sci. Eng. B* **2000**, 69-70, 23–28.
- (132) Dhillon, N. S. Micro-Columnated Loop Heat Pipe: The Future of Electronic Substrates, University of California, Berkeley, 2012.
- (133) Anthony, T. R. Anodic Bonding of Imperfect Surfaces. *J. Appl. Phys.* **1983**, 54 (5), 2419–2428.
- (134) Masuda, H.; Fukuda, K. Ordered Metal Nanohole Arrays Made by a Two-Step Replication of Honeycomb Structures of Anodic Alumina. *Science* **1995**, 268 (5216), 1466–1468.
- (135) Lee, W.; Park, S.-J. Porous Anodic Aluminum Oxide: Anodization and Templated Synthesis of Functional Nanostructures. *Chem. Rev.* **2014**, 114 (15), 7487–7556.
- (136) Sulka, G. D. Highly Ordered Anodic Porous Alumina Formation by Self-Organized Anodizing. In *Nanostructured materials in electrochemistry*; John Wiley & Sons, 2008; pp 1–116.
- (137) Sulka, G. D.; Parkoła, K. G. Anodising Potential Influence on Well-Ordered Nanostructures Formed by Anodisation of Aluminium in Sulphuric Acid. *Thin Solid Films* **2006**, 515 (1), 338–345.
- (138) O’sullivan, J. P.; Wood, G. C. The Morphology and Mechanism of Formation of Porous Anodic Films on Aluminium. In *Proceedings of the Royal Society of London A: Mathematical, Physical and Engineering Sciences*; The Royal Society, 1970; pp 511–543.
- (139) Parkhutik, V. P.; Shershulsky, V. I. Theoretical Modelling of Porous Oxide Growth on Aluminium. *J. Phys. D. Appl. Phys.* **1992**, 25 (8), 1258–1263.
- (140) Sulka, G. D.; Parkoła, K. G. Temperature Influence on Well-Ordered Nanopore Structures Grown by Anodization of Aluminium in Sulphuric Acid. *Electrochim. Acta* **2007**, 52 (5), 1880–1888.
- (141) Li, A. P.; Müller, F.; Birner, A.; Nielsch, K.; Gösele, U. Hexagonal Pore Arrays with a 50–420 nm Interpore Distance Formed by Self-Organization in Anodic Alumina. *J. Appl. Phys.* **1998**, 84 (11), 6023–6026.
- (142) Chu, S. Z.; Wada, K.; Inoue, S.; Isogai, M.; Katsuta, Y.; Yasumori, A. Large-Scale Fabrication of Ordered Nanoporous Alumina Films with Arbitrary Pore Intervals by Critical-Potential Anodization. *J. Electrochem. Soc.* **2006**, 153 (9), B384.

- (143) Nielsch, K.; Choi, J.; Schwirn, K.; Wehrspohn, R. B.; Gösele, U. Self-Ordering Regimes of Porous Alumina: The 10 Porosity Rule. *Nano Lett.* **2002**, *2* (7), 677–680.
- (144) Osmanbeyoglu, H. U.; Hur, T. B.; Kim, H. K. Thin Alumina Nanoporous Membranes for Similar Size Biomolecule Separation. *J. Memb. Sci.* **2009**, *343* (1-2), 1–6.
- (145) Furneaux, R. C.; Rigby, W. R.; Davidson, A. P. The Formation of Controlled-Porosity Membranes from Anodically Oxidized Aluminum. *Nature* **1989**, *337* (6203), 147–149.
- (146) Jiang, X.; Mishra, N.; Turner, J. N.; Spencer, M. G. Freestanding Alumina Membrane by Double-Layer Anodization. *IEEE Trans. Nanotechnol.* **2007**, *6* (3), 328–333.
- (147) Jung, H. Y.; Jung, S. M.; Gu, G. H.; Suh, J. S. Anodic Aluminum Oxide Membrane Bonded on a Silicon Wafer for Carbon Nanotube Field Emitter Arrays. *Appl. Phys. Lett.* **2006**, *89* (1), 13121.
- (148) Crouse, D.; Lo, Y.-H.; Miller, A. E.; Crouse, M. Self-Ordered Pore Structure of Anodized Aluminum on Silicon and Pattern Transfer. *Appl. Phys. Lett.* **2000**, *76* (1), 49.
- (149) Rabin, O.; Herz, P. R.; Lin, Y.-M.; Akinwande, A. I.; Cronin, S. B.; Dresselhaus, M. S. Formation of Thick Porous Anodic Alumina Films and Nanowire Arrays on Silicon Wafers and Glass. *Adv. Funct. Mater.* **2003**, *13* (8), 631–638.
- (150) Toh, C. S.; Kayes, B. M.; Nemanick, E. J.; Lewis, N. S. Fabrication of Free-Standing Nanoscale Alumina Membranes with Controllable Pore Aspect Ratios. *Nano Lett.* **2004**, *4* (5), 767–770.
- (151) Petukhov, D. I.; Napolskii, K. S.; Berekchiyan, M. V.; Lebedev, A. G.; Eliseev, A. A. Comparative Study of Structure and Permeability of Porous Oxide Films on Aluminum Obtained by Single- and Two-Step Anodization. *ACS Appl. Mater. Interfaces* **2013**, *5* (16), 7819–7824.
- (152) Sun, Z.; Kim, H. K. Growth of Ordered, Single-Domain, Alumina Nanopore Arrays with Holographically Patterned Aluminum Films. *Appl. Phys. Lett.* **2002**, *81* (18), 3458.
- (153) Van den Brink, J. Graphene: From Strength to Strength. *Nat. Nanotechnol.* **2007**, *2* (4), 199–201.
- (154) Geim, A. K.; Novoselov, K. S. The Rise of Graphene. *Nat. Mater.* **2007**, 183–

191.

- (155) Dikin, D. A.; Stankovich, S.; Zimney, E. J.; Piner, R. D.; Dommett, G. H. B.; Evmenenko, G.; Nguyen, S. T.; Ruoff, R. S. Preparation and Characterization of Graphene Oxide Paper. *Nature* **2007**, *448* (7152), 457–460.
- (156) Chen, H.; Müller, M. B.; Gilmore, K. J.; Wallace, G. G.; Li, D. Mechanically Strong, Electrically Conductive, and Biocompatible Graphene Paper. *Adv. Mater.* **2008**, *20* (18), 3557–3561.
- (157) Geim, A. K. Graphene: Status and Prospects. *Science* **2009**, *324* (5934), 1530–1534.
- (158) Eda, G.; Chhowalla, M. Chemically Derived Graphene Oxide: Towards Large-Area Thin-Film Electronics and Optoelectronics. *Adv. Mater.* **2010**, *22* (22), 2392–2415.
- (159) Nair, R. R.; Wu, H. A.; Jayaram, P. N.; Grigorieva, I. V.; Geim, A. K. Unimpeded Permeation of Water Through Helium-Leak-Tight Graphene-Based Membranes. *Science* **2012**, *335* (6067), 442–444.
- (160) Wang, J.-Y.; Yang, S.-Y.; Huang, Y.-L.; Tien, H.-W.; Chin, W.-K.; Ma, C.-C. M. Preparation and Properties of Graphene Oxide/polyimide Composite Films with Low Dielectric Constant and Ultrahigh Strength via in Situ Polymerization. *J. Mater. Chem.* **2011**, *21* (35), 13569.
- (161) Robinson, J. T.; Zalalutdinov, M.; Baldwin, J. W.; Snow, E. S.; Wei, Z.; Sheehan, P.; Houston, B. H. Wafer-Scale Reduced Graphene Oxide Films for Nanomechanical Devices. *Nano Lett.* **2008**, *8* (10), 3441–3445.
- (162) Hummers, Jr., W. S.; Offeman, R. E. Preparation of Graphitic Oxide. *J. Am. Chem. Soc* **1958**, *80* (1937), 1339.
- (163) Zhang, L.; Lu, Z.; Zhao, Q.; Huang, J.; Shen, H.; Zhang, Z. Enhanced Chemotherapy Efficacy by Sequential Delivery of siRNA and Anticancer Drugs Using PEI-Grafted Graphene Oxide. *Small* **2011**, *7* (4), 460–464.
- (164) Park, S.; Dikin, D. A.; Nguyen, S. T.; Ruoff, R. S. Graphene Oxide Sheets Chemically Cross-Linked by Polyallylamine. *J. Phys. Chem. C* **2009**, *113* (36), 15801–15804.
- (165) Park, S.; Lee, K.-S.; Bozoklu, G.; Cai, W.; Nguyen, S. T.; Ruoff, R. S. Graphene Oxide Papers Modified by Divalent Ions-Enhancing Mechanical Properties via Chemical Cross-Linking. *ACS Nano* **2008**, *2* (3), 572–578.

- (166) Hammond, P. T. Form and Function in Multilayer Assembly: New Applications at the Nanoscale. *Adv. Mater.* **2004**, *16* (15), 1271–1293.
- (167) Joseph, N.; Ahmadiannamini, P.; Hoogenboom, R.; Vankelecom, I. F. J. Layer-by-Layer Preparation of Polyelectrolyte Multilayer Membranes for Separation. *Polym. Chem.* **2014**, *5* (6), 1817–1831.
- (168) Zhang, G.; Gu, W.; Ji, S.; Liu, Z.; Peng, Y.; Wang, Z. Preparation of Polyelectrolyte Multilayer Membranes by Dynamic Layer-by-Layer Process for Pervaporation Separation of Alcohol/water Mixtures. *J. Memb. Sci.* **2006**, *280* (1-2), 727–733.
- (169) Zhang, G.; Yan, H.; Ji, S.; Liu, Z. Self-Assembly of Polyelectrolyte Multilayer Pervaporation Membranes by a Dynamic Layer-by-Layer Technique on a Hydrolyzed Polyacrylonitrile Ultrafiltration Membrane. *J. Memb. Sci.* **2007**, *292* (1-2), 1–8.
- (170) Durstock, M. F.; Rubner, M. F. Dielectric Properties of Polyelectrolyte Multilayers. *Langmuir* **2001**, *17* (25), 7865–7872.
- (171) Tokuhisa, H.; Hammond, P. T. Solid-State Photovoltaic Thin Films Using TiO₂, Organic Dyes, and Layer-by-Layer Polyelectrolyte Nanocomposites. *Adv. Funct. Mater.* **2003**, *13* (11), 831–839.
- (172) Mermut, O.; Lefebvre, J.; Gray, D.; Barrett, C. Structural and Mechanical Properties of Polyelectrolyte Multilayer Films Studied by AFM. *Macromolecules* **2003**, 8819–8824.
- (173) Jin, W.; Toutianoush, A.; Tieke, B. Use of Polyelectrolyte Layer-by-Layer Assemblies as Nanofiltration and Reverse Osmosis Membranes. *Langmuir* **2003**, *19* (7), 2550–2553.
- (174) Saren, Q.; Qiu, C. Q.; Tang, C. Y. Synthesis and Characterization of Novel Forward Osmosis Membranes Based on Layer-by-Layer Assembly. *Environ. Sci. Technol.* **2011**, *45* (12), 5201–5208.
- (175) Toutianoush, A.; Jin, W.; Deligöz, H.; Tieke, B. Polyelectrolyte Multilayer Membranes for Desalination of Aqueous Salt Solutions and Seawater under Reverse Osmosis Conditions. *Appl. Surf. Sci.* **2005**, *246* (4), 437–443.
- (176) Krasemann, L.; Tieke, B. Ultrathin Self-Assembled Polyelectrolyte Membranes for Pervaporation. *J. Memb. Sci.* **1998**, *150* (1), 23–30.
- (177) Krasemann, L.; Toutianoush, A.; Tieke, B. Self-Assembled Polyelectrolyte Multilayer Membranes with Highly Improved Pervaporation Separation of

Ethanol/water Mixtures. *J. Memb. Sci.* **2001**, *181* (2), 221–228.

- (178) Harris, J. J.; Stair, J. L.; Bruening, M. L. Layered Polyelectrolyte Films as Selective, Ultrathin Barriers for Anion Transport. *Chem. Mater.* **2000**, *12* (7), 1941–1946.
- (179) Krasemann, L.; Tieke, B. Selective Ion Transport across Self-Assembled Alternating Multilayers of Cationic and Anionic Polyelectrolytes. *Langmuir* **2000**, *16* (2), 287–290.
- (180) Gogotsi, Y.; Nikitin, A.; Ye, H.; Zhou, W.; Fischer, J. E.; Yi, B.; Foley, H. C.; Barsoum, M. W. Nanoporous Carbide-Derived Carbon with Tunable Pore Size. *Nat. Mater.* **2003**, *2* (9), 591–594.
- (181) Hoffman, E. N.; Yushin, G.; Wendler, B. G.; Barsoum, M. W.; Gogotsi, Y. Carbide-Derived Carbon Membrane. *Mater. Chem. Phys.* **2008**, *112* (2), 587–591.
- (182) Caro, J.; Noack, M.; Kölsch, P.; Schäfer, R. Zeolite Membranes – State of Their Development and Perspective. *Microporous Mesoporous Mater.* **2000**, *38* (1), 3–24.
- (183) Caro, J.; Noack, M. Zeolite Membranes – Recent Developments and Progress. *Microporous Mesoporous Mater.* **2008**, *115* (3), 215–233.
- (184) Xiao, R.; Maroo, S. C.; Wang, E. N. Negative Pressures in Nanoporous Membranes for Thin Film Evaporation. *Appl. Phys. Lett.* **2013**, *102* (12), 1–5.
- (185) McGovern, R. K.; Lienhard V, J. H. On the Potential of Forward Osmosis to Energetically Outperform Reverse Osmosis Desalination. *J. Memb. Sci.* **2014**, *469*, 245–250.
- (186) Duan, C.; Karnik, R.; Lu, M.-C.; Majumdar, A. Evaporation-Induced Cavitation in Nanofluidic Channels. *Proc. Natl. Acad. Sci.* **2012**, *109* (10), 3688–3693.
- (187) Hayward, A. T. J. Negative Pressure in Liquids: Can It Be Harnessed to Serve Man? *Am. Sci.* **1971**, *59*, 434–443.